

A Measurement of the Charged and  
Neutral  $B$  Meson Lifetimes Using Fully  
Reconstructed Decay Modes

by

Alan Richard Spies

A dissertation submitted to

The Johns Hopkins University

in conformity with the requirements for the

degree of Doctor of Philosophy

Baltimore, Maryland

©Copyright by Alan Richard Spies 1994, All rights reserved

1994

## Abstract

Particles containing the heavy bottom ( $b$ ) quark decay into particles containing the charm ( $c$ ) quark. Measuring the lifetimes for this decay gives important information about the weak interaction, e.g. the CKM matrix element  $|V_{cb}|$ . The lifetimes of the charged  $B_u$  and neutral  $B_d$  meson have been measured using  $19.3 \text{ pb}^{-1}$  of  $\bar{p}p$  collisions at  $\sqrt{s} = 1.8 \text{ TeV}$  recorded by the CDF experiment at Fermilab during the 1992-93 Tevatron Collider Run 1A[1]. Unbinned likelihood fits of the proper lifetime distribution of fully reconstructed  $B \rightarrow \Psi \mathbf{K}$  candidates, where  $\Psi$  represents either a  $J/\Psi$  or a  $\psi(2S)$  and  $\mathbf{K}$  represents a meson containing a strange ( $s$ ) quark, give  $c\tau^+ = 482 \pm 48 \pm 15 \mu\text{m}$  and  $c\tau^0 = 472 \pm 55 \pm 25 \mu\text{m}$ , and  $\tau^+/\tau^0 = 1.02 \pm 0.16 \pm 0.05$  where the first error is statistical and the second error is systematic. Combining the method and results of Reference [2] with the value of  $\tau^0$  quoted here yields  $|V_{cb}| = (36 \pm 5 \pm 4) \times 10^{-3}$ .

This thesis was written under the guidance of Professor Bruce Barnett.

## Acknowledgements

First and foremost, I owe a debt of thanks that I can never repay to my parents, David and Patricia Spies, and my sister, Cathy Funk.

Numerous people at Fermilab and Johns Hopkins were instrumental in helping me during my six years of graduate school. My thesis advisor, Professor Bruce Barnett, for whom I have tremendous respect. Istvan Szapudi for being a great friend and a super study partner. Rick Snider, Chris Boswell, Mark Shaw and Kathy Turner for their help while working on SVX hardware. John Skarha, Olivier Schneider, Weiming Yao and Marjorie Shapiro, my collaborating partners in this analysis, and from whom I learned how to do a HEP analysis the right way. Jeff Tseng, for many useful discussions about everything. Douglas Glenzinski for all of the free coffee, all day, everyday. Dave Storm, Dave Keavney, Jim Kirklin and Chris Nolle for the many great times while I was at JHU.

I would also like to thank Jack Taylor (a.k.a. The Old Man) at Rhodes College for being an inspiring physics professor. Many thanks also go to Marge and Barrie “Let’s Go Ice Fishing” Wilson for befriending Suzanne and me during our years in Chicagoland. Last but not least, my wife, Suzanne, for her constant help and support.

This thesis is dedicated to my Dad, who started and always encouraged my interest in physics ...

Alan R. Spies  
July 11, 1994  
AQQZGSSDOGT

# Contents

0.1	Introduction . . . . .	xiii
<b>1</b>	<b>Theoretical Background for <math>B</math> Lifetimes</b>	<b>18</b>
1.1	The Standard Model . . . . .	18
1.2	The Electroweak Interaction . . . . .	20
1.3	The CKM Matrix . . . . .	22
1.4	$\Psi$ Production and the Decay $B \rightarrow \Psi K$ . . . . .	23
1.5	The Lifetime of $b$ hadrons . . . . .	23
1.6	Mechanisms Responsible for $b$ Hadron Lifetime Differences . . . . .	28
<b>2</b>	<b>Experimental Apparatus</b>	<b>31</b>
2.1	The Accelerator . . . . .	31
2.2	The Collider Detector at Fermilab (CDF) . . . . .	35
2.2.1	Overview . . . . .	35
2.2.2	CDF Tracking Detectors . . . . .	35
2.2.3	Central Calorimetry Overview . . . . .	42
2.2.4	Muon Chambers . . . . .	43
<b>3</b>	<b>Charged Particle Tracking</b>	<b>49</b>
3.1	Helix Parameterization at CDF . . . . .	49
3.2	Track Reconstruction in the CTC . . . . .	50
3.3	Track Reconstruction in the SVX . . . . .	51
3.4	Available Track Fits at CDF . . . . .	53
<b>4</b>	<b>The Analysis</b>	<b>56</b>
4.1	$B$ Meson Reconstruction . . . . .	56
4.1.1	$J/\psi$ Dimuon Trigger . . . . .	57

4.1.2	Muon Selection . . . . .	57
4.1.3	Track Quality Cuts . . . . .	58
4.1.4	$J/\psi$ Reconstruction . . . . .	58
4.1.5	$\psi(2S)$ Reconstruction . . . . .	59
4.1.6	$K_S^0$ Reconstruction . . . . .	63
4.1.7	$B$ Reconstruction . . . . .	63
4.1.8	Final $B$ Candidate Selection . . . . .	65
4.2	$B$ Meson Decay Length . . . . .	72
4.2.1	Determining the Primary Vertex . . . . .	72
4.2.2	Determining $L_{xy}$ and $c\tau$ . . . . .	75
4.3	$B$ Meson Lifetime . . . . .	82
4.3.1	The Lifetime Probability Density Function . . . . .	82
4.3.2	Fitting Technique # 1 . . . . .	83
4.3.3	Fitting Technique # 2 . . . . .	87
4.3.4	Fitting Technique # 3 . . . . .	90
4.3.5	Confidence Level and Statistical Error Tests . . . . .	92
4.3.6	Statistical uncertainties . . . . .	99
4.4	Systematic uncertainties . . . . .	101
4.4.1	Systematic Uncertainties Obtained from CDF's Average $b$ -Hadron Lifetime Analysis . . . . .	102
4.4.2	Uncertainty due to the Resolution Function . . . . .	103
4.4.3	Background Parameterization Uncertainty . . . . .	106
4.4.4	Bias due to the fitting procedure . . . . .	110
4.5	Consistency Checks and Cross-Checks . . . . .	110
4.5.1	Events with Large Positive or Negative $c\tau$ Values . . . . .	111
4.5.2	$K^*(892)$ signal . . . . .	114
4.5.3	$B$ Impact Parameter . . . . .	115
4.5.4	The "Decay Length and $\Delta z$ " . . . . .	117
4.5.5	Using the Run-By-Run Beam Line Versus the Event-By- Event Primary Vertex . . . . .	117
4.5.6	Tighter $J/\psi$ and $\psi(2S)$ mass cuts . . . . .	120
4.5.7	$B$ Lifetimes Versus $\bar{B}$ Lifetimes . . . . .	122
4.5.8	"Time Dependence" . . . . .	122

<b>5</b>	<b>Conclusions and Comparisons</b>	<b>126</b>
5.1	Lifetime Results and Comparisons . . . . .	126
5.2	CDF Value for $V_{cb}$ . . . . .	127
5.3	Prospects for Future $B$ Lifetime Measurements at CDF . . . . .	127
<b>A</b>	<b>The Duplicate Removal Procedure</b>	<b>132</b>
A.1	Introduction . . . . .	132
A.2	The Duplicate Removal Procedure . . . . .	135
A.3	Duplicate Removal of the Form $B_u \leftrightarrow B_u(B_d \leftrightarrow B_d)$ . . . . .	137
A.3.1	$B_u \leftrightarrow B_u (B_d \leftrightarrow B_d)$ Duplicate Removal's Effect on the the $B$ Invariant Mass Distribution . . . . .	137
A.3.2	$B_u \leftrightarrow B_u (B_d \leftrightarrow B_d)$ Duplicate Removal's Effect on the the Measured $B$ Meson Lifetime . . . . .	139
A.4	Duplicate Removal of the Form $B_u \leftrightarrow B_d(B_d \leftrightarrow B_u)$ . . . . .	148
A.4.1	$B_u \leftrightarrow B_d(B_d \leftrightarrow B_u)$ Duplicate Removal's Effect on the $B$ Invariant Mass Distribution . . . . .	148
A.4.2	$B_u \leftrightarrow B_d(B_d \leftrightarrow B_u)$ Duplicate Removal's Effect on the Measured $B$ Meson Lifetime . . . . .	151
A.5	Conclusion . . . . .	160
<b>B</b>	<b>Lifetime Likelihood Function</b>	<b>163</b>

# List of Tables

1.1	Standard Model particle properties. . . . .	20
1.2	Standard Model gauge boson properties. . . . .	21
1.3	CLEO93 results for $ V_{cb} $ . . . . .	28
2.1	Geometric coverage of CDF muon detectors. . . . .	43
3.1	SVX tracking algorithm. . . . .	53
4.1	The requirements of the $J/\psi$ Dimuon Trigger. . . . .	57
4.2	Effect of the “duplicate removal” procedure. . . . .	69
4.3	Final number of reconstructed events. . . . .	70
4.4	Results of the two-step fitting procedure. . . . .	91
4.5	Results of the simultaneous lifetime fits. . . . .	95
4.6	Summary of results of the three lifetime fitting methods. . . . .	95
4.7	Summary of systematic uncertainties. . . . .	101
4.8	Systematic studies with a flat background. . . . .	107
4.9	$K^*(892)$ signal statistics. . . . .	115
4.10	Comparison of the “tight mass cuts” analysis with the default analysis. . . . .	124
4.11	Comparison of the lifetime results on $B$ and $\bar{B}$ events. . . . .	124
4.12	Comparison of the lifetime results on the first and second part of the data. . . . .	125
A.1	Effect of the “duplicate removal” procedure. . . . .	136
A.2	The number of $B$ events with duplicates. . . . .	138
A.3	The number of duplicates per channel in $B_u(B_d)$ events with $B_u(B_d)$ duplicates. . . . .	139

A.4 The number of duplicates per channel in $B_u(B_d)$ events with $B_d(B_u)$ duplicates. . . . .	151
--	-----

# List of Figures

1.1	Feynman diagrams for charged and neutral current couplings.	21
1.2	CDF integrated $b$ -quark cross-section measurements. . . . .	24
1.3	Internal spectator diagram for the decay $B \rightarrow \Psi K$ . . . . .	25
1.4	Spectator diagram for the semileptonic $\bar{B}^0$ meson decay. . . .	26
1.5	Diagram for $W$ exchange. . . . .	29
1.6	Feynman diagram that motivates Pauli Interference. . . . .	29
2.1	Schematic representation of accelerator complex at the Fermi National Accelerator Laboratory. . . . .	32
2.2	Diagram of steps involved in accelerating protons to 900 $GeV$ . . . . .	33
2.3	A view of CDF in the collision hall with RUN 1A upgrades. . . . .	36
2.4	Cross sectional view of CDF in the collision hall with Cartesian coordinates. . . . .	37
2.5	Isometric view of a single SVX barrel. . . . .	38
2.6	A cut-a-way view of 16 VTX modules. . . . .	39
2.7	$r - \phi$ view of the CTC. . . . .	41
2.8	A view in $r - \phi$ of a CMU chamber. . . . .	44
2.9	View of a single CMU cell . . . . .	45
2.10	Relationship between the muon incident and deflection angles. . . . .	47
3.1	Parameterization of the trajectory of a positively charged particle at CDF. . . . .	50
4.1	Dimuon mass distribution. . . . .	60
4.2	Dimuon mass distribution with $p_T > 15 GeV/c$ . . . . .	61
4.3	$J/\psi \pi\pi$ mass distribution. . . . .	62
4.4	$\pi\pi$ mass distributions. . . . .	64

4.5	<i>B</i> mass distributions. . . . .	71
4.6	Beam parameters measured in the SVX. . . . .	74
4.7	Combined $c\tau$ distributions for all reconstructed $B_u$ mesons. . .	77
4.8	Combined $c\tau$ distributions for all reconstructed $B_d$ mesons. . .	78
4.9	Decay length error and significance for all $B$ candidates. . . .	79
4.10	Error on $c\tau$ versus $c\tau$ for $B_u$ signal and peak candidates. . . .	80
4.11	Error on $c\tau$ versus $c\tau$ for $B_d$ signal and peak candidates. . . .	81
4.12	Fitting Technique # 1. . . . .	88
4.13	Fit of the combined $c\tau$ distributions of all reconstructed $B_u$ mesons. . . . .	93
4.14	Fit of the combined $c\tau$ distributions of all reconstructed $B_d$ mesons. . . . .	94
4.15	Monte Carlo tests of the simultaneous fit to the $B_u$ data. . . .	97
4.16	Monte Carlo tests of the simultaneous fit to the $B_d$ data. . . .	98
4.17	Background subtracted $c\tau$ distributions. . . . .	100
4.18	Average resolution functions. . . . .	105
4.19	Fit of the lifetime of the $B_u$ candidates with an additional flat background allowed to adjust. . . . .	108
4.20	Fit of the lifetime of the $B_d$ candidates with an additional flat background allowed to adjust. . . . .	109
4.21	Reconstructed $B_u$ decay with a 0.52 <i>cm</i> decay length (Run 42326, Event 78838). . . . .	112
4.22	Previous figure (Run 42326, Event 78838) magnified by x4, showing the presence of another secondary vertex. . . . .	113
4.23	$K^*(892)$ mass distributions. . . . .	116
4.24	Impact parameter distributions of the $B$ candidates. . . . .	118
4.25	The $z$ coordinate of the $B$ candidates as a function of decay length. . . . .	119
4.26	Comparison of decay length errors using VXPRIIM with those obtained from the beam line. . . . .	121
4.27	Resolution on the $J/\psi$ mass as a function of the $J/\psi$ transverse momentum. . . . .	123
5.1	Comparison of Recent $B_u$ Lifetime Measurements. . . . .	128

5.2	Comparison of Recent $B_d$ Lifetime Ratio Measurements. . . .	129
5.3	Comparison of Recent $B$ Lifetime Ratio Measurements. . . . .	130
A.1	The invariant mass distributions of $B_u$ candidates with $B_u$ duplicates. . . . .	140
A.2	The invariant mass distributions of $B_d$ candidates with $B_d$ duplicates. . . . .	141
A.3	The invariant mass of the selected $B_u$ candidate versus the $B_u$ duplicates. . . . .	142
A.4	The invariant mass of the selected $B_d$ candidate versus the $B_d$ duplicates. . . . .	143
A.5	The invariant mass distributions of $B_u$ candidates with $B_u$ duplicates, $c\tau > 100 \mu m$ . . . . .	144
A.6	The invariant mass distributions of $B_d$ candidates with $B_d$ duplicates, $c\tau > 100 \mu m$ . . . . .	145
A.7	The invariant mass of the selected $B_u$ candidate versus the $B_u$ duplicates, $c\tau > 100 \mu m$ . . . . .	146
A.8	The invariant mass of the selected $B_d$ candidates versus the $B_d$ duplicates, $c\tau > 100 \mu m$ . . . . .	147
A.9	Comparison of the $c\tau$ value of the selected $B_u(B_d)$ peak region candidate with the rejected $B_u(B_d)$ peak region candidates. . .	149
A.10	The invariant mass distributions of $B_u$ candidates with $B_d$ duplicates. . . . .	152
A.11	The invariant mass distributions of $B_d$ candidates with $B_u$ duplicates. . . . .	153
A.12	The invariant mass of the selected $B_u$ candidate versus the $B_d$ duplicates. . . . .	154
A.13	The invariant mass of the selected $B_d$ candidate versus the $B_u$ duplicates. . . . .	155
A.14	The invariant mass distributions of $B_u$ candidates with $B_d$ duplicates, $c\tau > 100 \mu m$ . . . . .	156
A.15	The invariant mass distributions of $B_d$ candidates with $B_u$ duplicates, $c\tau > 100 \mu m$ . . . . .	157

A.16	The invariant mass of the selected $B_u$ candidate versus the $B_d$ duplicates, $c\tau > 100 \mu m$ . . . . .	158
A.17	The invariant mass of the selected $B_d$ candidate versus the $B_u$ duplicates, $c\tau > 100 \mu m$ . . . . .	159
A.18	Comparison of $c\tau$ value of the selected $B_u(B_d)$ peak region candidate with the rejected $B_d(B_u)$ peak region candidates. . . .	161

## 0.1 Introduction

High energy physics endeavors to discover the ultimate building blocks of (anti)matter and to understand the forces that bind these building blocks together. These building blocks form everything around us – trees, cars, the stars, ourselves, everything. The matter that makes up our everyday world is composed of stable configurations of the fundamental building blocks. Experimental high energy physicists learn more about these fundamental objects by creating highly energetic, or excited, configurations, which ultimately decay back into stable ones. By studying the decay products, we learn what (anti)matter is composed of; by studying the ways in which these particles decay, we learn about the forces that govern these particles.

Consider the simplest atom, the hydrogen atom, which consists of a proton and an electron. The proton is an everyday example of what high energy physicists call hadrons. The electron is a familiar example of the family of particles referred to as leptons. Leptons are fundamental building blocks; protons, however, are not. Rather, protons, like all hadrons, are composed of still smaller particles called quarks. Hadrons which are composed of three quarks, like the proton, are called baryons. Hadrons composed of a quark and its antimatter equivalent, the antiquark, are called mesons. All of the experimental data collected so far confirm this relatively simple arrangement of the fundamental building blocks; i.e., all of (anti)matter can be grouped into two large categories known as hadrons and leptons. If the object is a lepton, it is a fundamental constituent of (anti)matter. If the object is a hadron, it is composed of the fundamental particles known as quarks. Finally, particles known as gauge bosons act as “force carriers”, i.e. fundamental particles interact with each other by exchanging gauge bosons. The theory that puts this in a neat and tidy package is known as the Standard Model; it will be given a more thorough treatment in Chapter 1. For now, let us focus on quark/antiquark pairs, i.e. mesons.

This thesis is concerned with a type of meson known as the  $B$  meson. It is so noted because it contains a bottom ( $b$ ) quark.  $B$  mesons can be produced when protons collide at high energies with their antimatter partner, antiprotons. These collisions occur at the Fermi National Accelerator Labora-

tory (Fermilab) in a proton-antiproton ( $p\bar{p}$ ) accelerator called the Tevatron at the rate of about 100,000 times per second. Surrounding the collision point, referred to as the interaction region, is a particle detector called the Collider Detector at Fermilab (CDF). This detector measures the energy and momentum of the particles produced when the protons collide with the antiprotons. At a rate of approximately 60 times per second, a  $B$  meson is produced in such a collision and subsequently decays. By studying the decay products of the  $B$  meson, we can learn its mass, its electric charge, its lifetime. By lifetime we refer to the amount of time a  $B$  meson exists before it decays into other particles. This thesis describes a measurement of the  $B$  meson's lifetime.

$B$  mesons used in this analysis can travel up to about 3  $mm$  due to relativistic time dilation before decaying into other particles, called daughter particles. Because of the high precision tracking capability of a device known as the Silicon Vertex Detector (SVX), the location of where the  $B$  meson decayed can be measured directly by forming the intersection of the tracks left by the charged daughter particles in the SVX. This process is called vertexing, and the vertex at which the  $B$  meson decayed is referred to as the secondary vertex. The point at which the  $B$  meson was produced is called the primary vertex. The distance the  $B$  meson traveled before it decayed, i.e. its observed decay length, is simply the difference between the primary and secondary vertices.

If all of the  $B$  meson's daughter particles have either a positive or negative electric charge and are detected in CDF, the event is said to be fully reconstructed, which means that the  $B$  meson's mass, momentum and light quark partner ( $\bar{u}$  or  $\bar{d}$ ) are completely determined. Knowing the  $B$  meson's light quark partner assures a pure sample of charged  $B_u$  and neutral  $B_d$  mesons, respectively. Precise measurements of the mass and momentum are needed because the equation that relates the observed decay length and the proper lifetime of the  $B$  meson depends on these terms, i.e.

$$\tau = L_{xy} \cdot \frac{B_{\text{mass}}}{B_{\text{PT}} \cdot c} \quad (0.1)$$

where  $L_{xy}$  is the transverse decay length,  $B_{\text{mass}}$  is the mass,  $B_{\text{PT}}$  is the transverse momentum, and  $c$  is the speed of light.

The  $B$  meson lifetime averaged over the various  $b$  hadrons is  $1.46 \pm 0.06(\text{sys}) \pm 0.06(\text{stat})$   $ps$ [3]. Qualitatively, the lifetimes ( $\tau$ ) of the individual bottom quark

(b) hadrons are expected to exhibit the following hierarchy:[4, 5] (see Section 1.6)

$$\tau(B_u^+) > \tau(B_s^0) \sim \tau(B_d^0) > \tau(\Lambda_b^0). \quad (0.2)$$

The expected value for  $\tau(B_u^+)/\tau(B_d^0)$  is 1.0 to 1.1. The most precise measurement of this ratio, adding the statistical and systematic uncertainties in quadrature, prior to the results described in this thesis was  $0.96 \pm 0.22$ [6], with values of  $\tau^+(\tau^0) = 1.47 \pm 0.26(1.52 \pm 0.22)$  ps[6]. It is worth noting that measurements leading to these results relied on inclusive decay modes and Monte Carlo techniques. Such measurements are plagued by systematic uncertainties. The method employed in this analysis, however, is conceptually simple and straightforward, is dominated presently by statistical, rather than systematic, uncertainties, and gives the most precise (and probably the most accurate) published values for  $\tau^+$ ,  $\tau^0$ , and  $\tau^+/\tau^0$  for the  $B_u$  and  $B_d$  mesons[1].

Largely because the bottom quark is much heavier than the charm quark[5] (see Section 1.6),  $\tau(B_u^+)/\tau(B_d^0)$  is not expected to deviate from 1.00 by the dramatic amount measured in the  $D$  meson case\*. Nevertheless, various QCD corrections are postulated to contribute to an analogous lifetime difference in the  $B$  meson system. Calculations by Tanimoto indicate that  $\tau(B_u^+)/\tau(B_d^0)$  must be greater than 1.00 in order to obtain reasonable semileptonic and inclusive  $b \rightarrow c\bar{c}s$  decay rates ( $\leq 12\%$  and  $\leq 20\%$ , respectively)[8]. However, a recent CLEO measurement of the 2-body  $B$  decay topology implies that  $\tau^+/\tau^0 < 1.00$ [9] since their results indicate that in the case of the  $B^+(B^0)$  meson, the internal spectator diagram contributes constructively(destructively) to the partial  $B^+(B^0)$  width. The aim of this analysis is to measure  $\tau(B_u^+)$ ,  $\tau(B_d^0)$  and their ratio with a previously unattainable precision in order to constrain/test theoretical predictions.

$B_u$  and  $B_d$  mesons produced in  $\bar{p}p$  collisions in Fermilab's Tevatron can decay via the fully hadronic decay chain given below (references to a specific charge state imply the charge conjugate as well throughout this thesis):

$$\begin{aligned} B_u &\rightarrow J/\psi K^+, \\ B_u &\rightarrow J/\psi K^*(892)^+, \\ B_u &\rightarrow \psi(2S)K^+, \end{aligned}$$

---

\* $\tau(D_s^+)/\tau(D_u^0) = 2.58 \pm 0.09 \pm 0.08$ [7]

$$B_u \rightarrow \psi(2S)K^*(892)^+,$$

and

$$\begin{aligned} B_d &\rightarrow J/\psi K_S^0, \\ B_d &\rightarrow J/\psi K^*(892)^0, \\ B_d &\rightarrow \psi(2S)K_S^0, \\ B_d &\rightarrow \psi(2S)K^*(892)^0, \end{aligned}$$

where

$$\begin{aligned} J/\psi &\rightarrow \mu^+ \mu^-, \\ \psi(2S) &\rightarrow J/\psi \pi^+ \pi^-, \quad J/\psi \rightarrow \mu^+ \mu^-, \\ K_S^0 &\rightarrow \pi^+ \pi^-, \\ K^*(892)^0 &\rightarrow K^+ \pi^-, \end{aligned}$$

and

$$K^*(892)^+ \rightarrow K_S^0 \pi^+, \quad K_S^0 \rightarrow \pi^+ \pi^-.$$

In all of these decay modes, the two daughter muons from the  $J/\psi$  provide a unique signature, or trigger, for  $B \rightarrow \Psi K$  events, where  $B$  represents either a  $B_u$  or a  $B_d$ ,  $\Psi$  represents either a  $J/\psi$  or a  $\psi(2S)$ , and  $K$  implies any of the strange mesons listed above. The two muons also facilitate the determination of the secondary vertex position of the  $B$  meson in the  $r - \phi$  plane, since muon tracks in the SVX are all that are required to precisely determine the secondary vertex of the parent  $B$  meson. The signed decay length in two dimensions,  $L_{xy}$ , is taken to be the difference between the nominal beam position and the secondary vertex position projected onto the  $B$  flight direction. Because the  $B$  mesons are fully reconstructed, the light quark partner of the  $b$  quark, i.e.  $\bar{u}$  or  $\bar{d}$ , is unambiguously determined. Full reconstruction of the events also enables a precise calculation of the relativistic boost factor,  $\beta\gamma$ . As a result, model independent proper decay length distributions for  $B_u$  and  $B_d$  mesons are obtained. From these, the individual lifetimes,  $\tau^+$  and  $\tau^0$ , are extracted using an unbinned maximum likelihood fit. The ratio,  $\tau^+/\tau^0$ , is then calculated, and a value of  $|V_{cb}|$  is obtained by combining a CLEO result with the CDF value for  $\tau^0$ .

During the 1980's, the surprising discovery and subsequent study of the dramatically different lifetimes of the charged  $D_d$  and neutral  $D_u$  mesons led not only to a better understanding of the mechanism responsible for this difference, but also to a more complete picture of charm quark ( $c$ ) decay. Because of the copious production of  $B$  mesons at  $\sqrt{s} = 1.8 \text{ TeV}$  at Fermi National Accelerator Laboratory (Fermilab), perhaps the Collider Detector at Fermilab (CDF), with its Silicon Vertex Detector (SVX), will make the 1990's the decade in which the analogous  $B$  meson regime is explored with equal rigor. The measurement and analysis described in the pages that follow represent a first step in achieving this goal.

This thesis describes an analysis performed at Fermilab with  $19.3 \text{ pb}^{-1}$  of data collected by CDF between May 12, 1992 and June 1, 1993. It is divided into 5 main sections:

1. Theoretical Framework
2. Experimental Facilities
3. Tracking at CDF
4. Analysis
5. Conclusions and Comparisons

Chapter 1 describes the current theoretical framework used to describe the interactions between fundamental particles, partons, in general, and focuses on expressions relevant to the decay of  $B$  mesons in particular. Chapter 2 describes the apparatus used to accelerate protons and antiprotons and to bring them into collision at  $\sqrt{s} = 1.8 \text{ TeV}$ . This chapter also describes the general characteristics of CDF subsystems used to detect  $B$  mesons, while chapter 3 focuses on the charged particle tracking detector that makes this analysis possible, namely the SVX. Chapter 4 describes the analysis procedure in detail, and this thesis ends, fittingly enough, with Chapter 5, the conclusion, where results of this measurement are listed and compared with theoretical expectations and previous measurements.

# Chapter 1

## Theoretical Background for $B$ Lifetimes

This section is devoted to theoretical topics relevant to the lifetime of hadrons containing a  $b$ -quark. A rapid overview of the standard model of particle interactions is first presented before focusing on the  $b$  quark. Because this analysis only considers  $B$  meson decays involving an intermediate daughter  $\Psi$ ,  $\Psi$  production at CDF will be quickly discussed and an estimate for the branching ratio of  $B \rightarrow \Psi X$  will be given. Next the  $b$  quark cross section at the Tevatron will be considered, followed by a more detailed treatment of the  $b$  quark lifetime. The lifetime discussion will ultimately give an equation for the  $b$  lifetime and will examine mechanisms that contribute to lifetime differences between  $b$  hadrons.

### 1.1 The Standard Model

The standard model of particle interactions, referred to simply as the Standard Model[10], describes three of the four interactions found in nature. These are the strong, weak and electromagnetic interactions. The fourth force, gravity, does not fall under the umbrella of the Standard Model for essentially two main reasons: (1) the relative strength of the gravitational interaction relative to the strong(weak)[electromagnetic] interaction is  $\sim 10^{-38}$ ( $\sim 10^{-33}$ )[ $\sim 10^{-36}$ ], and (2) an acceptable quantum field theory of gravity does not exist. The

fundamental fermions (spin 1/2 particles) of the Standard Model are referred to as leptons and quarks; these are listed in Table 1.1. According to the Standard Model, the fundamental particles are pointlike and massless; the Higgs boson is postulated to be responsible for the experimentally observed masses of the leptons and quarks[11]. Leptons and quarks are grouped in sets according to the way in which they interact. Leptons are grouped into three generations, with each generation having its own quantum number. For example, the muon and muon neutrino carry a muon lepton number. Similar to the leptons, the quarks also belong to one of three generations, but instead of a quantum number being associated with each generation of quarks, the individual quarks themselves carry a quantum number, referred to as the flavor of the quark. For example, the  $c$  and  $s$  quarks belong to the same generation, but each carry their own quantum number, charm and strangeness, respectively. Finally, gauge bosons, listed in Table 1.2, are associated with the quantized fields of the strong and electroweak interactions.

Strong interactions, according to the branch of the Standard Model known as Quantum Chromodynamics (QCD)[12], are described by the the group  $SU(3)$ , i.e. strong interactions are symmetric under local gauge transformations in  $SU(3)$ . According to QCD, quarks and gluons do not exist as free particles but are confined in colorless objects of  $q\bar{q}$  pairs called mesons or in  $qqq$  states called baryons.

The second branch of the Standard Model, referred to as the Electroweak or Glashow-Salam-Weinberg (GSW) Model[13], asserts that the weak and electromagnetic interactions are a manifestation of single electroweak force that is described by a  $SU(2)_L \otimes U(1)_L$  group, where the subscript  $L$  refers to “left-handed” and draws attention to the fact that the electroweak interaction is sensitive to the helicity of the particle. A process known as symmetry breaking is responsible for the fact that the electroweak force appears as two separate forces (weak and electromagnetic) at low energy scales. Because the decay of a  $b$  quark into a  $c$  quark lies in the domain of the weak interaction, additional details of the GSW model are presented in Section 1.2; QCD is mentioned here mainly for completeness, although the effect of gluon emission in weak annihilation diagrams is important and will be discussed in Section 1.6.

Generation:	1	2	3	$I_3$	Y	Q
Left – Handed Lepton Doublets	$\begin{pmatrix} \nu_e \\ e \end{pmatrix}_L$	$\begin{pmatrix} \nu_\mu \\ \mu \end{pmatrix}_L$	$\begin{pmatrix} \nu_\tau^* \\ \tau \end{pmatrix}_L$	1/2 -1/2	-1 -1	0 -1
Left – Handed Quark Doublets	$\begin{pmatrix} u \\ d \end{pmatrix}_L$	$\begin{pmatrix} c \\ s \end{pmatrix}_L$	$\begin{pmatrix} t \\ b \end{pmatrix}_L$	1/2 -1/2	1/3 1/3	2/3 -1/3
Right – Handed Lepton Singlets	$(e)_R$	$(\mu)_R$	$(\tau)_R$	0	-2	-1
Right – Handed Quark Singlets	$(u)_R$ $(d)_R$	$(c)_R$ $(s)_R$	$(t)_R$ $(b)_R$	0 0	4/3 2/3	-2/3 -1/3

Table 1.1: Properties of particles of the Standard Model[14, 15]; the superscript \* denotes particles for which only indirect evidence exists. Right handed neutrinos have not been observed and are not included in the Standard Model. The quantum numbers of the third component  $I_3$  of weak isospin, weak-hypercharge  $Y$  and the charge  $Q$  are related by  $Q = I_3 + \frac{1}{2}Y$ .

## 1.2 The Electroweak Interaction

According to the GSW Model, the left handed fermions form doublets of the  $SU(2)_L \otimes U(1)_L$  weak isospin group, while right handed fermions transform as singlets. The coupling constants of the electroweak interaction,  $g$  and  $g'$ , are related to the electric charge,  $e$ , and the weak mixing angle,  $\theta_W$ , by[10]

$$g \sin \theta_W = g' \cos \theta_W = e, \quad (1.1)$$

where  $g$ [ $g'$ ] is the coupling constant of the  $SU(2)$ [ $U(1)$ ] weak isospin[weak hypercharge] group and  $e$  is the coupling constant of the  $U(1)$  electromagnetic interaction. The gauge bosons of the electroweak field are the photon,  $\gamma$ , the  $Z^0$  and the  $W^\pm$ . The massive  $Z^0$  and  $W^\pm$  bosons are associated with the short range weak interaction, while the massless photon propagates the infi-

	Spin	Charge	Color	Mass ( $GeV/c^2$ )	Width ( $GeV/c^2$ )
$\gamma$	1	0	NA	$< 10^{-36}$	stable
$Z^0$	1	0	NA	$91.173 \pm 0.020$	$2.487 \pm 0.010$
$W^\pm$	1	$\pm 1$	NA	$80.22 \pm 0.26$	$2.12 \pm 0.11$
$g_i$ ( $i = 1, \dots, 8$ )	1	0	red, green, blue	0	NA

Table 1.2: Standard Model gauge boson properties[14]. The subscript  $i$  denotes the eight gluons of the QCD SU(3) color octet.

nite range electromagnetic force. The weak mixing angle,  $\theta_W$ , the  $Z^0$  mass and the  $W^\pm$  mass are related via[10]

$$\rho = \frac{M_W^2}{M_Z^2 \cos^2 \theta_W}. \quad (1.2)$$

Experimentally,  $\rho = 1$ [16]; hence, Eq. (1.2) is often given as

$$\sin^2 \theta_W = 1 - \frac{M_W^2}{M_Z^2}. \quad (1.3)$$

Feynman diagrams for various electroweak interactions are shown in Fig. 1.1.

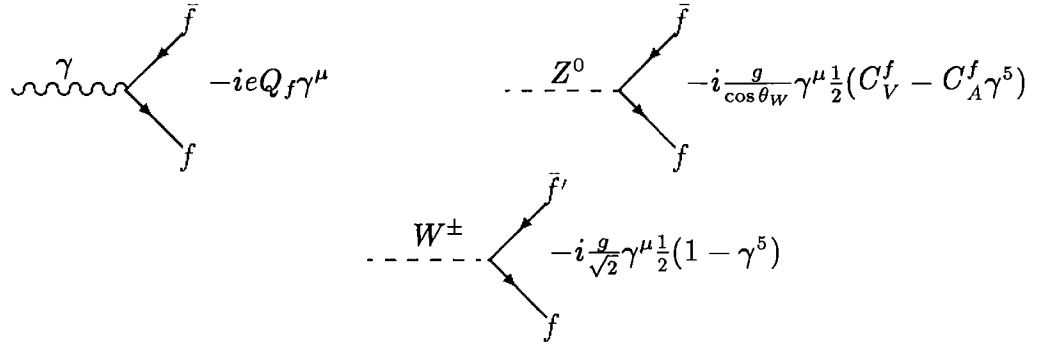


Figure 1.1: Feynman diagrams for charged and neutral current couplings[10]. The parameter  $C_V^f$  ( $C_A^f$ ) is the fermion vector(axial-vector) coupling constant, given by  $I_3^f - 2 \sin^2(\theta_W) Q_f$  ( $I_3^f$ ), where the  $f$  refers to the particular fermion,  $Q_f$  is the fermion charge, and  $I_3^f$  is the third component of the weak isospin.

### 1.3 The CKM Matrix

The decay of a  $b$  quark into a  $c$  quark involves a change in flavor and electric charge and occurs via an electroweak interaction. The weak eigenstates are rotated with respect to the observed mass eigenstates, i.e. the weak eigenstates are linear combinations of the mass eigenstates shown in Table 1.1. The rotation between the weak and mass eigenstates was first proposed by Cabibbo[17] to explain the long lifetime of  $s \rightarrow u$  transitions relative to  $u \rightarrow d$ . This model was later generalized by Kobayashi and Maskawa[18] to include all six quarks. According to this model, the left-handed quark doublets are arranged as follows:

$$\begin{pmatrix} u \\ d' \end{pmatrix} \quad \begin{pmatrix} c \\ s' \end{pmatrix} \quad \begin{pmatrix} t \\ b' \end{pmatrix} \quad (1.4)$$

where the  $d'$ ,  $s'$  and  $b'$  quarks are the mass eigenstates that are rotated with respect to the weak eigenstates  $d$ ,  $s$ , and  $b$ . By convention, the  $u$ ,  $c$  and  $t$  quarks are unmixed. The Cabibbo-Kobayashi-Maskawa (CKM) matrix relates the two bases, i.e.

$$\begin{pmatrix} d' \\ s' \\ b' \end{pmatrix} = \begin{pmatrix} V_{ud} & V_{us} & V_{ub} \\ V_{cd} & V_{cs} & V_{cb} \\ V_{td} & V_{ts} & V_{tb} \end{pmatrix} \begin{pmatrix} d \\ s \\ b \end{pmatrix} \quad (1.5)$$

The present 90% confidence level magnitudes of the individual CKM matrix elements are[14]

$$\begin{pmatrix} V_{ud} & V_{us} & V_{ub} \\ V_{cd} & V_{cs} & V_{cb} \\ V_{td} & V_{ts} & V_{tb} \end{pmatrix} = \begin{pmatrix} 0.9747 \text{ to } 0.9759 & 0.218 \text{ to } 0.224 & 0.002 \text{ to } 0.007 \\ 0.218 \text{ to } 0.224 & 0.9735 \text{ to } 0.9751 & 0.032 \text{ to } 0.054 \\ 0.003 \text{ to } 0.018 & 0.030 \text{ to } 0.054 & 0.9985 \text{ to } 0.9995 \end{pmatrix} \quad (1.6)$$

where unitarity and the existence of only three generations is assumed. The analysis described in this thesis actually provides a measurement of one of the CKM matrix elements,  $V_{cb}$ , as described in Section 5.2.

## 1.4 $\Psi$ Production and the Decay $B \rightarrow \Psi\mathbf{K}$

The analysis described in this thesis considers  $B$  meson decays of the form  $B \rightarrow \Psi\mathbf{K}$ , where  $\Psi$  represents either a  $J/\psi$  or a  $\psi(2S)$  and  $\mathbf{K}$  denotes  $K$ ,  $K_S^0$ , or  $K^*(892)$ . The trigger for this analysis (see Section 4.1.1) relies on the decay  $J/\psi \rightarrow \mu^+\mu^-$ . As shown in Fig. 1.2, the  $b$  cross section at the Tevatron is large enough (e.g. a factor of  $\sim 3 \times 10^4$  larger than at CESR and  $\sim 4 \times 10^3$  larger than at LEP[19]) to allow CDF to exploit the relatively small branching ratios[14, 20] of the decays considered here:

$$\text{BR}(B \rightarrow J/\psi X)\text{BR}(J/\psi \rightarrow \mu^+\mu^-) = (7.7 \pm 1.3) \times 10^{-4}$$

and

$$\text{BR}(B \rightarrow \psi(2S)X)\text{BR}(\psi(2S) \rightarrow J/\psi\pi^+\pi^-)\text{BR}(J/\psi \rightarrow \mu^+\mu^-) = (9.34 \pm 4.14) \times 10^{-5}.$$

The production of  $\Psi$  mesons at the Tevatron occurs via two mechanisms[21]: (1) by direct production via gluon fusion and (2) through the production and decay of  $b$  hadrons, i.e.  $gg, q\bar{q} \rightarrow b\bar{b}$  and  $gg \rightarrow b\bar{b}g$  with  $b \rightarrow B \rightarrow \Psi X$ [22]. As the  $b$  quark fragments,  $b$ -hadrons are produced in a highly non-perturbative process that currently can only be described by phenomenological models, e.g. Peterson *et al.* fragmentation model[23] The Feynman diagram that describes the decay modes considered in this analysis is the color mixed or internal spectator diagram, shown in Fig. 1.3. This diagram is “color suppressed” because the color of the  $\bar{c}, s$  quarks from the virtual  $W$  must match the color of the parent  $b$  quark.

## 1.5 The Lifetime of $b$ hadrons

The first observation in 1983 of the long lifetime ( $\sim 1$  ps) of the  $b$  quark by the MAC and MARK II collaborations at PEP[24] was unexpected, e.g. Barger, Long, and Pakvasa predicted that  $\tau_b < 0.12$  ps[25] using results from the strange meson sector. Up to 1983, it was generally assumed that mixing between the third and second generations, the mechanism responsible for  $b \rightarrow c$

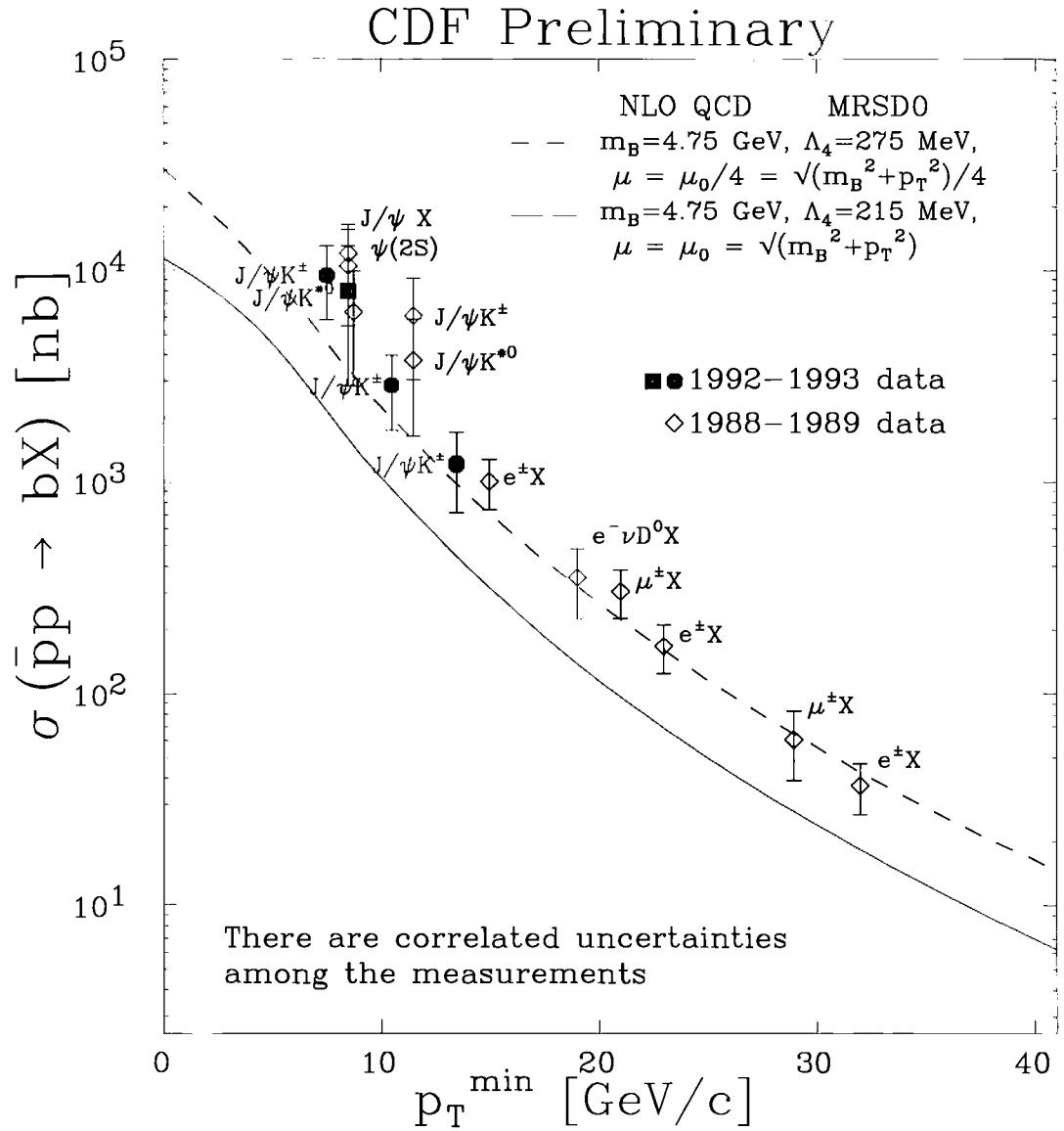


Figure 1.2: Integrated  $b$ -quark cross-section measurements made by CDF for  $|y| < 1.0$ . The  $\psi(2S)$  points assume that all  $\psi(2S)$  mesons come from the decay of  $b$ -quarks.

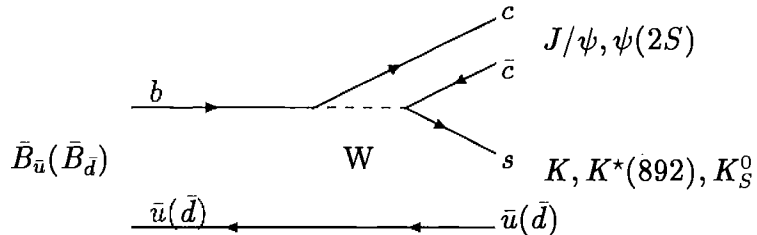


Figure 1.3: Internal spectator diagram for the decay  $B \rightarrow \Psi K$ .

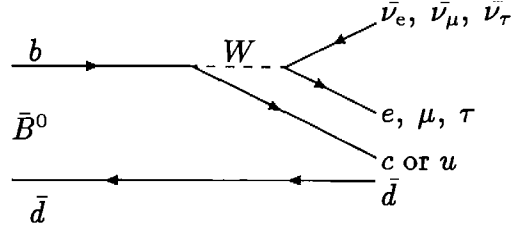
transitions, was essentially identical to mixing between the second and first generations. This assumption yields  $\tau_b \sim 0.1 \text{ ps}$ [4]. Hence, the observation of the long  $b$  lifetime was the first indication that the third and second generations are not as strongly coupled as the second and first.

When deriving an equation for the  $b$  quark lifetime, the expression for the semileptonic decay width is used because the uncertainties in the Standard Model parameters are smaller than in the hadronic case and because the semileptonic branching ratio is well measured[4]. The lifetime and the semileptonic decay width,  $\Gamma_{SL}$  are related by

$$\tau_b = \frac{1}{\Gamma_{total}} = \frac{\text{BR}_{SL}}{\Gamma_{SL}}. \quad (1.7)$$

The simplest diagrams that relate the lifetime of the  $b$  quark to a particular  $B$  meson are shown in Figs 1.3 and 1.4. These are referred to as spectator diagrams because the light  $u(d)$  valence quark does not participate in the decay. If the spectator diagram does in fact describe the decay of  $B$  mesons, the lifetimes of the  $B_u$  and  $B_d$  mesons should be equal. The principal aim of the analysis described in this thesis is to measure the degree to which these lifetimes differ. As will be discussed in Section 1.6, it is expected that non-spectator effects should cause no more than a 10% difference in the lifetime of the  $B_u$  and  $B_d$  mesons.

Given the semileptonic spectator diagram in Fig. 1.4, it is possible to express the decay amplitude as a simple product of the leptonic and hadronic


 Figure 1.4: Spectator diagram for the semileptonic  $\bar{B}^0$  meson decay.

currents (see e.g. [26]), i.e.

$$M_{SL}(b \rightarrow q) = -\frac{G_F}{\sqrt{2}} V_{qb} [\bar{q}\gamma^\mu(1 - \gamma_5)b] [\bar{l}\gamma^\mu(1 - \gamma_5)\nu_L], \quad (1.8)$$

where  $G_F$  is the Fermi coupling constant obtained from observed rates for muon decay, equal to  $1.16639 \times 10^{-5} \text{ GeV}^{-2}$  [14] and  $V_{qb}$  refers to the particular CKM matrix element governing the  $b \rightarrow q$  transition. Squaring  $M_{SL}$  and integrating over phase space yields

$$\Gamma_{SL}(b \rightarrow q) = \frac{G_F^2 m_b^5}{192\pi^3} \cdot |V_{qb}|^2 \cdot F(\epsilon), \quad (1.9)$$

where the term  $F(\epsilon) = F(\epsilon)_{PS} \times F(\epsilon)_{QCD}$  with  $F(\epsilon)_{PS}$  denoting a phase space term,  $F(\epsilon)_{QCD}$  describing a QCD correction term that describes the effect of  $b$  hadrons radiating gluons, and  $\epsilon \equiv \frac{m_q}{m_b}$ . The expression for the phase space term is

$$F(\epsilon)_{PS} = 1 - 8\epsilon^2 + \epsilon^6 - \epsilon^8 - 24\epsilon^4 \ln \epsilon, \quad (1.10)$$

while the QCD radiation correction term is given by

$$F(\epsilon)_{QCD} = 1 - \frac{2\alpha_s}{3\pi} g(\epsilon), \quad (1.11)$$

where  $\alpha_s$  is the strong coupling constant and

$$g(\epsilon) = \left( \pi^2 - \frac{31}{4} \right) (1 - \epsilon)^2 + \frac{3}{2}. \quad (1.12)$$

The Standard Model asserts that the  $b$  quark can decay only to a  $c$  or  $u$  quark. Combining Eq. (1.9) and Eq. (1.7) gives the lifetime of the  $b$  quark:

$$\tau_b = \frac{BR_{SL}}{\Gamma_{SL}} = \frac{BR_{SL}}{\frac{G_F^2 m_b^5}{192\pi^3} \cdot [F(\epsilon_u)|V_{ub}|^2 + F(\epsilon_c)|V_{cb}|^2]}. \quad (1.13)$$

Because  $|V_{ub}/V_{cb}| = 0.10 \pm 0.03$ [14], the  $F(\epsilon_u)|V_{ub}|^2$  term is generally neglected in Eq. (1.13), resulting in a model dependent method for extracting  $|V_{cb}|$  from a measurement of  $\tau_b$ . Such measurements are actually dominated by the uncertainty in  $m_b$  and by the quark decay model used to describe the inclusive semileptonic decay of the  $B$  meson.

An essentially model independent method of extracting  $|V_{cb}|$  that relies on Heavy Quark Effective Theory (HQET)[27] to describe  $B \rightarrow D^* \ell \bar{\nu}$  transitions is described in Reference [28]. HQET can be applied to hadrons containing a  $c$ ,  $b$  or  $t$  quark, denoted by  $Q$ . Such a hadron can be treated as an atom-like system, with the heavy  $Q$  quark defining the system's center of mass. As  $m_Q \rightarrow \infty$ , the heavy  $Q$  quark can be treated as a static source of gluons, the internal dynamics of the hadron become independent of the  $Q$  quark's spin and mass, and the universal function  $\xi(\nu \cdot \nu')$ , where  $\xi(\nu \cdot \nu')$  is the Isgur-Wise function[29] and  $\nu \cdot \nu'$  is the scalar product of the four-velocity  $\nu_\mu$ , can be used as the hadronic form factor. The term  $\nu \cdot \nu'$  is the rapidity given as

$$y = \nu \cdot \nu' = \frac{E_{D^*}}{m_{D^*}} = \frac{m_B^2 + m_{D^*}^2 - q^2}{2m_B m_{D^*}}, \quad (1.14)$$

where  $y = 1$  corresponds to the kinematic endpoint ( $c$  produced at rest relative to the  $b$ ), the kinematic region where HQET can reliably calculate the total  $b \rightarrow c$  decay rate. In practice, however,  $m_Q$  is not considered to be infinite, and a variety of model dependent corrections to the Isgur-Wise function are used as the hadronic form factor; a number of these are listed in Table 1.3. The experimentally observed decay rate at  $y \gtrsim 1$  for  $B \rightarrow D^*$  decays is not helicity suppressed, as is the case for  $B \rightarrow D \ell \bar{\nu}$  decays. As a result, the  $d\Gamma_{b \rightarrow c}/dy$  distribution for  $\bar{B}^0 \rightarrow D^{*+} \ell^- \bar{\nu}$  decays measured by CLEO[2] can be extrapolated to  $y = 1$ . A fit to these data yields the results presented in Table 1.3. Rather than averaging these, CLEO takes the ISGW form for  $\xi(y)$  and obtains  $|V_{cb}| = (37 \pm 5(stat) \pm 4(syst)) \times 10^{-3}$ [2].

Isgur-Wise $\xi(y)$ form	$ V_{cb} $ ( $10^{-3}$ )	$\hat{\rho}^2$
$1 - \hat{\rho}^2(y - 1)$	$38 \pm 6 \pm 4$	$1.2 \pm 0.5 \pm 0.3$
$\frac{2}{y+1} \exp(-(2\hat{\rho}^2 - 1)\frac{y-1}{y+1})$ BSW	$38 \pm 6 \pm 4$	$1.2 \pm 0.6 \pm 0.3$
$(\frac{2}{y+1})^{2\hat{\rho}^2}$ POLE	$38 \pm 5 \pm 4$	$1.1 \pm 0.5 \pm 0.2$
$\exp(-\hat{\rho}^2(y - 1))$ ISGW	$37 \pm 5 \pm 4$	$1.0 \pm 0.4 \pm 0.2$
$1 - \hat{\rho}^2(y - 1) + \epsilon^2(y - 1)^2$	$38 \pm 10 \pm 4$	$1.2 \pm 0.5 \pm 0.3$

Table 1.3: CLEO93 results for  $|V_{cb}|$ , a CKM matrix element, and the fit parameter  $\hat{\rho}^2$ , the charge radius, extracted from the  $d\Gamma_{b \rightarrow c}/dy$  distribution measured for  $\bar{B}^0 \rightarrow D^{*+} \ell^- \bar{\nu}$  decays.

## 1.6 Mechanisms Responsible for $b$ Hadron Lifetime Differences

Theorists generally predict the following hierarchy of  $b$  hadron lifetimes:[4, 5]

$$\tau(B_u^+) > \tau(B_s^0) \sim \tau(B_d^0) > \tau(\Lambda_b^0).$$

The ‘‘lifetime spread’’ of the  $b$  hadron system, generally expressed as  $\frac{\Gamma(B)_{\text{nonsect}}}{\Gamma(B)}$ , goes as  $\frac{1}{m_b^3}$ [5]. Hence, it is readily apparent that the significant lifetime differences which were observed between the  $c$  hadrons (e.g.  $\tau(D_d^+)/\tau(D_u^0) = 2.58 \pm 0.09 \pm 0.08$ [7]) should not manifest themselves in the equivalent  $b$  hadron regime, since  $(\frac{m_c}{m_b})^3 \approx 0.03$ ,  $\frac{\Gamma(B)_{\text{nonsect}}}{\Gamma(B)} \sim 8\%$ .

Two mechanisms contribute to lifetime differences between the  $b$  hadrons[5]:

1. Weak Annihilation (WA) processes like  $W$  exchange, shown in Fig. 1.5, affect the width of the  $\bar{B}^0$  meson, while
2. Pauli Interference (PI), shown in Fig. 1.6, modifies the  $B^-$  width, e.g.  $b\bar{u} \rightarrow c\bar{u}d\bar{u}$ .

The stronger of the two mechanisms is PI because WA is strongly suppressed by helicity and by the fact that the weak interaction has such a short range. The wave functions describing the  $b$  and light spectator  $u(d)$  quarks must overlap for WA to occur, causing the WA contribution to the spread in  $b$

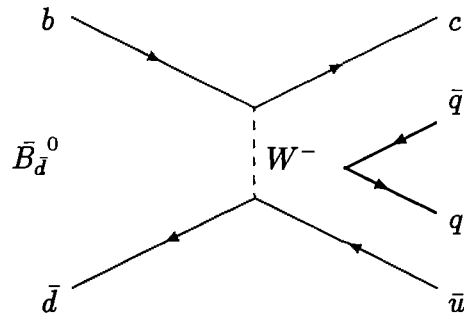


Figure 1.5: Diagram for  $W$  exchange.

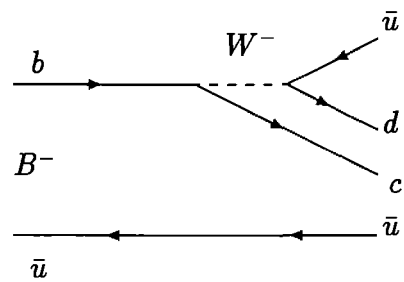


Figure 1.6: Feynman diagram that motivates Pauli Interference in  $B^-$  decays of the form  $b\bar{u} \rightarrow c\bar{u}d\bar{u}$ .

hadron widths to fall off like  $m_b^3$  relative to the PI contribution, even after the effects of gluon emission have been taken into account. The net effect of WA in the  $b(c)$  hadron sector is 1%(10-20%)[5]. Hence, PI is essentially responsible for the lifetime differences between the  $b$  hadrons, even though it is suppressed by the fact that the decay product  $\bar{u}$  quark wave function must overlap with that of the spectator  $\bar{u}$  in order for PI to occur. Symbolically, the contribution to the width of the  $B^-$  meson due to PI can be expressed as

$$\Gamma_B^- = \Gamma(B)_{\text{spect}} + \Delta\Gamma(B^-)_{\text{PI}}. \quad (1.15)$$

Eq. (1.15) ultimately leads to the following numeric result (see Reference [5] for details):

$$\frac{\tau_{B_u}}{\tau_{B_d}} = 1.0 \pm 0.05 \cdot \frac{f_B^2}{(200 \text{ MeV})^2}, \quad (1.16)$$

where  $f_B \sim 100 \text{ MeV}$  is the  $B$  meson decay constant. An analogous analysis in the  $c$  quark sector yields  $\frac{\tau_{D_d^+}}{\tau_{D_u}} \sim 2$ , which is consistent with the experimental result of  $2.58 \pm 0.09 \pm 0.08$ [7].

# Chapter 2

## Experimental Apparatus

### 2.1 The Accelerator

When operating in colliding beam mode, Fermilab's accelerator complex ultimately brings protons and antiprotons into collision in the superconducting Tevatron with a center of mass energy equal to  $1.8 \text{ TeV}$  at a luminosity that routinely exceeds  $5 \times 10^{30} \text{ cm}^{-2} \text{ s}^{-1}$ . Four principal subsystems work in concert to achieve this combination of high luminosity and high energy; they are the Linear Accelerator/Booster, the Antiproton Accumulator, the Main Ring and the Tevatron. It is a convention to refer to these four systems, when taken as a whole, as the Accelerator. The accelerator complex is shown in Fig. 2.1, while the steps involved in accelerating protons to  $900 \text{ GeV}$  are shown in Fig. 2.2. The purpose of this section is to outline the steps necessary to achieve this unprecedented combination of high energy coupled with high luminosity, ending with  $\bar{p}p$  collisions occurring at the nominal CDF interaction region, B0.

The source of initial protons is actually ionized hydrogen gas,  $H^-$ . The ions are first accelerated to  $750 \text{ KeV}$  by a Cockroft-Walton electrostatic accelerator. Next, these ions reach an energy of  $200 \text{ MeV}$  after traversing the Linear Accelerator (LINAC). As the hydrogen ions pass through a thin carbon strip, the electrons are stripped off and the resulting bare protons are injected into the Booster Ring, where they are accelerated to an energy of  $8 \text{ GeV}$ . The protons are assembled into six bunches before they are transferred to the Main Ring. Once in the Main Ring, one of two things may occur: (1) the proton



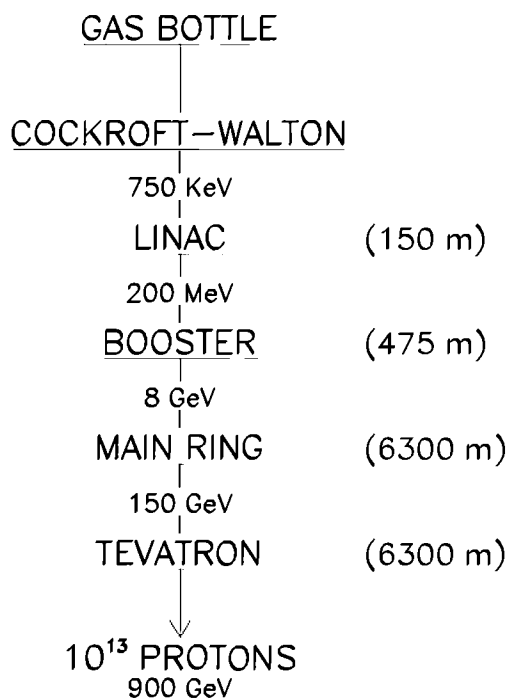


Figure 2.2: Diagram of steps involved in accelerating protons to 900 GeV. Any number between 1 and  $2 \times 10^{13}$  protons can be accelerated in a process that takes about 60 seconds.

bunches are accelerated to 150  $GeV$  and then transferred to the Tevatron, or (2) the proton bunches are accelerated to 120  $GeV$ , and focused to a transverse size of 1.5  $mm$  by a quadrupole magnet onto a Ni target[30]. Protons striking the Ni nuclei produce a variety of particles, including antiprotons. The antiprotons are momentum selected out of the decay products by a dipole magnet, focused by a lithium lens, and transferred to a debuncher, where the momentum spread of the antiprotons is reduced. The antiprotons are then injected into the  $\bar{p}$  Accumulator Ring, where they are stored into six bunches. Negatively charged pions, kaons, and muons simply have decayed away by the tenth turn in the Accumulator, and positrons fall out of the ring due to synchrotron radiation. The remaining antiprotons are allowed to collect, i.e. “stack”, until the  $\bar{p}$  stack has reached at least  $60 \times 10^{10}$  particles. It takes about 12 to 24 hours to attain a  $\bar{p}$  stack of  $60 \times 10^{10}$  particles. Once the stack is large enough, 6  $\bar{p}$  bunches, each containing  $4 \times 10^{10}$  particles, are injected into the Main Ring. The remaining  $\bar{p}$  particles are saved in the Accumulator Ring and become part of the next stack. The  $\bar{p}$  particles that have been injected into the Main Ring are accelerated to an energy of 150  $GeV$  before transfer to the Tevatron. Once in the Tevatron, protons and antiprotons are simultaneously accelerated to an energy of 900  $GeV$ , which yields a  $\bar{p}p$  energy of 1.8  $TeV$ .

Luminosity is governed by

$$L = \frac{N_p N_{\bar{p}} B f_0}{4\pi\sigma_b^2}, \quad (2.1)$$

where  $N_p$  and  $N_{\bar{p}}$  are the number of protons and antiprotons per bunch ( $12 \times 10^{10}$  and  $4 \times 10^{10}$ , respectively),  $B$  is the number of bunches (6),  $f_0$  is the revolution frequency (47.7  $kHz$ ), and  $\sigma_b$  is the transverse RMS bunch size, assumed horizontally and vertically equidistant. At an interaction region, e.g. B0 in Fig. 2.1, the time between  $\bar{p}p$  collisions is 3.49  $\mu s$ . The number of interactions per second is given by

$$R = L\sigma, \quad (2.2)$$

where  $R$  is the interaction rate,  $L$  is the luminosity, and  $\sigma$  is the interaction cross section. For example, the average luminosity during Run 1A was  $3 \times 10^{10} \text{ cm}^{-2}\text{s}^{-1}$ ; because the inelastic cross section is 46  $mb$ , about 138,000

potentially interesting interactions per second occurred at B0. The total luminosity delivered at B0 during Run 1A was  $27.2 \text{ pb}^{-1}$ , of which CDF wrote  $19.3 \text{ pb}^{-1}$  to 8 mm tape, yielding a detector efficiency of 71%.

## 2.2 The Collider Detector at Fermilab (CDF)

### 2.2.1 Overview

CDF is a general purpose detector designed to measure the energy and momentum of particles produced in  $\bar{p}p$  interactions. The several subsystems which comprise this azimuthally and forward-backward symmetric detector provide a complete picture of  $\bar{p}p$  interactions at B0 — charged particle tracking, momentum information, finely segmented calorimetry and muon identification. The purpose of this section is to describe briefly CDF and to focus on the subsystems used in this analysis. Consequently, only the central region of CDF will be considered; no discussion of the forward or plug regions of the detector will be presented here. Rather, the reader is referred to References [31, 32], which cover the entire detector in detail, including upgrades. A more detailed treatment of CDF's tracking detectors, with emphasis on the Silicon Vertex Detector (SVX), is given in Chapter 3.

When the Tevatron is operating in colliding beam mode, CDF is located in the B0 collision hall, see Fig. 2.3. CDF envelopes the nominal interaction region and provides nearly  $4\pi$  coverage. Using the geometric center of CDF as the origin, it is convenient to define a Cartesian coordinate system in which the  $z$  axis is taken to be the beamline, pointing in the proton flight direction, as is shown in Fig. 2.4. The  $x$  and  $y$  axes form a plane transverse to the beam, i.e. the  $r-\phi$  plane. The zenith angle,  $\theta$ , is measured with respect to the  $z$  axis, and is more commonly related to pseudorapidity, expressed as  $\eta = -\ln[\tan(\theta/2)]$ .

### 2.2.2 CDF Tracking Detectors

Three subsystems were responsible for charged particle tracking at CDF during Run 1A. These are the SVX, the Vertex Time Projection Chamber (VTX), and the Central Tracking Chamber (CTC). Both the SVX and the VTX are

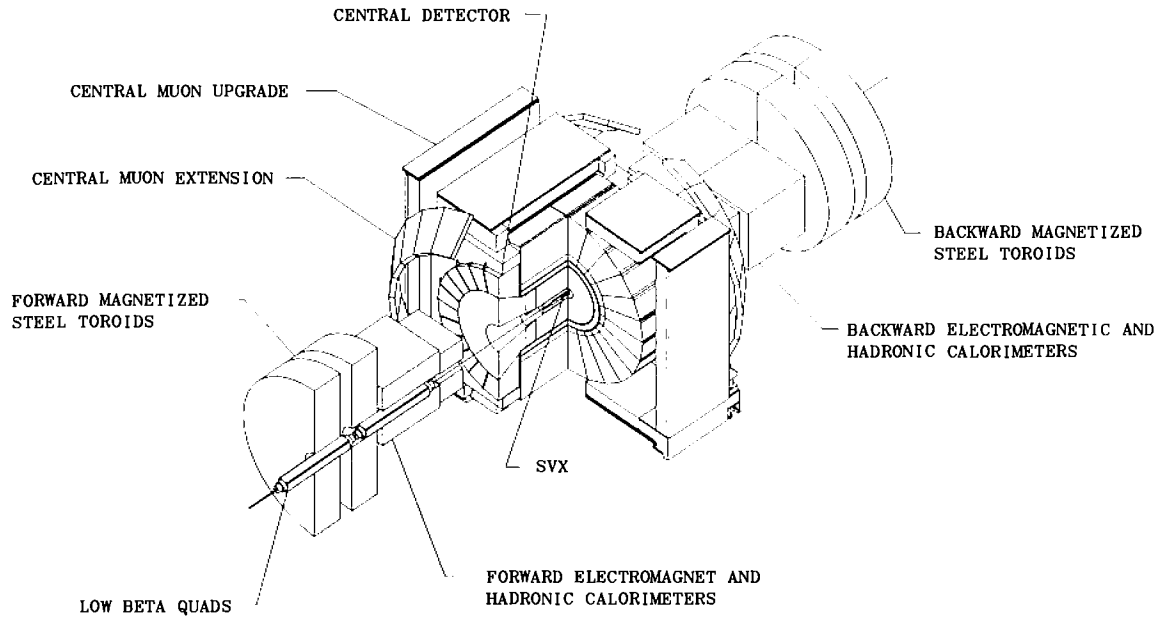


Figure 2.3: A view of CDF in the collision hall with RUN 1A upgrades.

upgrades and were installed in 1992 for Run 1A, while the CTC was installed in the original CDF and has been in use since the 1986 engineering run.

As its name suggests, the SVX[32] is a precise  $r - \phi$  tracking device that utilizes four layers of silicon microstrip detectors. The azimuthally symmetric SVX is located just outside the 1.9 cm radius beryllium beampipe. It spans  $\sim 51$  cm in  $z$  and covers the pseudorapidity range  $|\eta| < 1.9$ . The innermost(outermost) layer is 3.0(7.9 cm) from the beamline. The pitch between readout strips is 60  $\mu\text{m}$  (55  $\mu\text{m}$ ) on the 3 inner (1 outer) layers. The fine microstrip pitch combined with the use of pulse height information results in an individual hit resolution of 13  $\mu\text{m}$ . Fig. 2.5 shows an isometric view of one of the two SVX barrels. Both barrels are placed end-to-end at  $z \approx 0$ ; to allow space for cooling pipes and cables, there is actually a 2.15 cm gap between the barrels centered at  $z = 0$ . Because of this gap and the fact that the  $z$  position of the primary interaction varies as a gaussian of width 30 cm, the geometrical acceptance of the SVX is  $\sim 60\%$  that of the CTC. Nevertheless, the SVX is vital to this analysis because it enables the resolution of secondary vertices resulting from the decay of long lived particles, e.g.  $B$  mesons. The SVX track reconstruction will be discussed in greater detail in Section 3.3.

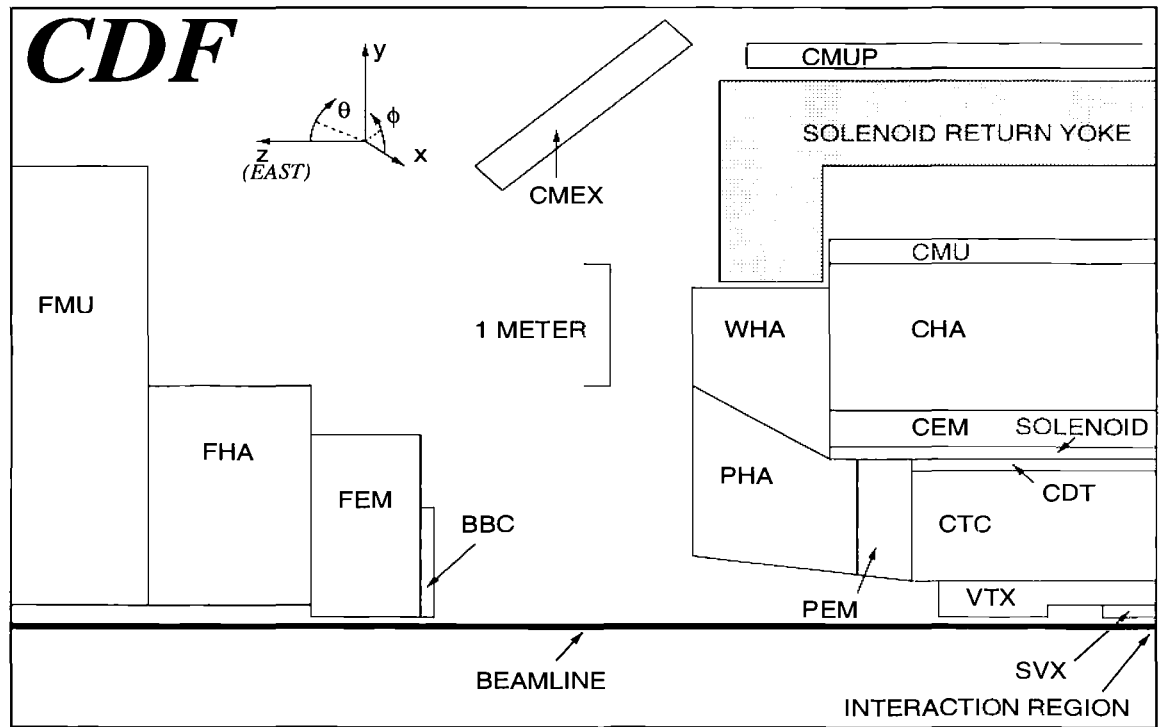


Figure 2.4: Cross sectional view of CDF in the collision hall with Cartesian coordinates.

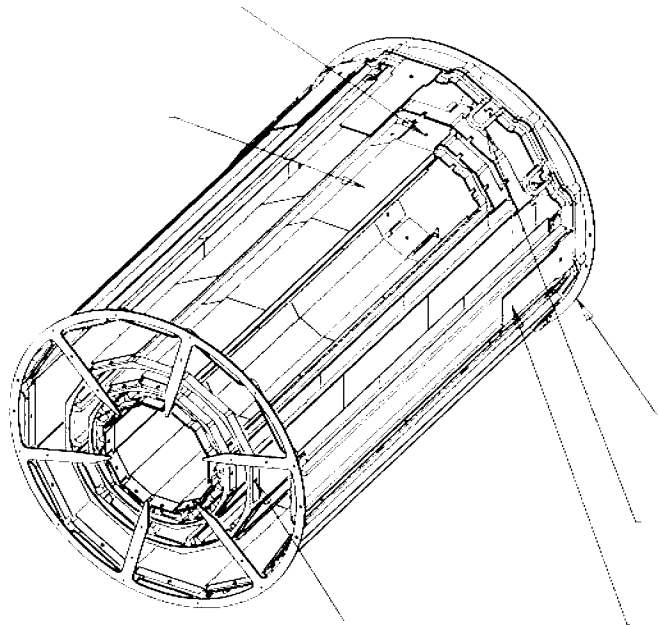


Figure 2.5: Isometric view of a single SVX barrel.

The SVX resides inside the VTX, which provides  $r-z$  tracking information. The VTX is a time projection chamber utilizing 28 argon-ethane drift modules which cover the pseudorapidity range  $|\eta| < 3.25$  over the full  $2\pi$  azimuthal range. A single module contains two drift regions. A single drift region spans 5 cm in  $z$ , which implies a maximum drift time of 400 ns, well within the 3.49  $\mu$ s beam crossing window. An isometric, cut-a-way view of 16 VTX modules is shown in Fig. 2.6. The VTX is used to determine the  $z$  position of

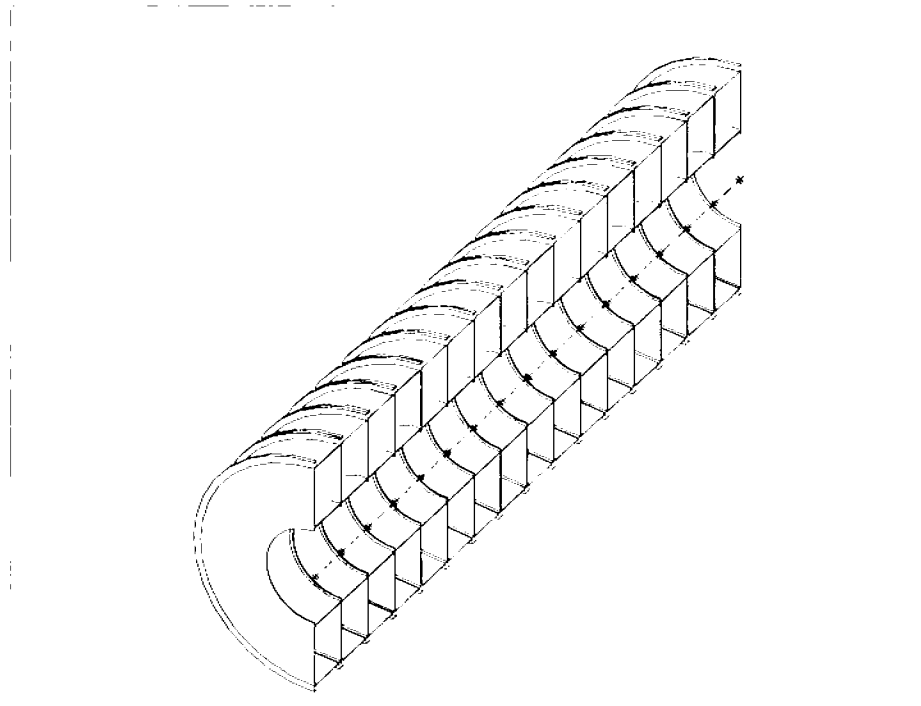


Figure 2.6: This figure shows a cut-a-way view of 16 VTX modules. Each module is 12 cm in length. Note that the drift plane in the center of each module is not shown.

the primary interaction to within 1 mm. As will be discussed in Section 4.2.1, the measured  $z$  position is used to calculate the nominal  $x$  and  $y$  position of the primary interaction vertex.

Particles exiting the VTX encounter the CTC. The CTC is a right cylindrical argon-ethane gas drift chamber 3.2 *m* in length, covering the pseudorapidity range  $|\eta| < 1$ . It provides  $r$ ,  $\phi$  and  $z$  tracking information via 9 radially distinct clusters of drift wires, numbered 0 through 8. These wire clusters are referred to as superlayers, and are clearly visible in Fig. 2.7. The innermost(outermost) superlayer has a nominal position in  $r$  of 78 *cm* (225 *cm*). The five even numbered superlayers (0,2,4,6,8) are referred to as axial superlayers because they have wires that are arranged parallel to the  $z$  axis and only provide  $r - \phi$  information. The four odd numbered superlayers (1,3,5,7) are known as stereo superlayers because they have wires that are tilted by  $\pm 3^\circ$  with respect to the  $z$  axis to give a stereo angle and  $z$  position measurement. Wires comprising a superlayer are grouped in cells which are clearly visible in Fig. 2.7 and are referred to as super cells. Axial super cells contain twelve sense wires, while each stereo super cell contains 6 sense wires. The plane containing the wires comprising a cell is tilted by  $45^\circ$  with respect to the radial direction. This tilt insures that the drift trajectories are nearly azimuthal by correcting for the Lorentz angle,  $\beta$ , given by

$$\tan(\beta) = \frac{vB}{kE} \quad (2.3)$$

where  $v$  is the drift velocity (*m/s*) in the absence of a magnetic field,  $B$  is the magnitude of the magnetic field (T),  $E$  is the electric field strength (*V/m*), and  $k$  is a constant that depends on the drift gas. For the argon-ethane-ethanol mixture used at CDF,  $k = 0.7$ . Because of this  $45^\circ$  tilt and the fact that cells within a superlayer overlap one another, high  $p_T$  tracks ( $> 2.5 \text{ GeV}/c$ ) produce at least one “prompt” hit (short drift time) per superlayer. This fact is used in the Central Fast Tracker[33], referred to as the CFT.

The CFT utilizes prompt hits in the 5 axial superlayers to measure the  $p_T$  of all high momentum tracks in an event within the 2.5  $\mu s$  allowed by the Level 2 trigger [34]. CDF uses a 3 level trigger system [35, 36, 37] to select out  $J/\psi \rightarrow \mu^+\mu^-$  events, which will be discussed in Section 4.1.1. Prompt hits on the 4392 axial sense wires are digitized and then read out within an 80 *ns* coincidence latch that is opened after beam crossing. The time over threshold wire chamber signals are piped into Lecroy 1879 TDCs (Time to Digital Converters). Pre-defined patterns of prompt hits map to 8

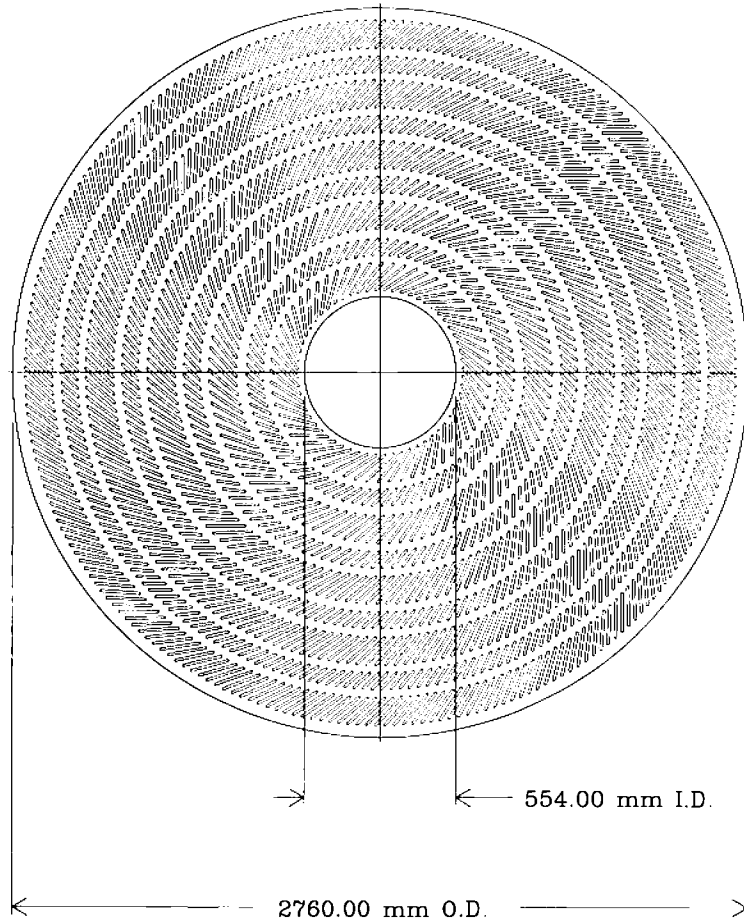


Figure 2.7:  $r - \phi$  view of the CTC.

$p_T$  bins; tracks producing these patterns are assigned to one or more bins, e.g.  $2.5 \text{ GeV}/c$ ,  $5 \text{ GeV}/c$ , etc. A second coincidence gate is opened  $500 - 650 \text{ ns}$  after beam crossing to look for delayed hits which are used to verify high  $p_T$  tracks. The momentum resolution achieved by this method is  $\frac{\delta p_T}{p_T} \approx 0.035$ , while the efficiency smoothly increases from 50% at  $p_T = 2.6 \text{ GeV}/c$  to 94% for  $p_T > 3.1 \text{ GeV}/c$ .

The entire tracking volume of CDF is contained in a superconducting solenoid of radius 1.8 m which generates a 1.5 T magnetic field. The direction of the  $B$  field is negative  $z$ , i.e.  $\vec{B} = -B\hat{e}_z$ . The strong solenoidal  $B$ -field, the precise impact parameter resolution provided by the SVX, and the large tracking radius enable CDF to boast a combined CTC/SVX transverse momentum resolution of  $\delta p_T/p_T = [(0.0009p_T)^2 + (0.0066)^2]^{\frac{1}{2}}$ .

### 2.2.3 Central Calorimetry Overview

CDF's central calorimetry system played only a minor role in muon identification in this analysis. The central calorimetry system consists of 4 central calorimetry arches. The Central Electromagnetic Calorimeter (CEM) provides nearly  $2\pi$  coverage in  $\phi$  and spans over 2 units of pseudorapidity,  $|\eta| < 1.1$ . Similarly, the Central Hadron Calorimeter (CHA) nearly covers the full  $2\pi$  in azimuth, and almost 2 units in pseudorapidity,  $|\eta| < 0.9$ . Each arch is composed of projective tower calorimetry wedges, each subtending  $15^\circ$  in  $\phi$  and 0.1 in  $\eta$ . Individual wedges are generally referred to as towers. Each tower measures both the electromagnetic and the hadronic energy deposited by particles.

The electromagnetic portion of the tower (CEM) consists of interleaving layers of lead and scintillator sheets which, including the solenoid coil, span approximately 18 radiation lengths. Light generated in the scintillating sheets is read out by photomultiplier tubes. This arrangement yields an electromagnetic energy resolution,  $\sigma_{E_{em}}/E_{em}$ , of  $0.137/\sqrt{E_{em}} \oplus 0.02$ , where  $\oplus$  indicates that 0.02 is added in quadrature. A proportional strip chamber is strategically located at a depth corresponding to the maximum average transverse shower development in order to provide shower profile information with a resolution of  $\pm 2 \text{ mm}$ . Hence, the central electromagnetic calorimetry system not only

Detector Type	Number of Modules	Azimuthal Acceptance	Longitudinal Acceptance	Interaction Length
CMU	2304	$2\pi$	$ \eta  < 0.65$	4.9
CMP	$\sim 1000$	$2\pi$	$ \eta  < 0.67$	$\sim 9$
CMX	1536	$1.3\pi$	$ 0.65 < \eta < 1.12 $	6 to 12

Table 2.1: This table lists the number of chambers, azimuthal and longitudinal acceptance, and the number of interaction lengths for the CMU, CMP and CMX muon detectors.

provides a precise energy determination, but also gives a detailed picture of the electromagnetic shower profile.

Interleaving layers of steel and scintillator comprise the hadronic portion of a central tower. Including the solenoid coil and the preceding electromagnetic region, the thickness of the CHA is equivalent to 4.9 interaction lengths. Light generated in the scintillating material is read out by photomultiplier tubes. The energy resolution of the CHA,  $\sigma_{E_{had}}/E_{had}$ , is  $0.50/\sqrt{E_{had}} \oplus 0.03$ .

## 2.2.4 Muon Chambers

CDF relies on three principle muon detectors: (1) the Central Muon (CMU) system, (2) the Central Muon Extension (CMX), (3) and the Central Muon Upgrade (CMP), which are all shown in Fig. 2.3. The CMX and CMP are upgrades for Run 1A, while the CMU is the original central muon system used by CDF. All of these detectors are y single wire proportional drift chambers sitting behind absorption steel, and essentially differ from each other only in their azimuthal and longitudinal coverage. General characteristics of these muon detectors are given in Table 2.1.

Three drift chambers per central calorimetry tower are located within a tower at a radius just outside the CHA. This system of  $48 \times 3 = 144$  drift chambers is referred to as the CMU. A total of 16 drift cells comprise a single drift chamber, as shown in Fig. 2.8. An individual cell is depicted in Fig. 2.9. Hence, the CMU employs  $144 \times 16 = 2304$  individual drift cells. Two sense

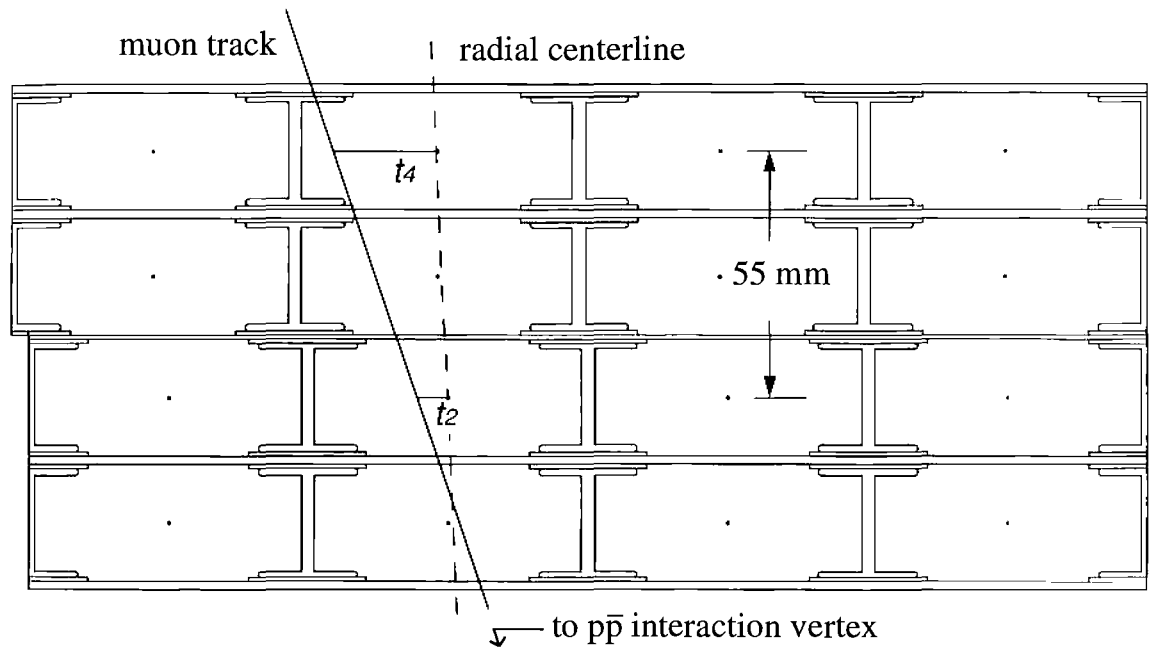


Figure 2.8:  $r - \phi$  view of a CMU chamber. A single sense wire is used in every other cell in a given chamber layer. The angle relative to the radial centerline and the muon track is related to the difference in drift times and is used to calculate the transverse momentum of the muon for the Level 1 trigger.

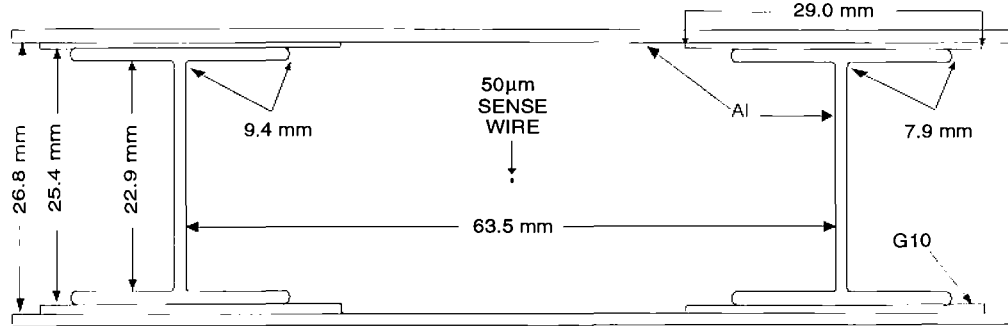


Figure 2.9: View of a single CMU cell

wires are used to detect hits in a given chamber layer, i.e. a single sense wire is used in every other cell. This fact halves the number of data channels (1152) that need to be read out without sacrificing spatial resolution. The CMU offers  $2\pi$  coverage in  $\phi$ , and covers  $|\eta| < 0.65$ . Muon candidates entering the CMU have traversed 4.9 interaction lengths and have a  $p_T$  of at least  $1.4 \text{ GeV}/c$ . The  $p_T$  of CMU tracks is obtained from the differences in drift times to the sense wires in alternating layers, see Fig. 2.8. Because the muon candidates have traversed through the solenoidal magnetic field,  $\vec{B}$ , they enter the CMU at an angle  $\alpha$  relative to the radial line-of-sight, as is shown in Figs 2.8 and 2.10. If  $\beta$  is the deflection angle due to the magnetic field, then

$$D \sin(\alpha) = L \sin\left(\frac{\beta}{2}\right), \quad (2.4)$$

where  $D$  is the distance from the beamline to the lower radius of the CMU ( $3.47 \text{ m}$ ), and  $L$  is the radius of the solenoid ( $1.44 \text{ m}$ ). The relationship

between  $\beta$  and  $p_T$  is given by

$$\sin\left(\frac{\beta}{2}\right) = \frac{eL|\vec{B}|}{2p_T}. \quad (2.5)$$

Combining Eqs. (2.4) and (2.5) yields

$$\alpha \simeq \frac{eL^2|\vec{B}|}{2Dp_T}. \quad (2.6)$$

Finally,  $\alpha$  is obtained from the difference in drift times between alternating layers,  $\Delta t$ , via

$$\Delta t = \frac{H\alpha}{v}, \quad (2.7)$$

where  $H$  is the spacing between the alternating sense wires ( $55.0 \text{ mm}$ ) and  $v$  is the drift velocity of the ionization electrons. Since

$$\Delta t \propto \alpha \propto [p_T]^{-1}, \quad (2.8)$$

smaller time differences imply larger track transverse momentum. This fact is used in the Level 1 trigger by flagging events with  $\Delta t$  less than a preset value. Details of the trigger system used to select out  $J/\psi \rightarrow \mu^+\mu^-$  events will be discussed in Section 4.1.1. Tracks are also reconstructed in the  $r - z$  plane by taking advantage of charge division on the sense wires. This method not only gives the  $z$  position of the muon to within  $1.2 \text{ mm}$ , but also determines in which cell a hit occurred in each layer.

The CMP is essentially an extension of the CMU with the improvement that the additional steel between the CMU and the CMP reduces the chances of hadrons producing hits in the CMP and thereby being misidentified as muons. The CMP consists of  $\sim 1000$  extruded Al drift tubes, each having dimension  $2.54 \times 15.25 \times 640 \text{ cm}$ . These are stacked 4 deep and are arranged in a rectangular box that encloses the central portion of CDF, see Fig. 2.3. The CMP provides symmetric,  $2\pi$  azimuthal coverage, and spans the pseudorapidity range  $|\eta| < 0.67$ . Particles entering the CMP have traversed  $\sim 9$  interaction lengths and have a  $p_T$  of at least  $2.5 \text{ GeV}/c$ . Unlike the CMU, each individual sense wire in a drift tube is connected to the readout electronics. However, like the CMU, digitized time-over-threshold data is sent to LeCroy

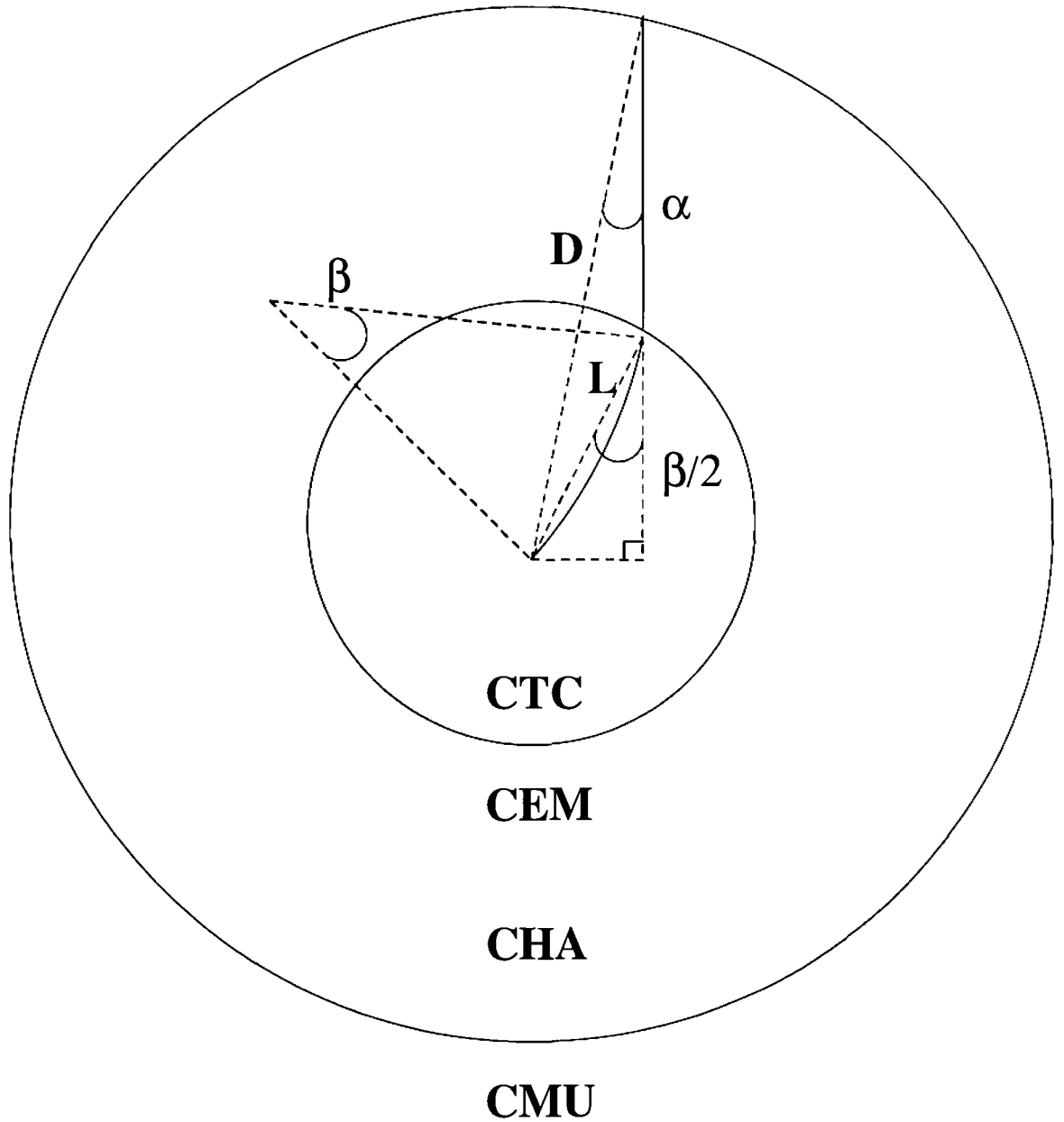


Figure 2.10: This figure demonstrates the relationship between the incident angle,  $\alpha$ , and the deflection angle,  $\beta$  of the muon candidate.

1879 TDCs. This method provides a transverse view of the candidate muon track and is used to set a Level 1 trigger flag in the manner described in the above paragraph. The sense wires in the CMP do not provide a stereo angle, nor are the readout electronics setup for charge division. As a result, the CMP does not provide a  $z$  coordinate for the candidate muon track.

The CMX[38] was added in 1992 to extend the  $\eta$  coverage in the central region of the detector. The CMX is comprised of 1536 drift cells, each having dimensions  $2.54 \times 15.24 \times 183$  cm. These drift cells are arranged onto 4 separate free standing arches in the following way: 48 cells are arranged in a staggered configuration that is 8 cells deep by 6 wide, forming an arc section; 8 of these arcs connected end-to-end form a single CMX arch, giving 384 cells per arch. These 8 layers of drift cells are sandwiched between two layers of scintillating material. Fig. 2.3 shows three of the four CMX arches located at the corners of the central CDF detector. Two arches taken together on either the west or east side of the central region of CDF span  $240^\circ$  in  $\phi$ , i.e.  $-45^\circ(105^\circ) < \phi < 75^\circ(225^\circ)$ . All four arches cover the pseudorapidity range  $|0.65 < \eta < 1.12|$ . Muons entering the CMX have traversed anywhere from 6 to 12 interaction lengths (depending on  $\eta$ ) and have a minimum  $p_T$  of  $2.3$  GeV/c. Hits in the CMX are recorded in coincidences between signals in the inner and outer scintillators and pulses on the drift wires. Track reconstruction in the CMX is essentially identical to that used in the CMP, which has been described above. The main difference lies in the fact that the drift wires of the CMX have an effective pitch angle of  $1.5^\circ$  with respect to each other due to the fact that sense wires are arranged in an arc. Hence, the CMX not only uses drift time differences to provide  $r - \phi$  track reconstruction, but also uses the effective stereo angle between adjacent sense wires to provide  $r - \theta$  track reconstruction. As has already been described in the above CMU and CMP paragraphs, a Level 1 trigger bit is set based on the measured drift time difference.

# Chapter 3

## Charged Particle Tracking

Crucial to this analysis is CDF's ability to precisely measure the helical path traversed by charged particles as they pass through the central detector's solenoidal magnetic field, where the axis of the helix is parallel to the  $\vec{B}$  field. This ability allows CDF not only to determine precisely the particle's momentum, but also to vertex the daughter tracks (constrain the tracks to come from a common  $(x, y, z)$  point) produced when  $B$  mesons decay. For these reasons, this chapter is devoted to charged particle tracking at CDF. In particular, the five parameters used at CDF to describe a helix will be discussed. Secondly, the method by which CTC tracks are reconstructed will be described. If an SVX track segment is available for a previously reconstructed CTC track segment, the technique used to incorporate the SVX information in the track "fit" will be detailed. Finally, the various types of track fits will be addressed in turn.

### 3.1 Helix Parameterization at CDF

This section is devoted to CDF's choice of helical track parameters. Five parameters are required to unambiguously describe a helix. The choice of these parameters is listed below and motivated in Fig. 3.1.

- $\cot \theta$ : cotangent of the polar angle at the distance of closest approach to the origin

- $\pm C$ : half curvature ( $\frac{1}{2} \cdot$  radius of curvature), where the  $\pm$  sign indicates the charge of the particle
- $z_0$ :  $z$  position at the distance of closest approach to the origin
- $D$ : signed distance of closest approach to the origin in the  $r - \phi$  plane
- $\phi_0$ : azimuthal angle relative to the positive  $x$  axis at the distance of closest approach to the origin

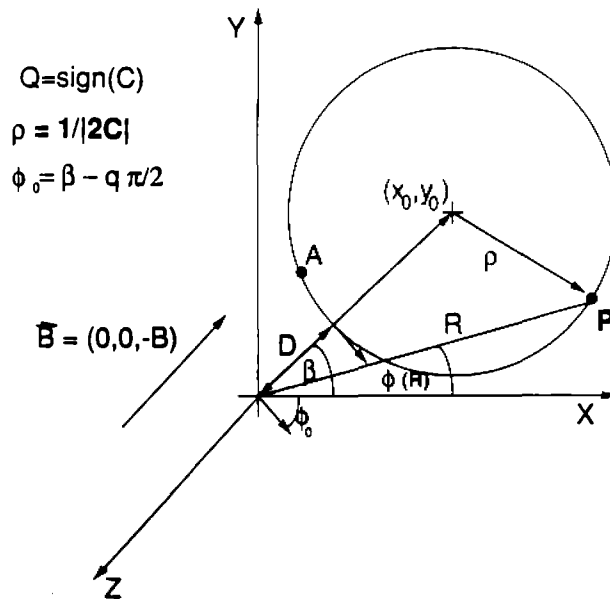


Figure 3.1: Parameterization of the trajectory of a positively charged particle at CDF.

## 3.2 Track Reconstruction in the CTC

The purpose of this brief section is to provide a schematic overview of the method used at CDF to transform hits in the CTC into track segments described by the five parameters listed in Section 3.1. The interested reader is referred to [39] for a more detailed treatment.

Generally speaking, track reconstruction starts in the outer radius of the CTC and works inward, through the VTX and SVX (when applicable) to the

beam line. Track reconstruction in the CTC occurs via two main steps. The first step is known as pattern recognition and involves associating groups of hits that resulted from the passage of a single charged particle through the CTC. Pattern recognition falls into two distinct classes, one for the  $r - \phi$  view using hit information from the 5 axial superlayers, and another in the  $r - z$  plane using hit information from the 4 stereo superlayers. Once hits have been assigned to a potential track, the second step is performing a final helical track fit to these groups of hits. The  $r - \phi$  track parameters ( $C, \phi_0, D$ ) are primarily obtained from fitting the axial hits, while the  $r - z$  track parameters ( $z_0, \cot \theta$ ) are gleaned from fitting the stereo hits. The version of offline code used to reconstruct tracks in the CTC in this analysis is known as Version 6.10.

### 3.3 Track Reconstruction in the SVX

Detailed treatments of SVX track reconstruction in the  $r - \phi$  plane can be found in References [32] and [40]; a cursory treatment is given here. Individual strips that have deposited charge above a predetermined threshold and their nearest neighbors are read out, digitized and stored for offline processing. The conversion of this “hit” information into SVX tracks is accomplished in three main steps: 1) Pedestal Subtraction, 2) Clustering, 3) Pattern Recognition and Track Fitting. These will be discussed in turn.

Charge levels are pedestal subtracted on a strip-by-strip basis, i.e. the measured charge recorded on each strip is subtracted by the nominal baseline charge level, or pedestal, due to both noise and the offset from ground for that particular strip. Pedestals for the 46080 strips were obtained roughly once every two days during standard calibration runs. Because the electrical performance of the SVX was stable on a time scale of at least two weeks, pedestal information was updated in the offline database an average of once every two weeks.

A process referred to as clustering involves assigning hits on adjacent strips on a given SVX layer to clusters (groups of associated hits on a particular layer). Clustering improves the spatial resolution of tracks by taking full ad-

vantage of the fact that the SVX records pulse height information. Clustering is performed in the following way:

1. Assign adjacent strips to groups, including known dead strips.
2. Apply a threshold based on the strip noise and the number of strips comprising the candidate cluster to each strip, excluding the known dead strips. Candidate clusters that survive this threshold cut are saved for later processing. For example, if the candidate cluster is comprised of a single strip, the charge level must be at least a factor of four larger than the charge level resulting from noise, i.e  $\geq 4\sigma$  effect, in order for this strip to be identified as a cluster.
3. If any strip(strips) in the candidate cluster fails(fail) the threshold cut described in Step [2], the candidate cluster is broken at that(those) strip(strips), resulting in at least two new candidate clusters. Step [2] is repeated on the new candidate clusters.
4. Once clusters have been identified, their positions are calculated by weighting the contribution of each strip in the cluster by the amount of deposited charge. The position of the strip in each case is taken to be the strip center. The spatial error for clusters containing four or more strips and/or with a total charge greater than  $\sim 12 fc^*$  is calculated via the equation

$$[(\text{strip pitch}) \times (\text{number of strips})] / \sqrt{12}. \quad (3.1)$$

Clusters not satisfying this requirement that contain either one, two or three strips are assigned an error of  $15 \mu m$ ,  $13 \mu m$ , or  $25 \mu m$ , respectively. These values are used because they give the normalized residual distributions from final track fits a width of one sigma.

The  $r - \phi$  SVX pattern recognition and track fitting algorithms start with clusters that have been identified in the manner described above. Pattern recognition and track fitting occur simultaneously because the SVX tracking

---

\*The value  $12 fc$  is just  $3 \times$  the charge left by a typical minimum ionizing particle, i.e  $4 fc$ .

algorithm uses the progressive method[41]. Basically, this algorithm starts with an existing CTC track and extrapolates it to the outermost layer of the SVX. Any candidate SVX clusters on this layer that fall within the search road are considered. The width of the search road is defined in terms of the track error matrix, which also takes into account multiple scattering and  $dE/dx$  corrections due to any material between the current measurement plane and the previous one. The existing track parameters and the error matrix are then updated using each cluster. Hence, if there are two or more clusters falling within a road on a given layer, two or more candidate tracks will be extrapolated to the next available inner layer. If there are no clusters that fall within a search road on a given SVX layer, the extrapolation simply proceeds to the next inner layer. This process is repeated until the algorithm reaches the innermost SVX layer. Finally, a single SVX track fit for a given CTC track is selected among multiple candidates based on the track fit  $\chi^2$  and the number of clusters on different layers used in the fit. Table 3.1 elucidates the final SVX track fit selection procedure. The version of offline code used to reconstruct and select tracks in the SVX in this analysis is known as Version 7.09.

First Choice	lowest $\chi^2$ using 4 clusters on 4 different layers
Second Choice	lowest $\chi^2$ using 3 clusters on 3 different layers
Third Choice	lowest $\chi^2$ using 2 clusters on 2 different layers

Table 3.1: This table demonstrates the method used to select a single SVX fit from multiple candidate fits for a given CTC track.

### 3.4 Available Track Fits at CDF

The purpose of this section is to list and described the types of track fits that were available offline to the user at the time this analysis was performed. These can be divided into two main classes: 1) Default track fits that are stored on disk in the default CDF data structure, YBOS[42], and 2) Post-fit track

parameters, i.e. tracking parameters resulting from the vertexing algorithm (Version 7.09 CTVMFT) and/or the magnetic field corrections (Version 7.09 TRKFIX). It is important to note that the post-fit track parameters always used the default track fits as input (see the listing below).

The default track fits available in YBOS format used in this analysis come in two flavors:

1. **CTC ONLY:** As the name suggests, the track parameters and the error matrix reflect only the CTC hit information. This type of default track fit was used as input to the vertexing algorithm (CTVMFT) after magnetic field corrections were applied (TRKFIX).
2. **SVX:** The track parameters and the error matrix are obtained from a combination of CTC and SVX hit information. This type of default track fit was used as input to the vertexing algorithm (CTVMFT) after magnetic field corrections were applied (TRKFIX).

Four types of post-fit track parameters/errors were used in this analysis:

1. **TRKFIX:** TRKFIX is a routine that applies magnetic field corrections to the default track fits listed above. All default track types used in this analysis were modified by TRKFIX before being passed to the vertexing routine (CTVMFT).
2. **VERTEX CONSTRAINED:** The five track parameters which are returned by CTVMFT reflect the fact that the tracks were constrained to come from a common point in space, e.g. the two muon tracks from a candidate  $J/\psi$  vertex.
3. **VERTEX + MASS CONSTRAINED:** Tracking parameters which are returned by CTVMFT that result from simultaneously constraining the tracks to come from a common point in space with a specific invariant mass, e.g. the two muons tracks from the  $J/\psi$  in a  $B_u \rightarrow J/\psi K^+$  candidate.
4. **VERTEX + MASS + POINTING CONSTRAINED:** Tracking parameters which are returned by CTVMFT that are obtained after the

tracks were constrained to come from the decay point of a particle of known mass which “points” in the  $r - \phi$  plane back to the production point, e.g. the pion tracks from the  $K_S^0$  in a  $B_d \rightarrow J/\psi K_S^0$  candidate.

More details concerning the various types of track fits used in this analysis can be found in Sections 4.1.3 through 4.1.7, which describe their use in  $B$  meson reconstruction/vertexing.

# Chapter 4

## The Analysis

The analysis described in this chapter is conceptually simple and straightforward.  $B$  mesons are fully reconstructed using exclusive decay modes of the form  $B \rightarrow \Psi \mathbf{K}$ , where  $\Psi$  represents either a  $J/\psi$  or  $\psi(2S)$  and  $\mathbf{K}$  denotes a  $K^+$ ,  $K_S^0$ , or  $K^*(892)$ . Next, the proper decay length,  $c\tau$ , is determined for each candidate. Finally, the proper lifetime,  $\tau$ , of the fully reconstructed  $B_u$  and  $B_d$  mesons is obtained by fitting the resulting  $c\tau$  distributions. Because the analysis naturally divides itself into three distinct steps, details of the methods and techniques used will be presented in three main sections; these are  $B$  Meson Reconstruction,  $B$  Meson Decay Length, and  $B$  Meson Lifetime. This chapter concludes with two sections that describe the systematic uncertainties and a variety of cross checks.

### 4.1 $B$ Meson Reconstruction

This section first describes the trigger used to define the  $J/\psi$  dataset. Next, it details the algorithms used to fully reconstruct  $B$  meson decays of the form  $B \rightarrow \Psi \mathbf{K}$ . Finally, this section ends with the techniques and cuts used to perform the final  $B_u(B_d)$  event selection.

### 4.1.1 $J/\psi$ Dimuon Trigger

As already mentioned in Section 2.2.2, CDF uses a 3 level trigger system [34, 35, 36, 37] to select out  $J/\psi \rightarrow \mu^+\mu^-$  events. The criteria that an event must meet in order to pass this trigger is presented in Table 4.1. Unlike a cross-section analysis, trigger efficiencies do not play a major role in a lifetime analysis at CDF. As will be shown in Section 4.4.1, a systematic error is assigned to the final lifetime result to account for the fact that the Level 2 trigger is somewhat sensitive to the impact parameter of the daughter muons from the parent  $J/\psi$ . Also, it is worth noting that kinematic cuts on the muons are chosen to fall well within the fully efficient regions of the Level 1 and 2 triggers. The interested reader is referred to Reference [43] for a detailed treatment of the efficiency of the Level 1 and Level 2  $J/\psi$  Dimuon Trigger. The Level 3 trigger efficiency is discussed in Reference [44].

Level 1	2 Central Muon (CMU) Stubs $p_T > 3 \text{ GeV}/c$
	Central Muon + Extension (CMX) Stubs $p_T > 3 \text{ GeV}/c$
	2 Extension Stubs (CMX) $p_T > 3 \text{ GeV}/c$
Level 2	<b>At Least One Track</b> with $p_T > 3 \text{ GeV}/c$
Level 3	Good Track - Muon Chamber Match 2 Opposite Sign Muons $2.8 \text{ GeV}/c^2 < \mu\mu \text{ Invariant Mass} < 3.4 \text{ GeV}/c^2$

Table 4.1: This table lists the requirements of the Level 1, Level 2 and Level 3  $J/\psi$  Dimuon Trigger.

### 4.1.2 Muon Selection

Muons leaving stubs in any of the three muon detectors (CMU, CMP and CMX) are considered in this analysis. Before they are used to form a candidate  $J/\psi$  invariant mass, they must pass a number of matching and quality cuts. Muons are required to have a  $p_T > 1 \text{ GeV}/c$  and a minimum energy deposition of at least  $100 \text{ MeV}$  in the associated hadron calorimeter. The hadron energy cut is used primarily to reject fake muon stub candidates due to main ring

splash in the CMX. A good matching in the  $r - \phi$  plane ( $\chi^2 < 9$ ) is required between the muon stub and the associated CTC track. For CMU muons, a similar matching cut is also applied in the  $r - z$  plane. Muons that have stubs associated to them in several muon sub-systems are accepted only if they do not hit both the CMP and the CMX (an unphysical muon stub) and if they meet the above selection criteria for at least one of the sub-systems.

Muon pairs passing the above criteria are winnowed further by requiring two oppositely charged muons with an invariant mass between 2.8 and 3.4  $GeV/c^2$ . At least one of the muons is required to have a  $p_T > 2.5 GeV/c$  (trigger verification). There are 131,236 events with at least one such muon pair. The Level 3 online selection cuts are repeated in the offline analysis because the Level 3 tracking algorithm is not as sophisticated as the one used in offline production.

### 4.1.3 Track Quality Cuts

To ensure that the vertex of the  $B$  meson is well measured, the following requirements are applied to all tracks that will be considered to form  $B$  candidates:

- at least 2 axial CTC superlayers having at least 5 hits;
- at least 2 stereo CTC superlayers having at least 2 hits;
- at least 2 SVX hits if the track is a  $J/\psi$  leg (muon).

For the muons, the combined CTC/SVX fit is used. For all the other tracks, the combined CTC/SVX fit is used if available; otherwise, the pure CTC-Only fit is used. Requiring SVX information only for the  $J/\psi$  legs (rather than for all the tracks) allows partial recovery from the SVX inefficiency which appeared at the end of Run 1A due to radiation induced pedestal shifts, but still ensures that at least two good SVX tracks are used to form the  $B$  vertex.

### 4.1.4 $J/\psi$ Reconstruction

Only those events containing at least one pair of oppositely charged muons with combined CTC/SVX tracks are considered. The SVX muon pairs are

vertex constrained, i.e. the two muons are constrained to come from a common point, and their invariant mass is recalculated using the new vertex constrained track parameters returned by CTVMFT (see Section 3.4). Figure 4.1 shows the dimuon mass distribution; the arrows, placed at  $\pm 80 \text{ MeV}/c^2$  around the world average value of the  $J/\psi$  mass ( $3.0969 \text{ GeV}/c^2$ ), indicate the mass cuts applied to define the  $J/\psi$  candidates. The selection window appears to be unreasonably wide in this plot. However, it actually corresponds to the  $\pm 3\sigma$  points for  $J/\psi$  events with a large transverse momentum,  $p_T > 15 \text{ GeV}/c$ , as demonstrated in Figure 4.2. A floating selection window based on the event  $p_T$  and measured mass error was used as a consistency check in the analysis (see Section 4.5.6), resulting in no significant changes in the final results, i.e. observed number of events or measured  $B$  meson lifetime. Estimating the  $J/\psi$  background under the peak in the  $\pm 80 \text{ MeV}/c^2$  mass window from the number of candidates outside this window but within a  $\pm 150 \text{ MeV}/c^2$  mass window (assuming a flat background) yields  $49631 \pm 261$  background subtracted  $J/\psi$  events.

#### 4.1.5 $\psi(2S)$ Reconstruction

All combinations of a  $J/\psi$  candidate and two oppositely charged tracks (different from the  $J/\psi$  tracks, assumed to be pions) are formed. Using CTVMFT, the two muons are mass constrained and all four tracks are required to come from a common vertex. Combinations with a  $\chi^2$  probability less than 1% are rejected. The invariant mass of the two pions must be less than  $600 \text{ MeV}/c^2$ , and the total transverse momentum must be larger than  $3 \text{ GeV}/c$ . The distribution of the invariant mass (computed with the mass-vertex constrained track parameters) is shown in Fig. 4.3. The  $\psi(2S)$  candidates are defined as all the combinations having a mass within  $\pm 20 \text{ MeV}/c^2$  of the world average value of the  $\psi(2S)$  mass ( $3.6860 \text{ GeV}/c^2$ ), as indicated by the arrows on Fig. 4.3. A fit to this distribution with a Gaussian function plus a parabolic background indicates  $764 \pm 53$   $\psi(2S)$  signal events.

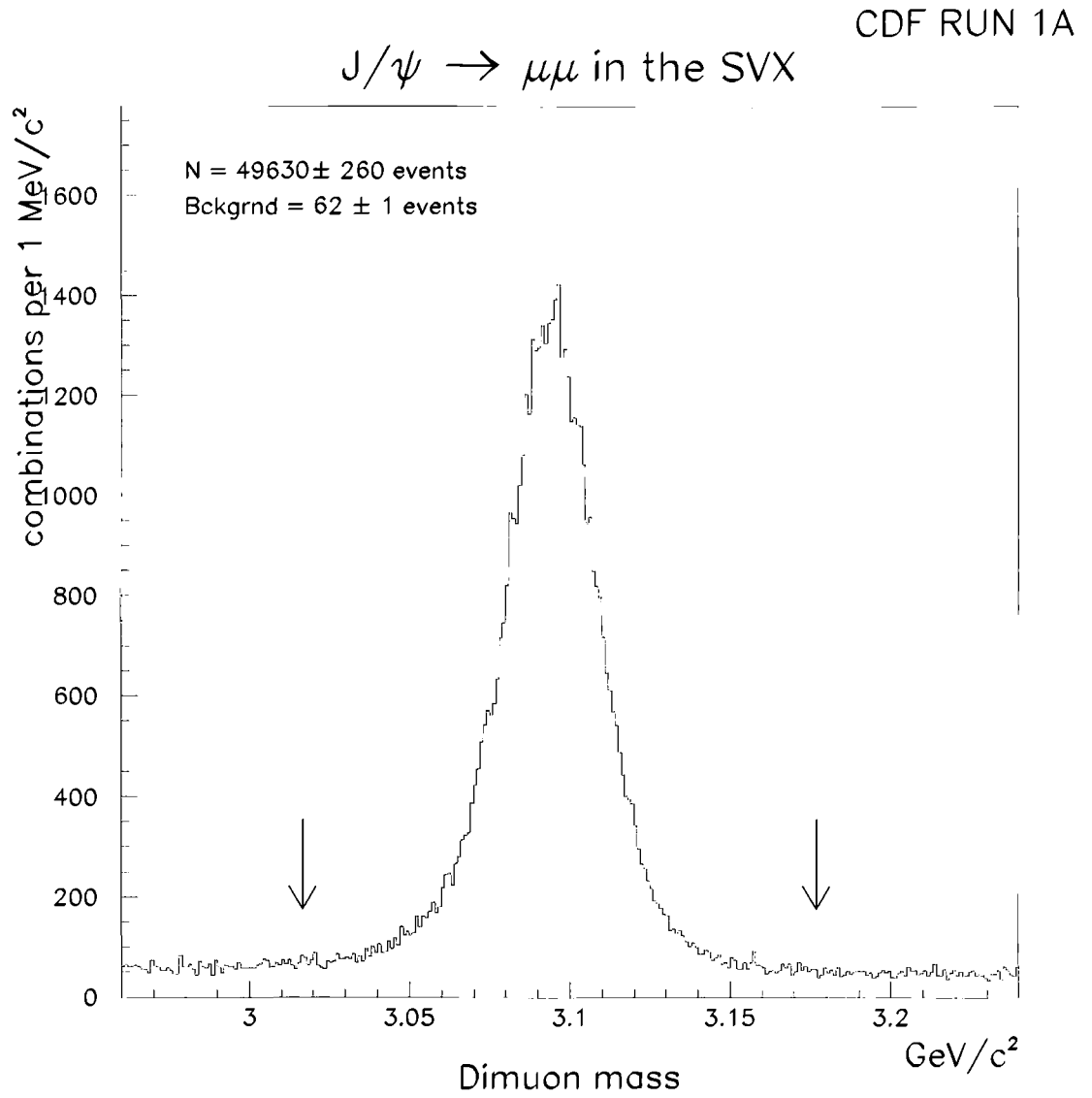


Figure 4.1: Dimuon mass distribution. The two muons are required to be found in the SVX and to come from a common vertex. The arrows, placed at  $\pm 80$  MeV/c<sup>2</sup> around the true  $J/\psi$  mass, indicate the mass cuts applied to define the  $J/\psi$  sample.

CDF RUN 1A

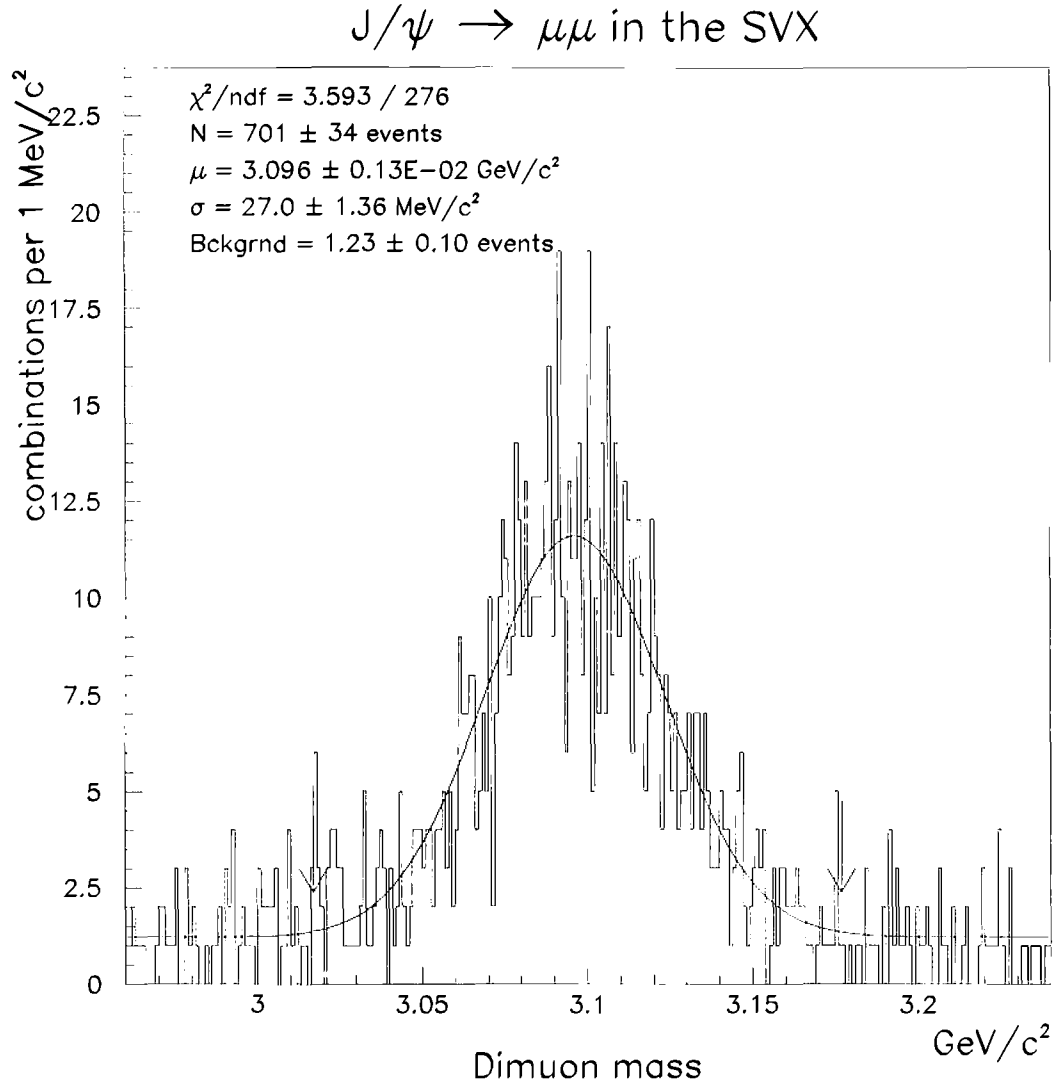


Figure 4.2: Dimuon mass distribution. The two muons are required to be found in the SVX and to come from a common vertex; the  $p_T$  of the  $J/\psi$  is required to be greater than  $15 \text{ GeV}/c$ . The arrows, placed at  $\pm 80 \text{ MeV}/c^2$  around the true  $J/\psi$  mass, indicate the mass cuts applied to define the  $J/\psi$  sample correspond to the  $\pm 3\sigma$  points.

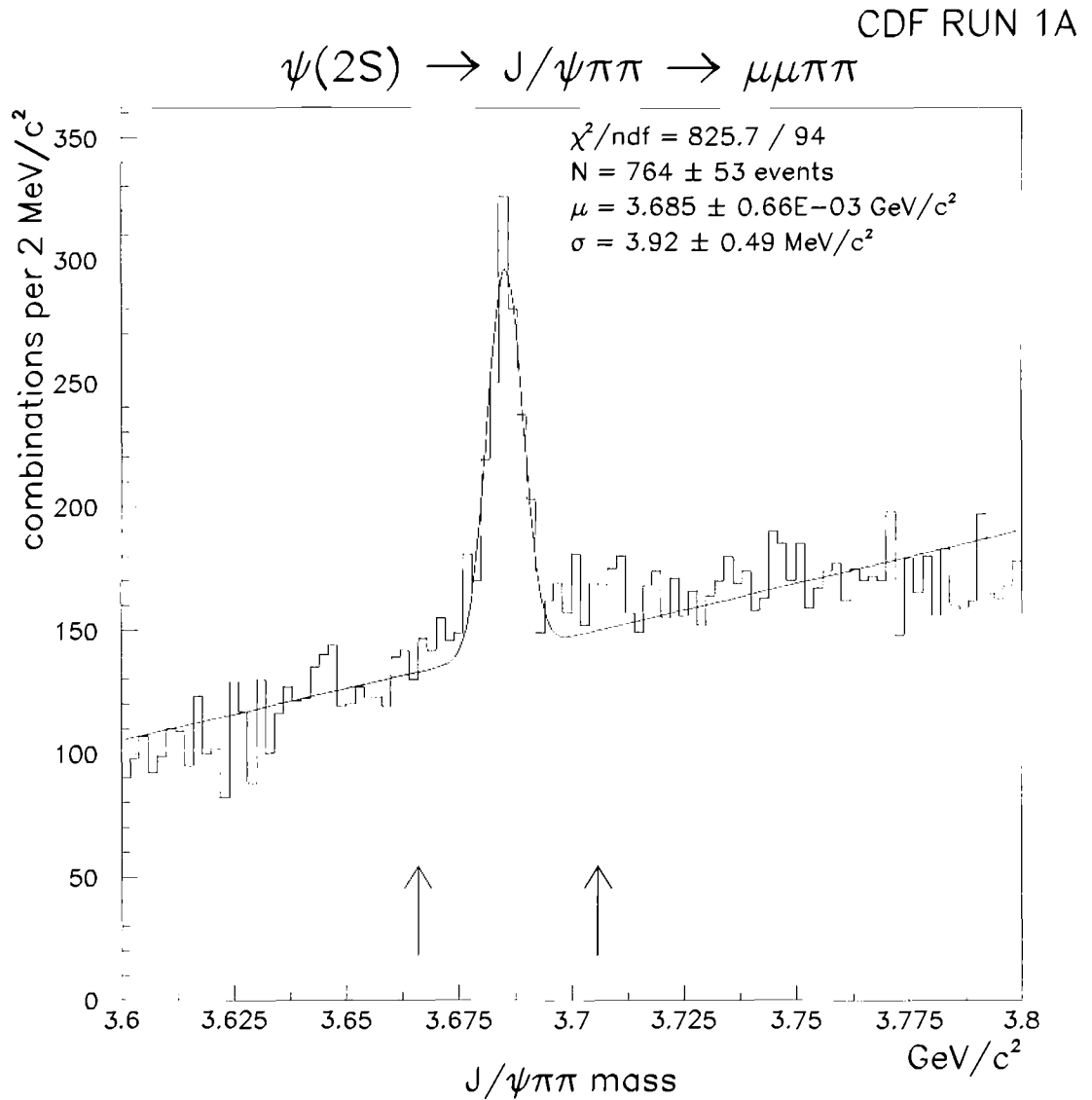


Figure 4.3:  $J/\psi \pi\pi$  mass distribution. The  $J/\psi$  is required to be found in the SVX. The 4 tracks are required to come from a common vertex, and the dimuon mass is constrained to the  $J/\psi$  mass. The arrows, placed at  $\pm 20$  MeV/c<sup>2</sup> around the true  $\psi(2S)$  mass, indicate the mass cuts applied to define the  $\psi(2S)$  sample.

### 4.1.6 $K_S^0$ Reconstruction

$K_S^0$  mesons are searched for among all combinations of two oppositely charged tracks (assumed to be pions) in the events that contain a  $J/\psi$  and that have a primary vertex measured by the SVX (see Section 4.2.1). Each pion is required to have an absolute value of the impact parameter (with respect to the beam line at the  $z$  of the primary vertex) at least twice as big as  $\sqrt{\sigma_D^2 + (40 \mu m)^2}$ , where  $\sigma_D^2$  is taken from the diagonal of the covariance matrix on the track parameters and where the  $40 \mu m$  accounts for the transverse size of the beam spot. The two pions are vertex constrained and a 1%  $\chi^2$  probability cut is applied. The  $K_S^0$  candidate is then required to have a positive decay length with respect to the  $J/\psi$  vertex, and its impact parameter (computed as the distance in the transverse plane between the  $K_S^0$  straight line trajectory and the  $J/\psi$  vertex) is required to be less than  $2 mm$ . The distribution of the invariant dipion mass (computed from the fitted track parameters) is shown in Fig. 4.4, separately for the CTC/CTC, SVX/SVX, and CTC/SVX combinations. The  $K_S^0$  candidates are defined as all the combinations having their mass within  $\pm 20 MeV/c^2$  of the world average value of the  $K_S^0$  mass ( $0.4977 GeV/c^2$ ), as indicated by the arrows. The number of  $K_S^0$  signal events with 0, 1, and 2 leg(s) in the SVX, determined from fits to these distributions of a Gaussian function plus a flat background, are  $1521 \pm 42$ ,  $1477 \pm 48$ , and  $5757 \pm 95$  respectively, yielding a total of  $8712 \pm 115$ , shown in the lower right hand plot of Fig. 4.4.

### 4.1.7 $B$ Reconstruction

$B$  meson reconstruction begins by combining all possible combinations of a  $J/\psi$  or  $\psi(2S)$  candidate with a track (assumed to be a  $K^\pm$ ), a  $K_S^0$  candidate, two oppositely charged tracks (assumed to be a  $K^\pm$  and a  $\pi^\mp$ ), or a  $K_S^0$  candidate plus a track (assumed to be a pion). The total  $p_T$  of the tracks that form a candidate kaon is required to be above  $1 GeV/c$  in order to limit the combinatorial background. Tighter, optimized  $p_T$  cuts will be applied later (see Section 4.1.8).

All the tracks in a given combination are processed by the vertexing algorithm, CTVMFT, assuming that they come from a  $B$  decay. This fit, performed simultaneously by CTVMFT, includes a vertex constraint of all the

CDF RUN 1A

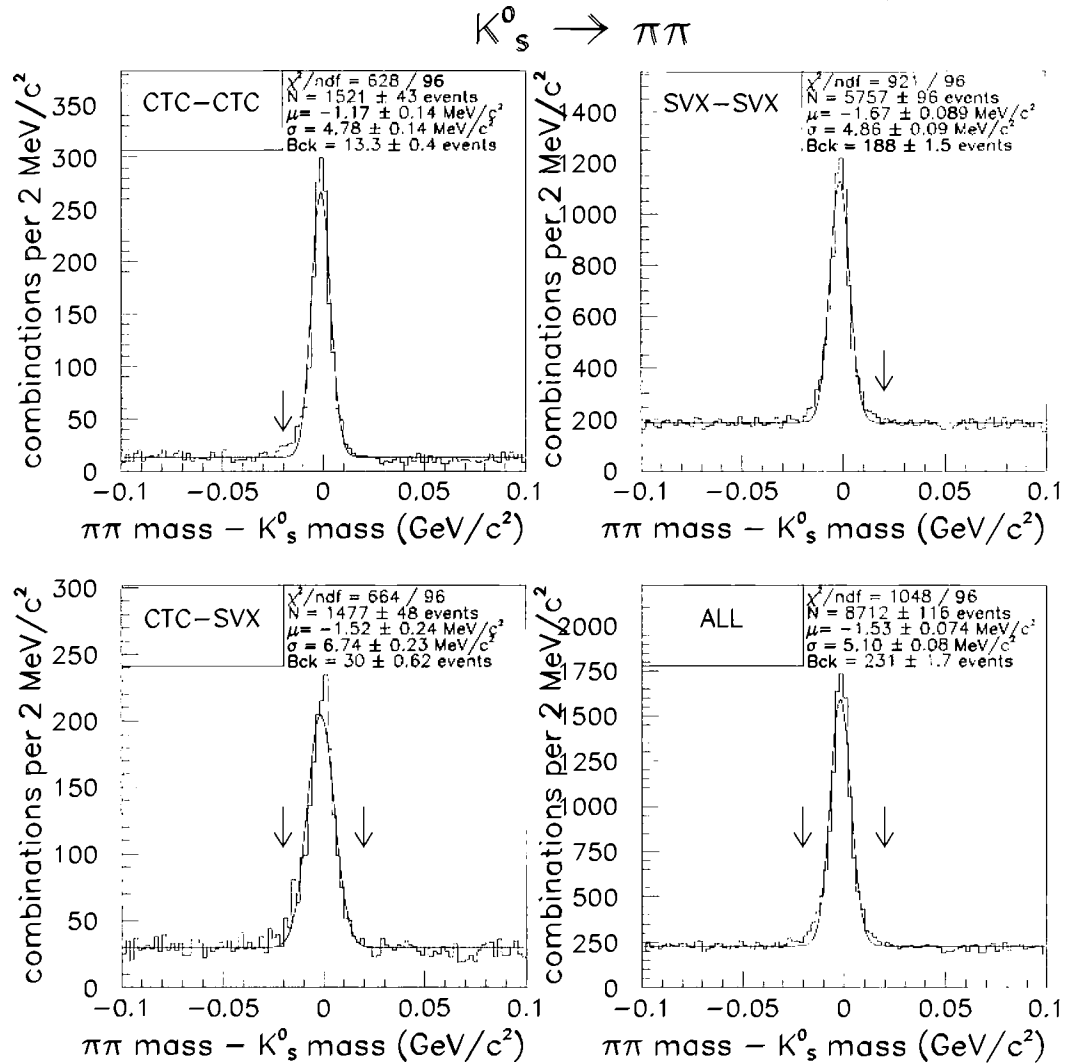


Figure 4.4:  $\pi\pi$  mass distributions. The quantity shown is the difference between the  $\pi\pi$  mass and the true  $K_S^0$  mass. Each histogram shows a particular configuration where 0, 1, 2 or any leg(s) of the  $K_S^0$  are measured in the SVX. The 2 tracks are required to come from a common vertex. The arrows, placed at  $\pm 20$  MeV/c<sup>2</sup> indicate the mass cuts applied to define the  $K_S^0$  sample.

tracks assigned to the  $B$  vertex and a mass constraint of the  $J/\psi$  candidate. If the combination contains a  $\psi(2S)$  candidate, that candidate is also mass constrained. Finally, in cases where the combination contains a  $K_S^0$  a second vertex constraint (tertiary vertex for the  $\sim 3$  cm decay length of the  $K_S^0$ ), an additional  $K_S^0$  mass constraint and a pointing constraint to the  $B$  vertex are added for that  $K_S^0$  candidate. Note that the  $B$  candidate is not forced to point back to the primary vertex (see Section 4.5.3). An overall 1% probability cut is applied on the  $\chi^2$  of this fit. From this point, only the track parameters returned by CTVMFT (see Section 3.4) are used in the analysis.

The combinations that include a  $K^*(892)$  candidate with a  $K^\pm\pi^\mp$  or  $K_S^0\pi^\mp$  mass more than  $80$  MeV/ $c^2$  away from the world average mass ( $0.8916$  GeV/ $c^2$  for  $K^*(892)^+$  and  $0.8961$  GeV/ $c^2$  for  $K^*(892)^0$ ) are rejected. Any combination that has a total  $p_T$  less than  $4$  GeV/ $c$  is also rejected to reduce the data sample size. This procedure does not throw away real  $B$  data because the  $J/\psi$  trigger eliminates  $B$  events with a  $p_T$  less than  $4$  GeV/ $c$ . In fact, tighter, optimized  $p_T$  cuts will be applied later (see Section 4.1.8).

### 4.1.8 Final $B$ Candidate Selection

This section describes the optimized  $p_T$  cuts, outlines a “duplicate removal procedure” used to make the final  $B$  candidate selection, and lists the total number of  $B_u$  and  $B_d$  events reconstructed in each of the eight decay channels considered.

#### Optimized $p_T$ Cuts

The analysis described in Section 4.1.7 was done with relatively low  $p_T$  cuts on the  $B$  and the  $K$ . These cuts are efficient for the reconstruction of the  $B$ , but also accept too much background. To correct this fact, the  $p_T$  cuts should be chosen to get the smallest statistical error on the background subtracted signals. The  $B$  candidates with a  $c\tau > 100$   $\mu m$  will largely determine the result of the lifetime fit because  $c\tau \geq 100$   $\mu m$  is significantly larger than the typical resolution (see Section 4.2.2). Hence, the  $p_T$  cuts were determined such that the signals with  $c\tau > 100$   $\mu m$  are optimized.

The study to determine the best  $p_T$  cuts was done in an earlier version of this analysis that required all tracks to be measured in the SVX, not just the muons from the  $J/\psi$ [45]. Hence, the optimum cuts may not be exactly the same for this version of the analysis because the background rates may be slightly different. However, this difference is a small perturbation in the analysis and, therefore, the results from the earlier version of this analysis are used, i.e. require  $p_T(\mathbf{K}) > 1.25 \text{ GeV}/c$  and  $p_T(B) > 6 \text{ GeV}/c$  in this analysis.

In this previous study, the number of signal events in the peak region as a function of the  $p_T$  cuts was obtained from Monte Carlo samples (normalized to the data using the  $J/\psi K^\pm$  channel), and the number of events in the sidebands was obtained from the real data. For each channel, this optimization was done in the following way: the  $p_T$  cut on the  $\mathbf{K}$  was varied from 1 to 3  $\text{GeV}/c$  in steps of 0.25  $\text{GeV}/c$ ; for each value of the  $p_T$  cut on the  $\mathbf{K}$ , the  $p_T$  cut on the  $B$  was varied from 4 to 6  $\text{GeV}/c$  in steps of 0.5  $\text{GeV}/c$ ; for each set of  $p_T$  cuts, the relative error on the number of signal events with  $c\tau > 100 \mu m$  was computed, and the optimum cuts were defined to be the ones that give the smallest relative error.

For the purpose of this optimization the number of signal events was computed as the difference between the number of candidates in the peak region and  $\frac{1}{2}$  of the number of candidates in the sidebands. The peak region is defined as a  $\pm 30 \text{ MeV}/c^2$  mass window around the world average value of the  $B$  meson ( $5.2786 \text{ GeV}/c^2$ ). The sidebands are two mass windows on either side of the peak region, each equal in width to the signal region, and centered at  $5.1886 \text{ GeV}/c^2$  and  $5.3686 \text{ GeV}/c^2$ . The results of this optimization did not depend heavily on the channels. Therefore, for the sake of simplicity, the same  $p_T$  cuts for all the channels were adopted —  $p_T(\mathbf{K}) > 1.25 \text{ GeV}/c$  and  $p_T(B) > 6 \text{ GeV}/c$ . These values were close to the optimum value for most of the channels (the channels with a  $K^*(892)^+$  preferred  $p_T(\mathbf{K}) > 1.50 \text{ GeV}/c$ , but this preference was not significant).

### Duplicate removal

The reconstruction described in Section 4.1.7 has been applied to all possible combinations, allowing more than one  $B$  candidate per event. Such “duplicate

candidates” could bias the lifetime measurements because two candidates in the same event would use the same  $J/\psi$  and, therefore, have  $B$  vertices very close to each other. Including these two (or more) vertices in the lifetime measurement would be almost equivalent to using the same  $B$  vertex twice. Furthermore, “duplicate candidates” could introduce a statistical correlation between the sample of  $B_u$  candidates and the sample of  $B_d$  candidates. Most of the duplicate candidates arise from the ambiguity of the mass assignment for the two tracks forming the  $K^*(892)^0$ , but other duplicate topologies are also present in the data. Details concerning the “duplicate removal procedure” are presented in Appendix A; salient points are addressed in this section.

The procedure used to select only one candidate per event is as follows:

1. In each event, all  $B$  candidates (in any of the eight considered channels) that satisfy  $p_T(\mathbf{K}) > 1.25 \text{ GeV}/c$  and  $p_T(B) > 6 \text{ GeV}/c$ , and that have a total mass within  $\pm 120 \text{ MeV}/c^2$  of the world average  $B$  mass (this mass window includes the signal region, the sidebands and the gaps between them), are considered.
2. If there are two  $\Psi K^*(892)^0$  candidates whose only difference is the mass assignment of the two tracks forming a  $K^*(892)^0$ , the CTVMFT  $\chi^2$  probabilities will be equal to each other. A single  $\Psi K^*(892)^0$  candidate is selected in this case by picking the one that has its  $K^*(892)^0$  mass closer to the world average value.
3. Pick the  $B$  candidate with the highest CTVMFT  $\chi^2$  probability.

Table 4.2 shows the effect on this duplicate removal procedure on the candidates with  $c\tau > 100 \mu m$ . The biggest effect is on the channels that use a reconstructed  $K^*(892)^0$  because of the  $K\pi$  mass assignment ambiguity. In particular, this procedure brings the  $B_d \rightarrow J/\psi K^*(892)^0$  signal (above background, with  $c\tau > 100 \mu m$ ) down from 88 to 66.5 candidates; among the 21.5 rejected candidates, 20 are discarded because of the presence of the same track combination in the event with a different mass assignment, and only 1.5 are discarded because another candidate in the same event (reconstructed with a different combination of tracks in any of the eight considered channels) has a better  $\chi^2$  value. Finally, as demonstrated in Appendix A, only 0.65%(1.4%) of

the  $B_u(B_d)$  candidates with an invariant mass within  $\pm 30 \text{ MeV}/c^2$  of the world average  $B$  mass had  $B_d(B_u)$  duplicates in the same region with  $c\tau > 100 \mu\text{m}$ .

### ***B* Mass Plots**

The final number of events for each of the channels is summarized in Table 4.3. A total of  $148 \pm 16 B^+$  and  $121 \pm 16 B^0$  mesons were reconstructed. Most charged  $B$  mesons are found in the  $J/\psi K^+$  channels, while most neutral  $B$  mesons are obtained in the  $J/\psi K^*(892)^0$  channel. Figure 4.5 shows the combined invariant mass distribution separately for the  $B_u$  and  $B_d$  channels.

Channel	‡ candidates in peak region		‡ candidates in side bands		‡ candidates in peak above background	
	$N_{before}^{peak}$	$N_{after}^{peak}$	$N_{before}^{side}$	$N_{after}^{side}$	$N_{before}$	$N_{after}$
$J/\psi K^+$	143	→ 141	62	→ 57	112	→ $112\frac{1}{2}$
$J/\psi K^*(892)^+$	8	→ 8	4	→ 3	6	→ $6\frac{1}{2}$
$\psi(2S) K^+$	5	→ 5	9	→ 7	$\frac{1}{2}$	→ $1\frac{1}{2}$
$\psi(2S) K^*(892)^+$	0	→ 0	0	→ 0	0	→ 0
Total $B_u$	156	→ 154	75	→ 67	$118\frac{1}{2}$	→ $120\frac{1}{2}$
$J/\psi K_S^0$	19	→ 17	8	→ 8	15	→ 13
$J/\psi K^*(892)^0$	148	→ 110	120	→ 87	88	→ $66\frac{1}{2}$
$\psi(2S) K_S^0$	1	→ 1	1	→ 1	$\frac{1}{2}$	→ $\frac{1}{2}$
$\psi(2S) K^*(892)^0$	19	→ 14	25	→ 13	$6\frac{1}{2}$	→ $7\frac{1}{2}$
Total $B_d$	187	→ 142	154	→ 109	110	→ $87\frac{1}{2}$

Table 4.2: Effect of the “duplicate removal” procedure on the  $B$  candidates with  $c\tau > 100 \mu m$ . For each channel and each mass region the following numbers are shown:

$N_{before}^{peak}$  = the number of candidates in the peak region with  $c\tau > 100 \mu m$  before duplicate removal

$N_{after}^{peak}$  = the number of candidates in the peak region with  $c\tau > 100 \mu m$  after duplicate removal

$N_{before}^{side}$  = the number of candidates in the side bands with  $c\tau > 100 \mu m$  before duplicate removal

$N_{after}^{side}$  = the number of candidates in the side bands with  $c\tau > 100 \mu m$  after duplicate removal

$N_{before}$  =  $N_{before}^{peak} - \frac{1}{2}N_{before}^{side}$  = the number of candidates above background (in the peak region) with  $c\tau > 100 \mu m$  before duplicate removal

$N_{after}$  =  $N_{after}^{peak} - \frac{1}{2}N_{after}^{side}$  = the number of candidates above background (in the peak region) with  $c\tau > 100 \mu m$  after duplicate removal

Channel	Number of $B$ candidate events in final selection			Estimate for the number of signal events
	Entire window $ \Delta m  < 120$	Peak region $ \Delta m  < 30$	Side bands $\begin{cases}  \Delta m  > 60 \\  \Delta m  < 120 \end{cases}$	
$J/\psi K^+$	1662	521	728	$157.0 \pm 26.5$
$J/\psi K^*(892)^+$	58	19	26	$6.0 \pm 5.0$
$\psi(2S) K^+$	77	20	40	$0.0 \pm 5.5$
$\psi(2S) K^*(892)^+$	4	1	1	$0.5 \pm 1.1$
Total $B_u$	1801	561	795	$163.5 \pm 27.6$
$J/\psi K_S^0$	65	31	23	$19.5 \pm 6.1$
$J/\psi K^*(892)^0$	2780	747	1332	$81.0 \pm 32.9$
$\psi(2S) K_S^0$	5	2	1	$1.5 \pm 1.5$
$\psi(2S) K^*(892)^0$	201	52	96	$4.0 \pm 8.7$
Total $B_d$	3051	832	1452	$106.0 \pm 34.6$

Table 4.3: Final number of reconstructed events for each channel and mass region. Mass ranges, defined in terms of the variable  $\Delta m$ , the difference between the measured mass of the reconstructed  $B$  and  $5.2786 \text{ GeV}/c^2$ , are indicated in  $\text{MeV}/c^2$ . The number of events shown in this table are those obtained after the duplicate removal procedure (without a  $c\tau > 100 \mu\text{m}$  cut). The last column shows the estimates for the number of signal events computed as the difference between the number of peak region events and one-half of the number of sideband events.

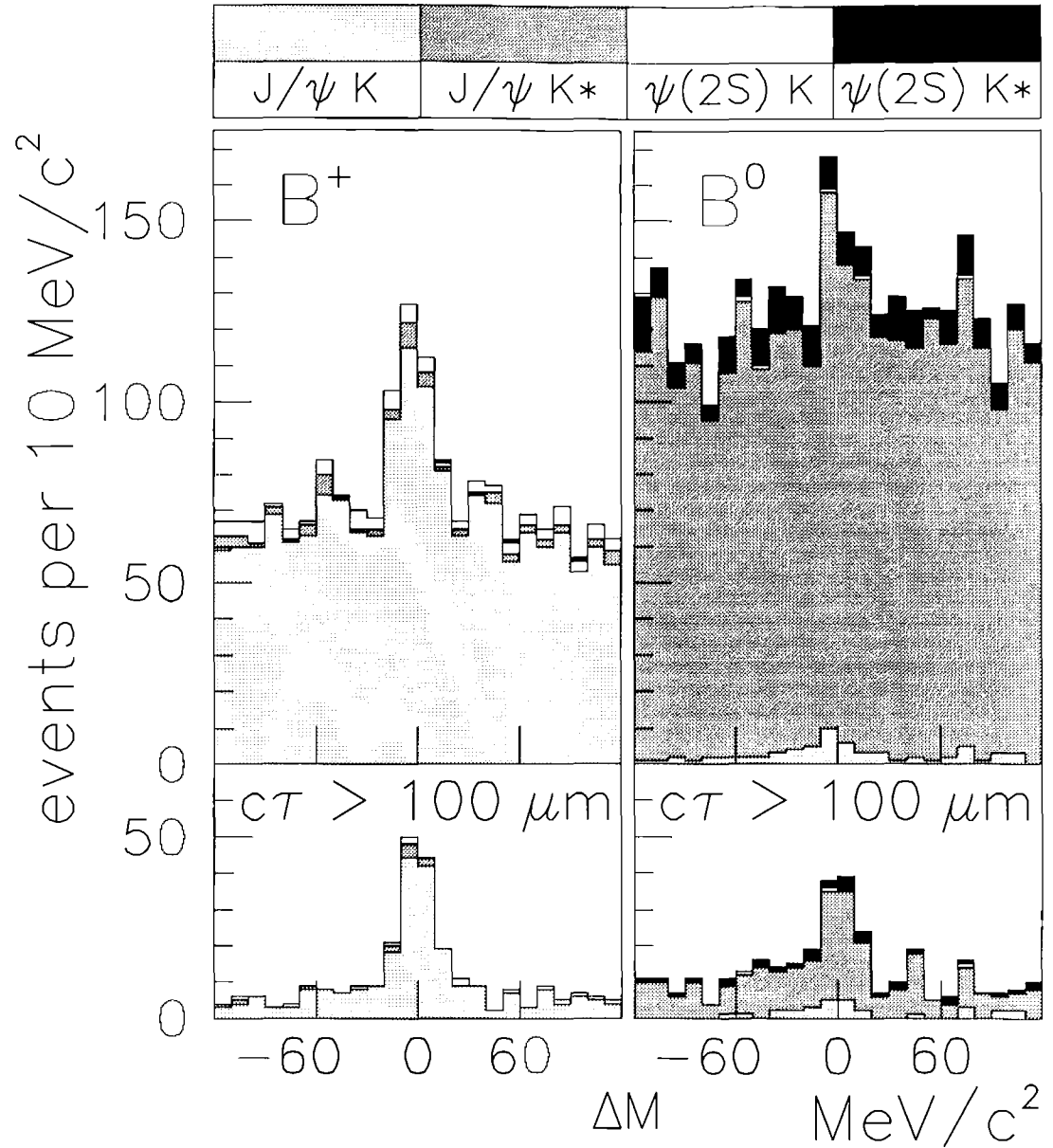


Figure 4.5:  $B$  mass distributions. The invariant mass distribution for all reconstructed  $B^+$  and  $B^0$  mesons.  $\Delta M$  is the difference between the measured mass and the world average  $B$ -meson mass. The upper plots show all events passing the selection described in the text. The lower plots show the subset of events with the proper decay length  $c\tau > 100 \mu\text{m}$ . In the lifetime fit, the peak region is defined as the 6 central bins, and the sideband regions are defined as the 6 leftmost and the 6 rightmost bins.

## 4.2 $B$ Meson Decay Length

This section describes the techniques used to determine the proper decay length of the fully reconstructed  $B_u(B_d)$  mesons. The process of measuring the  $B$  decay vertex, or secondary vertex, has already been described in Section 4.1.7. The sections that follow will concentrate on the primary vertex, or point at which the  $B$  meson was produced, on the signed decay length measured in the  $r - \phi$  plane,  $L_{xy}$ , and on the calculated proper decay length,  $c\tau$ .

### 4.2.1 Determining the Primary Vertex

Two methods of determining the creation vertex of the candidate  $B$  meson were considered in this analysis. These are (1) determine the primary vertex on an event-by-event basis and (2) calculate the  $(x, y)$  position of the primary vertex given the run-dependent beam line parameters as a function of the measured  $z$  position. The latter method is the one used in this analysis; Section 4.5.5 discusses the reasons for rejecting the event-by-event algorithm in this analysis.

As already mentioned in Section 2.2.2, the primary interaction region is distributed in  $z$  as a gaussian with a sigma of  $\sim 30$  cm. For those interactions occurring within the fiducial volume enclosed by the SVX, the beam position can be determined with effectively perfect precision. The algorithm used is described in detail in References [46, 47]. The procedure requires at least 250 tracks in each SVX barrel. Basically, it parameterizes the SVX measured impact parameter,  $D(\phi_0, Z_0)$ , of each track in terms of the slope and offset in  $x$  and  $y$ . Minimizing the  $\chi^2$  gives the 4 parameters and an error matrix. Iterations on the impact parameter of the tracks with respect to the fitted beam position are performed until 40% of the originally selected tracks are rejected. This procedure was performed at the beginning of each new run, and the resulting slopes and offsets were stored in the VTVZ YBOS[42] bank and in the CTC beam position database (CTCBPO).

Fig. 4.6 displays the results of the above procedure. Plot No. 1 of Fig. 4.6 is a projection of the beam onto the  $r - \phi$  plane at  $z = 0$ . It demonstrates

that the beam profile is circular and gaussian, while Plot No. 2 of Fig. 4.6, which is a slice of Plot No. 1 in  $x$ , shows that width of the beam is distributed as a gaussian with a sigma of  $\sim 40 \mu m$ . Note that the  $40 \mu m$  is not the error on the measurement but the actual physical width of the beam. Plot No. 3 of Fig. 4.6 gives the  $x$  coordinate of the beam line as a function of  $z$ . The beam line varied in  $x(y)$  during a store by an average of  $5 \mu m(11 \mu m)$ ; during a run these parameters were stable to within  $4 \mu m$  [47].

The procedure used to calculate the  $x$  and  $y$  coordinates of the primary interaction vertex is the following:

1. Because the run-by-run, SVX measured slope and offset values stored in the Version 6.15  $J/\psi$  YBOS[42] banks are incorrect\*, an alignment correction (translation/rotation) is added to these values via the TRKFIX module (see Section 3.4).
2. The  $z$  coordinate of the primary vertex is taken from one of the primary vertices available in the VTVZ bank; the one with the  $z$  coordinate closest to the  $z$  of the fitted  $J/\psi$  vertex is selected.
3. The  $x$  and  $y$  coordinates of the primary vertex are then obtained from the measured  $z$  coordinate using the run-dependent, SVX beam line parameters via the equation

$$x(y) = X_0(Y_0) + z \cdot M_x(M_y), \quad (4.1)$$

where  $M_x(M_y) = \frac{dx(dy)}{dz}$ . The error on the calculated  $x(y)$  coordinate is taken to be about the measured physical width of the beam, i.e.  $\sigma_{xx} \approx \sigma_{yy} \approx 40 \mu m$ . Because the profile of the beam is circular, the cross terms in the primary vertex error matrix are dropped, i.e. it is a 2-by-2 unit matrix  $\times (40 \mu m)^2$ .

---

\*Version 7.09 CTC tracking algorithm includes new CTC alignment corrections that shift the center of the CTC relative to the beam line. The SVX beam line parameters stored in the YBOS banks were obtained using Version 6.10 SVX tracking. Hence, the rotation/translation correction added by TRKFIX transforms the old SVX beam line values into the new Version 7.09 CTC reference frame.

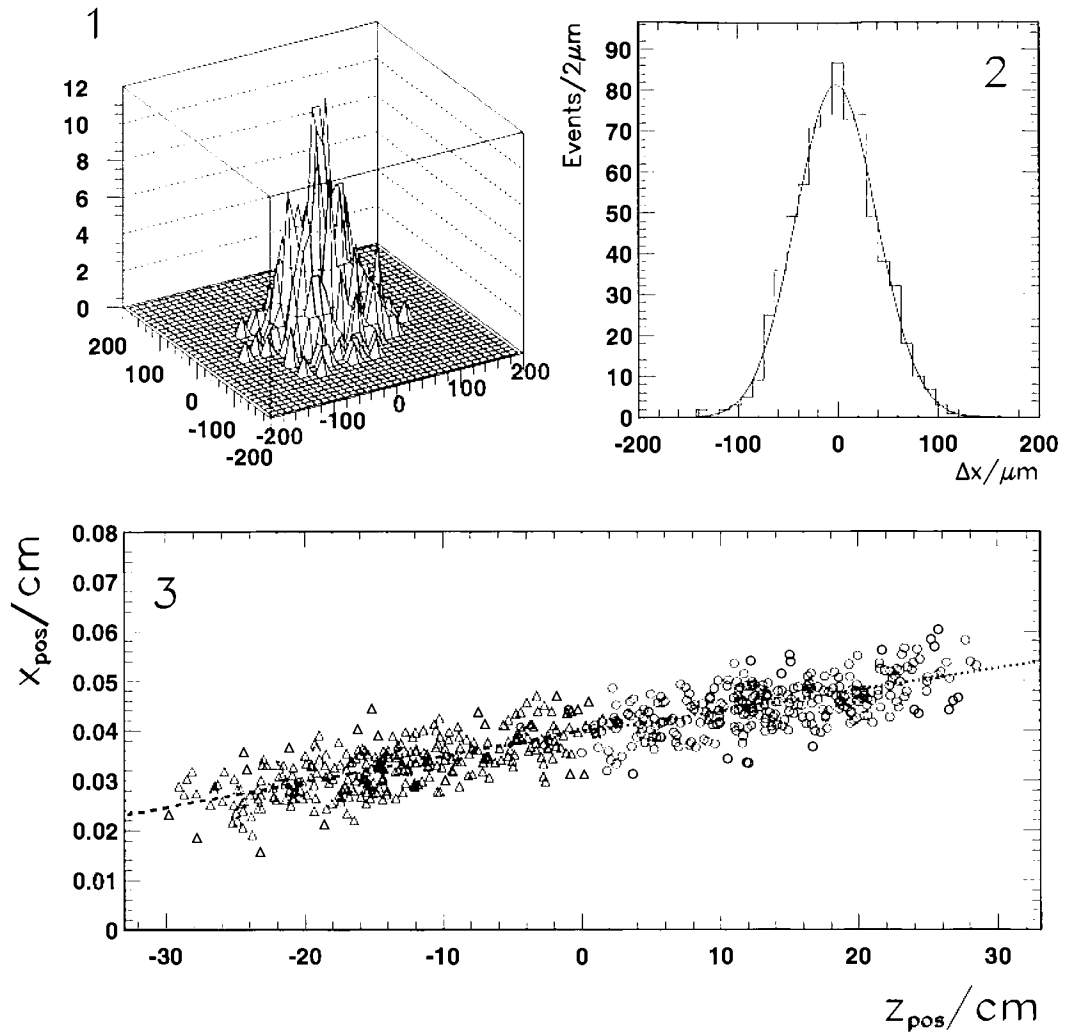


Figure 4.6: Beam-profile {1} and {2} at  $z = 0.0$  and the  $x$  – vs –  $z$ -distribution of the primary vertex {3} measured by the SVX. The beam profile is circular and gaussian in {1}, and the gaussian fit to {2} yields  $\sigma = 36 \mu\text{m}$ . The triangles(circles) indicate that the tracks were measured in SVX barrel 0(1).

4. If SVX beam line parameters are not available for the run in question, then no primary vertex is made available to this run (1% of the data), and the  $\psi(2S)$ ,  $K_S^0$  and  $B$  meson reconstruction steps are skipped. Nearly all (99%) of the Version 6.15  $J/\psi$  data in this analysis had SVX measured beam line parameters available, i.e. only 1,709 events over 205,606 events (0.8%) do not have a beam line measured by the SVX.

### 4.2.2 Determining $L_{xy}$ and $c\tau$

This section describes the method of measuring  $L_{xy}$  and calculating  $c\tau$ . The proper time,  $\sigma_{c\tau}$  and normalized error distributions for  $B_u(B_d)$  mesons are presented.

For each final  $B$  meson candidate a value of the proper decay length is computed as

$$c\tau = L_{xy} \frac{m_B}{|\vec{p}_T^B|} = \vec{X} \cdot \hat{p}_T^B \frac{m_B}{|\vec{p}_T^B|}, \quad (4.2)$$

where  $L_{xy}$  is the projection of the 2-dimensional vector joining the primary vertex to the  $B$  vertex,  $\vec{X}$ , onto the transverse momentum direction,  $\hat{p}_T^B$ , of the  $B$ , and where  $m_B$  is the world average  $B$  mass (5.2786  $GeV/c^2$  for  $B_u$ , 5.2787  $GeV/c^2$  for  $B_d$ ). This proper decay length will also be referred to as the “lifetime” throughout this thesis. Projecting  $\vec{x}$  onto the  $B$  meson’s transverse momentum provides a physically meaningful, signed decay length. For real  $B$  mesons,  $\vec{x}$  should point in the same direction as  $\hat{p}_T^B$ , giving a positive decay length. Candidates with a large  $|\vec{x}|$  but negative  $L_{xy}$  are unphysical and are recognized immediately as background candidates. The error on the “lifetime” of each candidate is computed from the 2-by-2 error matrix on the  $B$  vertex (returned by the vertexing algorithm CTVMFT) and the error matrix on the primary vertex, described in the previous section. When calculating  $\sigma_{c\tau}$ , the two vertexes are assumed to be uncorrelated, i.e. the error on the lifetime is not a function of azimuthal angle since the beam profile is circular; this would not hold if the beam profile were elliptical, as is the case at LEP [6]. Finally, the error in the direction of  $\vec{p}_T^B$  is altogether insignificant when compared with the 40  $\mu m$  uncertainty due to the physical width of the beam and is, therefore, neglected.

Figs 4.7 and 4.8 show the resulting  $c\tau$  distributions separately for  $B_u(B_d)$  signal and  $B_u(B_d)$  sideband regions. Note that the sideband regions were explicitly chosen to avoid the mass regions populated by poorly measured “real”  $B$  mesons, i.e.  $|mass - 5.2786 \text{ GeV}/c^2| > 60 \text{ MeV}/c^2$ , and by candidates with a missing  $\pi^0$ , i.e.  $(mass - 5.2786 \text{ GeV}/c^2) > -120 \text{ MeV}/c^2$ . A significant  $B$  meson lifetime is evident in the  $B_u(B_d)$  signal plots, while the corresponding sideband plots contain asymmetric tails, an indication that there is also a lifetime component in the sidebands. This apparent sideband lifetime is most probably due to a  $J/\psi$  from a  $b$ -hadron decay forming a good secondary vertex with a random track. Regardless of the source, the next section describes the procedure used to model the lifetime of the background and to extract  $c\tau$  from the signal distributions. Fig. 4.9 shows the  $B_u(B_d)$   $c\tau$  error and normalized error distributions. The average error on  $c\tau$  is  $\sim 40 \mu m$ , and the normalized error on  $c\tau$  has a fitted sigma of  $\sim 1.00$ , indicating that this error is calculated correctly (see Section 4.3.3). Finally, Figs 4.10 and 4.11 demonstrate that candidates with long lifetimes are not the result of poorly measured vertices; i.e., the measured value of  $c\tau$  is independent of the error on  $c\tau$  (see also Fig. 4.18).

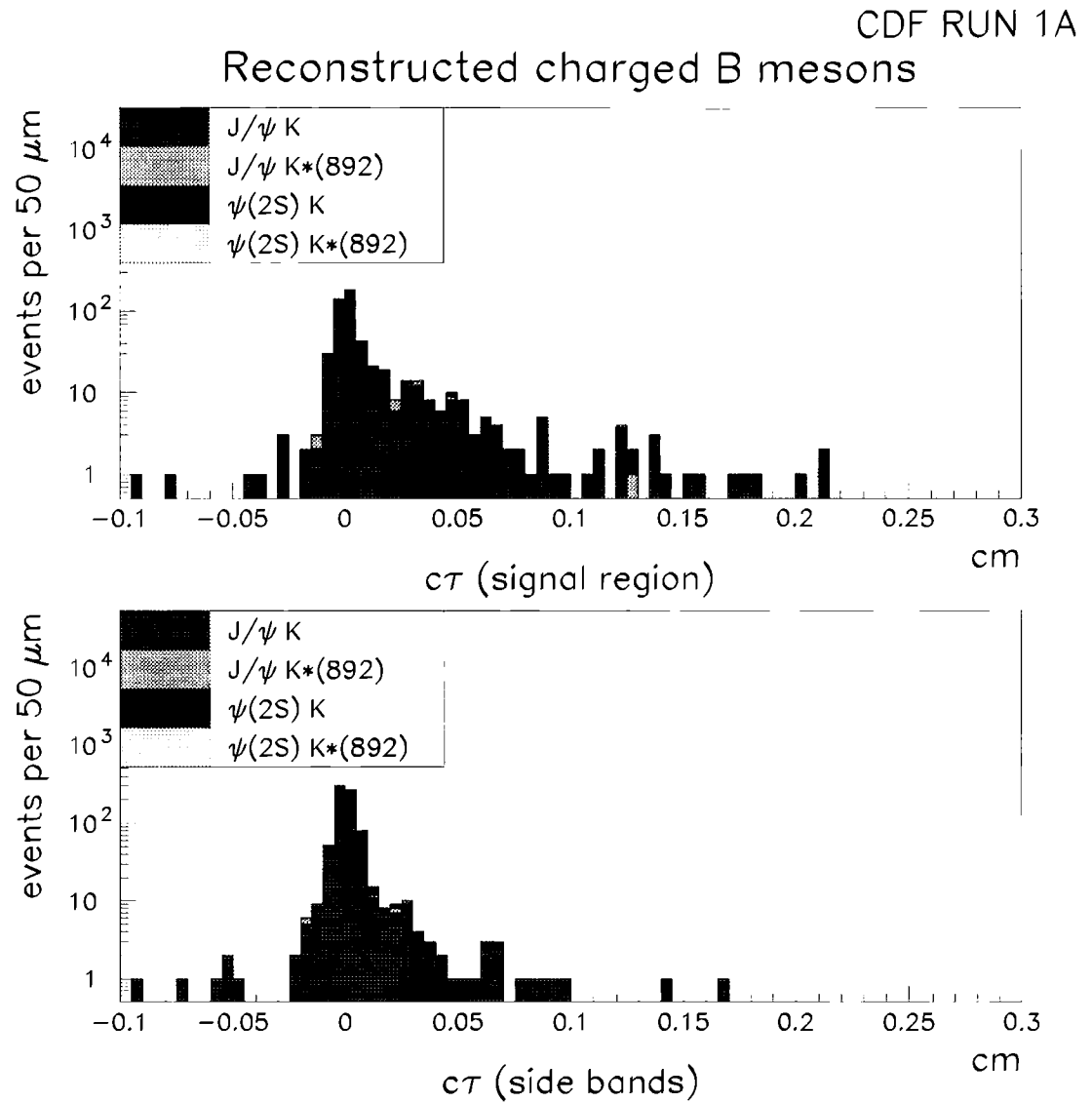


Figure 4.7: Combined  $c\tau$  distributions for all reconstructed  $B_u$  mesons. The shading indicates the particular decay channel.

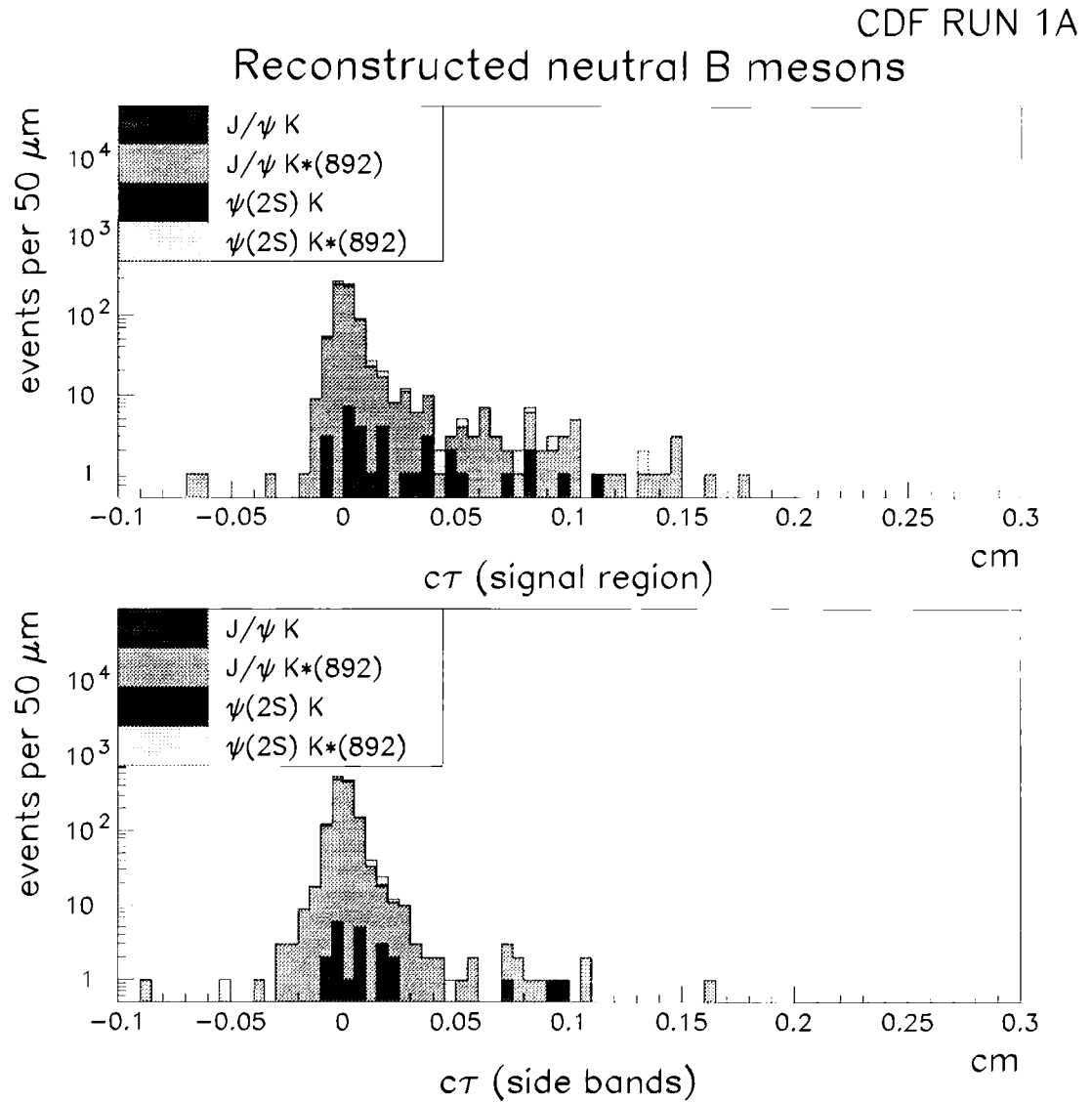


Figure 4.8: Combined  $c\tau$  distributions for all reconstructed  $B_d$  mesons. The shading indicates the particular decay channel.

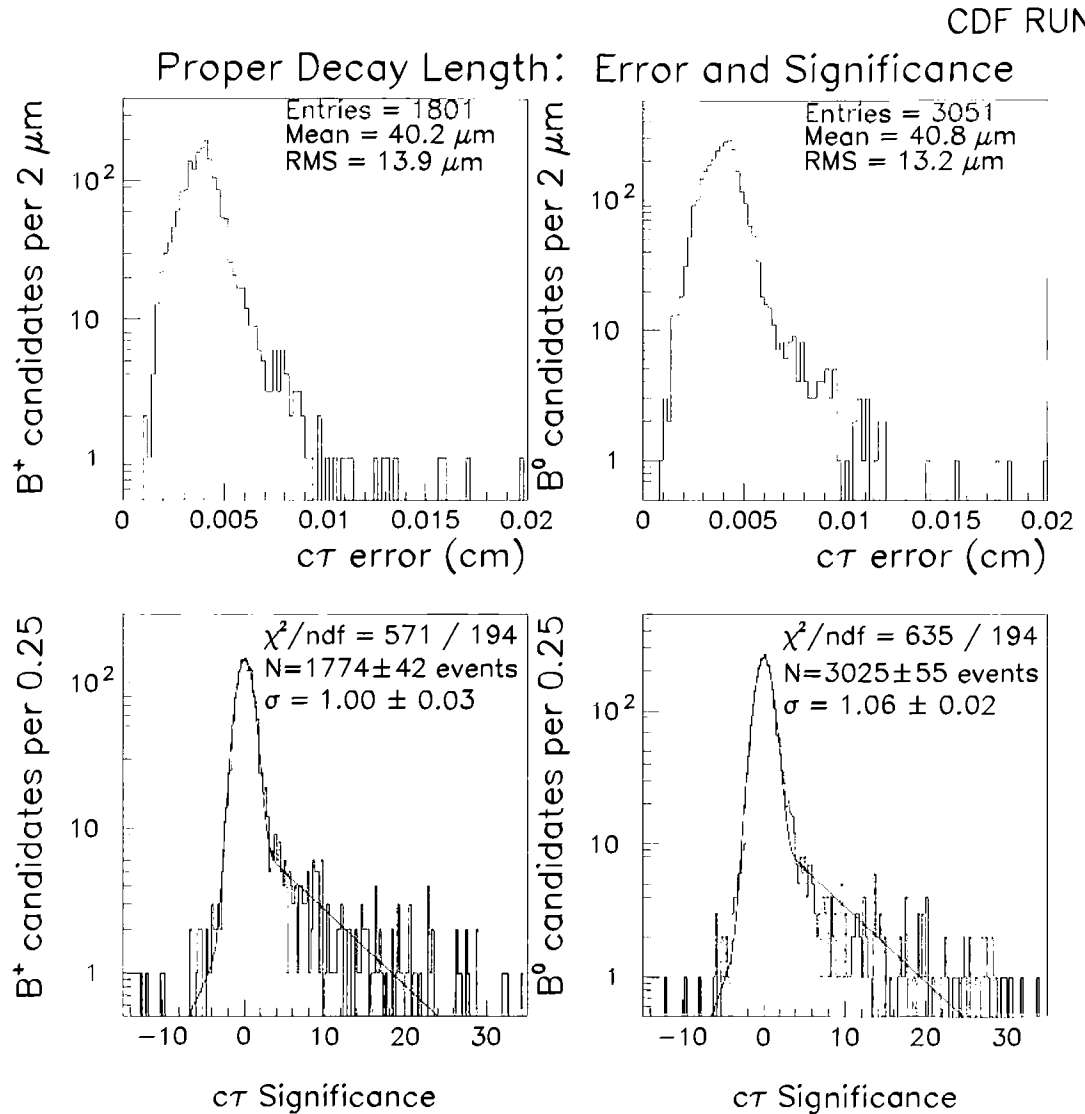


Figure 4.9: Top plots: Distribution of the error on the proper decay length, separately for the charged (left) and neutral (right)  $B$  candidates in a  $\pm 120 \text{ MeV}/c^2$  mass window around the average  $B$  mass. Bottom plots: Distribution of the proper decay length significance,  $\left(\frac{c\tau}{\sigma_{c\tau}}\right)$ , for the same samples. The curves are binned log-likelihood fits, assuming a gaussian centered at zero plus asymmetric exponential tails.

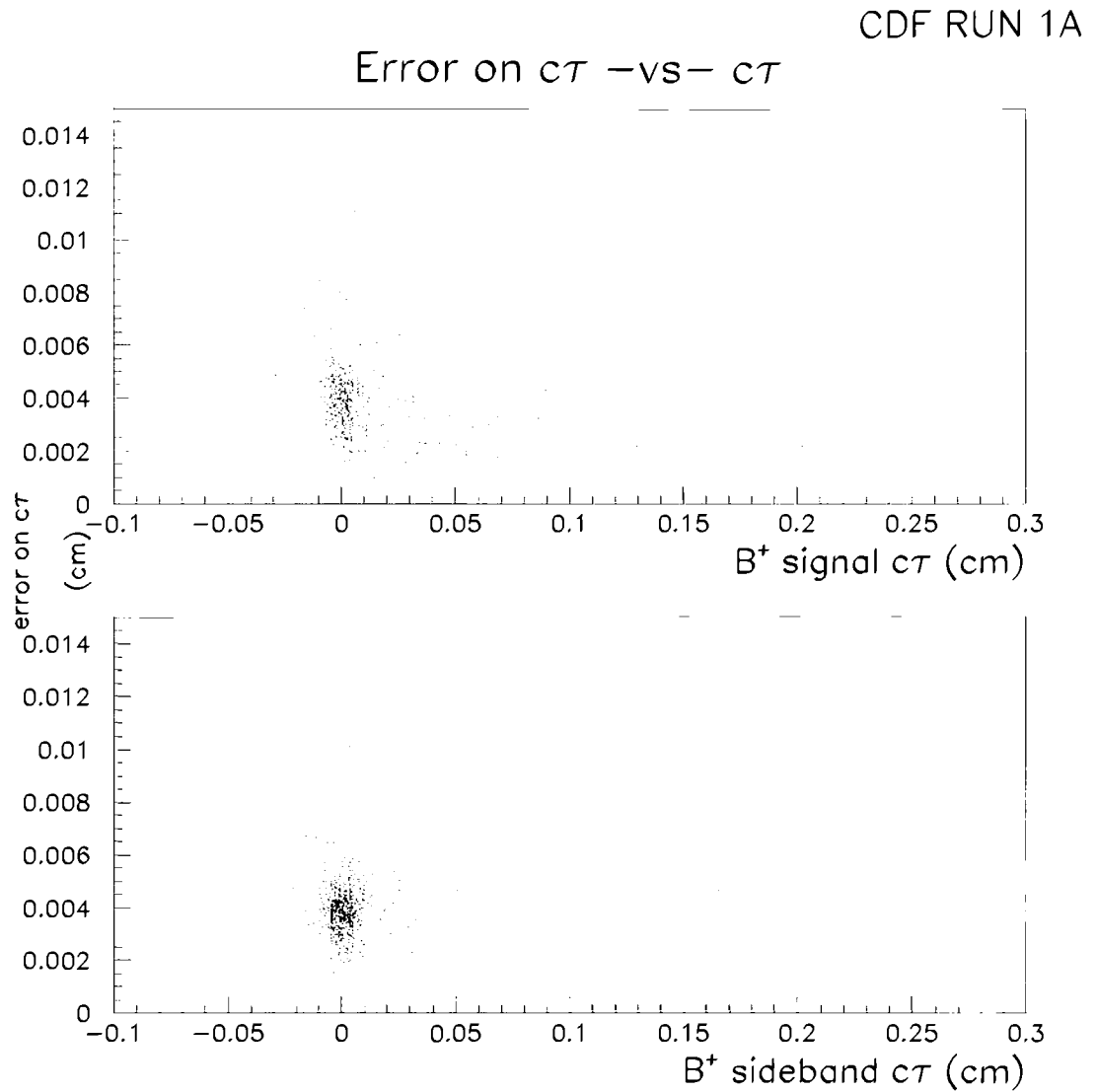


Figure 4.10: Error on  $c\tau$  versus  $c\tau$  for  $B_u$  signal and peak candidates. The distributions demonstrate that the measured value of  $c\tau$  is independent of the error on  $c\tau$  for  $c\tau < 3$  mm.

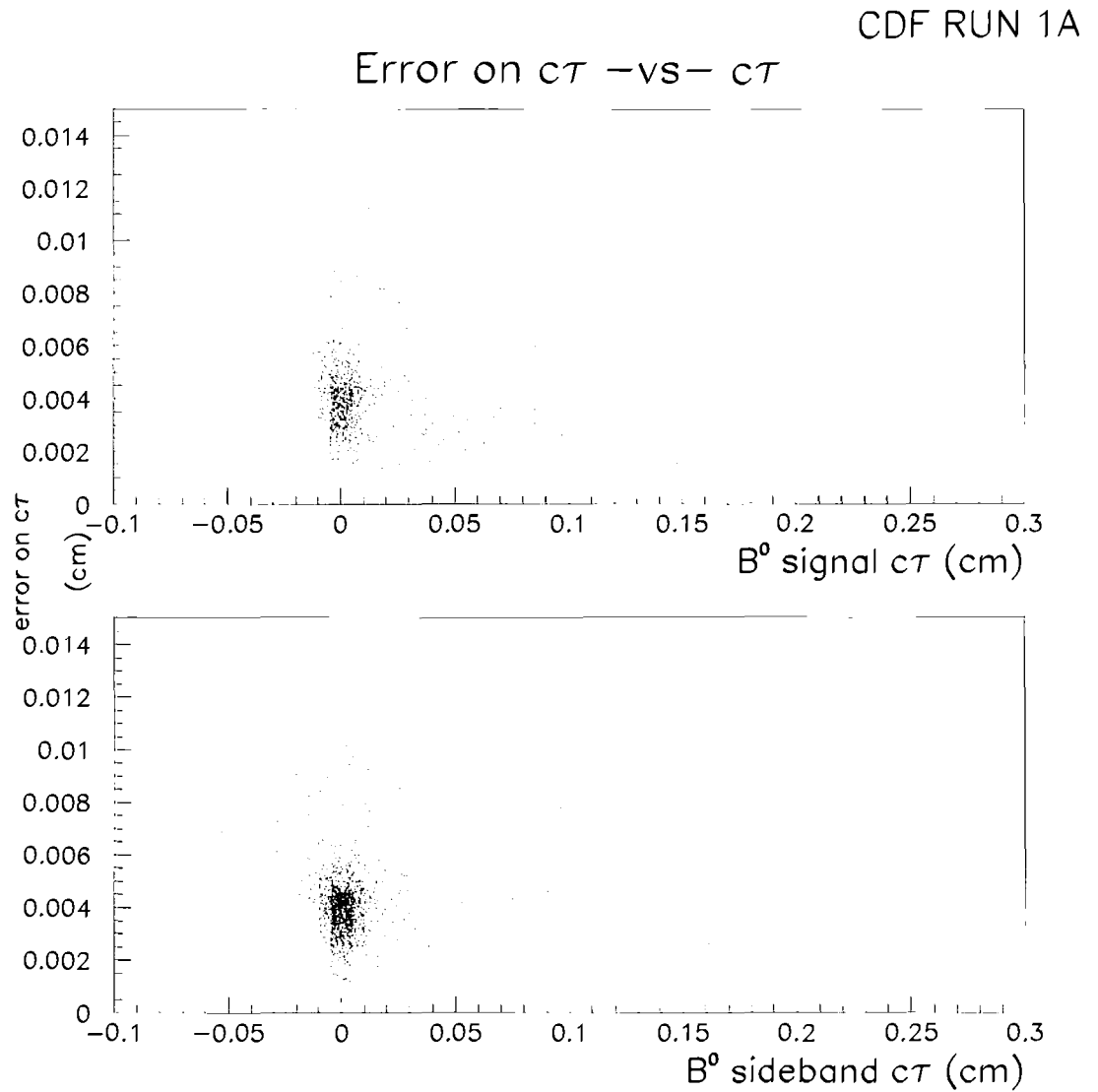


Figure 4.11: Error on  $c\tau$  versus  $c\tau$  for  $B_d$  signal and peak candidates. The distributions demonstrate that the measured value of  $c\tau$  is independent of the error on  $c\tau$  for  $c\tau < 3$  mm.

### 4.3 $B$ Meson Lifetime

This section describes the techniques used to extract the lifetime,  $c\tau$ , from the measured proper decay length distributions of the fully reconstructed  $B_u(B_d)$  mesons. First, a general overview of the lifetime *probability density function*, or PDF, is presented. Next, a variety of fitting techniques with varying levels of sophistication will be discussed. The results of these fits will be presented in turn. Then the results of fit confidence level and statistical error tests are discussed.

#### 4.3.1 The Lifetime Probability Density Function

The observed lifetime distributions, shown in Figs 4.7 and 4.8, are simply resolution transforms of the true lifetime PDFs[48], i.e.

$$f(x') = A \int dx [P(x; c\tau) + B(x; c\tau)] G(x; x'), \quad (4.3)$$

where  $f(x')$  is the observed lifetime distribution,  $A$  is a normalization factor,  $P(x; c\tau)$  is the signal lifetime PDF,  $B(x; c\tau)$  is the background lifetime PDF, and  $G(x; x')$  is the gaussian resolution function. Hence, if appropriately normalized, the measured lifetime distributions shown in Figs 4.7 and 4.8 are actual *observed PDFs*. This fact will be exploited in the discussion that follows regarding the fitting techniques used to extract  $c\tau$  from the data.

A number of assumptions about the measured lifetime PDFs must be addressed before giving explicit forms for  $P(x; c\tau)$  and  $B(x; c\tau)$ . These are as follows:

- The signal region contains both signal and background events. The proper decay lengths of the signal events are distributed according to an exponential function convoluted with a gaussian resolution function. The exponential slope is the proper decay length to be measured. The gaussian resolution for each event is the measurement error on  $c\tau$ .
- Background events in the signal region are assumed to have the same  $c\tau$  distribution as the events in the sideband region. The proper decay lengths of the background events are distributed according to the

sum of a gaussian resolution function and two exponential tails, where the exponentials are used to model the positive and negative lifetime tails[49]. It is further assumed that the background candidates have a linear mass distribution and that the peak and sideband regions are symmetric around the  $B$  mass.

Note that the gaussian resolution assumption is addressed in more detail in Section 4.4.2. Furthermore, the assumption concerning the asymmetric exponential tails in the background PDF is not motivated by a physical mechanism. Instead, exponential tails are selected simply because they are the most elementary functions that appear to describe the observed background distribution. Section 4.4.3 describes an alternate, extreme background parameterization that is used to assign a systematic uncertainty due to the particular choice of background parameterization.

Sections 4.3.2 through 4.3.4 describe three fitting techniques. All three methods are similar in that they involve maximizing a likelihood function. However, each fit differs substantially in detail, a fact that not only warrants a separate discussion for each method, but also enables a variety of consistency and cross checks in the lifetime analysis. The first method involves a binned fit of background subtracted  $B_u(B_d)$   $c\tau$  distributions starting with a minimum proper time greater than  $100 \mu m$ . The starting value of  $x'_0 = 100 \mu m$  was selected simply because it is a convenient value that happens to be much larger than the typical error on  $c\tau$  ( $\sim 40 \mu m$ , see Fig. 4.9). The second fit that is examined is essentially identical to the first with two main differences: (1) the fit is an unbinned fit, and (2) an actual fit is performed to the sideband data to subtract out the background. The final fit, discussed in Section 4.3.4, is also an unbinned fit, but it differs from the other two in that a likelihood function is maximized simultaneously for the sideband and peak  $c\tau$  distributions.

### 4.3.2 Fitting Technique # 1

This fitting technique is the least sophisticated of the three methods used in this analysis. Nevertheless, it provides an important test of the assertion that the observed peak  $c\tau$  distribution is indeed a lifetime PDF. The arithmetic mean of a quantity distributed according to an exponential distribution is

equal to the slope of the exponential. Furthermore, since the lifetime is just the slope of the exponential, the fitted value of the lifetime should not depend on the starting point of the fit, in this case the value of  $x'_0$ . For these reasons, a quick, binned likelihood fit to the background subtracted peak  $c\tau$  distributions is performed for peak events with  $c\tau > 100 \mu m$ . The results obtained from this fit are then compared with the mean value of the distributions and with results from the other two fits. The details of this procedure and the quantitative results/comparisons are given in the text below.

The mean value of an exponential PDF is equal to the slope of the exponential, i.e.

$$c\tau = \frac{1}{c\tau} \int_0^\infty dx x e^{-\frac{x}{c\tau}} \quad (4.4)$$

and

$$c\tau + 100 \mu m \simeq \frac{1}{c\tau} \int_{100}^\infty dx x e^{-\frac{x}{c\tau}}, \quad (4.5)$$

where the approximation in Eq. (4.5) is obtained assuming  $100 \mu m \ll c\tau$ . Given a pure exponential PDF, the mean value of the binned distribution (calculated in PAW[50], for example) should equal the slope obtained from fitting the distribution. Furthermore, since the fitted slope of an exponential does not depend on the initial starting value, it is convenient to consider only that part of the distribution with  $c\tau > 100 \mu m$ . Fig. 4.12 shows the results of using a pure exponential PDF (see Eqs. (4.15) and (4.16)) in a binned likelihood fit[48] on a background subtracted signal distribution for those events with  $c\tau > 100 \mu m$ . It is unnecessary to consider the resolution transform of the exponential PDF in this exercise because the effect of gaussian smearing for events with  $c\tau > 100 \mu m$  is essentially zero, i.e. substituting

$$G(x; x') = \frac{1}{\sqrt{2\pi}\sigma} \cdot \exp\left(-\frac{1}{2} \left[\frac{x' - x}{\sigma}\right]^2\right) \quad (4.6)$$

and

$$P(x) = \begin{cases} \frac{1}{\lambda} \cdot \exp\left(\frac{-x}{\lambda}\right) & 0 \leq x < \infty \\ 0 & x < 0 \end{cases} \quad (4.7)$$

into Eq. (4.3) yields

$$f(x') = A \int_0^\infty dx \exp\left(\frac{-x}{\lambda}\right) \cdot \exp\left(-\frac{1}{2} \left[\frac{x' - x}{\sigma}\right]^2\right), \quad (4.8)$$

where  $\lambda = c\tau$  and  $A = \frac{1}{\lambda\sqrt{2\pi}\sigma}$ . Substituting  $y = x' - x$  into Eq. (4.8) yields

$$f(x') = A \int_{-\infty}^{x'} dy \exp\left(\frac{-(x' - y)}{\lambda}\right) \exp\left(-\frac{1}{2}\left[\frac{y}{\sigma}\right]^2\right). \quad (4.9)$$

Combining the arguments of the exponentials in Eq. (4.9) and completing the square yields

$$f(x') = A \int_{-\infty}^{x'} dy \exp\left(\frac{-x'}{\lambda} - \frac{1}{2\sigma^2} \cdot \left(y - \frac{\sigma^2}{\lambda}\right)^2 + \frac{\sigma^2}{2\lambda^2}\right). \quad (4.10)$$

Combining common terms in Eq. (4.10) gives

$$f(x') = A \cdot \exp\left(\frac{\sigma^2}{2\lambda^2} - \frac{x'}{\lambda}\right) \cdot \int_{-\infty}^{x'} dy \exp\left(-\frac{1}{2}\left(\frac{y}{\sigma} - \frac{\sigma}{\lambda}\right)^2\right). \quad (4.11)$$

Substituting  $u = \frac{y}{\sigma} - \frac{\sigma}{\lambda}$  and  $dy = \sigma du$  into Eq. (4.11) gives the more illuminating form

$$f(x') = \frac{1}{\lambda} \cdot \exp\left(\frac{\sigma^2}{2\lambda^2} - \frac{x'}{\lambda}\right) \cdot \frac{1}{\sqrt{2\pi}} \int_{-\infty}^{\frac{x'}{\sigma} - \frac{\sigma}{\lambda}} du \exp\left(-\frac{1}{2}u^2\right). \quad (4.12)$$

The integral expression in Eq. (4.12) is just the CERN program library routine `freq(t)`[51], i.e.

$$\text{freq}(t) = \frac{1}{\sqrt{2\pi}} \int_{-\infty}^t du \exp\left(-\frac{1}{2}u^2\right). \quad (4.13)$$

Substituting Eq. (4.13) into Eq. (4.12) and taking advantage of the fact that  $\text{freq}(x) + \text{freq}(-x) = 1$  yields the important equation

$$f(x') = \frac{1}{\lambda} \cdot \exp\left(\frac{\sigma^2}{2\lambda^2} - \frac{x'}{\lambda}\right) \left[1 - \text{freq}\left(\frac{\sigma}{\lambda} - \frac{x'}{\sigma}\right)\right]. \quad (4.14)$$

Eq. (4.14) is the measured lifetime PDF for  $B$  mesons in the signal region. Hence, it can be combined with a suitable background PDF and used to fit a  $c\tau$  distribution that has not been background subtracted (see Sections 4.3.3 and 4.3.4). A simpler technique, i.e. the one being considered in this section, is to use Eq. (4.14) to fit a background subtracted  $c\tau$  distribution, noticing that for events with  $c\tau > 100 \mu m$ , Eq. (4.14) degenerates (to a good approximation) into a pure exponential PDF

$$f(x') \simeq \frac{1}{\lambda} \cdot \exp\left(\frac{x'}{\lambda}\right) \quad \text{for} \quad \begin{cases} \lambda \simeq 500 \mu m \\ \sigma \simeq 40 \mu m \\ \frac{x'}{\sigma} \geq 3.0 \end{cases}, \quad (4.15)$$

which is the desired result.

Eq. (4.16) gives the general form of the Poisson PDF for a binned likelihood function, where  $\sigma$  is common for all events and can be constrained to be equal to the bin width and the  $x'_i$  for each bin is distributed according to Eq. (4.15):

$$\mathcal{P}(\mu_i, N_i) = \frac{e^{-\mu_i} \mu_i^{n_i}}{n_i!}, \quad (4.16)$$

where

- $i$  denotes the  $i^{\text{th}}$  bin,
- $n_i$  is the number of events in the  $i^{\text{th}}$  bin,
- $\mu_i = \mathcal{A}f(x'_i; \lambda)$ ,
- $f(x'_i; \lambda)$  is just Eq. (4.15),
- $\mathcal{A}$  is a normalization constant;  $x'_i$  is the value of the center of the  $i^{\text{th}}$  bin; and  $\lambda$  is the fit parameter =  $c\tau$ .

The likelihood function is then

$$L = \prod_{i=1}^{N_{bins}} \mathcal{P}(\mu_i, N_i), \quad (4.17)$$

where  $\mathcal{P}$  is just Eq. (4.16), and the corresponding log-likelihood function\*

$$\mathcal{L} = -2 \log(L) \quad (4.18)$$

is minimized via MINUIT[52]. Fig. 4.12 shows the results of this binned log-likelihood fit.

In spite of its “back of the envelope” heritage, this procedure demonstrates a number of key characteristics concerning the measured lifetime PDFs. The lifetime of the  $B_u(B_d)$  sample obtained from this exercise is  $466 \pm 47 \mu\text{m}$  ( $513 \pm 59 \mu\text{m}$ ), which is consistent with the calculated difference between 100  $\mu\text{m}$  and the mean value of the distribution returned by PAW[50],  $572 - 100 = 472 \mu\text{m}$  ( $623 - 100 = 523 \mu\text{m}$ ). This fact shows that the background subtracted

---

\*  $-2 \log(L)$  is used simply because of mathematical facility, i.e. it is much simpler to manipulate a finite sum in FORTRAN than a finite product.

signal  $c\tau$  distributions do indeed behave as exponential PDFs. Furthermore, as will be shown in comparisons between these results and those presented in the Sections 4.3.3 and 4.3.4 and summarized in Table 4.6, the results are also consistent with fitting techniques that consider all of the events in the distribution, not just those events with  $c\tau > 100 \mu m$ . This fact demonstrates that the quoted lifetime values really are the slopes of a lifetime PDF because good agreement between results that use different values for the initial starting point,  $x'_0$ , is observed.

### 4.3.3 Fitting Technique # 2

The fitting technique described in this section is referred to as the two step fitting method because an unbinned, log-likelihood fit is performed separately for the sideband and signal  $c\tau$  distributions. In the two-step fit, the background parameters in the fit to the  $B_u(B_d)$  peak distribution are fixed to those obtained from fitting the  $B_u(B_d)$  sideband distribution. Also, the unbinned fit allows the  $\sigma$  of the gaussian resolution function to vary on an event-by-event basis instead of assigning a common  $\sigma$  for each bin as was done in the binned log-likelihood fit described in Section 4.3.2. Because the event-by-event  $c\tau$  error is taken to be the  $\sigma_i$ , where  $i$  denotes the  $i^{th}$  event, of the gaussian resolution function, the unbinned log-likelihood fit gives a “better” fit than the equivalent binned technique as long as the event-by-event errors are correctly determined. The top plots of Fig. 4.9 show the measured  $c\tau$  error distributions, while the bottom plots are the normalized versions of the upper plots ( $\frac{c\tau}{\sigma_{c\tau}}$ ). If the errors are correctly determined, the fit to the gaussian portion of the normalized distributions in the bottom plots should have a  $\sigma = 1.0$ , which is identically the case for the  $B_u$  mesons, approximately true for the  $B_d$  mesons ( $\sigma_{c\tau} = 1.06 \pm 0.02$ ). Section 4.4.2 describes the manner in which a systematic uncertainty is assigned due to incorrectly estimating the error on  $c\tau$  in the data. Finally, no  $c\tau$  cut is made on the events considered in the two-step fit; hence, the relative statistical errors should be smaller than those obtained in the binned fit described in Section 4.3.2.

If  $\alpha$  is the probability for a candidate in the peak region to be a real signal event, then the probability distribution function for any candidate  $i$  is given

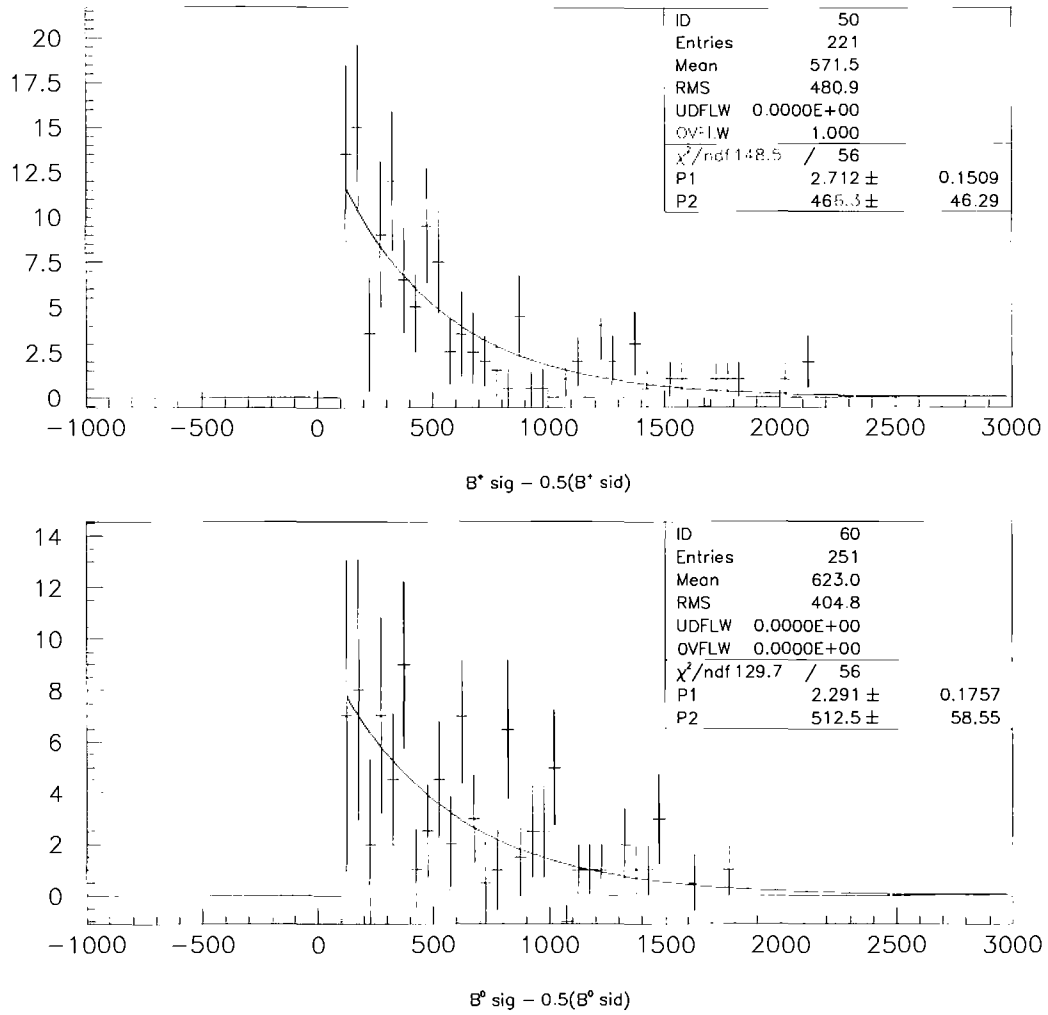


Figure 4.12: Fitting Technique # 1. Top(Bottom) plot shows a binned log-likelihood fit to the background subtracted  $B_u(B_d)$  signal  $c\tau$  distribution. The good agreement between  $\langle c\tau \rangle - 100 \mu\text{m}$  and the slope obtained from the fit to the data demonstrate that the measured background subtracted  $c\tau$  values distributions are indeed distributed according to an exponential (lifetime PDF).

by:

$$p(\mathbf{x}')_{\alpha,\lambda,\sigma_i,\lambda^-, \lambda^+, f^-, f^+} = \begin{cases} \alpha f(\mathbf{x}')_{\lambda,\sigma_i} + (1 - \alpha) g(\mathbf{x}')_{\sigma_i,\lambda^-, \lambda^+, f^-, f^+} & \text{peak} \\ g(\mathbf{x}')_{\sigma_i,\lambda^-, \lambda^+, f^-, f^+} & \text{sidebands} \end{cases} \quad (4.19)$$

The exact form of  $f(\mathbf{x}')_{\lambda,\sigma_i}$  is given by Eq. (4.14), where  $\sigma$  is replaced by  $\sigma_i$  and is taken to be the measured event-by-event error on  $c\tau$ . The expression for  $g(\mathbf{x}')_{\sigma_i,\lambda^-, \lambda^+, f^-, f^+}$  is obtained by convoluting a Dirac delta function (the *physics function* chosen to model the zero lifetime component of the background) with a gaussian resolution function and subsequently including asymmetric, falling exponential distributions to model the observed tails. The resulting observed background PDF (normalized to unity) is

$$g(\mathbf{x}')_{\sigma_i,\lambda^-, \lambda^+, f^-, f^+} = \begin{cases} \frac{1-f^- - f^+}{\sigma_i \sqrt{2\pi}} \exp\left(\frac{-x'^2}{2\sigma_i^2}\right) + \frac{f^+}{\lambda^+} \exp\left(\frac{-x'}{\lambda^+}\right) & x' > 0 \\ \frac{1-f^- - f^+}{\sigma_i \sqrt{2\pi}} \exp\left(\frac{-x'^2}{2\sigma_i^2}\right) + \frac{f^-}{\lambda^-} \exp\left(\frac{x'}{\lambda^-}\right) & x' < 0 \end{cases} \quad (4.20)$$

Note that Eq. (4.20) is continuous at  $x' = 0$  only if  $\frac{f^+}{\lambda^+} = \frac{f^-}{\lambda^-}$ , a condition which implies that the mechanisms responsible for both the negative and the positive tails are identical, when, in fact, they are not. Negative tails in the  $c\tau$  distributions are caused by poorly measured tracks, while positive tails not attributed to signal are the result of both poorly measured tracks and real  $B \rightarrow \Psi X$  events in which tracks not associated with the  $B$  were assigned to the secondary vertex. This additional source of long-lived, positive decay length background is responsible for the discontinuity at  $x' = 0$  in the background PDF. The convergence of the fit is not affected by this discontinuity since there are no events in the data with  $c\tau$  identically equal to 0.0; furthermore, a systematic uncertainty due to the particular choice of background parameterization is assigned to the final results, as described in Section 4.4.3.

In the two-step fit, the corresponding log-likelihood function,  $\mathcal{L} = -2 \log(L)$ , is minimized separately for the peak and sideband regions. The exact form of the likelihood function,  $L$ , in this case is given by

$$L = \prod_{i=1}^{N_{p,s}} p_{p,s}(\mathbf{x}')_{\alpha,\lambda,\sigma_i,\lambda^-, \lambda^+, f^-, f^+}, \quad (4.21)$$

where  $N_{p,s}$  is the total number of peak and sideband events, respectively, and  $p_{p,s}(\mathbf{x}')_{\alpha,\lambda,\sigma_i,\lambda^-, \lambda^+, f^-, f^+}$  is the observed PDF (the subscripts  $p, s$  refer to

specific form of the PDF that is appropriate for either the peak or sideband regions as indicated in Eq. (4.19)). In the first step, a fit to the sideband  $c\tau$  distribution determines the shape of the background. The result of this first fit is subtracted from the  $c\tau$  distribution of the peak region by fixing the background parameters ( $f^\pm$  and  $\lambda^\pm$ ) when fitting the peak region to the values obtained from the sideband fit. The overall normalization of the background to be subtracted is free to adjust to the data in the peak region, i.e. the fraction of background in the peak region,  $(1 - \alpha)$ , is a free parameter in the fit. An alternative method is to constrain the background fraction,  $(1 - \alpha)$ , to the value obtained from a fit to the  $B$  invariant mass distribution; consistent results are obtained with either method. A fit to the remaining peak distribution extracts the  $B$  meson lifetime,  $\lambda$ . Hence, there are 4 free parameters in the sideband fit:

$$\begin{aligned} f^- &= \text{the fraction of negative tail in the background;} \\ \lambda^- &= \text{the slope of the negative tail in the background;} \\ f^+ &= \text{the fraction of positive tail in the background;} \\ \lambda^+ &= \text{the slope of the positive tail in the background;} \end{aligned}$$

and 2 free parameters in the second fit to the peak region:

$$\begin{aligned} \lambda &= \text{the mean lifetime of the signal;} \\ \alpha &= \text{the fraction of signal in the peak region.} \end{aligned}$$

Both fits are performed using an unbinned log-likelihood method where the gaussian resolution function is assumed to have a sigma equal to the measured error on  $c\tau$  on an event-by-event basis. The results of these fits and their statistical errors, obtained via MINUIT[52], are shown in Table 4.4. They are in good agreement with the results from the fits presented in Sections 4.3.2 and 4.3.4 and summarized in Table 4.6.

#### 4.3.4 Fitting Technique # 3

The most sophisticated fitting technique of the ones considered in this analysis is the simultaneous, unbinned log-likelihood fitting technique. It was selected

Parameter		Fit results			
		Charged $B$		Neutral $B$	
$f^-$	[%]	2.1	$\pm$ 0.7	1.6	$\pm$ 0.4
$\lambda^-$	[ $\mu m$ ]	365	$\pm$ 104	526	$\pm$ 131
$f^+$	[%]	10.1	$\pm$ 1.4	10.6	$\pm$ 1.2
$\lambda^+$	[ $\mu m$ ]	293	$\pm$ 39	202	$\pm$ 20
$\lambda = c\tau$	[ $\mu m$ ]	485	$\pm$ 48	459	$\pm$ 52
$\alpha$	[%]	25.9	$\pm$ 2.6	14.9	$\pm$ 1.9
Lifetime ratio = $\tau^+/\tau^0 = 1.06 \pm 0.16$					

Table 4.4: Results of the two-step fitting procedure. The quoted errors are statistical only.

as the definitive fit for a number of reasons, but principal among these is the fact that this technique takes full advantage of the available statistics. Rather than effectively subtracting out the  $c\tau$  distribution due to background events in the peak region, the simultaneous fit uses a fraction of the peak distribution in addition to the entire sideband distribution to determine the shape of the background. Also, the number of background events in the peak region is constrained to be equal, within Poisson fluctuations, to one half of the number of events observed in the sidebands (the factor  $\frac{1}{2}$  comes from the fact that the width of the sideband region is equal to the twice the width of the peak region). Hence, the fraction of background in the peak region is neither fixed nor allowed to float freely. By taking into account Poisson fluctuations, the simultaneous fit considers the relatively small sample of  $B_u(B_d)$  mesons in a rigorous, statistically correct manner. The net result is a more precise background shape and an overall smaller statistical error in the final result.

The fit is performed as an unbinned log-likelihood fit within the context of MINUIT[52]. The function that is minimized is  $-2\ln(L)$  where the  $L$  is a likelihood function (the exact expression is given in Appendix B). Note that the PDF in this likelihood function can include non-gaussian tails in the resolution function. This feature is not used in the fitting procedure described

in this section, but is exploited when the possibility of a non-gaussian resolution function is considered in Section 4.4.2. The likelihood function in this fit depends on the following parameters:

- $\lambda$  = the mean proper decay length of the signal
- $\alpha$  = the fraction of signal in the peak region
- $n_{fit}$  = the number of signal events in the peak region
- $f^-$  = the fraction of negative tail in the background
- $\lambda^-$  = the slope of the negative tail in the background
- $f^+$  = the fraction of positive tail in the background
- $\lambda^+$  = the slope of the positive tail in the background

All 7 parameters are free. The fits reach a good convergence, and find well behaved minimum log-likelihood values. The results are displayed in Figs 4.13 and 4.14 and are shown with their statistical errors in Table 4.5. Note that the results of the simultaneous fit agree well with the results presented in Sections 4.3.2 and 4.3.3 and summarized in Table 4.6. The fit results described in this section are referred to as the “default fits”; they will be used to quote the final lifetime results in this analysis.

### 4.3.5 Confidence Level and Statistical Error Tests

This section describes the Monte Carlo technique used to determine the confidence level of the fit and to investigate the statistical errors returned by MINUIT[52]. The confidence level is determined separately for the simultaneous fit, for the fit to peak region only, and for the sideband fit only. The statistical error tests result from the same study used to determine the simultaneous fit confidence levels. It is important to make sure that MINUIT[52] returns sensible statistical errors because the overall error of the result is dominated by the statistical, rather than the systematic, uncertainty.

The confidence level of the simultaneous lifetime fit is estimated by first generating many Monte Carlo  $c\tau$  distributions that mimic the equivalent data distributions. Next, each of these distributions is passed through the identi-

CDF RUN 1A

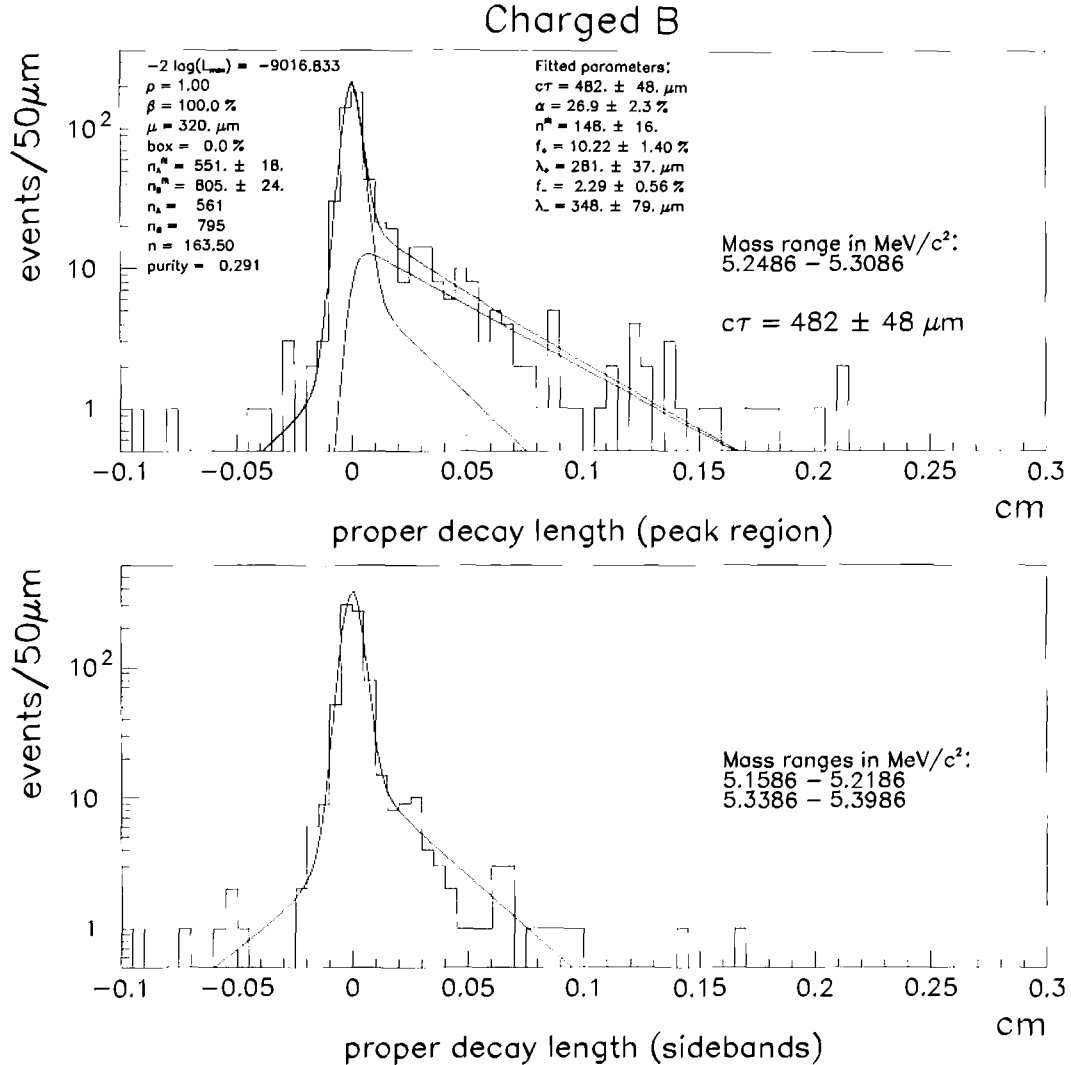


Figure 4.13: Fit of the combined  $c\tau$  distributions of all reconstructed  $B_u$  mesons. The 3 curves superimposed on the  $c\tau$  distribution of the peak region events (shown on top) are the contributions from the signal, the background, and their sum, as determined by the fitting procedure. The curve superimposed on the  $c\tau$  distribution of the sideband events (shown on bottom) is also the result of the same fit. The expressions for these curves is given by Eqs. (B.24) and (B.25) of Appendix B.

CDF RUN 1A

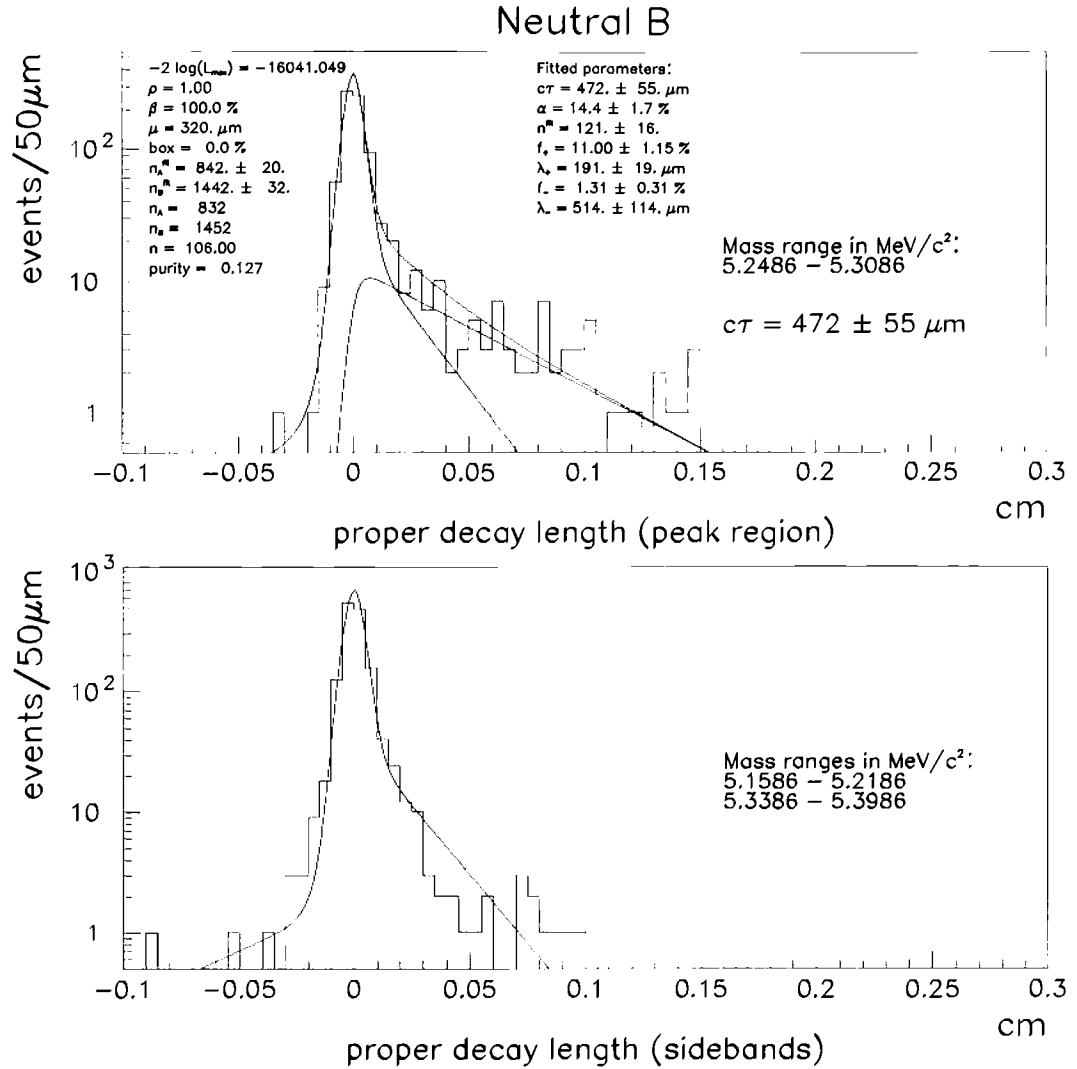


Figure 4.14: Fit of the combined  $c\tau$  distributions of all reconstructed  $B_d$  mesons. The 3 curves superimposed on the  $c\tau$  distribution of the peak region events (shown on top) are the contributions from the signal, the background, and their sum, as determined by the fitting procedure. The curve superimposed on the  $c\tau$  distribution of the sideband events (shown on bottom) is also the result of the same fit. The expressions for these curves is given by Eqs. (B.24) and (B.25) of Appendix B.

	Charged $B$	Neutral $B$
Parameter	Fit results	
$\lambda = c\tau$ [ $\mu m$ ]	482 $\pm$ 48	472 $\pm$ 55
$\alpha$ [%]	26.9 $\pm$ 2.3	14.4 $\pm$ 1.8
$n_{fit}$ [events]	148 $\pm$ 16	121 $\pm$ 16
$f^-$ [%]	2.3 $\pm$ 0.6	1.3 $\pm$ 0.3
$\lambda^-$ [ $\mu m$ ]	349 $\pm$ 79	514 $\pm$ 114
$f^+$ [%]	10.2 $\pm$ 1.4	11.0 $\pm$ 1.2
$\lambda^+$ [ $\mu m$ ]	281 $\pm$ 37	191 $\pm$ 19
$-2\ln(L_{max})$	-9017	-16041
Confidence level	43%	32%
Lifetime ratio = $\tau^+/\tau^0 = 1.02 \pm 0.16$		

Table 4.5: Results of the simultaneous lifetime fits. The errors are statistical only.

	Charged $B$	Neutral $B$
Fit Type	Fit Results ( $\mu m$ )	
Binned Likelihood	466 $\pm$ 47	513 $\pm$ 59
Two-Step Unbinned Likelihood	485 $\pm$ 48	459 $\pm$ 52
Simultaneous Unbinned Likelihood	482 $\pm$ 48	472 $\pm$ 55

Table 4.6: Summary of results of the three lifetime fitting methods. The errors are statistical only.

cal simultaneous fitting routine that was used for the data. From the results of all these fits, the distribution of  $-2\ln(L_{max})$ , i.e. the minimized value of  $-2\ln(L)$ , is obtained. The confidence level of the fit to the data is then calculated as the fraction of Monte Carlo samples that yield a value of  $-2\ln(L_{max})$  larger than that obtained from the fit to the data.

Each Monte Carlo sample is generated as follows:

1. The number of events in the peak and the sideband regions are randomly determined according to Poisson distributions with mean values equal to the number of events observed in the data.
2. For each event in the sample, a value for the error on the proper decay length is generated separately for the peak and sideband regions according to the distribution observed in the data.
3. For each event, a proper decay length is randomly generated according to a PDF that is given by the fit to the data; i.e., the PDF is parameterized as described in Appendix B and the values of the 7 parameters are fixed to the results obtained from the fit to the data.

A total of 1000  $B_u$  and 1000  $B_d$  Monte Carlo  $c\tau$  distributions were generated independently to mimic the equivalent data distributions. The distribution of  $-2\ln(L_{max})$  is shown on the upper left hand plot of Figs 4.15 and 4.16. The black circles show the value obtained when minimizing the actual data. From these distributions the confidence level of the fit to the data is estimated to be 43% for  $B_u$  and 32% for  $B_d$ . These probabilities indicate that the fits to the data are “good.”

To estimate the confidence level of the fit to the sideband  $c\tau$  distributions obtained from the  $B_u$  and  $B_d$  data samples, the procedure described above is repeated using a PDF suitable for the sideband distributions (see Eq. (4.20)). In this case, the parameters are fixed to those obtained from the two-step sideband fits to the data when generating the Monte Carlo samples. The resulting Monte Carlo sideband  $c\tau$  distributions are passed to the two step fitting routine, and the number of times that  $-2\ln(L_{max})$  is larger than that obtained from the two-step fit to the data is recorded. This procedure finds a 51% (40%) confidence level for the fit to the  $B_u(B_d)$  sideband data  $c\tau$  distributions.

MONTE CARLO

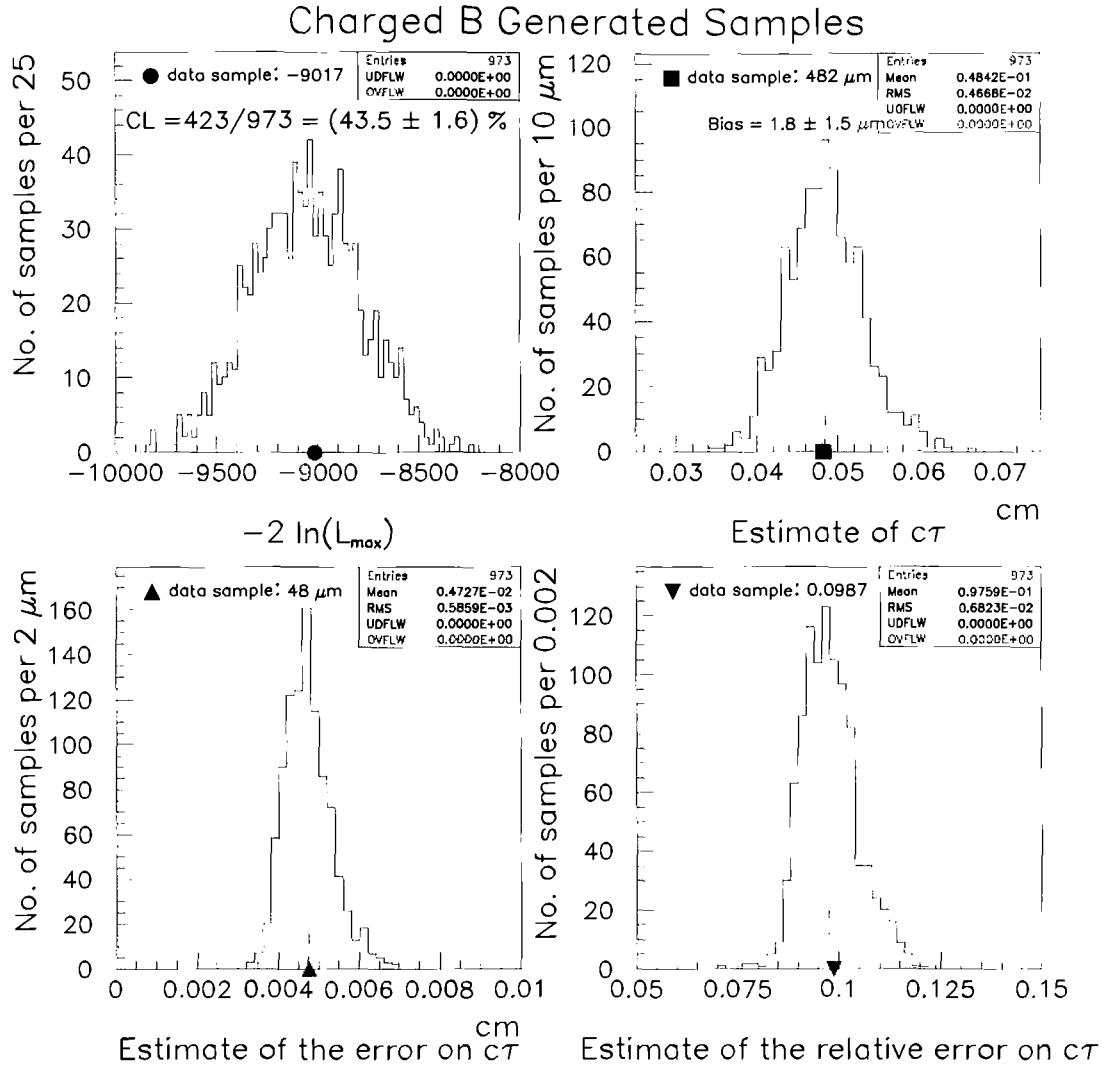


Figure 4.15: Top left plot: Distribution of the minimum value of  $-2 \ln(L)$ , the function minimized by MINUIT[52], obtained from Monte Carlo samples representing the charged  $B$  data. These samples were generated with parameters as shown in Table 4.5. The black circle shows the value obtained when fitting the real data. Other plots: Distribution of the fitted lifetime, the error on the fitted lifetime (as returned by MINUIT) and the relative error on the fitted lifetime. The distributions are obtained from the same Monte Carlo samples as above. The black symbols show the values obtained when fitting the data. The vertical dashed lines indicate the mean values of the histograms.

MONTE CARLO

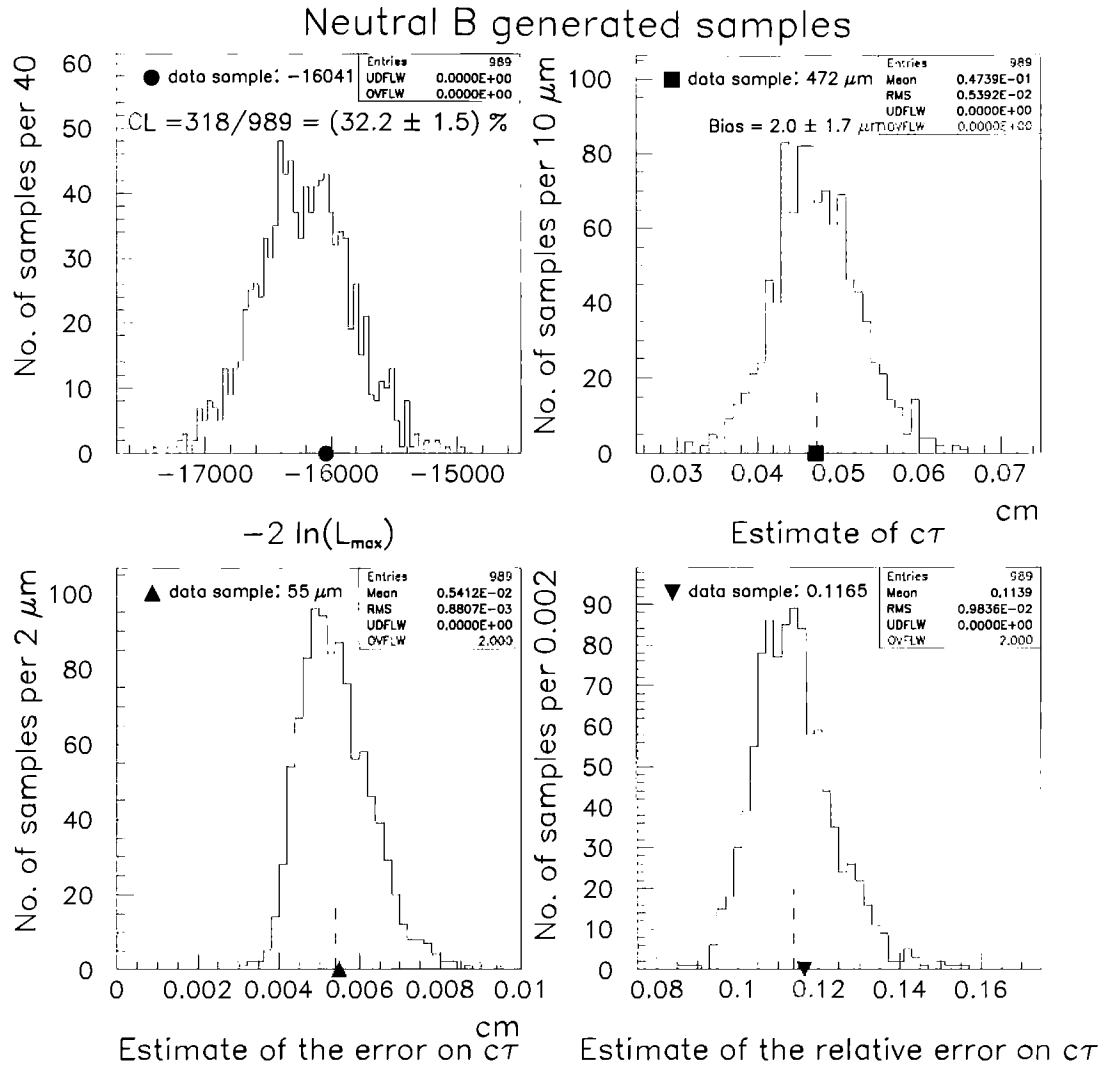


Figure 4.16: Top left plot: Distribution of the minimum value of  $-2 \ln(L)$ , the function minimized by MINUIT[52], obtained from Monte Carlo samples representing the neutral  $B$  data. These samples were generated with parameters as shown in Table 4.5. The black circle shows the value obtained when fitting the real data. Other plots: Distribution of the fitted lifetime, the error on the fitted lifetime (as returned by MINUIT) and the relative error on the fitted lifetime. The distributions are obtained from the same Monte Carlo samples as above. The black symbols show the values obtained when fitting the data. The vertical dashed lines indicate the mean values of the histograms.

Finally, the confidence level of the fit to the  $B_u$  and  $B_d$  peak  $c\tau$  data distributions is determined by calculating the bin-by-bin  $\chi^2$  using Fig. 4.17. The curve is not a fit to the displayed background subtracted data. Rather, it is simply the peak lifetime PDF obtained from the simultaneous fit overlaid on the background subtracted data. The  $\chi^2$  of the fit to the peak region is then trivially calculated using the center value of each bin, the functional form of the peak PDF, and the error on the number of events per bin. The corresponding confidence levels for various bin ranges are given in Fig. 4.17, but are generally around 20% (15%) for the  $B_u(B_d)$  peak data  $c\tau$  distributions.

### 4.3.6 Statistical uncertainties

Because the dominant uncertainty in the lifetime measurement is statistical, it is important to determine whether or not the statistical error is correctly estimated, i.e. that MINUIT[52] returns sensible errors. The statistical errors are checked by examining the distribution of the fitted values of the lifetimes obtained from the Monte Carlo samples described in Section 4.3.5. The RMS widths of these distributions give an “independent” estimate of the statistical uncertainty.

Figures 4.15 and 4.16 show the distribution of the fitted lifetime (upper right), the distribution of its error as returned by MINUIT (bottom left), and the distribution of the fitted lifetime divided by its error (bottom right), separately for the  $B_u$  and  $B_d$  Monte Carlo samples. The mean values of the errors are  $47.3 \pm 0.2 \mu\text{m}$  ( $B_u$ ) and  $54.1 \pm 0.3 \mu\text{m}$  ( $B_d$ ), in good agreement with the RMS widths of the lifetimes values obtained from fitting the Monte Carlo samples ( $46.7 \pm 1.1 \mu\text{m}$  and  $53.9 \pm 1.2 \mu\text{m}$ , respectively). This fact demonstrates that, on average, the errors are properly estimated by MINUIT[52].

To estimate the “error on the statistical error,” the RMS width of the relative error is considered because there is a strong correlation between the fitted lifetime and its statistical error, while there is no correlation between the fitted lifetime and its relative error. The distributions of the relative errors have RMS widths of 0.0068 and 0.0095, corresponding to  $3.3 \mu\text{m}$  and  $4.5 \mu\text{m}$  when multiplied by the lifetimes values obtained by fitting the data. This observation indicates that, even though MINUIT[52] does, on average, a good job of

CDF RUN 1A

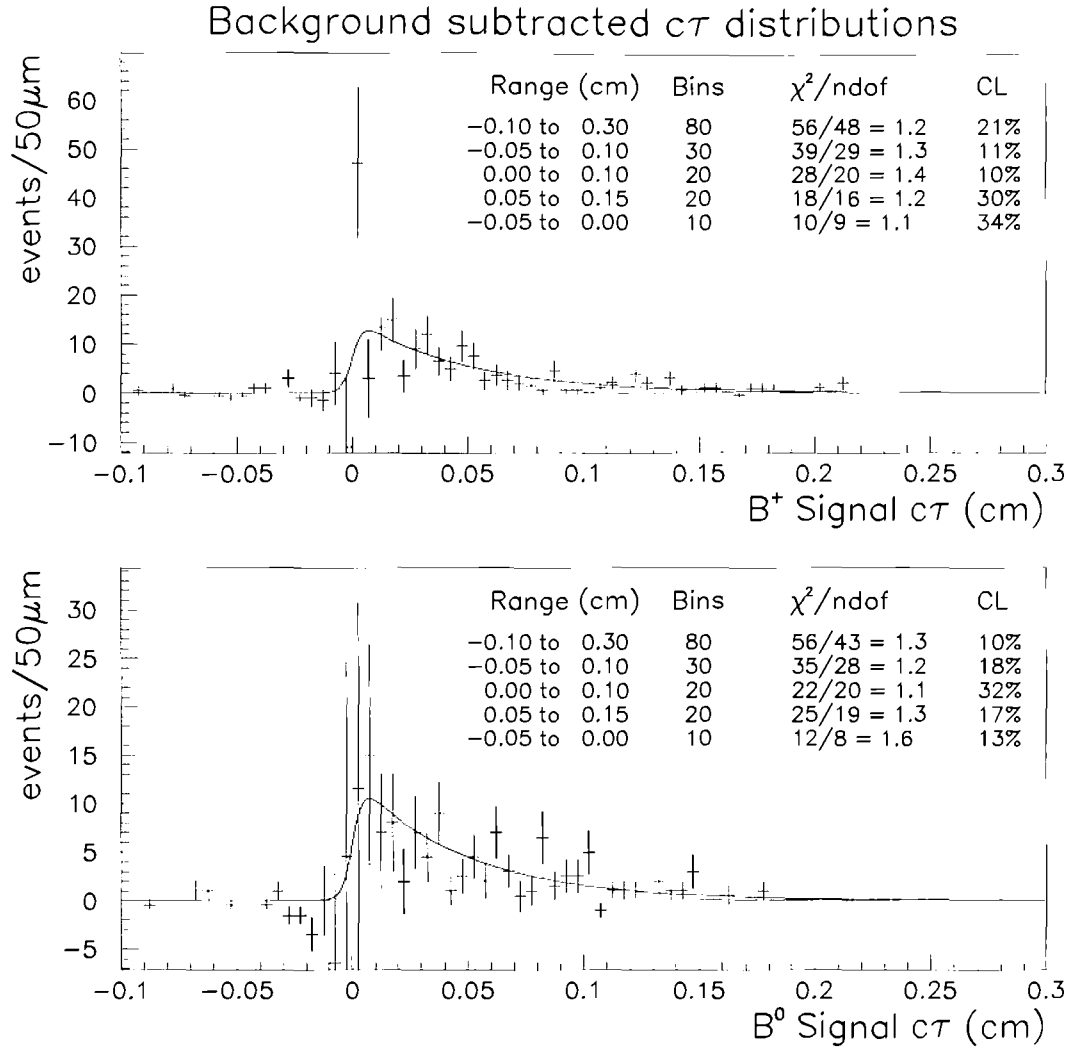


Figure 4.17: Background subtracted  $c\tau$  distributions. The content of each bin is equal to the number of peak region events minus one-half of the number of sideband events. The error bars are calculated assuming gaussian errors. The curves are the signal functions for the parameters indicated in Table 4.5 (not fits to these histograms). The  $\chi^2$  values are displayed for various  $c\tau$  ranges, and the number of degrees of freedom is taken as the number of non empty bins in each range.

Source of systematic error	Error on $B^+$	Error on $B^0$
Residual misalignment	10 $\mu m$	10 $\mu m$
Trigger bias	6 $\mu m$	6 $\mu m$
Beam stability	5 $\mu m$	5 $\mu m$
Resolution function uncertainty	7 $\mu m$	4 $\mu m$
Background parameterization	6 $\mu m$	21 $\mu m$
Fitting procedure bias	2 $\mu m$	2 $\mu m$
Total	16 $\mu m$	25 $\mu m$

Table 4.7: Summary of systematic uncertainties.

estimating the statistical errors, individual estimates of these errors could be different from the true errors at the 5  $\mu m$  level. It appears that the relative errors returned by the fits to the data samples both fluctuated up by a fraction of a sigma with respect to their true values, as illustrated in Figs 4.15 and 4.16 by the shift between the mean value of the distribution of the relative errors (vertical dashed line on the bottom right-hand histogram) and the corresponding data point (black inverted triangle). The final conclusion from this Monte Carlo study is that the statistical errors returned by MINUIT[52] are correct, and that, since the distributions of the fitted lifetimes are fairly symmetric around the mean values, it is not worth quoting the final results with asymmetric errors, i.e. the positive (negative) errors would just be a couple microns above (below) the parabolic errors.

## 4.4 Systematic uncertainties

Table 4.7 summarizes the various systematic uncertainties that have been studied and found to be significant or included in the final measurement. The total systematic uncertainty, computed as the quadratic sum of the individual contributions, is smaller than the statistical uncertainty at least by a factor of two. When calculating the uncertainty on the lifetime ratio, the first three uncertainties listed in Table 4.7 (residual misalignment, trigger bias, beam

stability) are assumed to be completely correlated in the charged and neutral lifetimes; the remaining errors are taken to be uncorrelated. Sections 4.4.1 through 4.4.4 give details about the various contributions to the total systematic uncertainties quoted in the final results. Other consistency checks are described in Section 4.5.

#### 4.4.1 Systematic Uncertainties Obtained from CDF's Average $b$ -Hadron Lifetime Analysis

Some systematic uncertainties can be taken directly from CDF's average  $b$ -hadron lifetime analysis[3] because that analysis relied on inclusive  $J/\psi$  decays in which the muons were measured in the SVX. Also, the identical  $J/\psi$  dimuon trigger (see Section 4.1.1) was used in the inclusive analysis. For these reasons, a number of systematic errors obtained in the inclusive analysis are applicable to the exclusive analysis described in this text. In particular, the uncertainty due to misalignment of the SVX with respect to the CTC, the uncertainty due to the acceptance of the trigger with respect to  $c\tau$ , and the uncertainty due to the stability of the beam line are taken from the inclusive lifetime analysis and will be discussed in turn.

##### Misalignment

The uncertainty due to misalignment is determined in the context of the internal alignment of the SVX[47]. Specifically, wedge-to-wedge misalignments and/or radial shifts of the silicon layers are possible causes of a bias in the lifetime. The internal alignment constants used for this analysis are identical to the ones used for the inclusive measurement. As a result, the uncertainty determined in the inclusive analysis,  $10 \mu m$ , can be used in this analysis. The global alignment constants, however, did change in the interim between the the inclusive analysis and this analysis, but, to first order, the alignment of the SVX (as a rigid body) with respect to the CTC does not affect the lifetime measurements because both the primary and the secondary vertices were measured using SVX information.

### Trigger

The same trigger ( $J/\psi$  dimuon trigger, see Section 4.1.1) is used for both the inclusive and the exclusive lifetime analyses. The systematic uncertainty due to possible trigger bias, determined to be  $6 \mu m$  in the inclusive analysis[47], is used in this analysis also.

### Beam Stability

The uncertainty due to possible instability of the beam line during a run,  $5 \mu m$ , is taken from the work done for the inclusive lifetime measurement[47]. This uncertainty is determined using only the runs in the first part of Run 1A. Nevertheless, it is valid to assume that the beam was stable throughout the entire course of the run because this uncertainty is related to the manner in which the Tevatron operates. No change in the Tevatron operation occurred in the course of Run 1A that would justify more work on the determination of this uncertainty. For this reason, a  $5 \mu m$  systematic uncertainty due to beam line stability, determined in the inclusive analysis, is included in the total systematic uncertainty in the exclusive lifetime analysis.

## 4.4.2 Uncertainty due to the Resolution Function

In this section, the uncertainty due to the modeling of the resolution function is addressed. It is assumed that the resolution function is gaussian and that the sigma of this gaussian is equal, on an event-by-event basis, to the measured error on the proper decay length. Based on the studies described below, the uncertainty on the  $B_u(B_d)$  meson lifetime due to possible non-gaussian tails in the resolution function is  $7 \mu m$  ( $4 \mu m$ ), while the uncertainty due to a possible error in the scale of the measured errors is  $1 \mu m$  ( $2 \mu m$ ).

### Non-gaussian tails

The best place to look in the data for evidence of non-gaussian tails in the resolution function is the negative  $c\tau$  region of the background subtracted signal. However, because the background is parameterized with exponential tails on both sides, these would automatically hide possible tails in the resolution

function itself. Similarly, the positive  $c\tau$  region for the signal is described with an exponential, again making it difficult to identify a tail in the resolution function. Figure 4.17 shows the proper decay length distributions of the background subtracted signals with  $50 \mu m$  binning. The overlaid curves are the signal functions as determined in the simultaneous fit described in Section 4.3.4. There is no evidence in these plots that the negative part of the signal distributions is not well described by the signal function. However, the statistical uncertainty of these distributions in the region between  $-200 \mu m$  and  $0 \mu m$  is large enough to allow for the existence of some amount of tail in the resolution function.

Figure 4.18 shows, separately for the the peak region and the sidebands, the “average resolution functions”. These functions (which are defined as the normalized sum of the gaussian resolution functions of all the  $B$  candidates in the corresponding mass region) have non-gaussian tails because the error on the proper decay length varies from candidate to candidate. The following distinction is important: the tails referred to in this section are not the tails of the average resolution functions; rather, they are the tails of the individual candidate resolution functions. The average resolution functions have widths of  $\sim 40 \mu m$  over nearly three orders of magnitude. This observation demonstrates that the measured value of  $c\tau$  is independent of the error on  $c\tau$ , i.e. candidates with large values of  $c\tau$  are not the result of poorly measured vertices, because all candidates are plotted regardless of their  $c\tau$ .

To assign a systematic uncertainty due to possible non-gaussian tails in the resolution function, the lifetimes are refit assuming that the resolution functions of all the events have identical symmetric non-gaussian tails. The low (high) side tail is parameterized as a growing (decaying) exponential function. Two new free parameters are added to the default fitting procedure:

- $\beta$  = the fraction of the resolution function which is gaussian;
- $\mu$  = the slope of the tails of the resolution function.

The equation for the convolution of the lifetime exponential with this new resolution function is given in Appendix B.

For the  $B_u$  events, the fit converges\* on  $\beta = 0.97 \pm 0.12$  and  $\mu = 448 \pm$

---

\*The convergence is good, and the error matrix can accurately be determined, but the

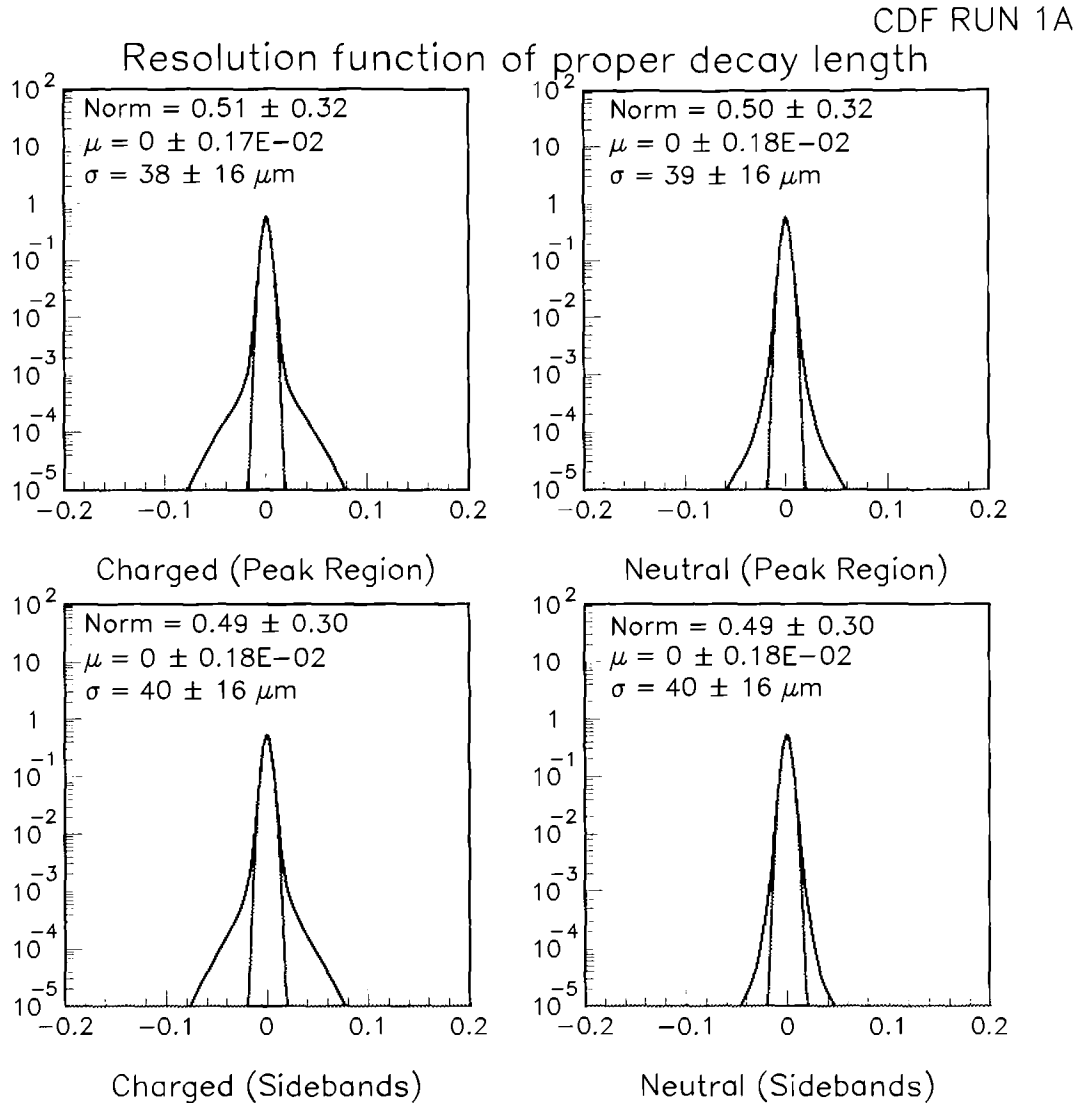


Figure 4.18: “Average resolution functions” shown separately for the peak and sideband regions, and for the charged and neutral  $B$  samples. These functions are the average of the individual gaussian resolution function of all the candidates in the corresponding sample. The gaussian curves are fits to these average resolution functions, showing that their central parts have a sigma of approximately  $40 \mu\text{m}$ .

702  $\mu m$ . This result is consistent with no tail in the resolution functions, but the fitted lifetime changes by  $-7 \mu m$ . Therefore a  $7 \mu m$  uncertainty is assigned to the charged lifetime due to possible tails in the resolution function. For the  $B_d$  sample, the fit converges with  $\beta$  at its upper limit (i.e.  $\beta = 1$ ), and the minimum cannot be improved (compared to the minimum found in the default fit). This fact indicates that the sample does not tolerate tails in the resolution function. However, a systematic uncertainty of  $4 \mu m$ , which is the amount by which the  $B_d$  fitted lifetime decreases when  $\beta$  and  $\mu$  are fixed to the values obtained in the charged case, is conservatively assigned to the  $B_d$  lifetime.

### Gaussian Sigma

The lifetime distributions are refit assuming that the resolution function is gaussian with a sigma equal to a scale factor  $\rho$  times the measured error on each event:

$\rho =$  a common scaling factor for the errors on the individual values of  $c\tau$ .

When this new parameter is free to adjust, the fits yield  $\rho = 1.01 \pm 0.03$  and  $\rho = 1.07 \pm 0.02$  while the fitted lifetimes change by  $1 \mu m$  and  $-2 \mu m$  in the charged and neutral case respectively.

Figure 4.9 shows, for all the  $B$  candidates in the full  $\pm 120 \text{ MeV}/c^2$  mass range, the distributions of the error on the proper decay length as well as the distributions of the proper decay length significance (proper decay length divided by its error). Fits to these significance distributions of functions similar to the ones used to describe the backgrounds (see Eq. (4.20)) indicate that the gaussian parts have sigmas equal to  $1.002 \pm 0.025$  (charged) and  $1.055 \pm 0.021$  (neutral), in agreement with the values obtained for  $\rho$ . Based on this study a  $1 \mu m$  ( $2 \mu m$ ) systematic uncertainty is assigned to the  $B_u$  ( $B_d$ ) lifetime.

### 4.4.3 Background Parameterization Uncertainty

Unlike the parameterization of the  $c\tau$  distribution from signal events (the exponential function convoluted with a resolution function) which has a physics MINOS[52] analysis fails, which is attributed to the fact that the  $1\sigma$  uncertainty on the tail covers unphysical regions in the space of the parameters.

Charged $B$			Neutral $B$		
“box” [%]	lifetime [ $\mu m$ ]	$-2 \ln(L_{max})$	“box” [%]	lifetime [ $\mu m$ ]	$-2 \ln(L_{max})$
0.0 fixed	$482 \pm 48$	-9016.8	0.0 fixed	$472 \pm 55$	-16041.1
1.0 fixed	$476 \pm 48$	-9017.5	0.6 fixed	$463 \pm 54$	-16051.6
1.5 fixed	$470 \pm 47$	-9015.5	1.4 fixed	$437 \pm 53$	-16051.4
$0.5 \pm 0.5$	$482 \pm 48$	-9018.4	$1.0 \pm 0.4$	$451 \pm 54$	-16052.6

Table 4.8: Systematic studies with a flat background.

justification (the decays of the  $B$  mesons), the asymmetric, falling exponential parameterization of the background events is arbitrary because there is no *a priori* reason to expect that the background  $c\tau$  distribution due to candidates with mismeasured tracks should follow an exponential. The background parameterization has been chosen to be as simple as possible while describing the data in a reasonable way. Although the confidence levels of the fits performed with this arbitrary background function are satisfactory, there might be some systematic error associated to this choice of parameterization. In order to evaluate this uncertainty the proper decay length distributions are refit with a different background parameterization. The change in the fitted value of the lifetimes is taken to be a reasonable estimate of this uncertainty.

To be conservative, a new background parameterization that is extreme in that it is expected to directly affect the fitted lifetimes is selected. To this end, a flat contribution to the background between 0.0 and 0.2  $cm$ , the region where the background and the signal “compete” the most for events in the peak region, is included. This flat component adds one more free parameter to the simultaneous fitting procedure:

$$\text{box} = \text{the fraction of background in the flat component.}$$

The results with this new parameterization are shown in Figs 4.19 and 4.20 and in the last line of Table 4.8.

The fitted fractions of background in the flat component are  $(0.5 \pm 0.5)\%$  and  $(1.0 \pm 0.4)\%$ , the fitted lifetimes change by  $0 \mu m$  and  $-21 \mu m$ , and the minimum values of  $-2 \ln(L_{max})$  go down by 1.6 and 11.5 units for the charged

CDF RUN 1A

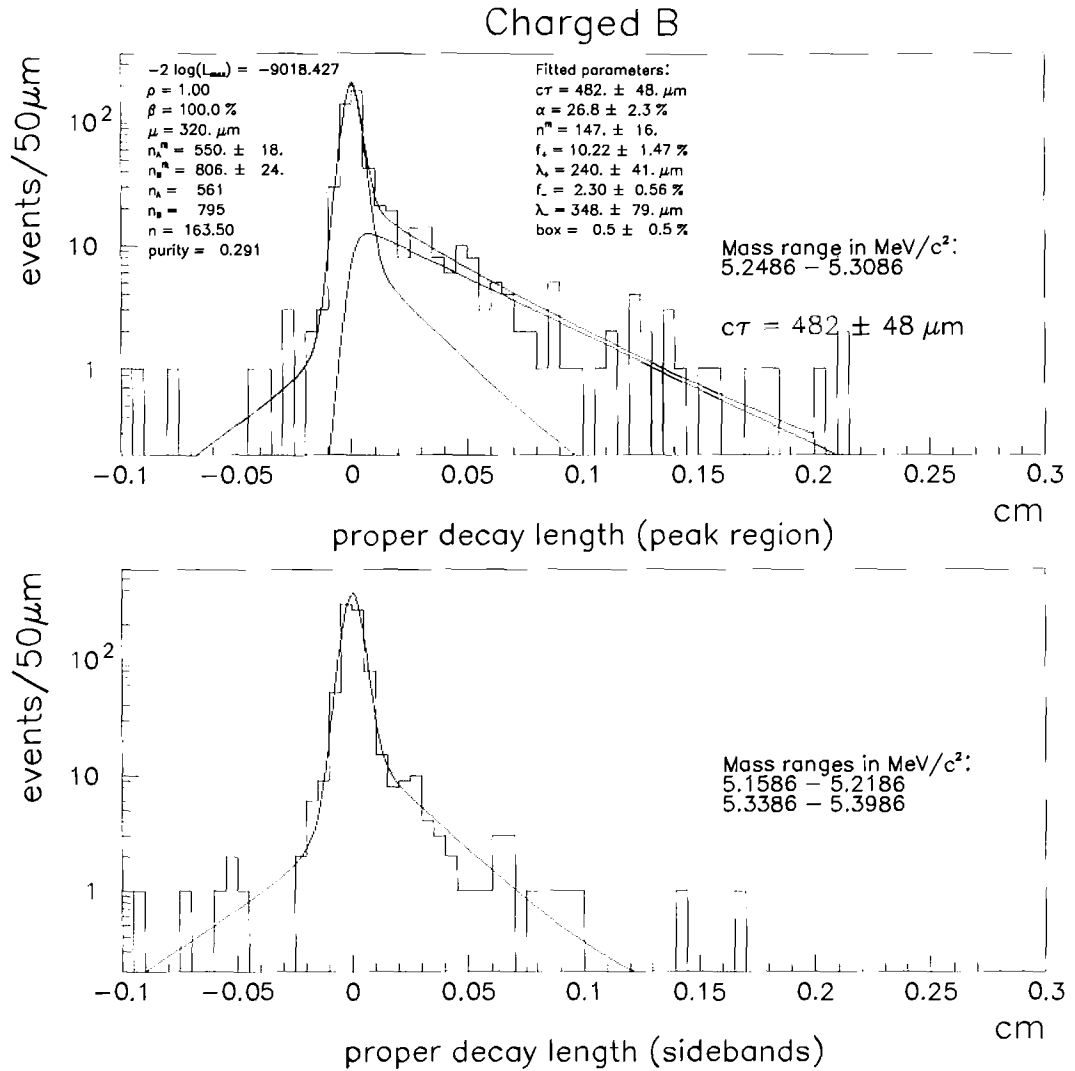


Figure 4.19: Fit of the lifetime of the  $B_u$  candidates with an additional flat background allowed to adjust. The uncertainty on the background parameterization is determined from this fit.

CDF RUN 1A

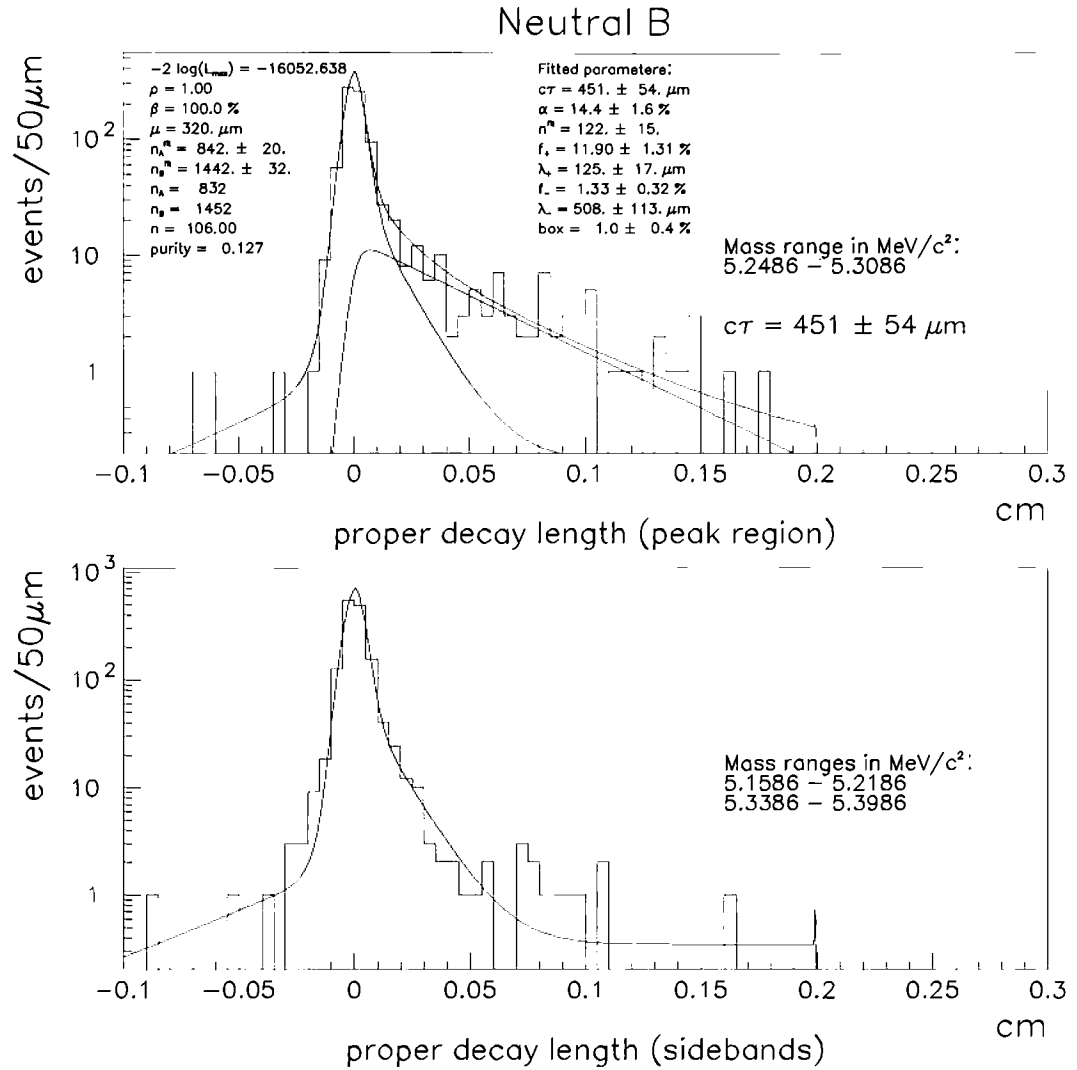


Figure 4.20: Fit of the lifetime of the  $B_d$  candidates with an additional flat background allowed to adjust. The uncertainty on the background parameterization is determined from this fit.

and neutral  $B$  mesons respectively. Additional fits are made where the parameter “box” is fixed at  $\pm 1$  statistical error around the value returned by the previous fits. In the case of the charged  $B$  mesons, the lifetime changes by  $6 \mu m$  and  $-2 \ln(L_{max})$  goes down by 0.7 (compared to the default fit) if the “box” is fixed to 1%. For the neutral case, variations of the fitted lifetime of order  $10 - 15 \mu m$  around the result are obtained when the “box” was free to adjust. Based on this study, systematic uncertainties of 6 (charged) and 21  $\mu m$  (neutral) are assigned due to a possible inability to correctly describe the background shape.

#### 4.4.4 Bias due to the fitting procedure

Figures 4.15 and 4.16 show the distributions of the fitted lifetimes obtained from the Monte Carlo samples. The shift of the mean values of these distributions with respect to the true values of the lifetimes used to generate the samples (which are also the values of the fitted lifetimes from the data samples, as shown in Table 4.5) is a good indication of the bias due to the fitting procedure itself. These shifts are equal to  $1.8 \pm 1.5 \mu m$  and  $2.0 \pm 1.7 \mu m$  for the charged and neutral case, respectively. Although these shifts are compatible with zero given the Monte Carlo statistics, a  $2 \mu m$  systematic error due to the possible existence of a bias is assigned to the lifetime results.

### 4.5 Consistency Checks and Cross-Checks

This section is a collection of various checks that have been performed to gain confidence in the analysis, the  $B$  signals and the lifetime results. The numerical results of these checks are not used to determine or correct the final numbers quoted in the conclusion of Section 5. Their purpose is mainly to bring additional justification to various assumptions of the analysis, and to answer questions that have been raised by the CDF collaboration during the course of this analysis.

### 4.5.1 Events with Large Positive or Negative $c\tau$ Values

A number of  $B_u$  and  $B_d$  peak events with long positive ( $c\tau > 1500 \mu m$ ) or negative ( $c\tau < -150 \mu m$ ) lifetimes have been hand-scanned[53] in an effort to understand the pathologies responsible for large, negative values of  $c\tau$ , and to see if large, positive values of  $c\tau$  are, in fact, valid. The details of this hand-scan study involved reprocessing the raw data files, i.e. DST files, of 8 peak region events with Version\_7\_09 TRCONTROL, followed by a modified Version\_7\_09 SVX Retracking Module, T709\_SVCN[54]. This module creates a special YBOS[42] bank, SVCN, that contains cluster,  $\chi^2$  per layer, and hit pattern information for all possible SVX tracks.

The four events with large positive  $c\tau$  values have well measured SVX tracks which are cleanly associated with a secondary vertex in the event display and they contain muons that are well separated in  $\phi$ . In addition, two of the events have clear evidence for the presence of a second  $B$ . For one of these events, Fig. 4.21 shows the reconstructed exclusive decay and Fig. 4.22 is a  $\times 4$  magnification of the same event showing evidence of a second displaced vertex. In other words, these are “good”  $B$  candidates that just happen to have a large lifetime.

The events with large negative  $c\tau$  values have poorly measured muon tracks in the SVX, and/or the  $\Delta\phi$  opening angle in the  $r - \phi$  plane between the two muons is  $\leq 2$  degrees. The two muon tracks from the  $\Psi$  candidate largely determine the vertex position. Because the SVX provides only an  $r - \phi$  view of an event, it is crucial for the transverse opening angle of these two tracks to be large enough to allow the vertexing algorithm to take full advantage of the SVX tracking information. In the limit that this opening angle becomes zero, the  $J/\psi$  vertex becomes “undefined”; basically any additional track will form with the two muons a reasonable 3-track vertex in the transverse plane. The probability to obtain a junk  $B$  candidate in this case seems quite high. Finally, no clean secondary vertices are observed in the event displays, a further indication that indeed these candidates are just combinatoric background resulting from poorly measured tracks.

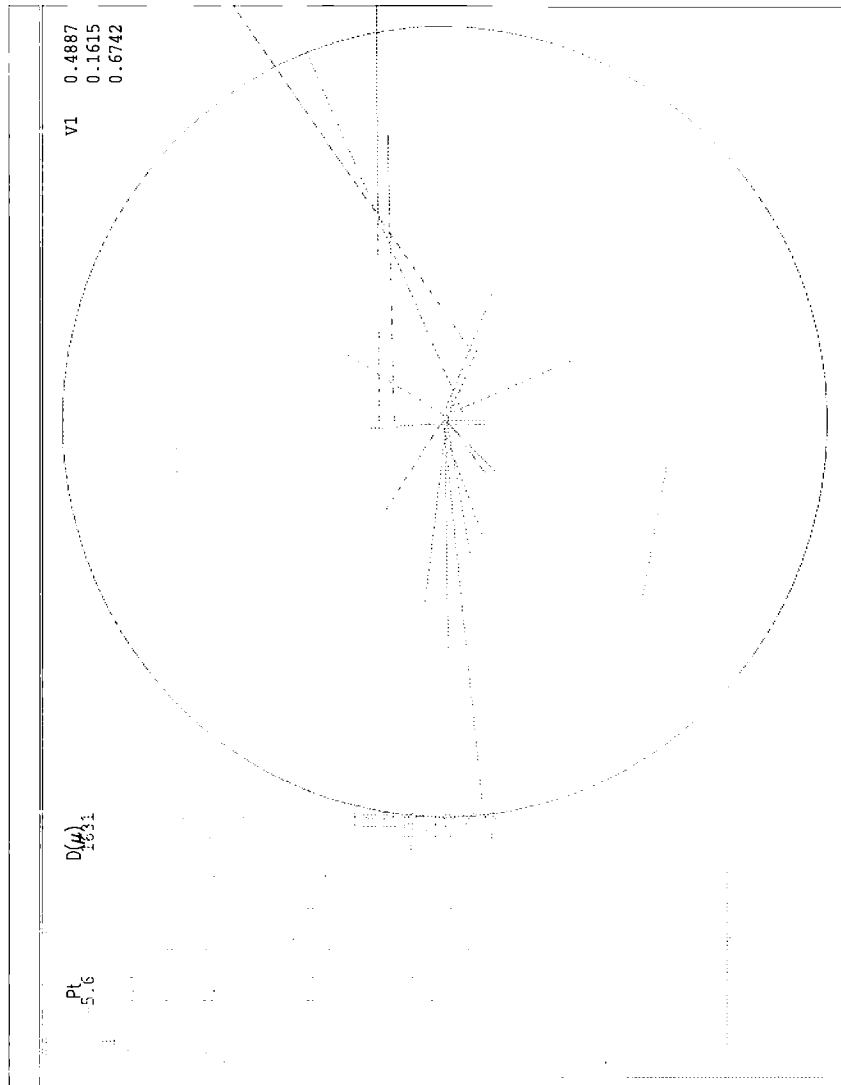


Figure 4.21: Reconstructed  $B_u$  decay with a 0.52 cm decay length (Run 42326, Event 78838).

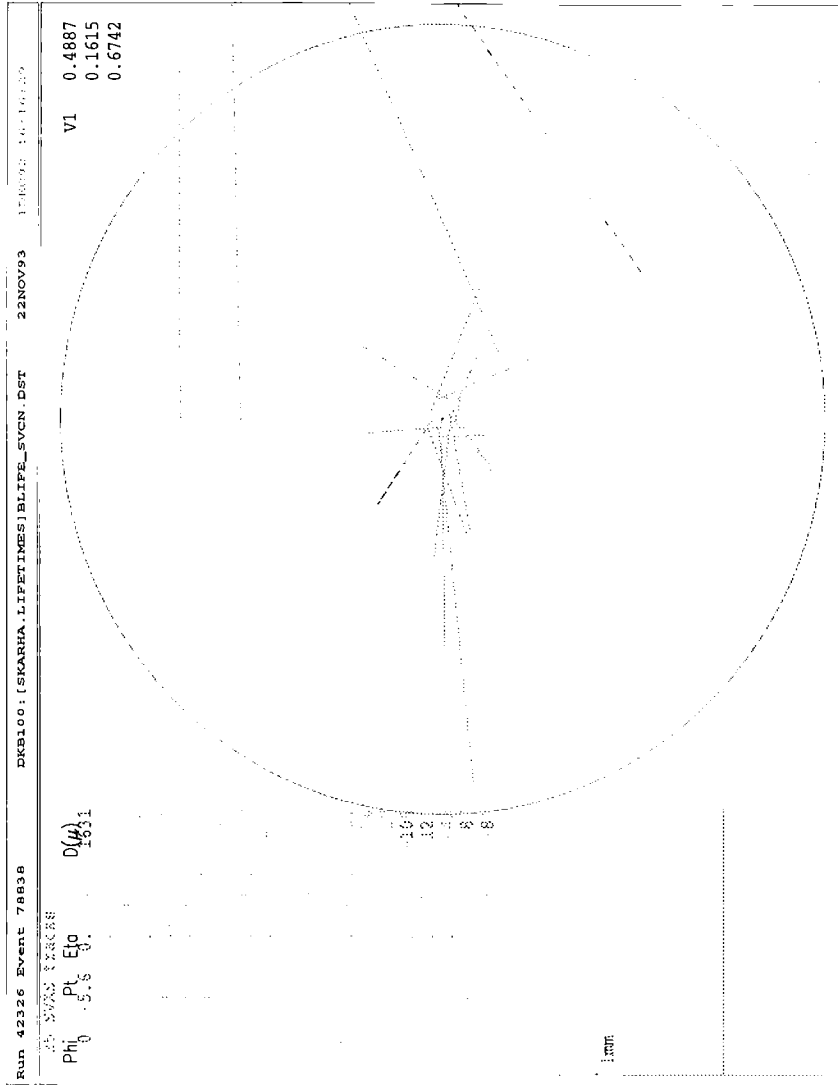


Figure 4.22: Previous figure (Run 42326, Event 78838) magnified by x4, showing the presence of another secondary vertex.

### 4.5.2 $K^*(892)$ signal

The natural width of the  $K^*(892)$  is broad (compare  $\Gamma_{K^*(892)} = 50 \text{ MeV}/c^2$  with  $\Gamma_{J/\psi} = 86 \text{ keV}/c^2$ ). Hence, observing a  $K^*(892)$  signal above the enormous combinatoric background is difficult in the data. Nevertheless, it is important to check whether the  $K^*(892)$  candidates in the reconstructed  $B \rightarrow \Psi K^*(892)$  are indeed selected from a resonance instead of from random, combinatoric background.

To look for the  $K^*(892)$  signals from the  $B$  samples the procedure is as follows:

1. Start with the sample of  $B$  candidates before the duplicate removal procedure has been applied. Duplicate  $B$  events must be included because the duplicate removal procedure may artificially create or enhance a peak at the  $K^*(892)$  mass since it selects the  $K^*(892)$  candidate with a reconstructed mass closer to the world average  $K^*(892)$  mass.
2. Remove the  $\pm 80 \text{ MeV}/c^2$  mass cut that would have been applied around the world average  $K^*(892)$  mass. Removing this mass window provides ample room to measure the level of combinatoric background.
3. Select only  $B$  candidates in the peak region ( $\pm 30 \text{ MeV}/c^2$  around the world average  $B$  mass).
4. Require that the proper decay length of the  $B$  candidates is larger than 100 microns. This provides a clean sample of  $B$  mesons and subsequently reduces the combinatoric background under the  $K^*(892)$  peak.
5. Plot separately the  $K^\pm \pi^\mp$  mass of the remaining  $B_d$  candidates, and the  $K_S^0 \pi^\pm$  mass of the remaining  $B_u$  candidates.

According to Table 4.2, there should be a  $K^*(892)^+$  signal of  $6 \pm 3$  events, and a  $K^*(892)^0$  signal of  $94.5 \pm 14.3$  events (these numbers are the sum of the numbers of  $B$  candidates in the peak region above background for the  $B \rightarrow J/\psi K^*(892)$  and  $B \rightarrow \psi(2S) K^*(892)$  channels, before the duplicate removal procedure). Note that these expectations become  $6.5 \pm 3.0$  and  $74.0 \pm 12.2$  after duplicate removal.

	Results of the fit to the $K^*(892)$ mass plot (B-W + linear background)		Expectation based on $B$ signal (Table 4.2)
	Mass [ $MeV/c^2$ ]	Signal [evts]	
$K^*(892)^+$ from $B \rightarrow J/\psi$ and $\psi(2S)$	$895 \pm 17$	$7.8 \pm 3.9$	$6.0 \pm 3.0$
$K^*(892)^+$ from $B \rightarrow J/\psi$ only	$896 \pm 14$	$9.6 \pm 4.2$	$6.0 \pm 3.0$
$K^*(892)^0$ from $B \rightarrow J/\psi$ and $\psi(2S)$	$897 \pm 7$	$97.1 \pm 17.3$	$94.5 \pm 14.3$
$K^*(892)^0$ from $B \rightarrow J/\psi$ only	$899 \pm 8$	$86.6 \pm 16.3$	$88.0 \pm 13.3$

Table 4.9:  $K^*(892)$  signal statistics.

Figure 4.23 shows four different  $K^*(892)$  mass distributions in  $20 MeV/c^2$  bins: the  $K_S^0\pi^\pm$  mass of the  $B_u \rightarrow J/\psi$  and the  $B_u \rightarrow \psi(2S)$  candidates, the  $K^\pm\pi^\mp$  mass of the  $B_d \rightarrow J/\psi$  and the  $B_d \rightarrow \psi(2S)$  candidates, the  $K_S^0\pi^\pm$  mass of the  $B_u \rightarrow J/\psi$  candidates only, and the  $K^\pm\pi^\mp$  mass of the  $B_d \rightarrow J/\psi$  candidates only. A non-relativistic Breit-Wigner function above a polynomial background has been used to fit each of these distributions, using a binned maximum-likelihood method. The width of the Breit-Wigner has been fixed to  $50 MeV/c^2$ , the natural width of the  $K^*(892)$ . In the case of the  $K_S^0\pi^\pm$  mass plots, a linear function is used to describe the background. In the case of the  $K^\pm\pi^\mp$  mass plots, both a linear function and a quadratic function are alternatively selected for the background description. The results of the fits with a linear background, as well as the expectation for the signals (computed from Table 4.2) are summarized in Table 4.9. In all cases, the fitted  $K^*(892)$  signals (obtained assuming a linear background) agree well with the expectations, and the fitted masses are compatible with the world average values ( $891.6 MeV/c^2$  for the  $K^*(892)^+$  and  $896.1 MeV/c^2$  for the  $K^*(892)^0$ ).

### 4.5.3 $B$ Impact Parameter

The  $B$  candidates in this analysis were not required to come from the primary vertex, i.e. no pointing constraint in CTVMFT was applied and no impact parameter cut was made. Fig. 4.24 shows that the impact parameter of the

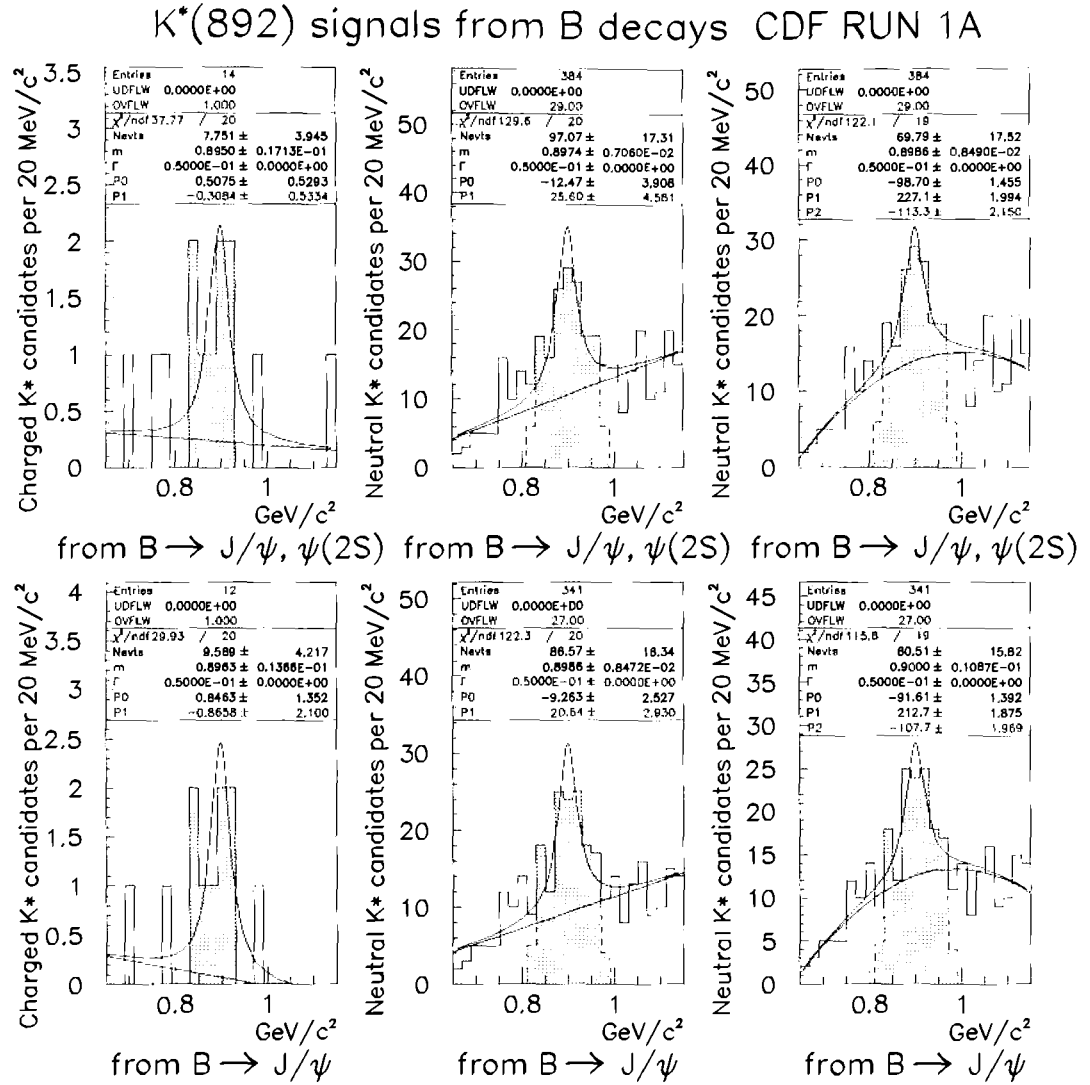


Figure 4.23: Left column: Distribution of the  $K_S^0 \pi^\pm$  mass in the  $K^*(892)^+$  region. The curves are fits of a Breit-Wigner function over a linear background. Middle column: Distribution of the  $K^\mp \pi^\pm$  mass in the  $K^*(892)^0$  region. The curves are fits of a Breit-Wigner function over a linear background. Right column: Same distributions as in the middle column, except that the background is modeled with a quadratic function. Top row: all the  $K^*(892)$  candidates. Bottom row: only the  $K^*(892)$  candidates from  $B \rightarrow J/\psi K^*(892)$  decays. Shaded areas: the shaded events are the ones used for the lifetime measurements ( $\pm 80 \text{ MeV}/c^2$  window around the world average)

$B$  candidates with respect to the primary vertex is distributed according to a gaussian for almost two orders of magnitude. After all the cuts of the analysis are applied, only  $\sim 1\%$  of all the candidates seem to be very unlikely to come from the primary vertex.

#### 4.5.4 The “Decay Length and $\Delta z$ ”

One method that can be used to determine whether or not the primary vertex was selected in a reasonable way is to look at the distribution of the difference in  $z$  between the secondary vertex ( $B$  vertex) and the primary vertex. Fig. 4.25 shows that this distribution is fairly gaussian with a sigma of  $0.46 - 0.47$  cm, which is of the order of the expected resolution in  $z$  of the CDF tracking. Note that when  $c\tau$  is requested to be above  $100$   $\mu m$ , this sigma increases by  $430$   $\mu m$ , giving some indication of the flight of the  $B$  in the  $r - z$  plane.

#### 4.5.5 Using the Run-By-Run Beam Line Versus the Event-By-Event Primary Vertex

The primary vertex used in this analysis is determined from the average beam line measured by the SVX for each run. The size of the beam spot is approximately  $40$   $\mu m$  and contributes directly to the error on the individual proper decay lengths. Another possibility would be to use a primary vertex that is measured for each event using tracks in the SVX. Such a primary vertex finder is available at CDF and is called VXPRI. If the VXPRI algorithm was used to determine the primary vertex, the error on the measured proper decay lengths would become smaller, because VXPRI uses the average beam line, in addition to tracks in the event (the error returned on the primary vertex is guaranteed to never exceed the size of the beam spot, even in case of a low multiplicity event). Nevertheless, studies described in this section demonstrate that a better measurement of the primary vertex (as provided by VXPRI) does not improve significantly the precision of the lifetime results.

By considering 509  $B_u$  events, which satisfy a Version\_7\_08 SVX  $\chi^2$  probability cut of  $> 1\%$  and have been reprocessed with Version\_7\_09, it has been determined that VXPRI returns, on average, a  $16$   $\mu m$  error on the  $x$  and  $y$

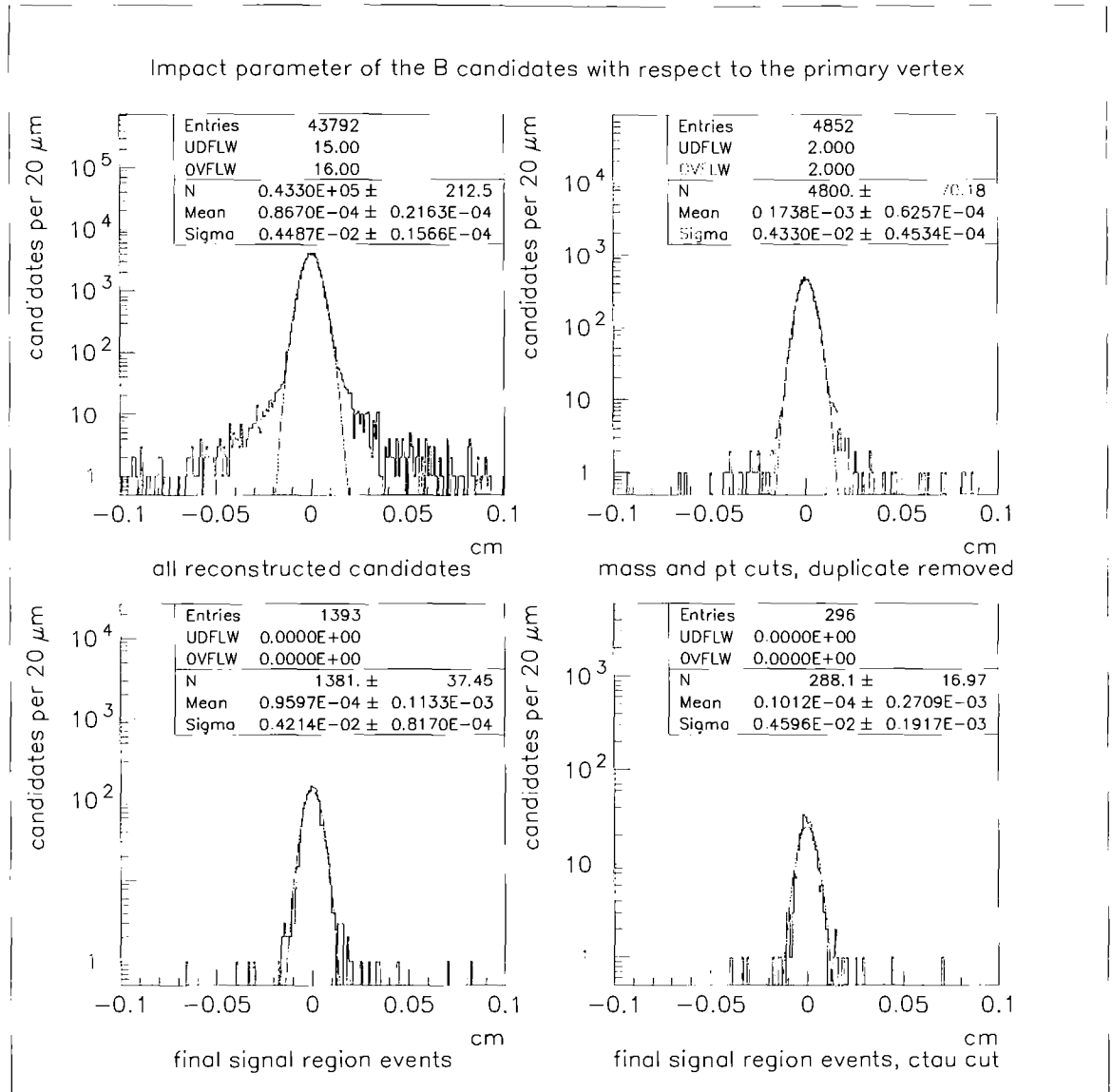


Figure 4.24: Distributions of the impact parameter of the  $B$  candidates with respect to the primary vertex (on the beam line) at various stages of the analysis.

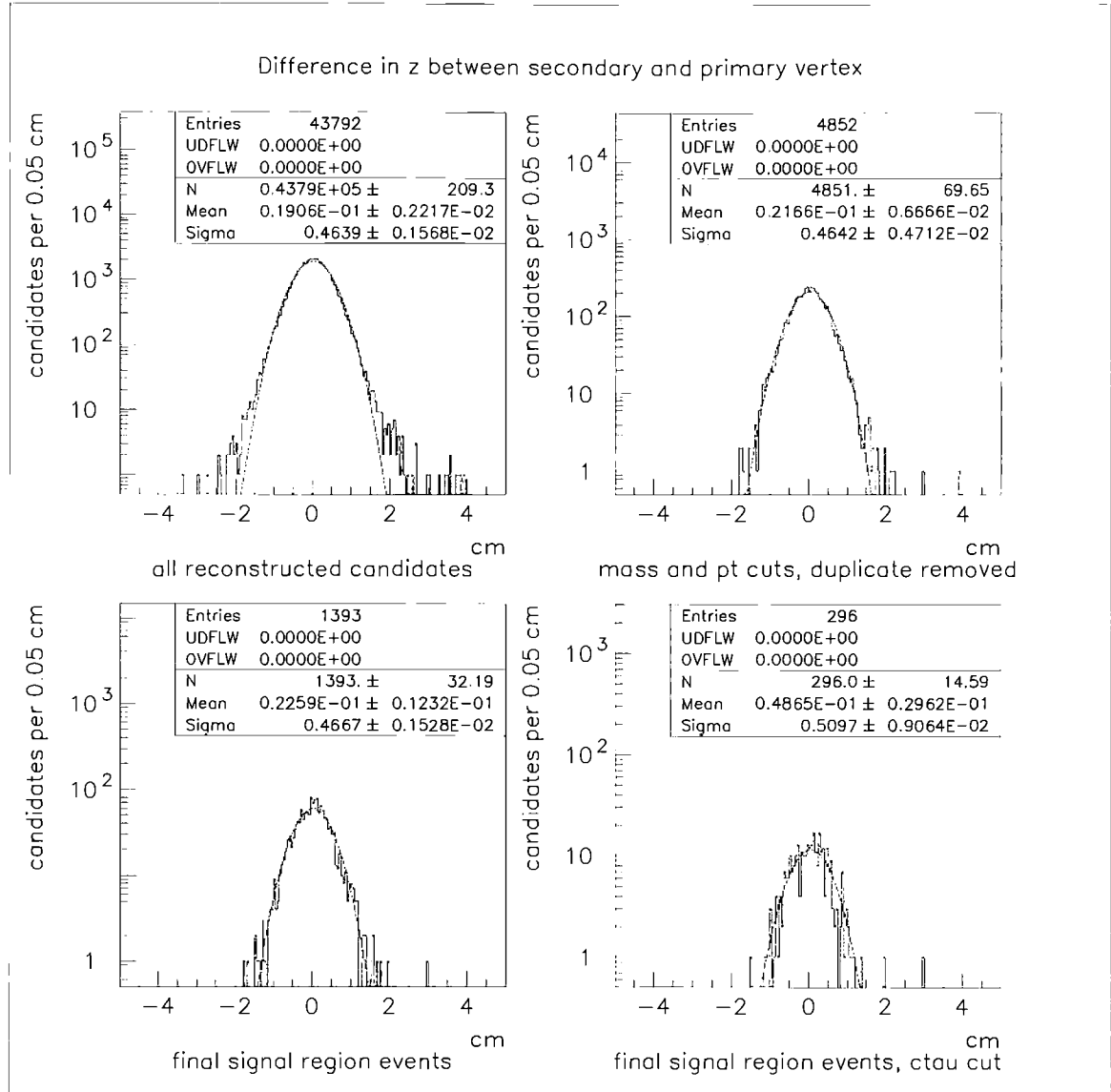


Figure 4.25: Distributions of the  $z$  coordinate of the  $B$  vertex minus the  $z$  coordinate of the primary vertex (on the beam line) at various stages of the analysis.

primary vertex coordinates. Propagating these errors yields  $29.3 \mu m$  for the average error on  $c\tau$  using the event-by-event vertex, while the average error on  $c\tau$  using the beam line is  $38.1 \mu m$  (see Fig. 4.26).

To assess the effect of this smaller error on the lifetime measurements, the Monte Carlo studies described in Sections 4.3.5 and 4.3.6 are repeated with a single modification in the generation of the Monte Carlo samples: all the generated values of the error on the proper decay lengths are multiplied by 0.76 to simulate the use of the VXPRES resolution. Otherwise, everything else is the same, including the sequence of random numbers. The average of the errors returned by MINUIT on the fitted lifetime for the  $B_u$  ( $B_d$ ) Monte Carlo sample is  $46.6 \pm 0.2 \mu m$  ( $53.5 \pm 0.3 \mu m$ ). Hence, the average error on the lifetimes decreases by  $1 \mu m$  at most when using the event-by-event vertex. In other words, a primary vertex resolution of  $40 \mu m$  is already “good enough” when compared with the long lifetime ( $\sim 480 \mu m$ ) of the  $B$  meson. Finally, using the event-by-event primary vertex method involves an additional systematic uncertainty that would need to be evaluated since tracks from the other  $B$  in the event, if included in the primary vertex determination, would bias the primary vertex measurement.

#### 4.5.6 Tighter $J/\psi$ and $\psi(2S)$ mass cuts

As can be seen on Figs 4.1 and 4.3, the mass cuts applied on the  $J/\psi$  and  $\psi(2S)$  candidates seem unjustifiably broad, when, in fact, the large fixed mass windows are motivated by the  $p_T$  dependence of the measured mass width (mass error  $\propto$  error on  $p_T = [(0.0009p_T)^2 + (0.0066)^2]^{\frac{1}{2}} \cdot p_T$ , see Fig. 4.2). These apparently wide mass windows are, in practice, tighter than they appear because the  $J/\psi$  and  $\psi(2S)$  candidates are always mass constrained in the CTVMFT fit of the  $B$  candidates. Hence,  $J/\psi$  and  $\psi(2S)$  candidates that have a mass significantly different from their world average values will tend to produce large  $\chi^2$  values in the CTVMFT fits. Since a  $\chi^2$  probability cut is applied, the fixed mass windows are actually fairly tight.

To check this expectation, the analysis is redone with tighter mass cuts. The  $\psi(2S)$  mass cut is tightened from  $\pm 20 \text{ MeV}/c^2$  to  $\pm 12.5 \text{ MeV}/c^2$ . For the  $J/\psi$  candidates, in addition to requiring the absolute value of the differ-

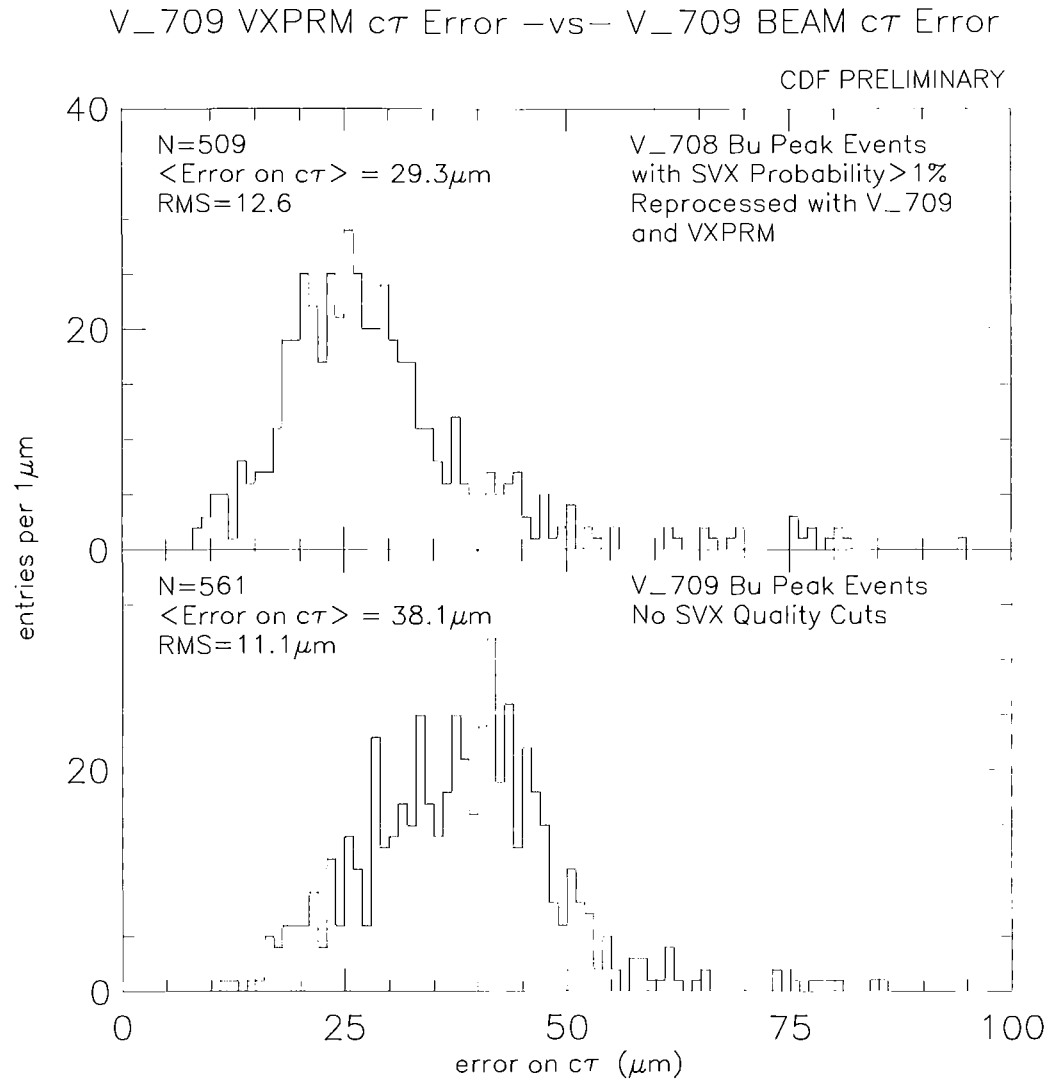


Figure 4.26: Distribution of the error on the proper decay lengths of  $B_u$  candidates using the primary vertex returned by VXPRIM (top plot) or a primary vertex determined from the average beam line parameter (see Sections 4.2.1 and 4.5.5 for details).

ence between the  $\mu\mu$  mass and the  $J/\psi$  world average mass to be less than  $80 \text{ MeV}/c^2$ , the measured mass is also required to be less than  $3\sigma$ , where the value of  $\sigma$  is parameterized as a function of the  $p_T$  of the  $\mu\mu$  combination. This parameterization is obtained as follows:

1. Plot the  $\mu\mu$  mass combinations in 6  $p_T$  ranges, 2 to 4, 4 to 6, 6 to 8, 8 to 10, 10 to 15, and  $> 15 \text{ GeV}/c$ .
2. Plot the fitted sigma of the  $\mu\mu$  mass distribution versus the corresponding mean  $p_T$  (see Fig. 4.27).
3. Fit the 6 points to obtain

$$\sigma = 9.582 + 1.031 p_T,$$

where  $\sigma$  is expressed in  $\text{MeV}/c^2$  and  $p_T$  is expressed in  $\text{GeV}/c$ .

Table 4.10 compares some of the relevant results of this “tight mass cuts” analysis with the default analysis. The excellent agreement in the results obtained from the two methods indicates that the vertex  $\chi^2$  cut on the  $B$  candidates effectively tightened the fixed  $J/\psi$  and  $\psi(2S)$  mass windows, as expected.

### 4.5.7 $B$ Lifetimes Versus $\bar{B}$ Lifetimes

This consistency check is performed by dividing the samples of  $B$  candidates into 3 categories: 1) events with a reconstructed candidate containing a  $b$  quark, 2) events with a reconstructed candidate containing a  $\bar{b}$  quark, and 3)  $J/\psi K_S^0$  and  $\psi(2S) K_S^0$  events for which it is not possible to distinguish between  $b$  and  $\bar{b}$ . The lifetimes fits are then performed separately on the samples corresponding to category 1) and 2). The results, shown in Table 4.11, agree with each other.

### 4.5.8 “Time Dependence”

As an additional consistency check, the lifetime fits are performed separately on the first part of the data (run  $< 44000$ ) and on the second part of the data (run  $> 44000$ ). The results, shown in Table 4.12, agree with each other.

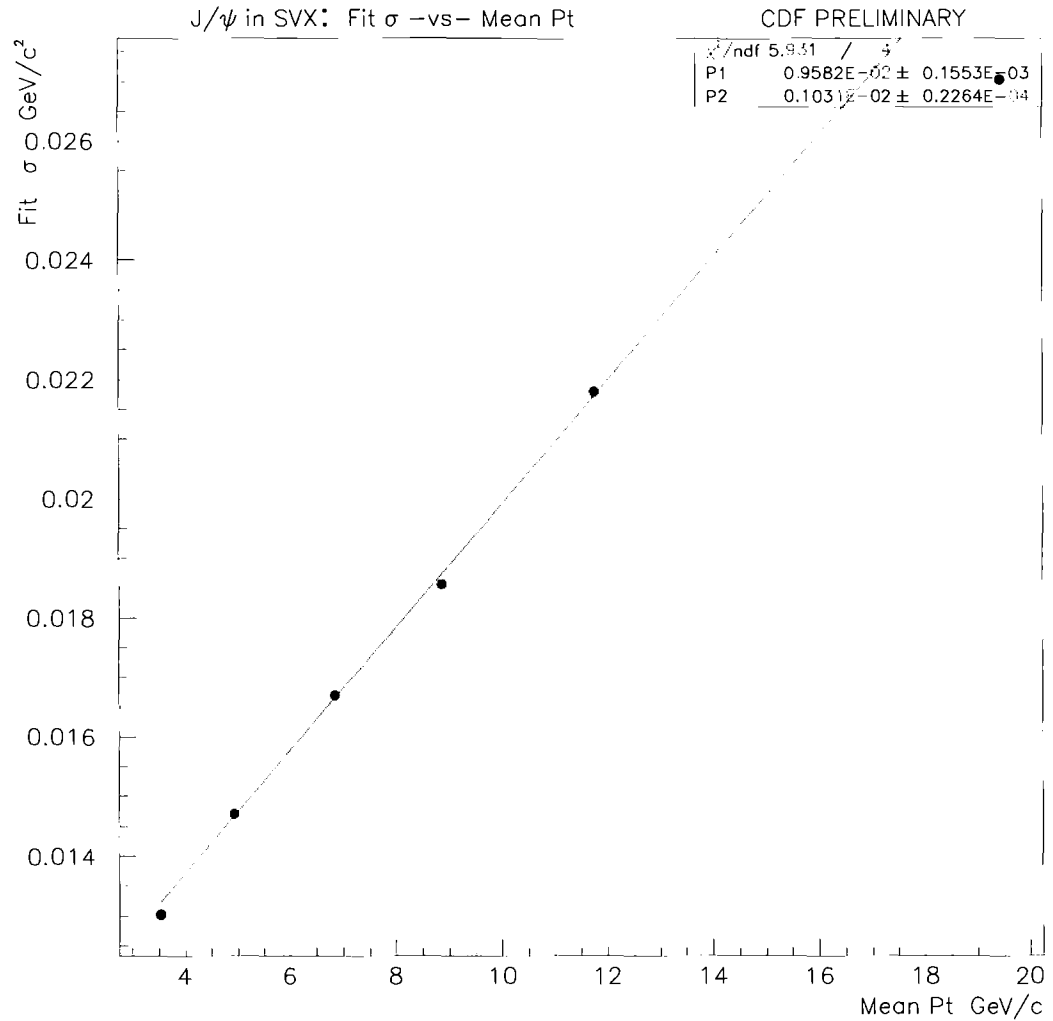


Figure 4.27: Resolution on the  $J/\psi$  mass as a function of the  $J/\psi$  transverse momentum. The data points were determined by fitting the  $J/\psi$  mass spectrum for all the  $J/\psi$  candidates in the corresponding  $p_T$  bin. The curve is a linear fit of the fitted width of the  $J/\psi$  signal versus the average  $p_T$  in the bin.

	Tight mass cuts		Default analysis	
	$B_u$	$B_d$	$B_u$	$B_d$
Number of events in peak above background with $c\tau$ above $100 \mu m$	119.5	87.5	120.5	87.5
Number of events in peak region	559	826	561	832
Number of events in sideband regions	791	1448	795	1452
Fitted signal [evts]	$147 \pm 16$	$120 \pm 16$	$148 \pm 16$	$121 \pm 16$
Fitted lifetime [ $\mu m$ ]	$485 \pm 48$	$473 \pm 55$	$482 \pm 48$	$472 \pm 55$

Table 4.10: Comparison of the “tight mass cuts” analysis with the default analysis.

	bottom = -1		bottom = +1	
	$b\bar{u}$	$b\bar{d}$	$\bar{b}u$	$\bar{b}d$
Number of events in peak region	293	392	268	407
Number of events in sideband regions	414	717	381	711
Fitted signal [evts]	$78 \pm 12$	$44 \pm 10$	$70 \pm 11$	$58 \pm 11$
Fitted lifetime [ $\mu m$ ]	$477 \pm 67$	$530 \pm 103$	$488 \pm 68$	$463 \pm 77$

Table 4.11: Comparison of the lifetime results on  $B$  and  $\bar{B}$  events.

	Run < 44000		Run > 44000	
	$B_u$	$B_d$	$B_u$	$B_d$
Number of events in peak region	280	392	281	440
Number of events in sideband regions	368	703	427	749
Fitted signal [evts]	$80 \pm 12$	$62 \pm 11$	$68 \pm 11$	$59 \pm 12$
Fitted lifetime [ $\mu m$ ]	$474 \pm 63$	$481 \pm 77$	$492 \pm 72$	$457 \pm 78$

Table 4.12: Comparison of the lifetime results on the first and second part of the data.

# Chapter 5

## Conclusions and Comparisons

This chapter presents the measured lifetime values of the  $B_u$  and  $B_d$  mesons and their ratio. These results are compared with existing measurements. Next, it describes the use of the  $B^0$  lifetime to determine  $V_{cb}$ . Finally, prospects for improving the precision of these measurements in the future are discussed.

### 5.1 Lifetime Results and Comparisons

The final lifetime results of this analysis are:

$$c\tau^+ = 482 \pm 48 \pm 16 \mu m,$$

$$c\tau^0 = 472 \pm 55 \pm 25 \mu m,$$

or

$$\tau^+ = 1.61 \pm 0.16 \pm 0.05 ps,$$

$$\tau^0 = 1.57 \pm 0.18 \pm 0.08 ps,$$

and

$$\tau^+/\tau^0 = 1.02 \pm 0.16 \pm 0.05,$$

where the first uncertainty is statistical and the second is systematic. These results are based on the entire CDF Run 1A data ( $19.3 pb^{-1}$ ).

This analysis obtains the most precise (and probably the most accurate) values currently published[1] of  $\tau^+$ ,  $\tau^0$ , and  $\tau^+/\tau^0$  for the  $B$  meson. These

measurements are consistent with those presented in References [55] and [56], but have a smaller uncertainty. Because the decay modes are fully reconstructed in this analysis, the  $B$  meson momentum is precisely determined, thereby eliminating systematic uncertainties due to estimating the  $B$  meson momentum present in previous measurements. They are also consistent with recent average  $b$ -hadron lifetime measurements ( $1.49 \pm 0.038$  ps) [57]. Graphical comparisons with recent LEP direct  $B$  lifetime measurements are presented in Figs 5.1–5.3. The term “direct” refers to the fact that an actual primary(secondary) vertex is measured and that the charge of the  $B$  meson is determined in these analyses. Numerous “indirect” measurements exist that rely on fits to impact parameter distributions or event topologies. Such analyses have been used to determine the average  $b$  lifetime, but these indirect methods are rapidly being supplanted by direct methods and are, therefore, not considered in this comparison.

## 5.2 CDF Value for $V_{cb}$

The measurement of  $\tau^0$  can be combined with CLEO measurements of the  $q^2$  dependence of the partial width for  $B^0 \rightarrow D^{*-}\ell^+\nu_\ell$  to extract a value of  $|V_{cb}|$ [28] (see Section 1.5).

$$\Gamma_{b \rightarrow c} \propto \frac{1}{\tau_b} \propto |V_{cb}|^2 \xi(y)^2. \quad (5.1)$$

Using Eq. (5.1), the results of Reference [2] ( $|V_{cb}| = (37 \pm 5 \pm 4) \times 10^{-3}$ ) and the value of  $\tau^0$  quoted here,  $|V_{cb}| = (36 \pm 5 \pm 4) \times 10^{-3}$ [58]. Using CDF’s direct measurement of  $\tau^0$ , there is no increase in the overall error on  $|V_{cb}|$ , and any systematic uncertainty associated with using the inclusive lifetime is eliminated.

## 5.3 Prospects for Future $B$ Lifetime Measurements at CDF

As shown in Section 1.6, theoretical expectations for  $\frac{\tau(B^+)}{\tau(B^0)}$  are that this quantity is equal to 1.0 to within  $\sim 10\%$ . Certainly before the end of CDF Run

Comparison of  $\tau^+$  Measurements

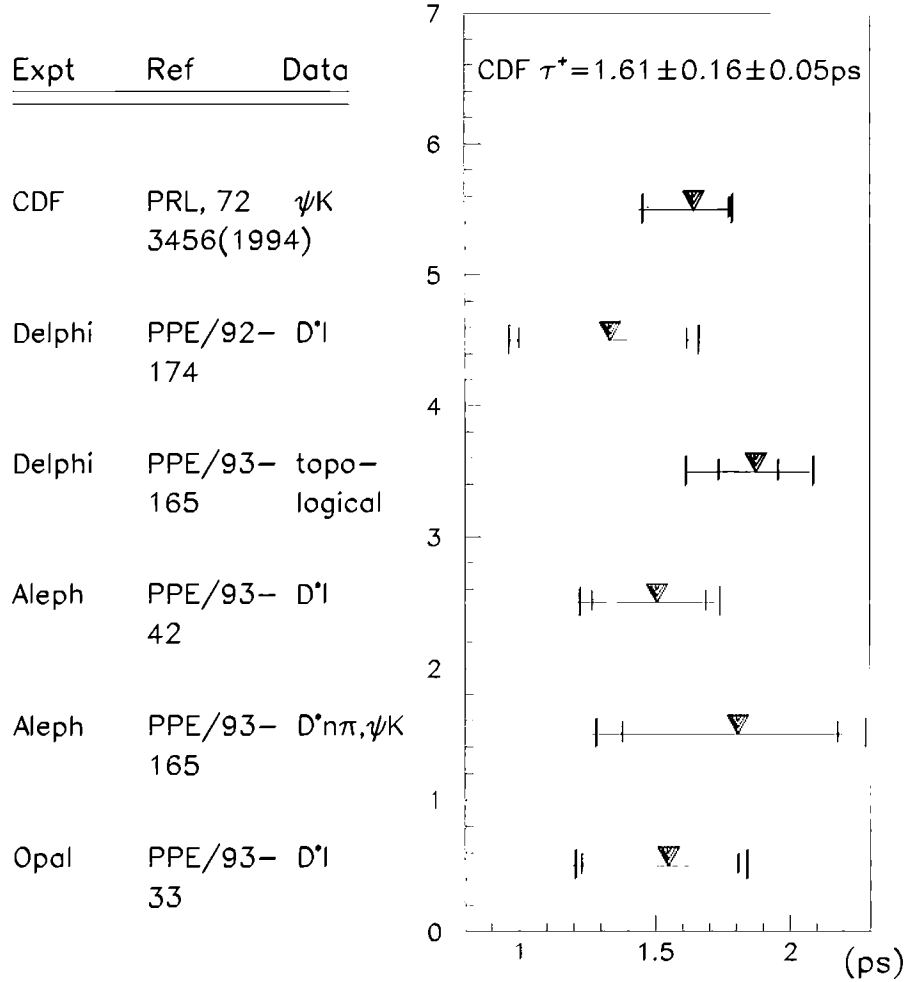


Figure 5.1: Comparison of Recent  $B_u$  Lifetime Measurements. Smaller(Larger) tick marks indicate statistical(total) uncertainties.

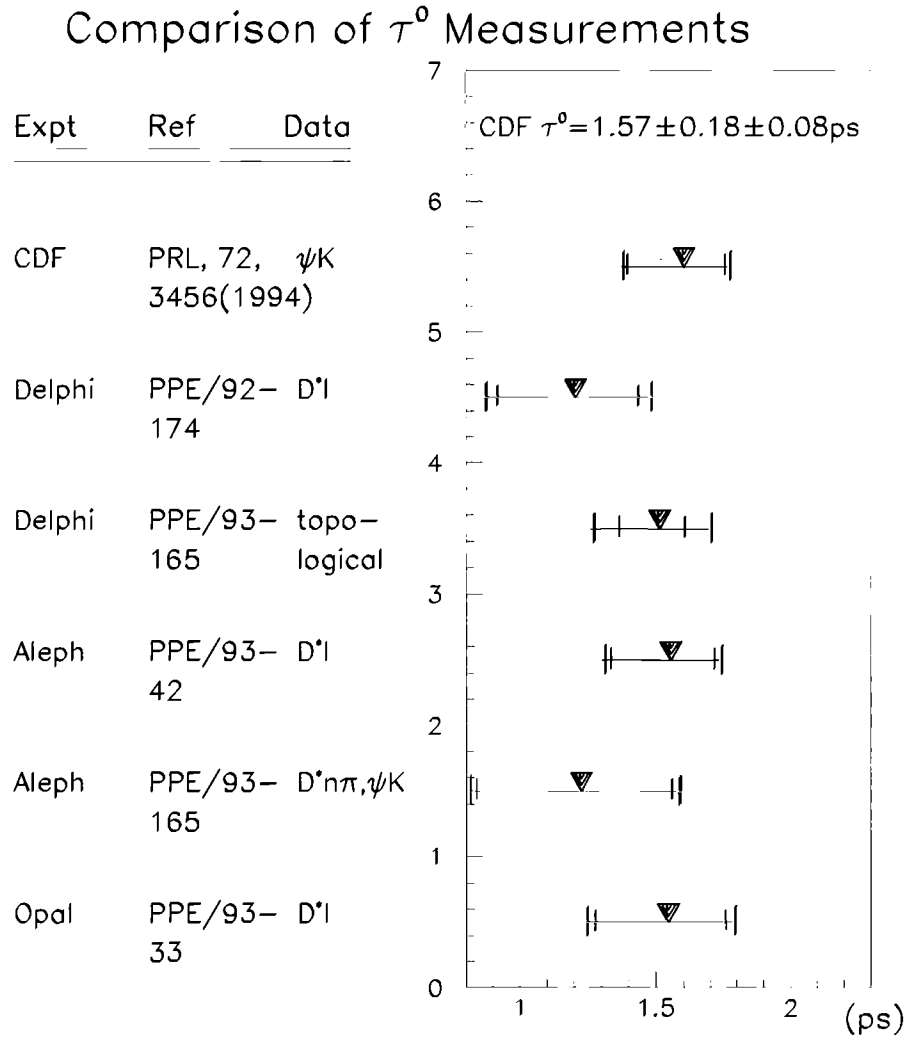


Figure 5.2: Comparison of Recent  $B_d$  Lifetime Measurements. Smaller(Larger) tick marks indicate statistical(total) uncertainties.

### Comparison of $\tau^+/\tau^0$ Measurements

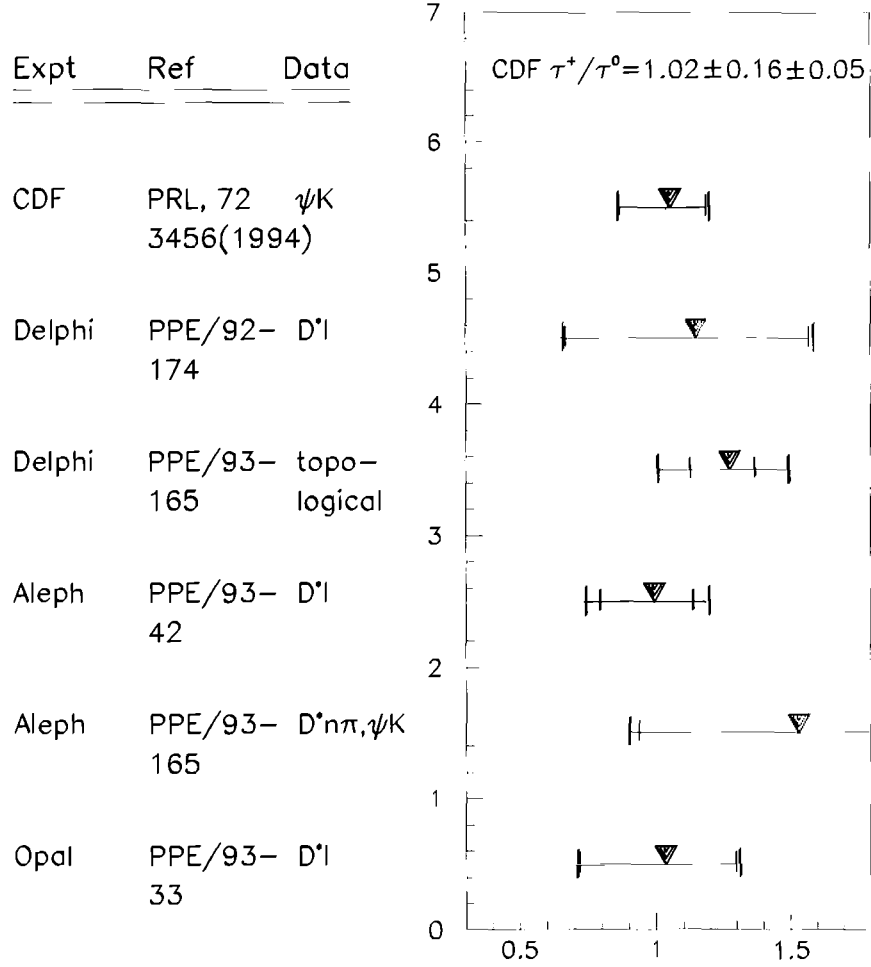


Figure 5.3: Comparison of Recent  $B$  Lifetime Ratio Measurements. Smaller(Larger) tick marks indicate statistical(total) uncertainties.

1B, CDF will be in a position to come tantalizingly close to this precision once the results of its lepton-charm  $B$  lifetime analysis[59] are finalized and are subsequently combined with those obtained in this analysis. A little further down the road, combining CDF Run 1A data with CDF Run 1B data should give a factor of 4 increase in the size of the data sample. A factor of 4 increase in the number of reconstructed  $B$  mesons will reduce the statistical error in the lifetime results by a factor of 2, i.e. a  $\sim 5\%$  statistical error in the lifetimes, and an  $\sim 8\%$  statistical error in their ratio can be attained using fully reconstructed decays. Furthermore, combining the results of the Run 1A + Run 1B version of this analysis with a Run 1A + Run 1B  $B$  lifetime analysis using lepton-charm events could provide an additional factor of  $\sim 2$  reduction because the statistical uncertainty in the Run 1A versions of both analyses are essentially equal. Also, the systematic uncertainty is comparable in both methods and should certainly not increase. Therefore, it is not unreasonable to expect a combined CDF lifetime result for the  $B_u$  and  $B_d$  mesons with an overall uncertainty of  $\sim 3\%$  and a combined CDF  $B$  lifetime ratio with a precision of  $\sim 6\%$ . The bottom line is that CDF will certainly be able to measure  $\frac{\tau(B^+)}{\tau(B^0)}$  to better than 10% and will be able to test theoretical predictions by the end of CDF Run 1B.

# Appendix A

## The Duplicate Removal Procedure

This appendix is divided into 4 sections. Section 1 gives an overview of the potential biases that could be introduced into the lifetime analysis by the use of a duplicate removal procedure. Section 2 describes the duplicate removal procedure in some detail and presents a table that demonstrates its effect on the signal to noise. Section 3 considers those events in which a  $B_u(B_d)$  candidate was selected among multiple  $B_u(B_d)$  candidates. It is demonstrated that the duplicate removal procedure does not bias the number of events nor the lifetime of the  $B_u(B_d)$  samples by a measurable amount. Section 4 considers those events in which  $B_d(B_u)$  duplicates were rejected in favor of a  $B_u(B_d)$  candidate. It is shown that the duplicate removal procedure does not systematically favor a specific region of the  $B$  invariant mass distribution (bias the number of events), nor does it measurably bias the lifetime of either the  $B_u$  or the  $B_d$  meson.

### A.1 Introduction

The duplicate removal procedure selects a single  $B$  meson candidate in events containing multiple  $B$  meson candidates based on the CTVMFT  $\chi^2$  probability. Hence, the selected candidate's daughter particles reconstruct to a secondary vertex "better" than the daughter particles of the rejected candi-

date(s). If the event contains a *real B* meson, a duplicate removal procedure based on the CTVMFT  $\chi^2$  probability should preferentially select the *real B* meson over combinatoric background candidates since daughter particles from the *real B* in the event should be associated with a *real* secondary vertex. However, this procedure does not guarantee that the *real B* meson will be selected in an event containing additional background candidates, since it is possible for the background candidate(s) to have a better  $\chi^2$  probability.

If the event does not contain a *real B* meson, the combinatoric background candidate that is selected among multiple background candidates should not come from a specific invariant mass range, nor should  $B_u(B_d)$  background candidates be favored over  $B_d(B_u)$  background candidates. If the odds of rejecting a duplicate peak background candidate are the same as rejecting a duplicate sideband background candidate, no bias is introduced either in the number of  $B_u(B_d)$  peak events, or in their lifetime since an incorrect choice will contribute the same in all bins within statistics and is equally likely in either the  $B_u$  or  $B_d$  case.

The duplicate removal procedure can bias the measured lifetime results in at least two ways. Multiple  $B_u(B_d)$  candidates in an event that use different tracks for the strange meson have different values of  $p_T$ . These candidates will have the same  $L_{xy}$  within errors because the different kaon candidates are combined with the same  $\Psi$ . The calculated  $c\tau$ , however, will be different; i.e.,

$$c\tau = L_{xy} \frac{M_B}{|\vec{p}_T^B|} = \vec{X} \cdot \hat{p}_T^B \frac{M_B}{|\vec{p}_T^B|}. \quad (\text{A.1})$$

Hence, multiple  $B_u(B_d)$  candidates in an event using different tracks for the strange meson will have different  $c\tau$  values. If two or more duplicate candidates of this type happen to fall in the peak region ( $|mass - 5.2786| < 0.030 \text{ GeV}/c^2$ ), the measured lifetime may be biased since the duplicate removal procedure is not 100% efficient\* for selecting the *real B* meson. This type of duplicate scenario (events with duplicates in the peak region) occurs

---

\*The efficiency of the duplicate removal procedure is expected to be better than 50% in the  $B_u$  case. Table A.1 demonstrates that the  $B_u$  signal<sup>2</sup>/background increases after the duplicate removal procedure is applied. The  $B_d$  case is dominated by candidates using a  $K^*(892)^0$ , as is shown in Table A.3. Picking the  $B_d$  candidate with the  $K\pi$  mass closer to the world average  $K^*(892)^0$  mass is known to be  $\sim 65\%$  efficient[60].

no more than  $\sim 9\%$  ( $\sim 6\%$ ) of the time for candidates with(out) a  $c\tau > 100 \mu\text{m}$  cut, where  $B_d \leftrightarrow B_d$  duplicates arising from the  $K\pi$  mass ambiguity of the  $K^*(892)^0$  are neglected since the reconstructed  $p_T$  does not depend on the mass assigned to the individual tracks forming the  $K^*(892)^0$ . We assign no systematic uncertainty due to this effect for reasons discussed in Section 3.2, Section 4.2, and the Conclusion.

The duplicate removal procedure will bias not only the lifetime measurement, but also the number of events in the final samples if it preferentially rejects background  $B_u(B_d)$  events that fall in a specific invariant mass range. For example, if the duplicate removal procedure systematically favors events that fall in the peak region over those that happen to fall in the low mass sideband region, regardless of whether or not there is a *real*  $B$  meson in the event, this procedure would, in fact, bias the final number of events and the lifetime of the  $B_u$  and  $B_d$  samples. Consider the effect of  $B_u$  peak candidates being systematically selected over  $B_d$  lower mass sideband candidates. Such a bias would inflate the number of  $B_u$  peak events and would bias the measured lifetime of both the  $B_u$  and the  $B_d$  events.

For the reasons outlined above, two questions must be addressed if the duplicate removal procedure is to be used in a  $B$  meson lifetime analysis. These are:

1. Does the duplicate removal procedure bias the measured lifetime obtained from the final  $B_u$  and  $B_d$  events?
2. Does the duplicate removal procedure bias the number of reconstructed  $B_u$  and  $B_d$  candidates by preferentially rejecting background candidates which fall in a specific invariant mass range?

This appendix will demonstrate that the duplicate removal procedure used in the Run 1A exclusive lifetime analysis does not bias the number of signal events by a measurable amount, nor does it introduce a measurable bias in lifetime of the selected  $B_u$  and  $B_d$  samples.

Given the potential pitfalls of the duplicate removal procedure, why use it all? The Run 1A exclusive  $B$  lifetime measurement is dominated by statistical uncertainty. If events with duplicates were simply removed from the final

sample, the statistical error would increase dramatically. On the other hand, including duplicate events in the final  $B_u$  and  $B_d$  samples would be equivalent to using the same  $B$  vertex multiple times and would also introduce a statistical correlation between the two samples. These considerations motivated the decision to use a duplicate removal procedure.

## A.2 The Duplicate Removal Procedure

Because we looked for  $B \rightarrow \Psi \mathbf{K}$  events, where  $\Psi$  is a  $J/\psi$  or  $\psi(2S)$  and  $\mathbf{K}$  is a  $K^+$ ,  $K^*(892)^+$ , or  $K_S^0$ , on an event-by-event basis, we occasionally had more than one  $B$  candidate passing the final event selection cuts. When this occurred, we applied a duplicate removal procedure to select a single  $B$  candidate out of the multiple candidates in the event. This procedure consisted of two parts applied in the following order:

1. If there are two  $\Psi K^*(892)^0$  candidates whose only difference is the mass assignment of the two tracks forming a  $K^*(892)^0$ , the CTVMFT  $\chi^2$  probabilities will be equal to each other. A single  $\Psi K^*(892)^0$  candidate is selected in this case by picking the one that has its  $K^*(892)^0$  mass closer to the world average value.
2. Pick the  $B$  candidate with the highest CTVMFT  $\chi^2$  probability.

Table A.1 shows the effect on this “duplicate removal” procedure on the candidates with  $c\tau > 100 \mu m$ . The biggest effect is on the channels that use a reconstructed  $K^*(892)^0$  because of the  $K\pi$  mass assignment ambiguity. In particular, this procedure brings the  $B_d \rightarrow J/\psi K^*(892)^0$  signal (above background, with  $c\tau > 100 \mu m$ ) down from 88 to 66.5 candidates. Among the 21.5 rejected candidates, 20 are discarded because of the presence of the same track combination in the event with a different mass assignment, and only 1.5 are discarded because another candidate in the same event (reconstructed with a different combination of tracks in any of the eight considered channels) has a better  $\chi^2$  value.

Channel	‡ candidates in peak region		‡ candidates in side bands		‡ candidates in peak above background	
	$N_{before}^{peak}$	$\rightarrow$ $N_{after}^{peak}$	$N_{before}^{side}$	$\rightarrow$ $N_{after}^{side}$	$N_{before}$	$\rightarrow$ $N_{after}$
$J/\psi K^+$	143	$\rightarrow$ 141	62	$\rightarrow$ 57	112	$\rightarrow$ $112\frac{1}{2}$
$J/\psi K^*(892)^+$	8	$\rightarrow$ 8	4	$\rightarrow$ 3	6	$\rightarrow$ $6\frac{1}{2}$
$\psi(2S) K^+$	5	$\rightarrow$ 5	9	$\rightarrow$ 7	$\frac{1}{2}$	$\rightarrow$ $1\frac{1}{2}$
$\psi(2S) K^*(892)^+$	0	$\rightarrow$ 0	0	$\rightarrow$ 0	0	$\rightarrow$ 0
Total $B_u$	156	$\rightarrow$ 154	75	$\rightarrow$ 67	$118\frac{1}{2}$	$\rightarrow$ $120\frac{1}{2}$
$J/\psi K_S^0$	19	$\rightarrow$ 17	8	$\rightarrow$ 8	15	$\rightarrow$ 13
$J/\psi K^*(892)^0$	148	$\rightarrow$ 110	120	$\rightarrow$ 87	88	$\rightarrow$ $66\frac{1}{2}$
$\psi(2S) K_S^0$	1	$\rightarrow$ 1	1	$\rightarrow$ 1	$\frac{1}{2}$	$\rightarrow$ $\frac{1}{2}$
$\psi(2S) K^*(892)^0$	19	$\rightarrow$ 14	25	$\rightarrow$ 13	$6\frac{1}{2}$	$\rightarrow$ $7\frac{1}{2}$
Total $B_d$	187	$\rightarrow$ 142	154	$\rightarrow$ 109	110	$\rightarrow$ $87\frac{1}{2}$

Table A.1: Effect of the “duplicate removal” procedure on the  $B$  candidates with  $c\tau > 100 \mu m$ . For each channels and each mass region the following numbers are shown:

$N_{before}^{peak}$  = the number of candidates in the peak region with  $c\tau > 100 \mu m$  before duplicate removal

$N_{after}^{peak}$  = the number of candidates in the peak region with  $c\tau > 100 \mu m$  after duplicate removal

$N_{before}^{side}$  = the number of candidates in the side bands with  $c\tau > 100 \mu m$  before duplicate removal

$N_{after}^{side}$  = the number of candidates in the side bands with  $c\tau > 100 \mu m$  after duplicate removal

$N_{before}$  =  $N_{before}^{peak} - \frac{1}{2} N_{before}^{side}$  = the number of candidates above background (in the peak region) with  $c\tau > 100 \mu m$  before duplicate removal

$N_{after}$  =  $N_{after}^{peak} - \frac{1}{2} N_{after}^{side}$  = the number of candidates above background (in the peak region) with  $c\tau > 100 \mu m$  after duplicate removal

### A.3 Duplicate Removal of the Form $B_u \leftrightarrow B_u(B_d \leftrightarrow B_d)$

In this section, events in which one or more  $B_u(B_d)$  duplicates were rejected in favor of another  $B_u(B_d)$  candidate will be considered. Table A.2 lists the number of  $B_u(B_d)$  events containing a duplicate  $B_u(B_d)$  candidate in various subsets of the final  $B_u$  and  $B_d$  event samples. Table A.3 lists the number of duplicate  $B_u(B_d)$  candidates in  $B_u(B_d)$  events by decay channel. These candidates could bias the number and lifetime of the final  $B_u(B_d)$  peak events if the duplicate removal procedure favors a particular region of the  $\pm 120 \text{ MeV}/c^2$  mass region. This class of duplicate candidates (excluding the  $B_d \rightarrow \Psi K^*(892)^0$ ) can also bias the measured lifetime because multiple  $B$  candidates that fall in the peak region using different tracks for the strange meson will have different  $p_T$  values. These two issues will be addressed in turn.

#### A.3.1 $B_u \leftrightarrow B_u (B_d \leftrightarrow B_d)$ Duplicate Removal's Effect on the the $B$ Invariant Mass Distribution

If the duplicate removal procedure selects or rejects  $B_u \leftrightarrow B_u (B_d \leftrightarrow B_d)$  duplicates that fall in a specific invariant mass range, both the number of  $B_u(B_d)$  peak events and the measured lifetime will be biased. Figs A.1–A.8 demonstrate that the duplicate removal procedure does not preferentially reject  $B_u(B_d)$  candidates with  $B_u(B_d)$  duplicates that fall in a particular mass range within statistics. Notice that in Fig. A.4 and in Figs A.6 and A.8 there appears to be a  $B_d$  signal in both the selected and rejected  $B_d$  samples. This observation indicates that there is a  $B_d$  signal in those  $B_d$  events with  $B_d$  duplicates. This signal is also present in the invariant mass distribution of the rejected  $B_d$  candidates because selecting a  $B_d \rightarrow J/\psi K^*(892)^0$  candidate by choosing the one with a  $K^*(892)^0$  mass closer to the world average value is  $\sim 65\%$  efficient for signal[60]. Hence, this correlation between the selected and rejected  $B_d$  candidates' invariant mass is expected and does not bias the lifetime since the calculated  $c\tau$  is the same regardless of the mass assigned to the tracks forming the  $K^*(892)^0$ . There does not appear to be a  $B_u$  signal either in Fig. A.1, or in Fig. A.5, indicating that  $B_u$  events with  $B_u$  duplicates

$B_u(B_d)$ Selection	Number of Selected Candidates	Number of Events with $B_u$ Duplicates	Number of Events with $B_d$ Duplicates
$B_u \pm 120$ $MeV/c^2$ window, no $c\tau$ cut	1801 events	251 (14%) events in $\pm 120 MeV/c^2$ window	357 (20%) events in $\pm 120 MeV/c^2$ window
$B_d \pm 120$ $MeV/c^2$ window, no $c\tau$ cut	3051 events	427 (14%) events in $\pm 120 MeV/c^2$ window	1312 (43%) events in $\pm 120 MeV/c^2$ window
$B_u \pm 120$ $MeV/c^2$ window, $c\tau > 100 \mu m$ cut	264 events	10 (3.8%) events in $\pm 120 MeV/c^2$ window	22 (8.3%) events in $\pm 120 MeV/c^2$ window
$B_d \pm 120$ $MeV/c^2$ window, $c\tau > 100 \mu m$ cut	328 events	22 (6.7%) events in $\pm 120 MeV/c^2$ window	101 (31%) events in $\pm 120 MeV/c^2$ window
$B_u \pm 30$ $MeV/c^2$ peak, no $c\tau$ cut	561 events	15(2.7%) events in $\pm 30 MeV/c^2$ peak	34 (6.1%) events in $\pm 30 MeV/c^2$ peak
$B_d \pm 30$ $MeV/c^2$ peak, no $c\tau$ cut	832 events	30 (3.6%) events in $\pm 30 MeV/c^2$ peak	168 (20%) events in $\pm 30 MeV/c^2$ peak
$B_u \pm 30$ $MeV/c^2$ peak, $c\tau > 100 \mu m$ cut	154 events	1 (0.65%) event in $\pm 30 MeV/c^2$ peak	1 (0.65%) event in $\pm 30 MeV/c^2$ peak
$B_d \pm 30$ $MeV/c^2$ peak, $c\tau > 100 \mu m$ cut	142 events	2 (1.4%) events in $\pm 30 MeV/c^2$ peak	28 (20%) events in $\pm 30 MeV/c^2$ peak

Table A.2: This table shows the number of  $B$  events with duplicates. The  $B_d \leftrightarrow B_u$  duplicate column includes duplicates resulting from the  $K\pi$  mass ambiguity of the  $K^*(892)^0$ . The indicated selection cuts are in addition to the default analysis cuts. The  $\pm 120 MeV/c^2$  window includes both the peak, gap and sideband regions. The  $\pm 30 MeV/c^2$  window includes only the peak region.

$B_d$ Event Selection	Number of Duplicates per Channel			
$\pm 120 \text{ MeV}/c^2$ window, no $c\tau$ cut, 1312 events	$B_d \rightarrow$ $J/\psi K_S^0$ , 7 duplicates	$B_d \rightarrow$ $J/\psi K^*(892)^0$ , 1224 duplicates	$B_d \rightarrow$ $\psi(2S)K_S^0$ , 0 duplicate	$B_d \rightarrow$ $\psi(2S)K^*(892)^0$ , 145 duplicates
$\pm 120 \text{ MeV}/c^2$ window, $c\tau > 100 \mu\text{m}$ cut, 101 events	$B_d \rightarrow$ $J/\psi K_S^0$ , 0 duplicates	$B_d \rightarrow$ $J/\psi K^*(892)^0$ , 86 duplicates	$B_d \rightarrow$ $\psi(2S)K_S^0$ , 0 duplicates	$B_d \rightarrow$ $\psi(2S)K^*(892)^0$ , 19 duplicates
$B_u$ Event Selection	Number of Duplicates per Channel			
$\pm 120 \text{ MeV}/c^2$ window, no $c\tau$ cut, 251 events	$B_u \rightarrow$ $J/\psi K^+$ , 220 duplicates	$B_u \rightarrow$ $J/\psi K^*(892)^+$ , 11 duplicates	$B_u \rightarrow$ $\psi(2S)K^+$ , 29 duplicates	$B_u \rightarrow$ $\psi(2S)K^*(892)^+$ , 2 duplicates
$\pm 120 \text{ MeV}/c^2$ window, $c\tau > 100 \mu\text{m}$ cut, 10 events	$B_u \rightarrow$ $J/\psi K^+$ , 8 duplicates	$B_u \rightarrow$ $J/\psi K^*(892)^+$ , 1 duplicate	$B_u \rightarrow$ $\psi(2S)K^+$ , 1 duplicate	$B_u \rightarrow$ $\psi(2S)K^*(892)^+$ , 0 duplicates

Table A.3: This table shows the number of duplicates per channel in  $B_u(B_d)$  events with  $B_u(B_d)$  duplicates. The indicated selection cuts are in addition to the default analysis cuts.

are purely combinatoric background events.

### A.3.2 $B_u \leftrightarrow B_u$ ( $B_d \leftrightarrow B_d$ ) Duplicate Removal's Effect on the the Measured $B$ Meson Lifetime

Only those  $B_u(B_d)$  events with one or more duplicate  $B_u(B_d)$  candidates that fall in the peak region are considered in the discussion that follows. We find 15(21) such  $B_u(B_d)$  events. Duplicate  $B_d \rightarrow \Psi K^*(892)^0$  peak candidates resulting from the  $K\pi$  mass ambiguity of the  $K^*(892)^0$  are not considered since they have the same  $c\tau$ . Also, events with duplicates in the sideband regions are not considered for two reasons: (1) when fitting for the lifetime, the sideband events are parameterized with the background function only; and (2) the duplicate removal procedure does not reject candidates from a particular

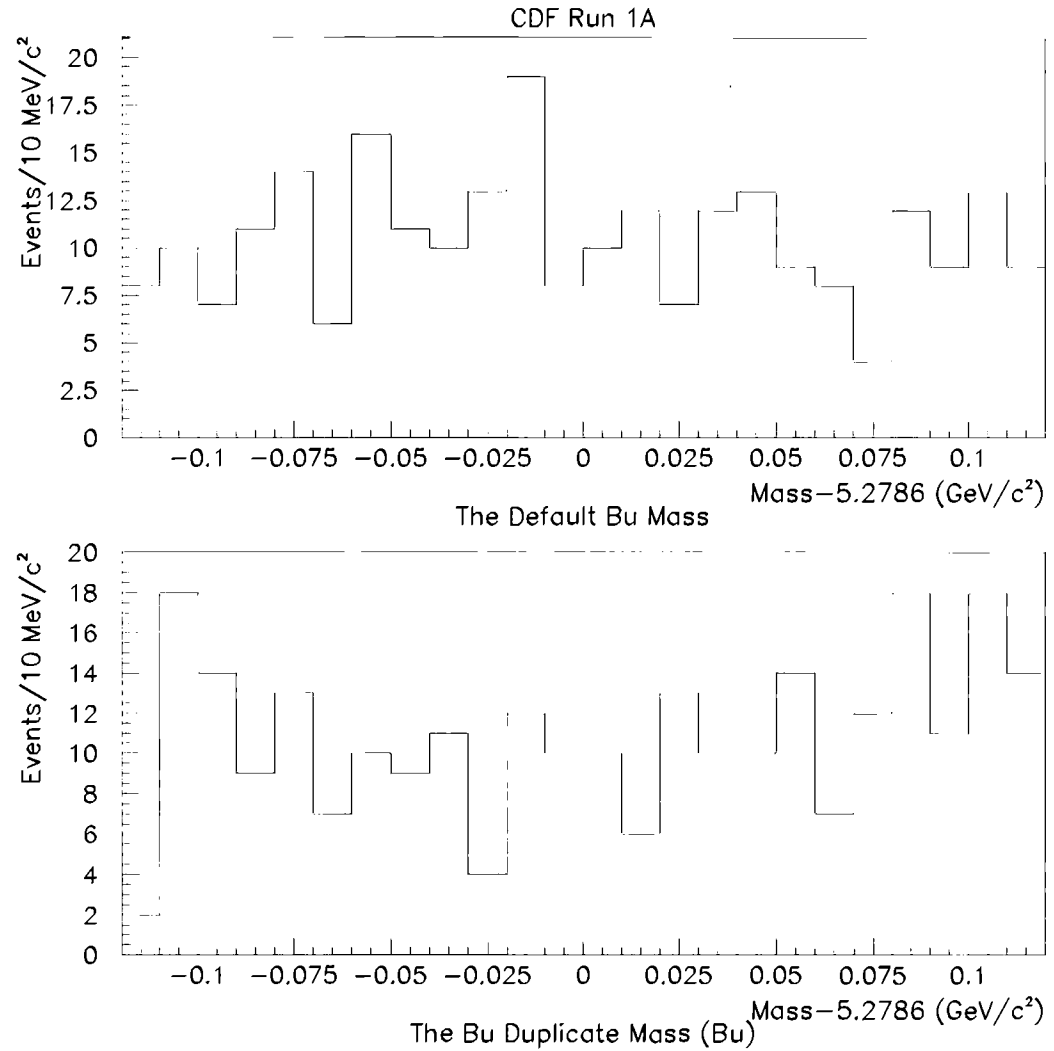


Figure A.1: Top plot: Invariant  $B_u$  mass distribution ( $\text{mass} - 5.2786 \text{ GeV}/c^2$ ) of candidates selected by the duplicate removal procedure. Only those events with  $B_u$  duplicates are plotted. This plot contains 251 entries. Bottom plot: Invariant mass distribution ( $\text{mass} - 5.2786 \text{ GeV}/c^2$ ) of the rejected  $B_u$  duplicates. This plot contains 262 entries.

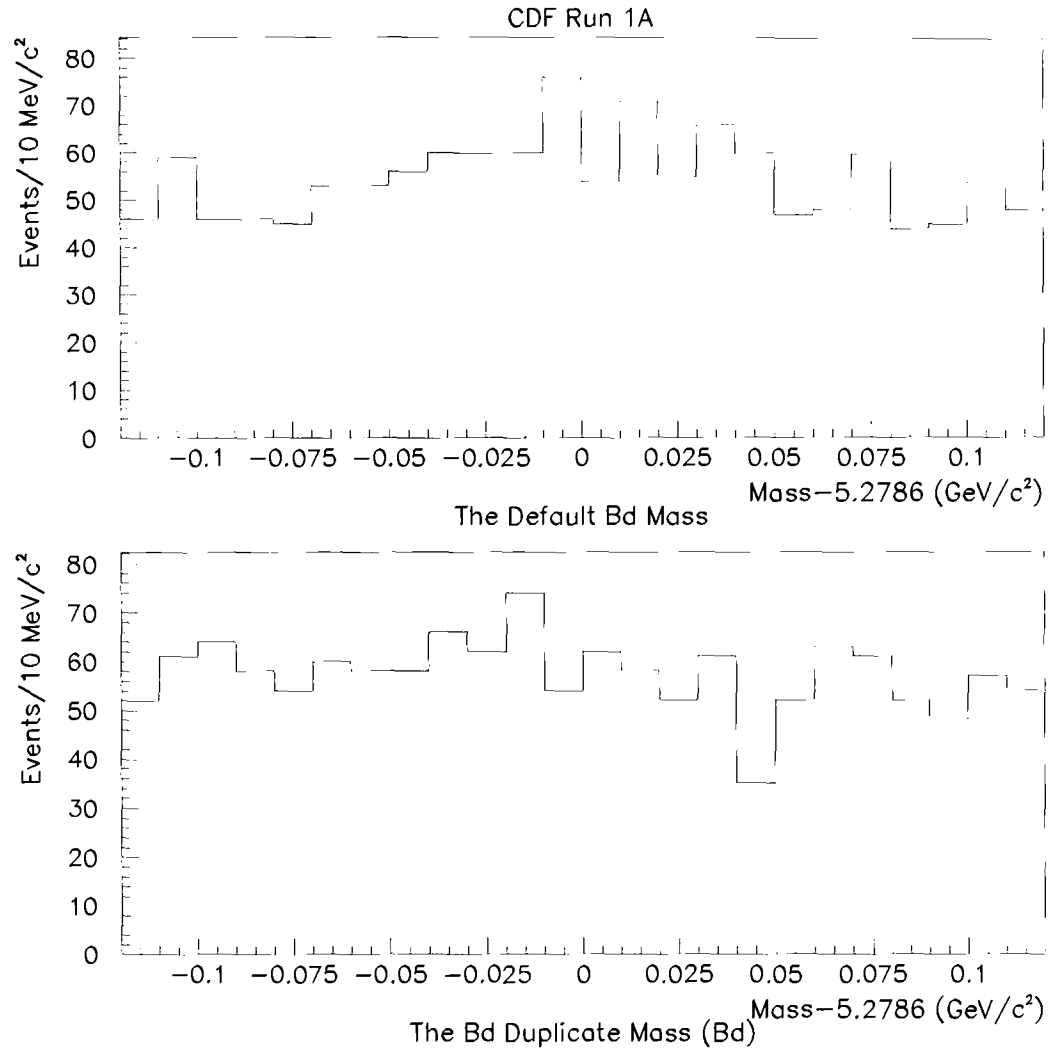


Figure A.2: Top plot: Invariant  $B_d$  mass distribution ( $\text{mass} - 5.2786 \text{ GeV}/c^2$ ) of candidates selected by the duplicate removal procedure. Only those events with  $B_d$  duplicates are plotted. This plot contains 1312 entries. Bottom plot: Invariant mass distribution ( $\text{mass} - 5.2786 \text{ GeV}/c^2$ ) of the rejected  $B_d$  duplicates. This plot contains 1376 entries.

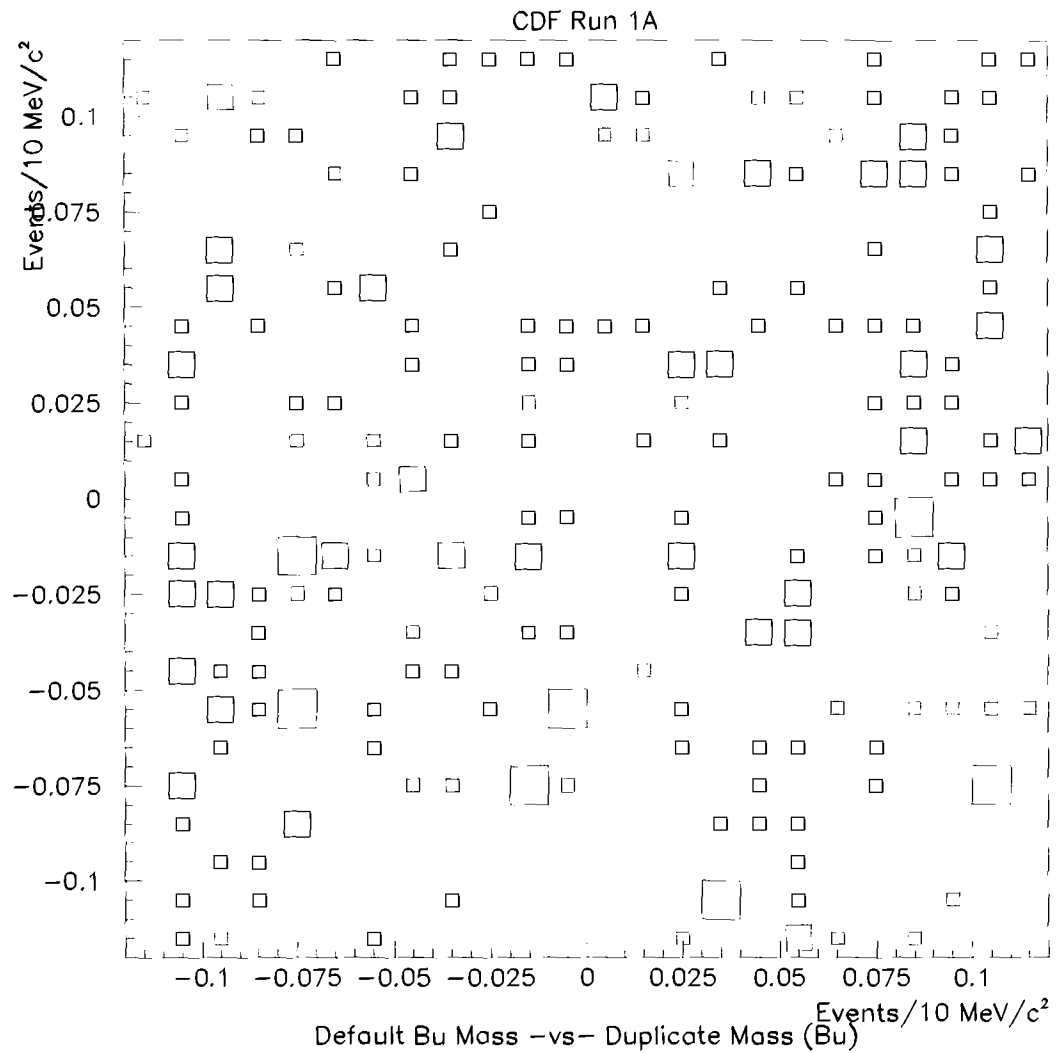


Figure A.3: Scatter plot of the invariant mass distribution (mass –  $5.2786 \text{ GeV}/c^2$ ) of the selected  $B_u$  candidate versus the invariant mass distribution (mass –  $5.2786 \text{ GeV}/c^2$ ) of the rejected  $B_u$  duplicates. Only those  $B_u$  events containing a  $B_u$  duplicate are plotted. This plot contains 262 entries.

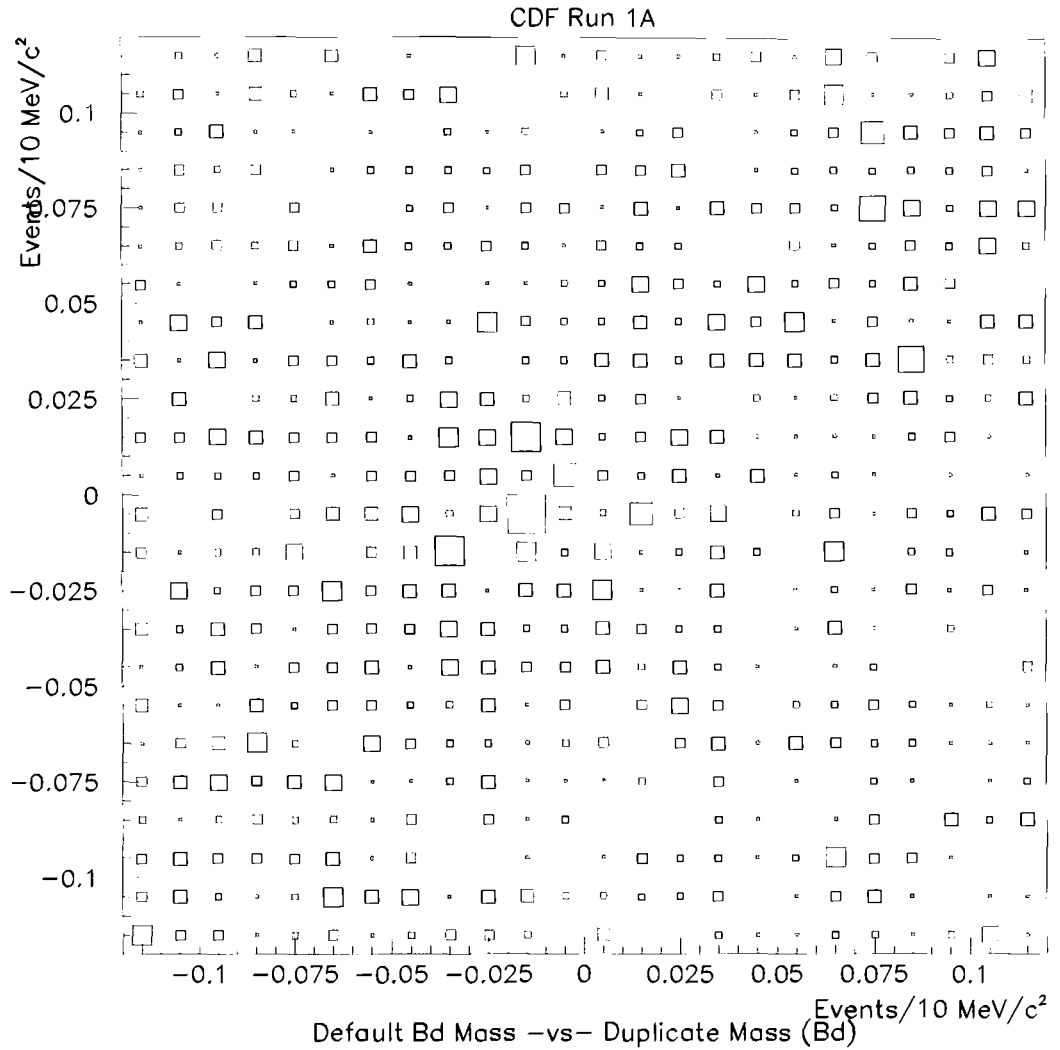


Figure A.4: Scatter plot of the invariant mass distribution (mass –  $5.2786 \text{ GeV}/c^2$ ) of the selected  $B_d$  candidate versus the invariant mass distribution (mass –  $5.2786 \text{ GeV}/c^2$ ) of the rejected  $B_d$  duplicates. Only those  $B_d$  events containing a  $B_d$  duplicate are plotted. This plot contains 1376 entries.

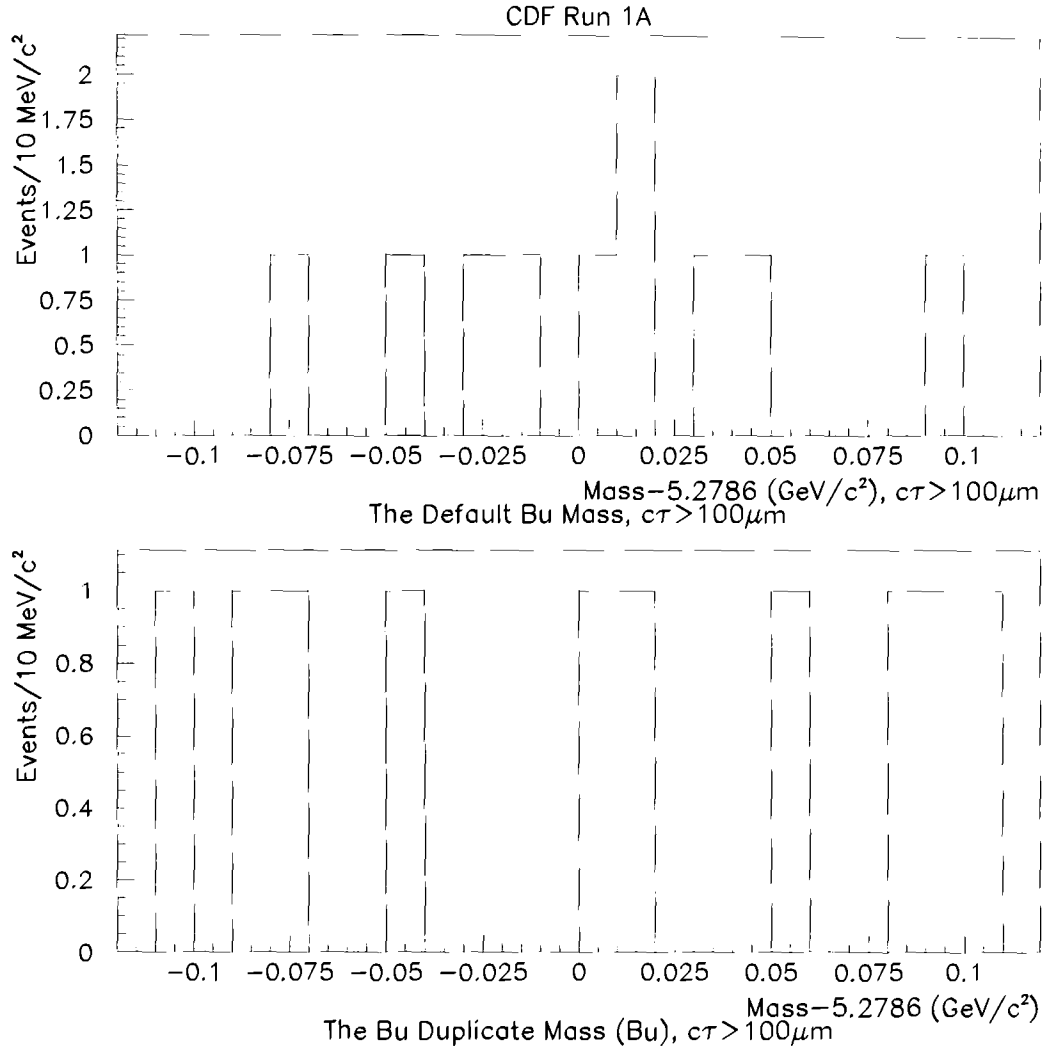


Figure A.5: Top plot: Invariant  $B_u$  mass distribution ( $\text{mass} - 5.2786 \text{ GeV}/c^2$ ) of candidates selected by the duplicate removal procedure. Only those events with  $B_u$  duplicates are plotted. This plot contains 10 entries. Bottom plot: Invariant mass distribution ( $\text{mass} - 5.2786 \text{ GeV}/c^2$ ) of the rejected  $B_u$  duplicates. This plot contains 10 entries.

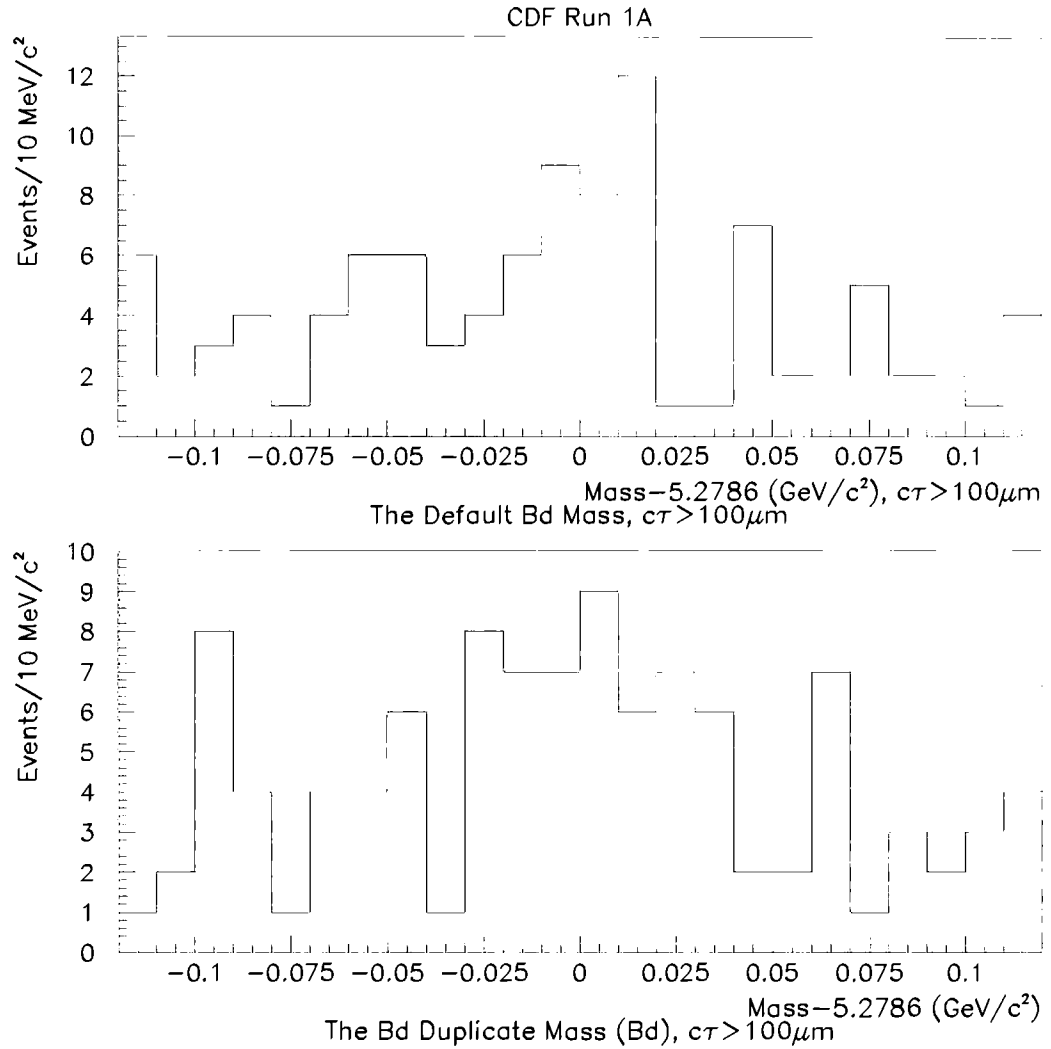


Figure A.6: Top plot: Invariant  $B_d$  mass distribution (mass  $- 5.2786 \text{ GeV}/c^2$ ) of candidates selected by the duplicate removal procedure. Only those events with  $B_d$  duplicates are plotted. This plot contains 101 entries. Bottom plot: Invariant mass distribution (mass  $- 5.2786 \text{ GeV}/c^2$ ) of the rejected  $B_d$  duplicates. This plot contains 105 entries.

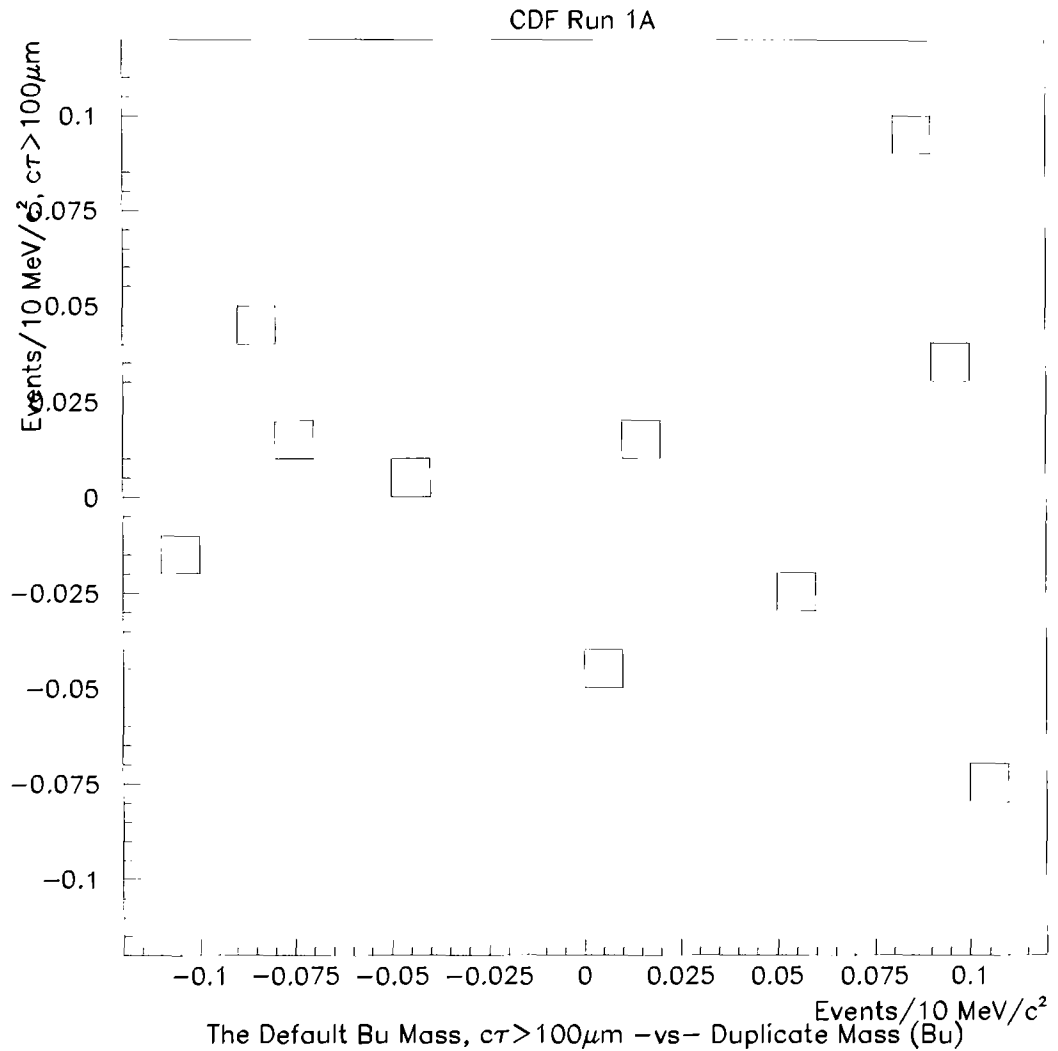


Figure A.7: Scatter plot of the invariant mass distribution (mass – 5.2786  $GeV/c^2$ ) of the selected  $B_u$  candidate versus the invariant mass distribution (mass – 5.2786  $GeV/c^2$ ) of the rejected  $B_u$  duplicates. Only those  $B_u$  events containing a  $B_u$  duplicate are plotted. This plot contains 10 entries.

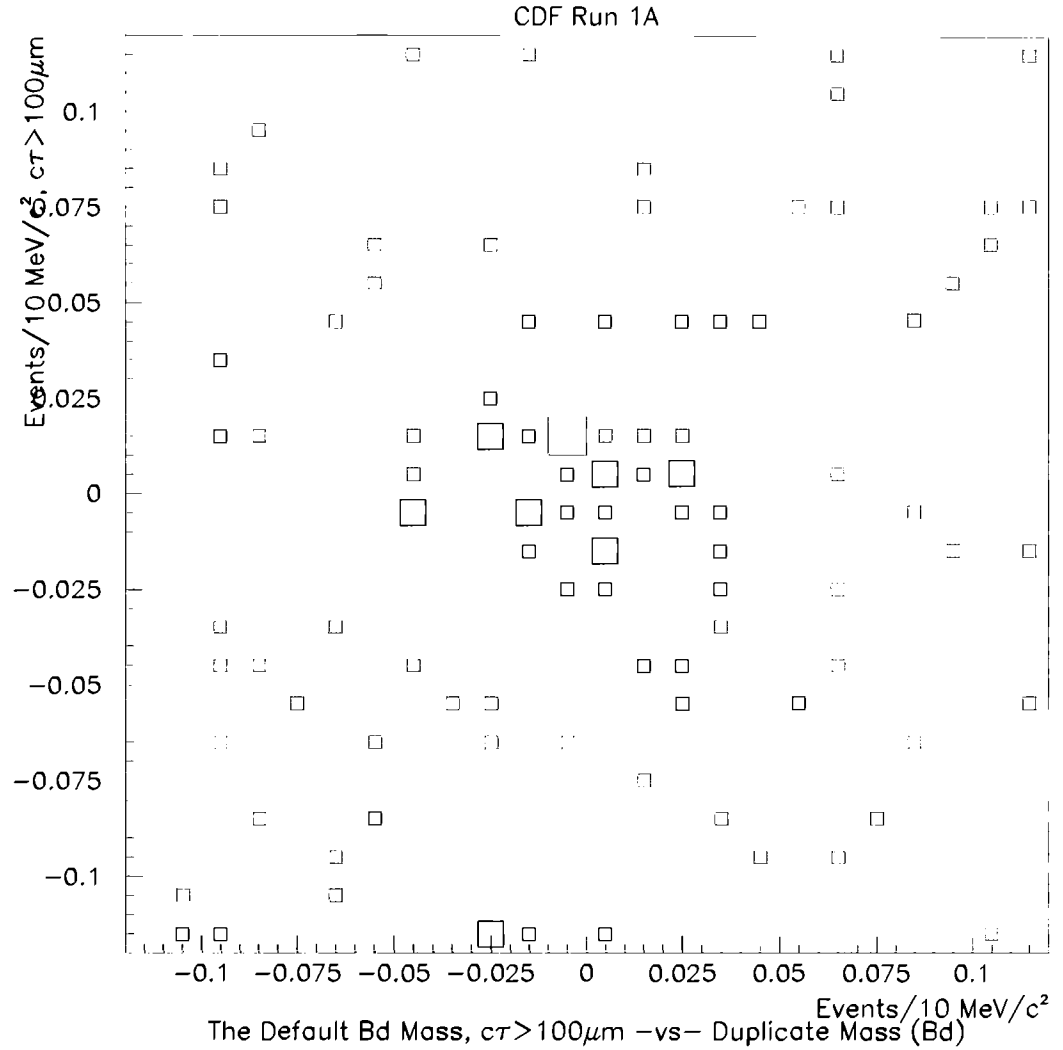


Figure A.8: Scatter plot of the invariant mass distribution (mass –  $5.2786 \text{ GeV}/c^2$ ) of the selected  $B_d$  candidate versus the invariant mass distribution (mass –  $5.2786 \text{ GeV}/c^2$ ) of the rejected  $B_d$  duplicates. Only those  $B_d$  events containing a  $B_d$  duplicate are plotted. This plot contains 105 entries.

invariant mass region, e.g. upper sideband or lower gap regions. Fig. A.9 demonstrates that, despite the fact that the selected  $B_u(B_d)$  candidate has a different  $p_T$  for the strange meson candidate than the rejected  $B_u(B_d)$  candidate(s),  $|\Delta c\tau/\sigma| < 3.0$  for all  $B_u$  events and for all but one  $B_d$  event ( $3.7\sigma$  difference). Also, the distributions are symmetrically centered around 0 within statistics, indicating that there is no systematic shift in  $c\tau$  due to  $p_T$  mismeasurement. For these reasons, we assign no systematic error to the lifetime due to selecting a single  $B_u(B_d)$  peak candidate among duplicate  $B_u(B_d)$  peak candidates based on the CTVMFT  $\chi^2$  probability.

## A.4 Duplicate Removal of the Form $B_u \leftrightarrow B_d(B_d \leftrightarrow B_u)$

In this section, events in which  $B_d(B_u)$  duplicates were rejected in favor of a  $B_u(B_d)$  candidate will be considered, since such events could bias the measured  $B_u(B_d)$  lifetime if the “other”  $B$  meson is systematically selected or rejected. Table A.2 lists the number of  $B_u(B_d)$  events containing a duplicate  $B_d(B_u)$  candidate in various subsets of the final  $B_u$  and  $B_d$  event samples. Table A.4 lists the number of duplicate  $B_u(B_d)$  candidates in  $B_d(B_u)$  events by decay channel. As an example, suppose there are 100  $B_u$  candidates in the peak region, of which 30 events had a  $B_d$  candidate also falling in the peak region that was rejected based on the CTVMFT  $\chi^2$  probability. If the duplicate removal procedure systematically made the incorrect choice in selecting the  $B_u$  candidates over the  $B_d$  candidates, the  $B_u$  lifetime is biased by including these 30 events.

### A.4.1 $B_u \leftrightarrow B_d(B_d \leftrightarrow B_u)$ Duplicate Removal’s Effect on the $B$ Invariant Mass Distribution

There is no discernable  $B$  peak in Figs A.10–A.17, indicating that  $B_u(B_d)$  events with  $B_d(B_u)$  duplicates are just combinatoric background. The fraction of events in the final  $\pm 120 \text{ MeV}/c^2$   $B_u(B_d)$  sample that contain  $B_d(B_u)$  duplicates is  $20\% \pm 1.2\%$  ( $14\% \pm 0.7\%$ ). It is reasonable to expect that the

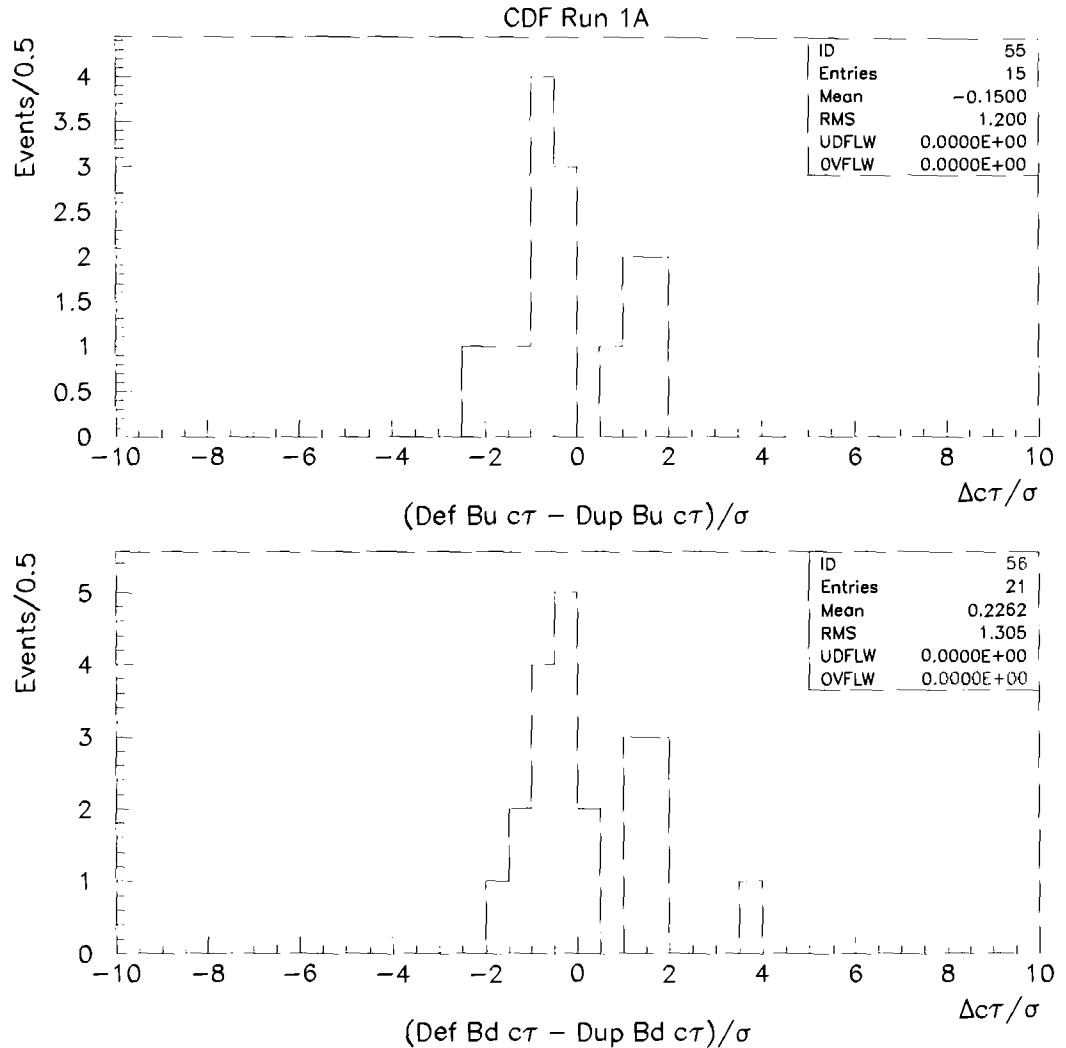


Figure A.9: d

duplicates,  $c\tau > 100 \mu\text{m}$ .] Top plot:  $(c\tau \text{ of the selected } B_u \text{ peak candidate} - c\tau \text{ of rejected } B_u \text{ peak candidate(s)})/\sigma$ . There are no entries with  $|\Delta c\tau/\sigma| > 3.0$ . Bottom plot:  $(c\tau \text{ of selected } B_d \text{ peak candidate} - c\tau \text{ of rejected } B_d \text{ peak candidate(s)})/\sigma$ . There is only one entry with  $|\Delta c\tau/\sigma| > 3.0$ .  $B_d \rightarrow \Psi K^*(892)^0$  duplicates resulting from the  $K\pi$  mass ambiguity of the  $K^*(892)^0$  are not included in this plot because they will have the same  $c\tau$ .

fraction of  $B_u$  events with duplicate  $B_d$  candidates is larger than the fraction of  $B_d$  events with duplicate  $B_u$  candidates. For every final  $B_u$  candidate, there are  $1.69 \pm 0.05$  final  $B_d$  candidates. Notice that  $(14\% \pm 0.7\%) \times (1.69 \pm 0.05) = 24\% \pm 1.4\%$ , which is within  $3\sigma$  of 20% (all errors have been calculated assuming uncorrelated systematic errors). Normalized for the relative number of events, the fraction of  $B_u$  events with  $B_d$  duplicates equals the fraction of  $B_d$  events with  $B_u$  duplicates within statistics. This fact demonstrates that the duplicate removal procedure does not favor  $B_u(B_d)$  events over  $B_d(B_u)$  events. As a result, the duplicate removal procedure does not introduce a bias in the number of  $B_u(B_d)$  events in the final  $\pm 120 \text{ MeV}/c^2$  sample within statistics. Similarly, the fraction of  $B_u(B_d)$  events with  $c\tau > 100 \mu\text{m}$  containing a rejected duplicate  $B_d(B_u)$  is  $8.3\% \pm 1.8\%$  ( $6.7\% \pm 1.5\%$ ). Again, the larger fraction in the  $B_u$  case is attributed to the fact that there are  $1.2 \pm 0.1$   $B_d$  candidates for every  $B_u$  candidate with a  $c\tau > 100 \mu\text{m}$ . Notice that  $(6.7\% \pm 1.5\%) \times (1.2 \pm 0.1) = 8.0\% \pm 1.9\%$ , which is within  $3\sigma$  of 8.3% (all errors have been calculated assuming uncorrelated systematic errors). This fact not only demonstrates that the duplicate removal procedure does not favor  $B_u(B_d)$  events over  $B_d(B_u)$  events within statistics, but also indicates that this aspect of the duplicate removal procedure does not depend on the lifetime of the  $B_u(B_d)$  events.

Further evidence that the duplicate removal procedure does not bias the number of final  $B_u(B_d)$  events by preferentially selecting a specific invariant mass region is provided by Figs A.12 and A.13, which plot the selected  $B_u(B_d)$  candidate's invariant mass versus the rejected  $B_d(B_u)$  duplicate's invariant mass. No discernible pattern is observed in either of these two plots, which demonstrates that the duplicate removal procedure does not favor a particular region of the invariant mass distribution considered in the lifetime analysis. The invariant mass distributions for events with duplicates are shown in Figs A.10 and A.11. Finally, the above plots are repeated in Figs A.14–A.17, but this time a  $c\tau$  cut has been applied to the selected  $B_u(B_d)$  events, but not to their  $B_d(B_u)$  duplicates. Again, no discernible pattern is observed in the scatter plots. In conclusion, the duplicate removal procedure does not bias the final number of  $B_u$  or  $B_d$  events, either by selecting one over the other (e.g.  $B_d$  over  $B_u$ ), or by selecting candidates out of a specific invariant mass

$B_u$ Event Selection	Number of Duplicates per Channel			
$\pm 120 \text{ MeV}/c^2$ window, no $c\tau$ cut, 357 events	$B_d \rightarrow$ $J/\psi K_S^0$ , 8 duplicates	$B_d \rightarrow$ $J/\psi K^*(892)^0$ , 344 duplicates	$B_d \rightarrow$ $\psi(2S)K_S^0$ , 1 duplicate	$B_d \rightarrow$ $\psi(2S)K^*(892)^0$ , 23 duplicates
$\pm 120 \text{ MeV}/c^2$ window, $c\tau > 100 \mu\text{m}$ cut, 22 events	$B_d \rightarrow$ $J/\psi K_S^0$ , 3 duplicates	$B_d \rightarrow$ $J/\psi K^*(892)^0$ , 18 duplicates	$B_d \rightarrow$ $\psi(2S)K_S^0$ , 0 duplicates	$B_d \rightarrow$ $\psi(2S)K^*(892)^0$ , 2 duplicates

$B_d$ Event Selection	Number of Duplicates per Channel			
$\pm 120 \text{ MeV}/c^2$ window, no $c\tau$ cut, 427 events	$B_u \rightarrow$ $J/\psi K^+$ , 382 duplicates	$B_u \rightarrow$ $J/\psi K^*(892)^+$ , 13 duplicates	$B_u \rightarrow$ $\psi(2S)K^+$ , 47 duplicates	$B_u \rightarrow$ $\psi(2S)K^*(892)^+$ , 0 duplicates
$\pm 120 \text{ MeV}/c^2$ window, $c\tau > 100 \mu\text{m}$ cut, 22 events	$B_u \rightarrow$ $J/\psi K^+$ , 20 duplicates	$B_u \rightarrow$ $J/\psi K^*(892)^+$ , 0 duplicates	$B_u \rightarrow$ $\psi(2S)K^+$ , 2 duplicates	$B_u \rightarrow$ $\psi(2S)K^*(892)^+$ , 0 duplicates

Table A.4: This table shows the number of duplicates per channel in  $B_u(B_d)$  events with  $B_d(B_u)$  duplicates. The indicated selection cuts are in addition to the default analysis cuts.

range (e.g.  $B_u$  peak over  $B_d$  sidebands).

#### A.4.2 $B_u \leftrightarrow B_d(B_d \leftrightarrow B_u)$ Duplicate Removal's Effect on the Measured $B$ Meson Lifetime

$B_u(B_d)$  events that fall within the peak region of the invariant mass distribution determine the  $B_u(B_d)$  lifetime. As shown in Fig. A.18, although the distributions are symmetrically centered around 0 within statistics, a number of duplicate candidates in which  $B_u \leftrightarrow B_d(B_d \leftrightarrow B_u)$  differ significantly in  $c\tau$  ( $|\Delta c\tau/\sigma| > 3.0$ ). It is reasonable to expect that the calculated  $c\tau$  of a selected  $B_u(B_d)$  candidate is significantly different from that of the rejected  $B_d(B_u)$  duplicate since there is generally an extra track in the  $B_d$  reconstruction relative to the  $B_u$  reconstruction, e.g. compare  $B_u \rightarrow \Psi K^+$  with

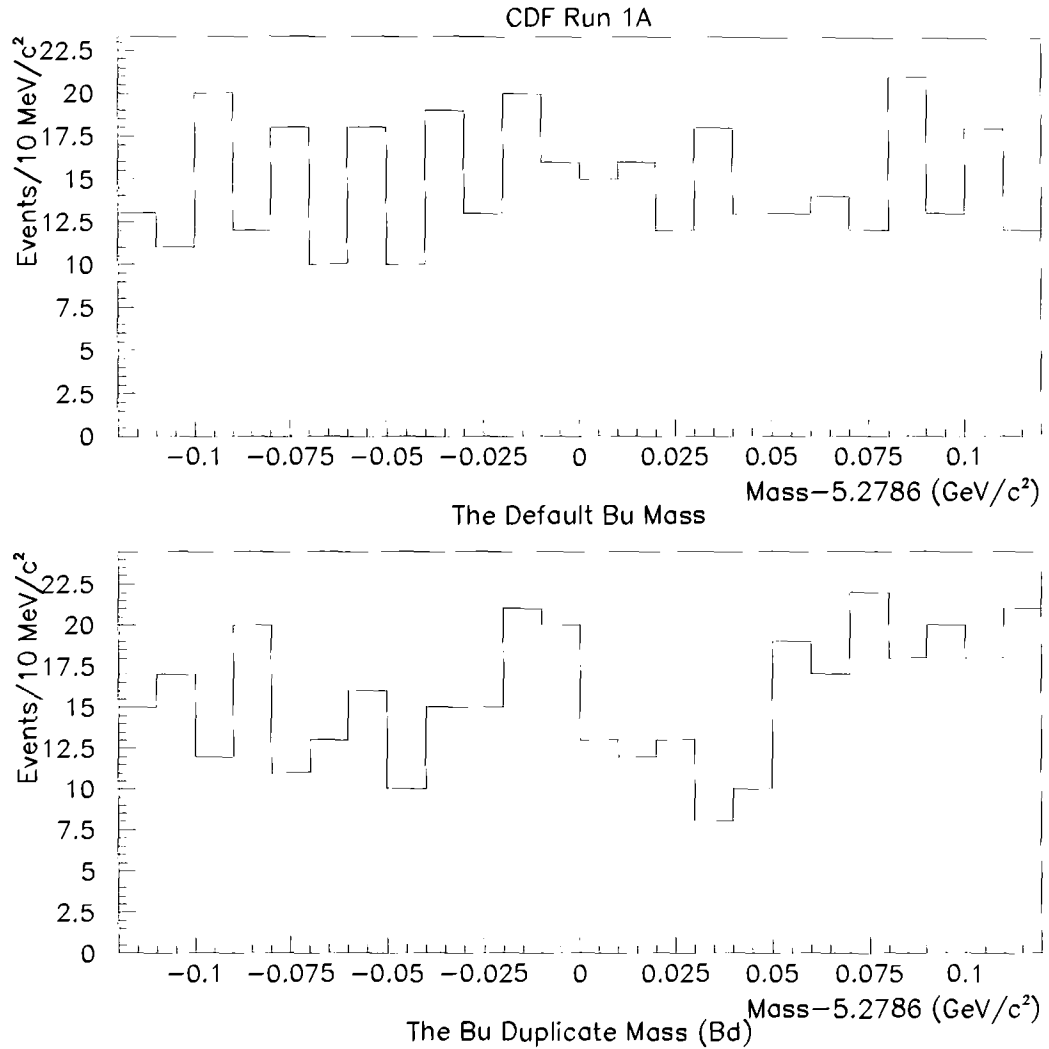


Figure A.10: Top plot: Invariant  $B_u$  mass distribution (mass  $- 5.2786 \text{ GeV}/c^2$ ) of candidates selected by the duplicate removal procedure. Only those events with  $B_d$  duplicates are plotted. This plot contains 357 entries. Bottom plot: Invariant mass distribution (mass  $- 5.2786 \text{ GeV}/c^2$ ) of the rejected  $B_d$  duplicates. This plot contains 376 entries.

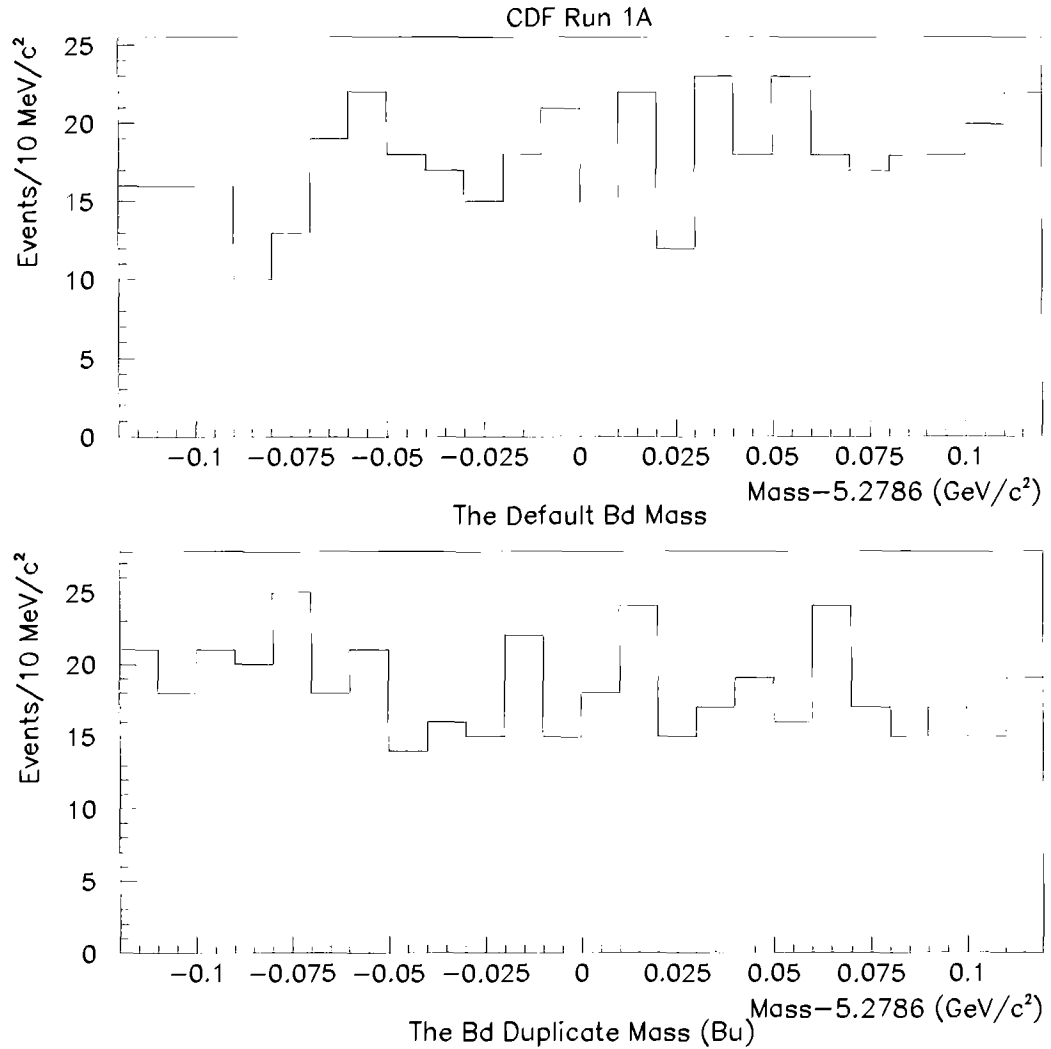


Figure A.11: Top plot: Invariant  $B_d$  mass distribution ( $\text{mass} - 5.2786 \text{ GeV}/c^2$ ) of candidates selected by the duplicate removal procedure. Only those events with  $B_u$  duplicates are plotted. This plot contains 427 entries. Bottom plot: Invariant mass distribution ( $\text{mass} - 5.2786 \text{ GeV}/c^2$ ) of the rejected  $B_u$  duplicates. This plot contains 442 entries.

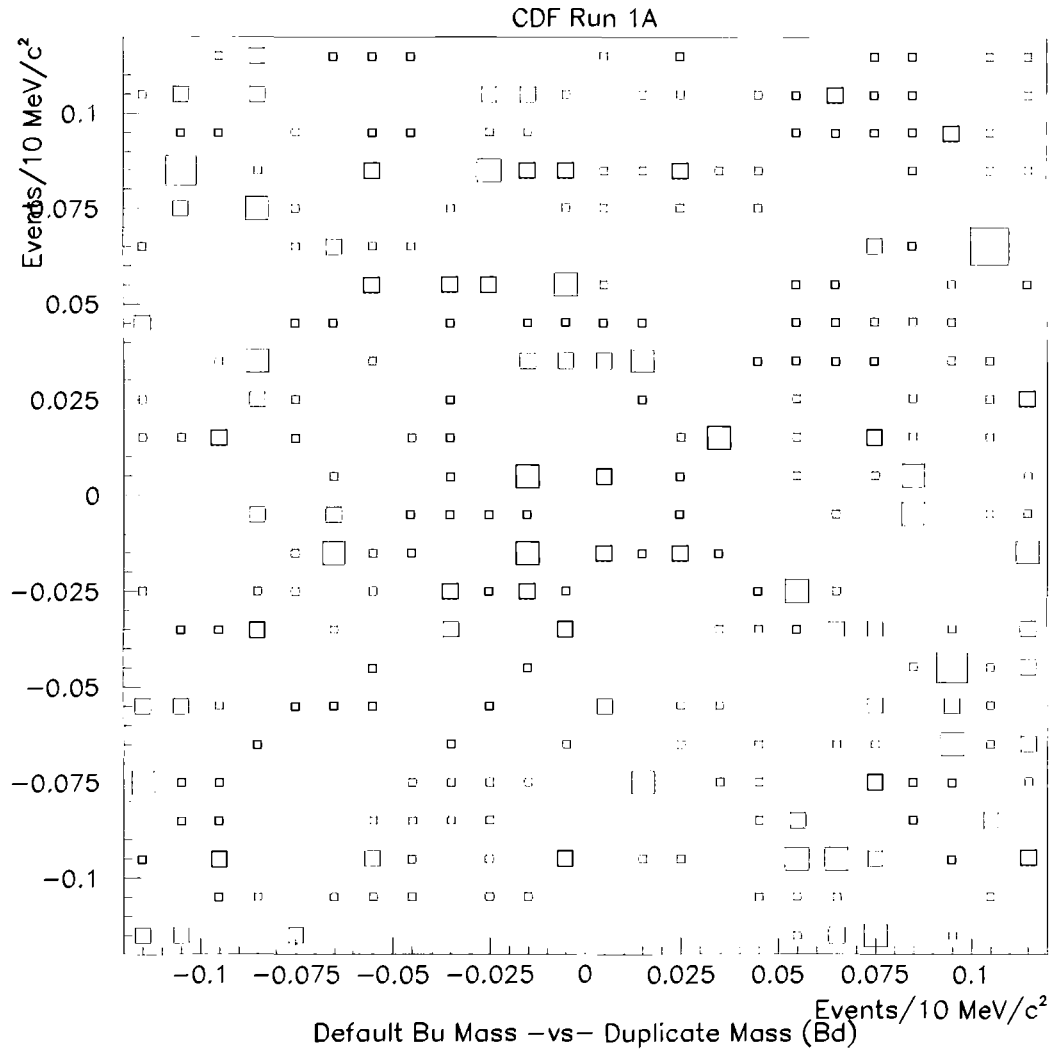


Figure A.12: Scatter plot of the invariant mass distribution (mass  $- 5.2786 \text{ GeV}/c^2$ ) of the selected  $B_u$  candidate versus the invariant mass distribution (mass  $- 5.2786 \text{ GeV}/c^2$ ) of the rejected  $B_d$  duplicates. Only those  $B_u$  events containing a  $B_d$  duplicate are plotted. This plot contains 376 entries.

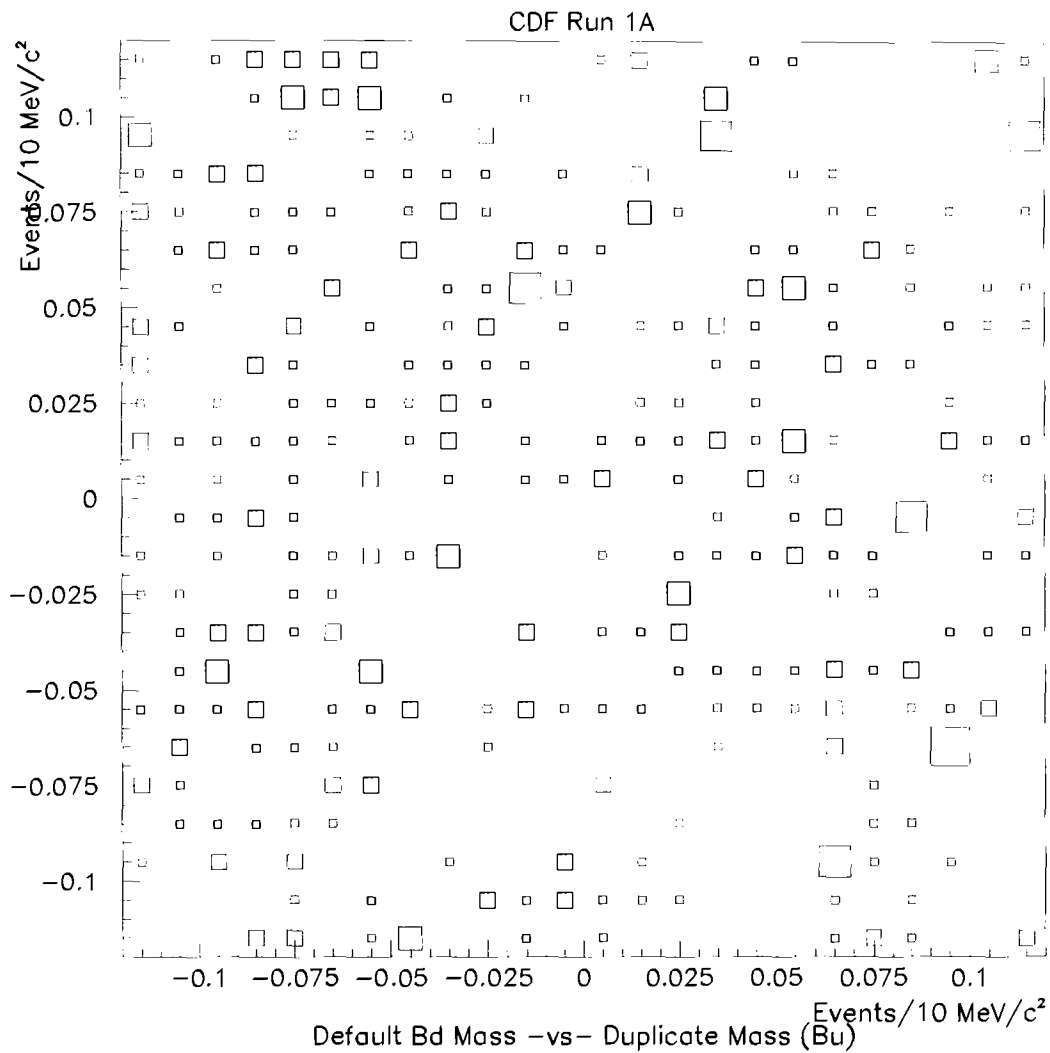


Figure A.13: Scatter plot of the invariant mass distribution (mass –  $5.2786 \text{ GeV}/c^2$ ) of the selected  $B_d$  candidate versus the invariant mass distribution (mass –  $5.2786 \text{ GeV}/c^2$ ) of the rejected  $B_u$  duplicates. Only those  $B_d$  events containing a  $B_u$  duplicate are plotted. This plot contains 442 entries.

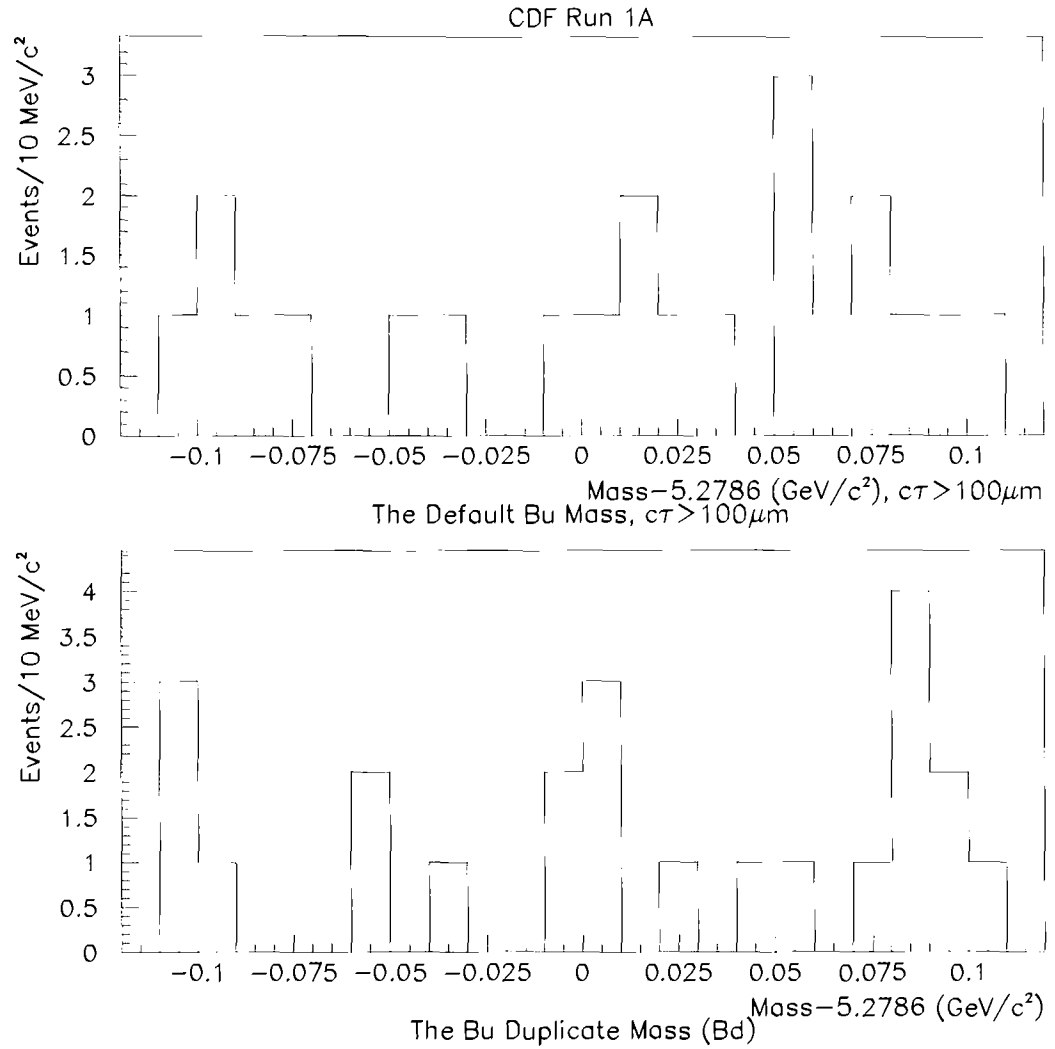


Figure A.14: Top plot: Invariant  $B_u$  mass distribution (mass  $- 5.2786 \text{ GeV}/c^2$ ) of candidates selected by the duplicate removal procedure having a  $c\tau > 100 \mu m$ . Only those events with  $B_d$  duplicates are plotted. This plot contains 22 entries. Bottom plot: Invariant mass distribution (mass  $- 5.2786 \text{ GeV}/c^2$ ) of the rejected  $B_d$  duplicates. This plot contains 23 entries.

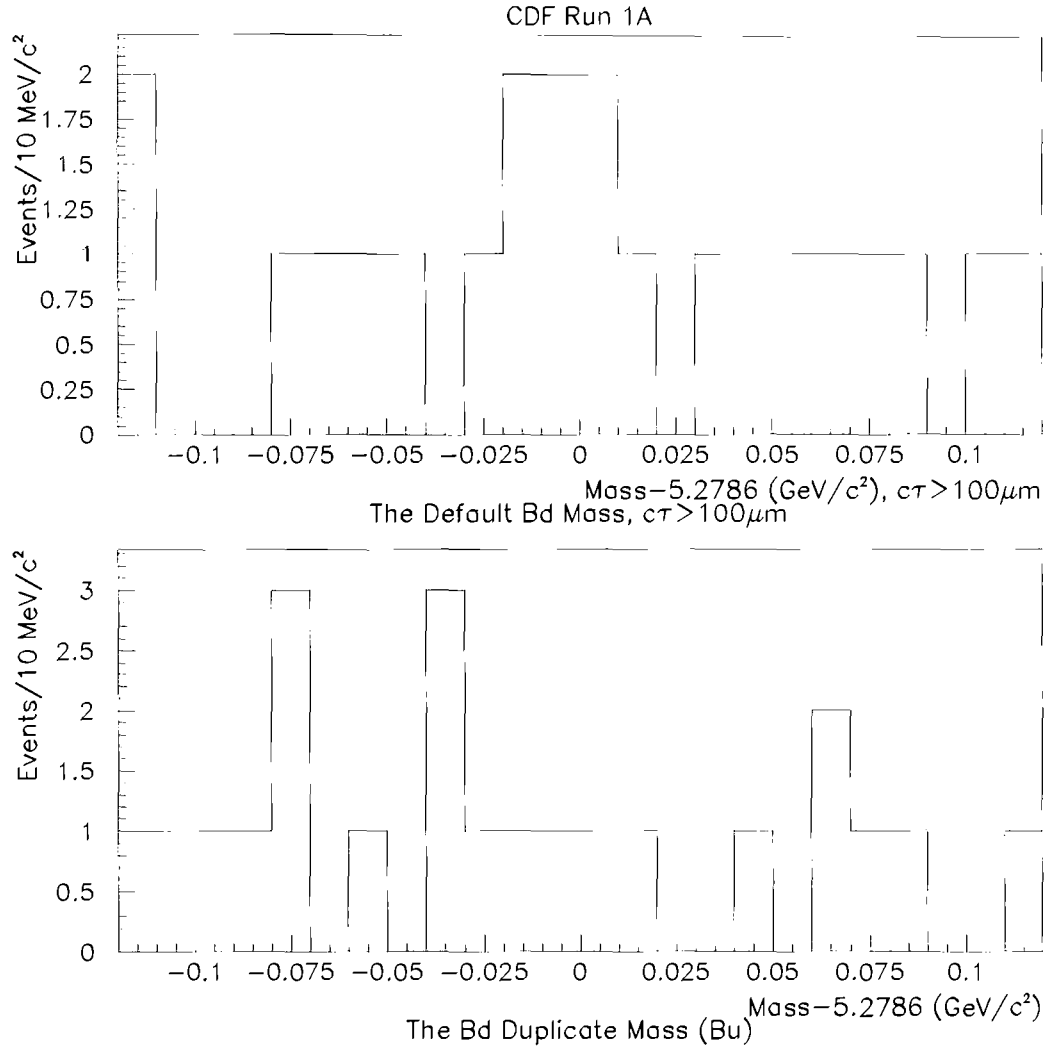


Figure A.15: Top plot: Invariant  $B_d$  mass distribution (mass  $- 5.2786 \text{ GeV}/c^2$ ) of candidates selected by the duplicate removal procedure having a  $c\tau > 100 \mu\text{m}$ . Only those events with  $B_u$  duplicates are plotted. This plot contains 22 entries. Bottom plot: Invariant mass distribution (mass  $- 5.2786 \text{ GeV}/c^2$ ) of the rejected  $B_u$  duplicates. This plot contains 22 entries.

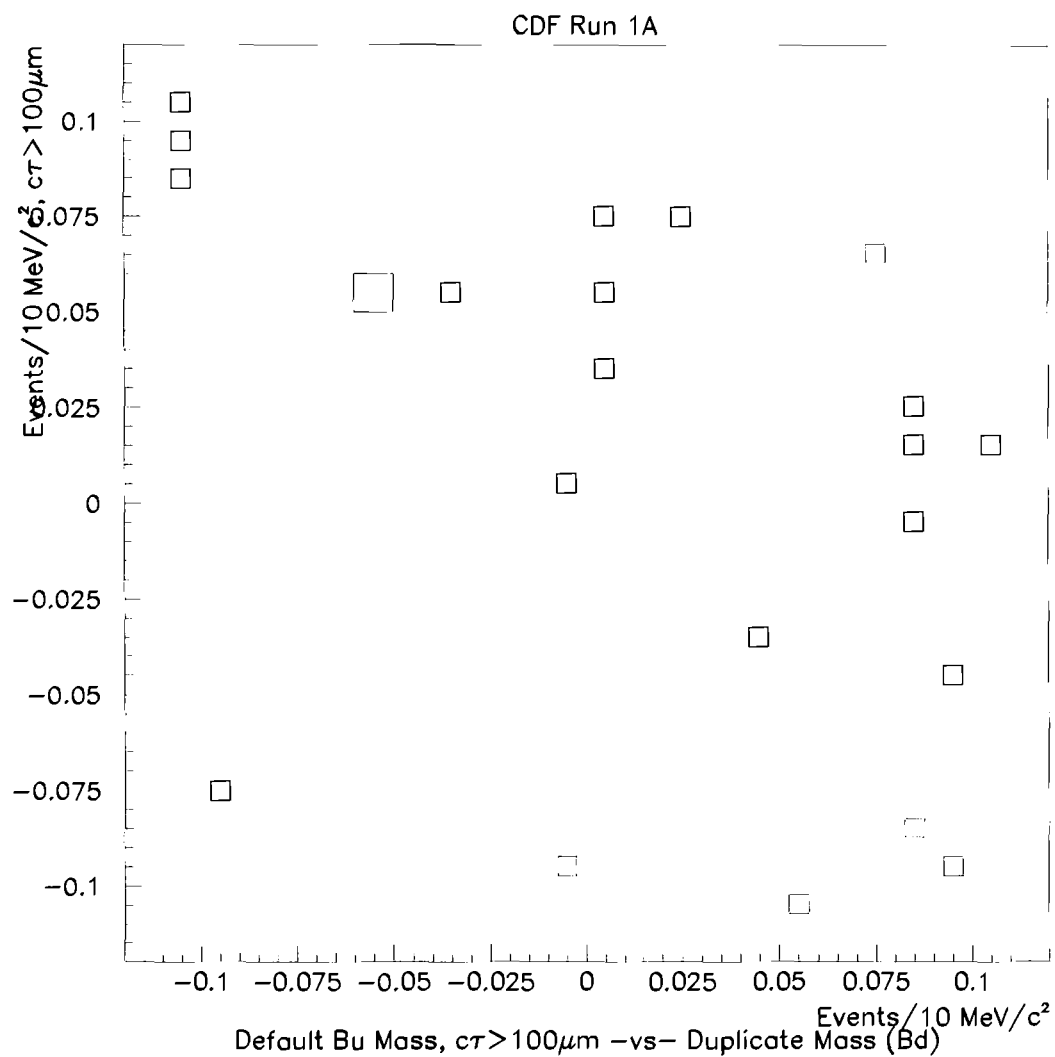


Figure A.16: Scatter plot of the invariant mass distribution (mass – 5.2786  $GeV/c^2$ ) of the selected  $B_u$  candidate versus the invariant mass distribution (mass – 5.2786  $GeV/c^2$ ) of the rejected  $B_d$  duplicates. Only those  $B_u$  events containing a  $B_d$  duplicate are plotted. This plot contains 23 entries.

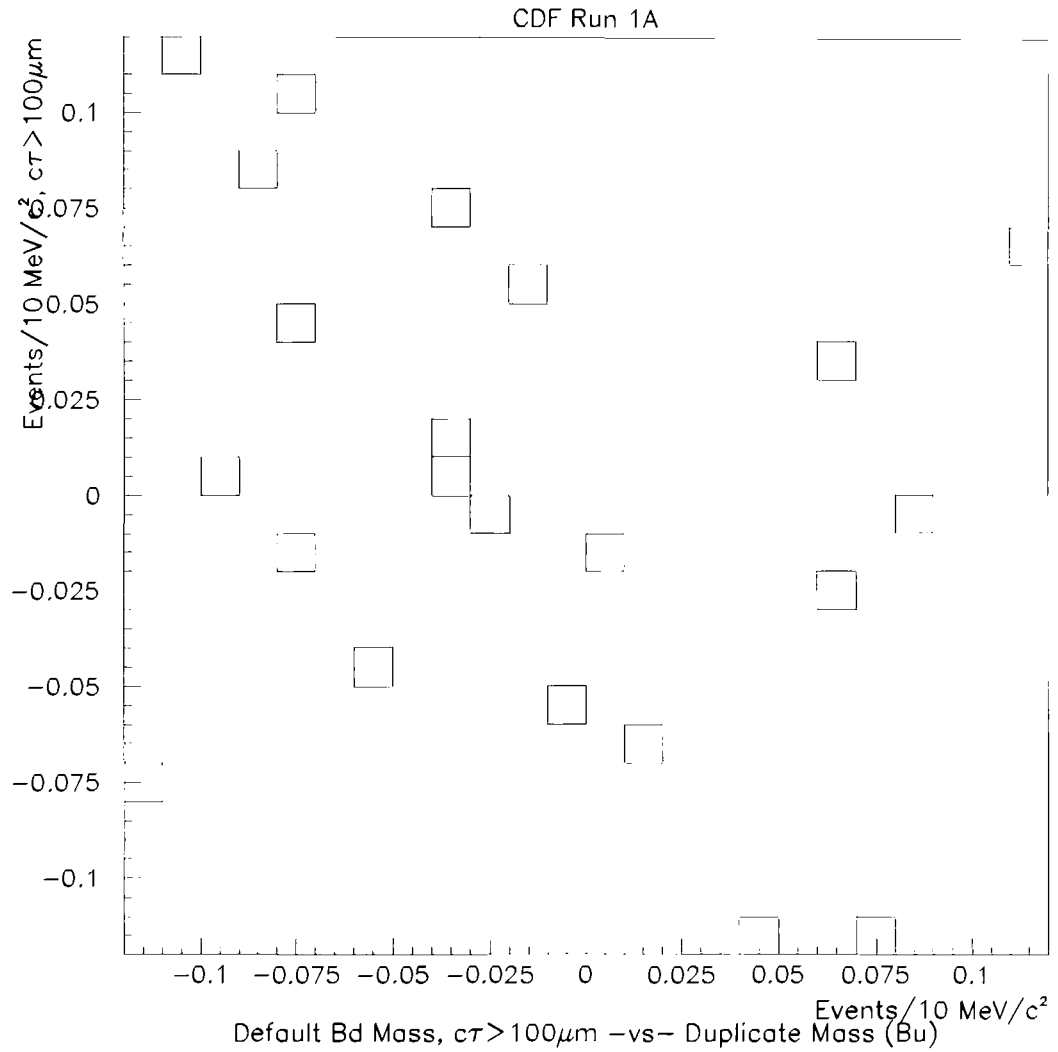


Figure A.17: Scatter plot of the invariant mass distribution (mass –  $5.2786 \text{ GeV}/c^2$ ) of the selected  $B_d$  candidate versus the invariant mass distribution (mass –  $5.2786 \text{ GeV}/c^2$ ) of the rejected  $B_u$  duplicates. Only those  $B_d$  events containing a  $B_u$  duplicate are plotted. This plot contains 22 entries.

$B_d \rightarrow \Psi K_S^0$ . As shown in Fig. A.18, 4(8)  $B_u(B_d)$  events have  $|\Delta c\tau/\sigma| > 3.0$ . For this reason and for reasons already discussed in Section 3.2, we only consider  $B_u(B_d)$  events with  $B_d(B_u)$  duplicates that happen to fall in the peak mass range in the following discussion. Table A.2 shows that we have 34(30)  $B_u(B_d)$  events satisfying this criterion.

Three tests were applied to check for biases introduced in the lifetime of the  $B_u$  and  $B_d$  mesons by this class of duplicate events:

1. Remove the 34(30)  $B_u(B_d)$  events with  $B_d(B_u)$  duplicates and refit for the lifetime. The observed shift in the lifetimes is  $\Delta c\tau^+ = +9 \pm 69 \mu m$  and  $\Delta c\tau^0 = +11 \pm 79 \mu m$ , assuming uncorrelated statistical errors. Note that the statistical uncertainty of the value of  $c\tau$  returned by the fit is  $\sim 50 \mu m$ .
2. Remove 34(30)  $B_u(B_d)$  events chosen at random and refit for the lifetime. The observed shift in the lifetimes is  $\Delta c\tau^+ = +4 \pm 69 \mu m$  and  $\Delta c\tau^0 = +10 \pm 79 \mu m$ , assuming uncorrelated statistical errors. Note that the statistical uncertainty of the value of  $c\tau$  returned by the fit is  $\sim 50 \mu m$ .
3. Replace the 34(30)  $B_u(B_d)$  candidates selected by the duplicate removal procedure with the 30(34) rejected candidates and refit for the lifetime. The observed shift in the lifetimes is  $\Delta c\tau^+ = -8 \pm 69 \mu m$  and  $\Delta c\tau^0 = +5 \pm 79 \mu m$ , assuming uncorrelated statistical errors. Note that the statistical uncertainty of the value of  $c\tau$  returned by the fit is  $\sim 50 \mu m$ .

The observed shift in the mean value of  $c\tau$  returned by the fit in all three cases is negligible compared to the statistical error on the measurement. Also, the observed shift of order  $\pm 10 \mu m$  is consistent with observed shifts obtained from consistency checks described in Section 4.5. For these reasons, no systematic uncertainty due to selecting a  $B_u(B_d)$  peak candidate among multiple  $B_d(B_u)$  peak candidates is assigned to the measured  $B$  meson lifetimes.

## A.5 Conclusion

This analysis represents the first high statistics, direct measurement of the  $B_u$  and  $B_d$  meson lifetimes. Because this measurement was dominated by

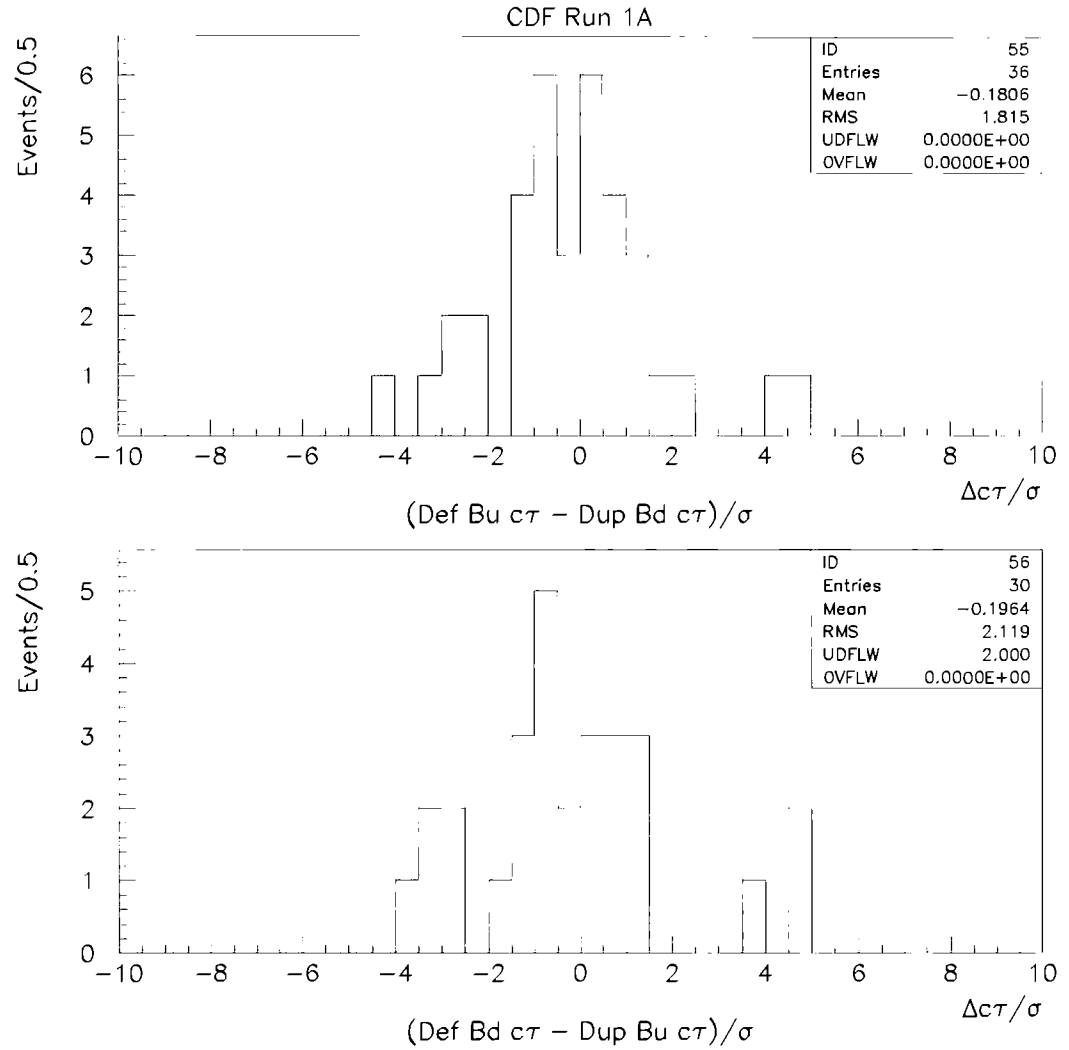


Figure A.18: Top plot: ( $c\tau$  of the selected  $B_u$  peak candidate -  $c\tau$  of rejected  $B_d$  peak candidate(s))/ $\sigma$ . There are 4 entries with  $|\Delta c\tau/\sigma| > 3.0$ . Bottom plot: ( $c\tau$  of selected  $B_d$  peak candidate -  $c\tau$  of rejected  $B_u$  peak candidate(s))/ $\sigma$ . There are 8 entries with  $|\Delta c\tau/\sigma| > 3.0$ .

statistical uncertainties, every attempt was made to lower the statistical error. This aim motivated the decision to select a single candidate among duplicate  $B$  candidates passing selection cuts in an event, rather than to reject such events altogether. This study has shown that the duplicate removal procedure did not measurably bias the final number of  $B_u(B_d)$  events, nor did it measurably bias their lifetime given the available statistics. Nevertheless, it is arguable that a systematic error of  $\sim 5 \mu m$  should have been included in the total systematic uncertainty calculation. This additional systematic uncertainty would add  $< 1 \mu m$  to the total systematic error quoted in the  $B_u$  and  $B_d$  lifetimes and is therefore negligible.

# Appendix B

## Lifetime Likelihood Function

This appendix derives the generalized equations for the unbinned likelihood fit performed simultaneously on the peak and sideband regions. In the discussion that follows, let  $i$  denote each  $B$  meson candidate; let  $x'_i$  be the measured proper decay length; let  $e'_i$  be the measured error on  $x'_i$ ; and let  $x_i$  denote the *real* proper decay length.

It is assumed that the measured proper decay length  $x'_i$  of a candidate that has its mass falling in one of the sideband regions has a probability density function (PDF) given by

$$g_{\sigma_i, \lambda^-, \lambda^+, f^-, f^+}(x') = \begin{cases} \frac{1-f^- - f^+}{\sigma_i \sqrt{2\pi}} \exp\left(\frac{-x'^2}{2\sigma_i^2}\right) + \frac{f^+}{\lambda^+} \exp\left(\frac{-x'}{\lambda^+}\right) & x' > 0 \\ \frac{1-f^- - f^+}{\sigma_i \sqrt{2\pi}} \exp\left(\frac{-x'^2}{2\sigma_i^2}\right) + \frac{f^-}{\lambda^-} \exp\left(\frac{x'}{\lambda^-}\right) & x' < 0. \end{cases} \quad (\text{B.1})$$

The function  $g_{\sigma_i, \lambda^-, \lambda^+, f^-, f^+}(x')$ , normalized to unity, is the sum of a Gaussian function centered at zero with a width  $\sigma_i$  and two exponential tails with slopes  $\lambda^-$  (negative side) and  $\lambda^+$  (positive side); these tails represent a fraction  $f^+$  and  $f^-$  of the total distribution. The function  $g_{\sigma_i, \lambda^-, \lambda^+, f^-, f^+}(x')$  is not continuous at  $x' = 0$  (unless  $\frac{f^+}{\lambda^+} = \frac{f^-}{\lambda^-}$ ). The fact that  $\frac{f^+}{\lambda^+} \neq \frac{f^-}{\lambda^-}$  when using the values returned from the fit to the data simply indicates that the physical mechanism responsible for negative tails is different from the one causing positive tails. The overwhelming majority of negative tails are the result of poorly measured tracks, while positive tails are caused both by poorly measured tracks and by a significant number of real  $B$  candidates in which one or more tracks combined with the  $\Psi$  actually come from the underlying event. These poorly

measured  $B$  candidates are responsible for the combinatoric background with large positive values of  $c\tau$ , but do not contribute to events with negative values of  $c\tau$ . Hence, it is to be expected that  $g(x')$  obtained from the fit to the data is not continuous at  $x' = 0$ . The discontinuity of the background PDF at  $x' = 0$  does not affect the convergence of the fit because no data candidates are observed with  $x'$  identically equal to 0.0. A candidate that has a mass falling in the peak region, but is actually contributing to the background under the true signal, is assumed to be distributed according to the same distribution  $g_{\sigma_i, \lambda^-, \lambda^+, f^-, f^+}(x')$ .

It is assumed that the proper decay length  $x'_i$  of a true  $B$  meson candidate with a mass falling in the peak region has a PDF given by the convolution of a “physics PDF” with a resolution function. The physics function, an exponential distribution with a lifetime  $\lambda = c\tau$ , is given by

$$p_\lambda(x) = \begin{cases} \frac{1}{\lambda} \exp\left(\frac{-x}{\lambda}\right) & x \geq 0 \\ 0 & x < 0. \end{cases} \quad (\text{B.2})$$

The resolution function is assumed to be symmetric; it is parameterized as a linear combination of a gaussian distribution (body) and exponential distributions (tails) as follows:

$$r_{\sigma_i, \beta_i, \mu_i}(y) = \beta_i r_{\sigma_i}^{body}(y) + (1 - \beta_i) r_{\mu_i}^{tails}(y) \quad (\text{B.3})$$

$$r_{\sigma_i}^{body}(y) = \frac{1}{\sigma_i \sqrt{2\pi}} \exp\left(\frac{-y^2}{2\sigma_i^2}\right) \quad (\text{B.4})$$

$$r_{\mu_i}^{tails}(y) = \frac{1}{2\mu_i} \exp\left(\frac{-|y|}{\mu_i}\right), \quad (\text{B.5})$$

where  $\sigma_i$  and  $\beta_i$  are the width and the fraction of the gaussian body, and  $\mu_i$  is the slope of the exponential tails. The PDF for a signal event is then given by:

$$f_{\lambda, \sigma_i, \beta_i, \mu_i}(x') = \int_{-\infty}^{+\infty} p_\lambda(x) r_{\sigma_i, \beta_i, \mu_i}(x' - x) dx \quad (\text{B.6})$$

$$= \beta_i f_{\lambda, \sigma_i}^{body}(x') + (1 - \beta_i) f_{\lambda, \mu_i}^{tails}(x'), \quad (\text{B.7})$$

where

$$f_{\lambda, \sigma_i}^{body}(x') = \int_{-\infty}^{+\infty} p_\lambda(x) r_{\sigma_i}^{body}(x' - x) dx \quad (\text{B.8})$$

$$= \frac{1}{\lambda} \exp\left(\frac{\sigma_i^2}{2\lambda^2} - \frac{x'}{\lambda}\right) \left[1 - \text{freq}\left(\frac{\sigma_i}{\lambda} - \frac{x'}{\sigma_i}\right)\right], \quad (\text{B.9})$$

where freq is just a CERN program library routine[51]

$$\text{freq}(t) = \frac{1}{\sqrt{2\pi}} \int_{-\infty}^t du \exp\left(-\frac{1}{2}u^2\right), \quad (\text{B.10})$$

and

$$f_{\lambda,\mu_i}^{\text{tails}}(x') = \int_{-\infty}^{+\infty} p_{\lambda}(x) r_{\mu_i}^{\text{tails}}(x' - x) dx \quad (\text{B.11})$$

$$= \begin{cases} \frac{1}{\lambda - \mu_i} \left[-\frac{1}{2} \exp\left(\frac{-x'}{\mu_i}\right) + \frac{\lambda}{\lambda + \mu_i} \exp\left(\frac{-x'}{\lambda}\right)\right] & x' > 0 \\ \frac{1}{\lambda + \mu_i} \left[+\frac{1}{2} \exp\left(\frac{\pm x'}{\mu_i}\right)\right] & x' < 0 \end{cases} \quad (\text{B.12})$$

$$= \frac{\lambda^2}{\lambda^2 - \mu_i^2} p_{\lambda}(x') + \frac{\mu_i}{\mu_i - \lambda \text{sign}(1, x')} r_{\mu_i}^{\text{tails}}(x') \quad x' \neq 0, \quad (\text{B.13})$$

where  $\text{sign}(1, x')$  is just the FORTRAN intrinsic function that assigns the sign of the second argument to the absolute value of the first. The function  $f_{\lambda,\mu_i}^{\text{tails}}(x')$  is continuous at  $x' = 0$ , i.e.

$$\lim_{x' \lesssim 0} f_{\lambda,\mu_i}^{\text{tails}}(x') = \lim_{x' \gtrsim 0} f_{\lambda,\mu_i}^{\text{tails}}(x') = \frac{1}{2(\lambda + \mu_i)}, \quad (\text{B.14})$$

and that

$$\lim_{\mu_i \rightarrow \lambda} f_{\lambda,\mu_i}^{\text{tails}}(x') = \frac{1}{2} \left[ r_{\lambda}^{\text{tails}}(x') + \frac{x'}{\lambda} p_{\lambda}(x') \right]. \quad (\text{B.15})$$

If  $\alpha$  is the probability for a candidate in the peak region to be a real signal event, then the PDF for any candidate  $i$  is given by:

$$h_{\alpha,\lambda,\sigma_i,\beta_i,\mu_i,\lambda^-, \lambda^+, f^-, f^+}(x') = \begin{cases} \alpha f_{\lambda,\sigma_i,\beta_i,\mu_i}(x') + (1 - \alpha) g_{\sigma_i,\lambda^-, \lambda^+, f^-, f^+}(x') & \text{for the peak region} \\ g_{\sigma_i,\lambda^-, \lambda^+, f^-, f^+}(x') & \text{for the sidebands.} \end{cases} \quad (\text{B.16})$$

Let  $m_A$  be the “width” of the peak region (or the number of bins in the peak region) and  $n_A$  the number of candidates found in the peak region. Let  $m_B$  be the total “width” of the sideband regions (or the total number of bins in the sideband regions) and  $n_B$  the number of candidates found in the

sideband regions. The measured numbers  $n_A$  and  $n_B$  are random variables following Poisson distributions. Let  $\bar{n}_A$  and  $\bar{n}_B$  be the mean values of these distributions.

If the background candidates have a flat mass spectrum (or if the background candidates have a linear distribution in mass and the peak and sideband regions are symmetric around the  $B$  mass) then the following must be true:

$$\alpha = 1 - \frac{\bar{n}_B}{\bar{n}_A} \frac{m_A}{m_B}. \quad (\text{B.17})$$

The above equation is just the mathematical form of the assumption that the average number of observed events per bin in the sidebands is equal to the average number of background candidates per bin under the signal in the peak region. Defining  $\bar{n}_{true}$  as the expectation value of the number of true signal candidates in the peak region,  $\bar{n}_A$  and  $\bar{n}_B$  can be expressed as functions of  $\bar{n}_{true}$  as follows:

$$\bar{n}_A = \frac{1}{\alpha} \bar{n}_{true} \quad (\text{B.18})$$

$$\bar{n}_B = \frac{1 - \alpha}{\alpha} \frac{m_B}{m_A} \bar{n}_{true} \quad (\text{B.19})$$

The likelihood of observing  $n_A$  candidates in the peak region with proper decay lengths  $x'_i$ ,  $i = 1, \dots, n_A$ , and  $n_B$  candidates in the sideband regions with proper decay lengths  $x'_i$ ,  $i = n_A + 1, \dots, n_A + n_B$ , is given by:

$$L = \frac{e^{-\bar{n}_A} \bar{n}_A^{n_A}}{n_A!} \cdot \frac{e^{-\bar{n}_B} \bar{n}_B^{n_B}}{n_B!} \cdot \prod_{i=1}^{n_A+n_B} h_{\alpha, \lambda, \sigma_i, \beta_i, \mu_i, \lambda^-, \lambda^+, f^-, f^+}(x'_i). \quad (\text{B.20})$$

This likelihood depends in principle on  $3n_A + 3n_B + 7$  independent parameters which are  $\lambda$ ,  $\alpha$ ,  $\lambda^-$ ,  $\lambda^+$ ,  $f^-$ ,  $f^+$ ,  $\bar{n}_{true}$ , and  $\sigma_i$ ,  $\beta_i$ ,  $\mu_i$ ,  $i = 1, \dots, n_A + n_B$  (the parameters  $\bar{n}_A$  and  $\bar{n}_B$  depend indeed on  $\alpha$  and  $\bar{n}_{true}$  as shown by Eqs. (B.18) and (B.19)). These parameters can obviously not be all determined by maximizing  $L$ .

If the estimate  $e'_i$  of the error on  $x'_i$  are a good enough approximation for  $\sigma_i$ , all of the  $\sigma_i$  can be fixed to their measured estimates  $e'_i$ . Nevertheless, if the overall normalization of the errors is uncertain, the  $\sigma_i$  can be assumed to be proportional to the  $e'_i$ , i.e.

$$\sigma_i = \rho e'_i, \quad \text{for } i = 1, \dots, n_A + n_B. \quad (\text{B.21})$$

In order to further reduce the number of parameters it can be assumed that all the  $\beta_i$  and all the  $\mu_i$  are equal:

$$\beta_i = \beta, \quad \mu_i = \mu, \quad \text{for } i = 1, \dots, n_A + n_B. \quad (\text{B.22})$$

In this case, the likelihood depends on only 10 parameters:

$$L(\lambda, \alpha, \bar{n}_{true}, \rho, \beta, \mu, \lambda^-, \lambda^+, f^-, f^+) = \frac{e^{-\bar{n}_A} \bar{n}_A^{n_A}}{n_A!} \cdot \frac{e^{-\bar{n}_B} \bar{n}_B^{n_B}}{n_B!} \cdot \prod_{i=1}^{n_A+n_B} h_{\alpha, \lambda, \rho e'_i, \beta, \mu, \lambda^-, \lambda^+, f^-, f^+}(x'_i), \quad (\text{B.23})$$

where  $\bar{n}_A$  and  $\bar{n}_B$  are given by Eqs. (B.18) and (B.19). Estimates for the 10 independent parameters  $\lambda, \alpha, \bar{n}_{true}, \rho, \beta, \mu, \lambda^-, \lambda^+, f^-,$  and  $f^+$  are obtained by maximizing  $L$ . In practice,  $-2\ln(L)$  is minimized using MINUIT[52].

The results of the fit are displayed as two histograms (see Figs 4.13 and 4.14) of the quantity  $x'$  with a bin size of  $\Delta x'$ . The first histogram is filled with the candidates falling in the peak region and displayed on top of a curve  $F_A(x')$ . The second histogram is filled with the candidates falling in the sideband regions and displayed on top of a curve  $F_B(x')$ . The functions  $F_A$  and  $F_B$  are given by

$$F_A(x') = \bar{n}_A \Delta x' \cdot \frac{1}{n_A} \sum_{i=1}^{n_A} \left[ \alpha f_{\lambda, \rho e'_i, \beta, \mu}(x') + (1 - \alpha) g_{\rho e'_i, \lambda^-, \lambda^+, f^-, f^+}(x') \right], \quad (\text{B.24})$$

$$F_B(x') = \bar{n}_B \Delta x' \cdot \frac{1}{n_B} \sum_{i=1}^{n_B} g_{\rho e'_i, \lambda^-, \lambda^+, f^-, f^+}(x'), \quad (\text{B.25})$$

where  $\bar{n}_A$  and  $\bar{n}_B$  are given by Eqs. (B.18) and (B.19), and where  $\lambda, \alpha, \bar{n}_{true}, \rho, \lambda^-, \lambda^+, f^-,$  and  $f^+$  have their values that maximize the likelihood  $L$ . These functions are not normalized to the number of events in the histograms, but rather to the number of events returned by the fit, i.e.

$$\int F_A(x') dx' = \bar{n}_A \Delta x' \quad ; \quad \int F_B(x') dx' = \bar{n}_B \Delta x'. \quad (\text{B.26})$$

# Bibliography

- [1] F. Abe *et al.*, Phys. Rev. Lett. **72** 3456 (1994).
- [2] G. Crawford *et al.*, CLEO CONF 93-30, *A Measurement of  $BR(\bar{B}^0 \rightarrow D^{*+}l^{-}\bar{\nu})$* , contributed paper to the 1993 Lepton-Photon Conference, August, 1993, Ithaca, New York.
- [3] F. Abe *et al.*, Phys. Rev. Lett. **71** 3421 (1993).
- [4] S. Stone (ed.), *B Decays*, World Scientific, Singapore, 1992.
- [5] I. Bigi and N. G. Uraltsev, Phys. Lett. **B280** 271 (1992); I. Bigi, B. Block, M. Shifman, N. Uraltsev and A. Vainshtein, CERN-TH.7132/94, *Non-Leptonic Decays of Beauty [sic] Hadrons — from Phenomenology to Theory*, to be published in *B Decays*, 2nd edition, S. Stone (ed.), World Scientific, Singapore, 1994.
- [6] Aleph Collaboration, CERN-93-42, *Measurement of the  $\bar{B}^0$  and  $B^-$  Meson Lifetimes*, submitted to Phys. Lett. **B**, March, 1993.
- [7] J. Raab *et al.*, Phys. Rev. **D37** 2391 (1988).
- [8] M. Tanimoto, Phys. Lett. **B274** 463 (1992).
- [9] H. Nelson *et al.*, UCSB-94-01, *Heavy Quark Hadronic Weak Decays from CLEO-II*, contributed paper to the International Europhysics Conference on High Energy Physics, July, 1993, Marseille, France.
- [10] An excellent introduction to the Standard Model is F. Halzen and A. Martin, *Quarks and Leptons: An Introductory Course in Modern Particle Physics*, John Wiley and Sons; New York, New York, 1984; an ex-

cellent, detailed treatment of the Standard Model is C. Quigg, *Gauge Theories of the Strong, Weak, and Electromagnetic Interactions*, Benjamin/Cummings Publishing Company; Menlo Park, California, 1983.

- [11] P. W. Higgs, *Phys Rev. Lett.* **13** 508 (1964).
- [12] C. N. Yang and R. L. Mills, *Phys. Rev.* **96** 191 (1954); H. Fritzsch, M. Gell-Mann and H. Leutwyler, *Phys. Lett.* B47 365 (1973).
- [13] S. L. Glashow, *Nucl. Phys.* **22** 579 (1961); S. Weinberg, *Phys. Rev. Lett.* **19** 1264 (1967); A. Salam, *Elementary Particle Theory*, N. Svartholm (ed.), Almquist and Wiksells, Stockholm, 367, 1969.
- [14] Particle Data Group, *Phys. Rev* D**45** (1992).
- [15] F. Abe *et al.*, *Phys. Rev. Lett* **73** 225 (1994).
- [16] J. Kim *et al.*, *Rev. Mod. Phys.* **53** 211 (1981).
- [17] N. Cabibbo, *Phys. Rev. Lett.* **10** 531 (1963).
- [18] M. Kobayashi and K. Maskawa, *Prog. Theor. Phys.* **49** 652 (1973).
- [19] C. Hill, Fermilab 93/256-T, (1993).
- [20] H. Albrecht *et al.*, *Phys. Lett.* B**199** 451 (1987); M. S. Alam *et al.*, *Phys. Rev.* D**34** 3279 (1986).
- [21] F. Abe *et al.*, *Phys. Rev. Lett.* **69** 3705 (1992).
- [22] E. W. N. Glover, F. Halzen and A. D. Martin, *Phys. Lett.* B**185** 441, (1987).
- [23] C. Peterson *et al.*, *Phys. Rev.* D**27** 105 (1983).
- [24] E. Fernandez *et al.*, *Phys. Rev. Lett.* **51** 1022 (1983); N. S. Lockyer *et al.*, *Phys. Rev. Lett.* **51** 1316 (1983).
- [25] V. Barger, W. F. Long and S. Pakvasa, *J. Phys.* G**5** L147 (1979).
- [26] J. Bjorken, *Nucl. Phys.* B**11** 325 (1989).

- [27] B. E. Palladino, *HQET - A Short Review*, IFT-P.018/94, to be published in the proceedings of Hadrons '94, Brazil.
- [28] M. Neubert, Phys. Lett. **B264** 455 (1991).
- [29] N. Isgur and M. B. Wise, Phys. Lett. **B232** 113 (1989); N. Isgur and M. B. Wise, Phys. Lett. **B237** 527 (1990); A. F. Falk, H. Georgi, B. Grinstein and M. B. Wise, Nucl. Phys. **B343** 1 (1990).
- [30] S. C. O'Day, personal communication.
- [31] F. Abe *et al.*, Nucl. Inst. and Meth. **A271** 387 (1988) and references therein.
- [32] D. Amidei *et al.*, FERMILAB PUB-94/024-E, submitted to Nucl. Inst. and Meth.; B. Barnett *et al.*, Nucl. Inst. and Meth. **A315** 125 (1992); O. Schneider *et al.*, Proceedings of the 7<sup>th</sup> Meeting of the American Physical Society, Division of Particles and Fields, Fermilab, Nov 1992, World Scientific Press, 1743.
- [33] G. W. Foster, J. Freeman, C. Newman-Holmes and J. Patrick, Nucl. Inst. and Meth. **A269** 93 (1988).
- [34] W. Badgett *et al.*, *The CDF Level 2 Trigger For The 1992-93 Run*, CDF Internal Note 2016 (1993).
- [35] D. Amidei *et al.*, Nucl. Inst. and Meth. **A269** 51 (1988).
- [36] T. Carroll *et al.*, *it CDF Level 3 Trigger*, CDF Internal Note 895 (1989) and in Proceedings of Workshop on Triggering and Data Acquisition for Experiments at the Superconducting Super Collider, Toronto, Canada.
- [37] A. Caner and A. Mukherjee, *Level 3 Dimuon Trigger*, CDF Internal Note 1564 (1991).
- [38] P. Schlabach, personal communication.
- [39] M. Spahn *et al.*, *A Study of Tracking Systematics in the CTC*, CDF Internal Note 1539 (1991).

- [40] H. Wenzel, *Tracking in the SVX*, CDF Internal Note 1790 (1992).
- [41] F. Bedeschi, *An Inexpensive Method for Global Track Fitting and Track Segment Matching*, CDF Internal Note 371 (1985).
- [42] D. Quarrie and B. Troemel, *YBOS Programmers Reference Manual*, CDF Internal Note 156 (1991).
- [43] F. DeJongh and R. Hans, *Level 1 and Level 2 Low  $P_t$  Central Muon Trigger Efficiencies for Run 1A*, CDF Internal Note 1999 (1993).
- [44] F. DeJongh, *Level 3 Dimuon Efficiency for Run 1A*, CDF Internal Note 1984, (1993).
- [45] F. Bedeschi *et al.*, *A Measurement of  $B^\pm$  and  $B^0$  Lifetimes Using Exclusive Decay Channels*, CDF Internal Note 2141, (1993).
- [46] H. Wenzel, *Fitting the Beam Position with the SVX*, CDF Internal Note 1924 (1993).
- [47] H. Wenzel, *Measurement of the Inclusive  $B$ -Lifetime Using  $J/\psi$ 's at the CDF-Experiment*, PhD Thesis, Rheinisch-Westfälische Technische Hochschule Aachen, 1993.
- [48] A. G. Frodesen, O. Skjeggstad, and H. Tøfte, *Probability and Statistics in Particle Physics*, 1979, Columbia University Press, NY.
- [49] F. Abe *et al.*, *Phys. Rev. Lett.* **71** 3421 (1993).
- [50] CERN Application Software Group, *PAW: Physics Analysis Workstation*, CERN (1992).
- [51] CERN Application Software Group, *CERNLIB: Short Writeups*, CERN (1992).
- [52] F. James and M. Roos, *MINUIT: Function Minimization and Error Analysis*, CERN (1989).
- [53] O. Schneider, J. Skarha and A. Spies, *Examination of the Extreme Tails of the Exclusive  $B$  Lifetime Distribution*, CDF Internal Note 2373 (1993).

- [54] P. Derwent, personal communication.
- [55] S. Wagner *et al.*, Phys. Rev. Lett. **64** 1095 (1990); P. Abreu *et al.*, Z. Phys. **C57** 181 (1993); D. Buskulic *et al.*, Phys. Lett. **B297** 449 (1992); D. Buskulic *et al.*, Phys. Lett. **B307** 194 (1993); D. Buskulic *et al.*, Phys. Lett. **B314** 459 (1993); P.D. Acton *et al.*, Phys. Lett. **B307** 247 (1993).
- [56] H. Albrecht *et al.*, Phys. Lett. **B275** 195 (1992); R. Fulton *et al.*, Phys. Rev. **D43** 236 (1991); M. Artuso *et al.*, *A Measurement of the Charged and Neutral B Meson Lifetime Ratio*, contributed paper to the 1993 Lepton-Photon Conference, August 1993, Ithaca, New York.
- [57] W. Venus, *Recent Results on Bottom Physics above Threshold*, to be published in the proceedings of the 1993 Lepton-Photon Conference, August, 1993, Ithaca, New York.
- [58] J. Skarha,  $|V_{cb}|$  *Using the CDF Exclusive  $B^0$  Lifetime Measurement*, CDF Internal Note 2380 (1993)
- [59] F. Ukegawa, Y. Cen and A. B. Wicklund, *Measurement of Charged and Neutral B Meson Lifetimes Using Electron-Charm Events*, CDF Internal Note 2598 (1994).
- [60] S. Vejcik III, *A Measurement of the B Quark and Neutral B Meson Production Cross Sections in Proton-Antiproton Collisions at a Center of Mass Energy of 1.8 TeV*, PhD Thesis, The Johns Hopkins University, 1992.

**Vita**

The author was born in Norman, Oklahoma to David and Patricia Spies on November 4, 1966. He attended public schools in Picayune, Mississippi before entering Rhodes College in Memphis, Tennessee where he received the Bachelor of Science degree and was initiated into  $\Phi BK$  in May, 1988. He began graduate study in September, 1988, at The Johns Hopkins University in Baltimore, Maryland and received the Master of Arts degree in October, 1990. His research in experimental high energy physics began on the CDF collaboration at Fermilab in Batavia, Illinois during the summer of 1990 and culminated in a doctoral thesis, *A Measurement of the Charged and Neutral B Meson Lifetimes Using Fully Reconstructed Decay Modes*.